High-frequency acoustoelectronic phenomena in miniband superlattices

Apostolos Apostolakis, MSci

A Doctoral Thesis

Submitted in partial fulfilment of the requirements for the award of
Doctor of Philosophy of Loughborough University

February 2017

Abstract

The motion of a quantum particle in a periodic potential can generate rich dynamics in the presence of a driving field. Such systems include, but are not limited to, semiconductor superlattices which exhibit a very anisotropic band structure that results into pronounced nonlinearities and high carrier mobility. In this thesis, we investigate the semiclassical dynamics and electron transport in a spatially periodic potential driven by a propagating wave.

Firstly, we examine the transport features of an electron in a single miniband superlattice driven by a high-frequency acoustic plane wave. In this system, the nonlinear electron dynamics crucially depends on the amplitude of the acoustic wave. The transport characteristics are studied by means of a non-linearised kinetic model. In particular, to provide a realistic description of the directed transport, we employ the exact path-integral solutions of the Boltzmann transport equation. The calculated electron drift velocity and the time-averaged velocity show a nonmonotonic dependence upon the amplitude of the acoustic wave with multiple pronounced extrema. We found out that the changes in the velocity-amplitude characteristics are directly associated with a series of global bifurcations due to topological rearrangements of the phase space of the system. These dramatic transformations are connected with superlattice intraminiband transitions, and accompanied by inelastic emission (absorption) of the quantum particle. The bifurcations also signify the transitions between different dynamical regimes, involving unconfined electron motion, wave-dragging and phonon-assisted Bloch oscillations. Each regime has a characteristic spectral fingerprint, which manifests itself in appearance of specific high-frequency components in the spectra of the corresponding averaging trajectory.

Secondly, we consider to use the acoustically pumped superlattices for an amplification of THz electromagnetic waves, involving the mechanisms similar to the Bloch gain in electrically biased superlattices. In particular, we predict the tunable THz gain due to nonlinear oscillations which are associated with the localised motion of electrons confined by a propagating potential wave. Traditionally, one of the key issues which emerges from considering different schemes for achieving small signal gain in superlattices, is the control of electric stability. Here, it is shown that for our case of the fast miniband electrons driven by an acoustic wave, terahertz gain can occur without the electric instability. Additionally, we find that the characteristic changes in the averaged velocities are connected to the shape of gain profiles. Consequently, the analytic findings, which determine the transitions between different dynamical regimes at the bifurcations, hold up for the behaviour of amplification of high-frequency electromagnetic waves. The increase of the miniband width, results in an enhancement of the effect of phase space restructuring on the drift velocity and high-frequency gain.

Finally, we analyse the case for a superlattice device utilising acoustic waves with a very slow propagation speed. Benefiting from a simple solution of the Boltzmann equation, here we clarify the role of spatial nonlinearity both in miniband electron dynamics and in amplification of an electromagnetic wave. We show that nonlinear Bloch oscillations occur at a single critical value of the wave amplitude, inducing high negative differential drift velocity. Within this model, we also explain how the amplification of a high-frequency signal can arise below the threshold for an excitation of Bloch oscillations.

Acknowledgements

First and foremost I would like to thank my supervisors, Dr Kirill Alekseev and Dr Alexander Balanov, for their untiring support and intuitive mentoring. Alexander and Kirill not only encouraged me to complete this thesis but they essentially provided all the pillars to deepen my knowledge and understanding about physics. It still strikes me as fascinating that they are able to explain complex physical phenomena with a simple and coherent way without diminishing the fine details. Aside from the experience of working with them, I was always enjoying our discussions that reflected their sharp wit and amicable attitude.

I would also like to thank all the people in physics department of Loughborough University for their helpful mentality and creating a positive work environment. A special thanks goes to Professor Feo Kusmartsev for fruitful discussions that attracted my attention to different aspects in phenomena taking place in superlattices. Here I would like to acknowledge all my office mates in room W210 for having the same concerns but also indulging in beautiful discussions. This includes Dr Alan Wu, Dr Mike Pierpoint, Dr Dirk Visser, Aidan Wilkinson, Richard Cole and Vasilis Tzanos.

I am honestly grateful to my friends that I have met here in Loughborough for all the stories, experiences and thoughts we have shared together but above all for their guileless interest and encouragement.

Last but not least, I would like to express my gratitude to my family for their unconditional love and support, especially to my parents Philippos and Konstantina and my brother Kostas for their empathetic lexis and praxis.

Contents

Chapter 1

Introduction

The fabrication of the devices which can be utilised in high-performance electronic applications, constantly regenerates the intense research interest. A number of efficient devices have been already synthesized by tuning the electronic properties related to the nature of materials and device engineering. In particular, it is useful to list the type of materials engaged in the so-called modern day electronic revolution [1, 2]: semiconductors for active components of a device, metals for contacts and high band-gap materials for insulation. Therefore elemental semiconductors, such as silicon (Si) or germanium (Ge) located in column IV of the periodic table of chemical elements, provide a class of materials functional for transistors. Compound semiconductors including GaAs (group III-V) for example, have attractive properties such as high speed, and thus they play a valuable role in microwave detectors [3] or photonic devices [4]. Beyond III-V compounds suitable in injection layers and light emitting diodes (LED). Although, the semiconductor systems exhibit brilliant efficiency, especially in integrated circuits, it should be readily appreciated that their scaling limits are associated with power and thermal challenges [5, 6]. That is why even today, many high-power devices are based not on semiconductors but on vacuum technology. Examples include magnetrons as microwave generators [7], and traveling-wave tubes [8] which are used into electronics to amplify signals in the microwave range. These devices though are dictated by technical constraints related to system design or performance. For example, the size of a magnetron is determined by the operating frequency. This delimits the surface area available for heat dissipation and the maximal operating power. Given this emphasis, every material presents inherited limitations and can offer pragmatic solutions only to a specific set of problems. A common approach to circumvent the difficulties associated with physical restraints of natural materials, it is the investigation of new technical schemes or designing novel artificial materials. Beyond this technological-driven perspective, new materials pose scientific challenges and the chance to deal with new complicated properties.

In this thesis, we theoretically study the electron transport in semiconductor superlattices (SLs) which spans a wide range of quantum mechanical and kinetic phenomena [9–12]. These phenomena are associated with high-frequency electrodynamical properties, affecting the carrier dynamics in such a way, which leads to emission of terahertz (THz) radiation. Therefore, SLs become one of the prime choices for the development of THz devices involved in generating, amplifying, mixing and detecting high-frequency electromagnetic radiation [13–17]. L. Esaki and R. Tsu more than 40 years ago, introduced the man-made superlattice[1] employing periodic heterostructures to mimic solids [9, 10]. To create this type of artificial structure, two different semiconductor materials of almost equal lattice constant, but with different energy bands, are periodically layered, resulting in the modulation of potential energy only in one direction, the one perpendicular to the planar layers. It was recognised that negative differential conductance (NDC) under the condition of the realisation of Bloch oscillations should appear in the current-voltage characteristic of a superlattice structure. It was also pointed out that the emergence of NDC up to frequencies on the order of the Bloch oscillation frequency, makes the SL a potential candidate to provide an active medium in a amplifier or a oscillator operating in the THz regime [9]. However, NDC effects emerge also in devices such as Gunn oscillators [20–22] practically induced due to the formation of charge domains triggered by uneven electric field distribution along the device. In this case, the origin of negative differential conductivity can be understood as a change in the state of the system, attempting to find a minimum total energy for the system and thus resulting to the electric instability [23]. This argument led, Esaki and Tsu to study experimentally a single SL unit cell[2] (a quantum well between barriers), to avoid any domain formation [24]. The double-barrier single well structure was a remarkable achievement, demonstrating resonant tunneling accompanied again by negative differential conductance. The experimental realisation of RTD [24, 25] stimulated the direction of research towards semiconductor quantum heterostructures, thereby helping to achieve terahertz RDTs [26, 27], and quantum cascade lasers (QCLs) [28, 29]. It is worth noting that adjusting the specific sequence of quantum wells and barriers of the semiconductor heterostructure allows both the electronic and optical properties to be tailored at will. Interestingly, the structure of QCLs enables them to operate and emit in the mid-to far-infra-red bands of electromagnetic spectrum. In princi-

---

[1] At almost the same time Yu. A. Romanov *et al.* proposed a model of semiconductor superlattice on the basis of a semiconductor crystal with periodically varying chemical composition [18, 19].

[2] resonant tunneling via man-made double barrier heterostructures goes under the name of the resonant tunneling diode (RTD).

ple, electrons in quantum cascade lasers propagate through a potential staircase of multiple coupled quantum wells, making feasible the population inversion between energy sub-bands (quantised levels). The development of the QCL stemmed from the initial idea of R. F. Kazarinov and R. A. Suris in 1971 [30] proposing to use the intersubband transitions in a biased superlattice for light amplification, and it was experimentally realised by J. Faist *et al.* almost thirty years later [28]. At present, the design flexibility has expanded the achievable wavelength of QCLs to 3.7-5 µm and the terahertz regime, and enhanced the overall performance in terms of output power and efficiency [31, 32]. However, despite the continuous efforts to advance towards high-temperature operation of these devices, the quantum cascade lasers are still limited in cryogenic operation. The increased sensitivity of QC Laser performance to temperature is associated with thermionic emission out of the quantum structure into the continuum states and the thermal backfilling of the lower laser level [31–33].

In a superlattice, the barrier thickness can be so small that carriers can tunnel in neighbouring wells. As a result, instead of the quantized energy levels, relatively narrow energy minibands are formed that correspond to extended states which are called Bloch states [10, 34]. Excluding the possibility of electron to move between energy bands [35], and assuming that it can travel between scattering events a distance in k–space larger than the dimensions of the zone, it would be possible for a dc electric field E_{dc} to induce a motion, where the electron returns periodically to its initial state. The frequency, $\omega_B = eE_{dc}d/\hbar$ (where $e < 0$ is the electron charge), of these oscillations which are referred as Bloch oscillations, is proportional to the applied electric field E_{dc} and lattice period d. Scattering rate, however, for conventional materials is significant larger than ω_B and therefore excludes the possibility of Bloch oscillations. In that case, the picture of electron transport can be described by Drude model [36]. On the other hand, the restriction to observing Bloch oscillations in natural crystals may be undone in SLs, where the large effective SL period substantially increases the frequency of the Bloch oscillations allowing the particle to Bloch oscillate before scattering. The experimental observation of Bloch oscillations has been possible in different occasions by implementing several optical methods [37]. These optical techniques initially included degenerate four-wave mixing experiments [38] and later on time-domain terahertz spectroscopy was used to detect electromagnetic "Bloch" radiation [13]. One of the important features of the realisation of Bloch oscillations in SL is that they survive at room temperature [39]. Hence, the structure of superlattices makes them the ideal solid in which to explore the use of Bloch oscillations.

An alternative approach to achieve gain in SLs is to use the mechanism which is related to the so-called Bloch gain. In this case, as was initially pointed out by Ktitorov *et al.* in 1972, the electrons oscillating at Bloch frequency ω_B in the presence of dissipation, should provide gain for frequencies $\omega < \omega_B$ [40]. This prediction was based on semiclassical arguments, raising the possibility of inversionless lasing in dc biased SL. Subsequently, the discussion over Bloch gain triggered the interest for designing a device where a superlattice under constant electric bias is connected to a resonator whose mode frequency is tunable to the desirable frequency range. The device was named Bloch oscillator and it continues through to the present day to be considered as the holy grail of the semiconductor community. Although, considerable efforts have been devoted to develop a continuous wave Bloch oscillator [9], only transient THz emission from Bloch oscillations was obtained so far. The difficulties of realising the Bloch oscillator have been associated to the formation of destructive electric domains in the region of negative differential conductivity [41, 42]. Previously, different theoretical schemes have been proposed to overcome the electric instability in conditions of NDC [11, 43, 44]. The proposed models included the demonstration of stable THz gain in superlattices using modulated bias [15] and also with a tilted magnetic field applied [45]. The use of phononic waves though, opens new opportunities to enhance the perfomance of superlattice oscillators [46]. This argument is based on the recent finding that acoustic waves in SLs can induce THz electron dynamics even when no bias voltage is applied [47, 48].

In general, the interaction between electrons and acoustic phonons plays a significant role in the transient transport, optical and kinetic properties in crystals [49]. The concept of "phonon" has arisen as a way for interpreting the vibrations in a crystal lattice [50]. Specifically, defined as a quantum of the lattice vibrational field, by analogy with the photons of the electromagnetic waves, it can be assigned as the quasi-particle of the wave travelling through the lattice which, if longitudinally polarised is referred to as acoustic (sound) wave. In the past few decades, there has been an intensive research activity towards the the development of connection between phonon physics and dynamics of periodic materials and structures. This class of systems, which is often referred to as phononic materials [51], includes devices such as phononic crystals [52], acoustic diodes [53] controlling the sound transmission and current developments of acoustic cloaking [54] employing metamaterials.
One of the interesting aspects of phonon properties, it is that they can be used for manipulation and control of electrons in nanostructures. On this basis, considering high-frequency (GHz and THz) phonons, allows extended schemes to electronics. Therefore, the semiconductor superlattice structure is not only prescribed with distinct electronic and photonic properties but also the interaction of phonons with electrons which is associated with a number of interesting and important transport phenomena in SLs [55–58]. Actually, even at some fundamental level the superlattice displays well-defined phonon properties [1, 59]. The reciprocal space is folded

for electrons due to structure of SL and results into a set of novel features (formation of minibands, localisation, large gaps between minibands). In the same way some of these characteristics have implications in phonon spectra. Acoustic waves of low frequency unlike optical phonons, propagate almost unhindered similar to crystal quartz which exhibits a high quality factor [60]. Consequently, acoustic phonons should demonstrate pronounced SL effects. Recently, it was discovered that superlattices enable the processes of amplification and control of coherent hypersound oscillations [56–58]. In addition, it was shown that the acoustical excitation of semiconductor heterostructures can lead to high-frequency carrier transport and thus resulting in emission of electromagnetic waves [48, 61, 62]. The existing of theoretical basis provides a fertile background for the understanding of the related high-frequency acoustoelectronic phenomena [47, 63–65]. Nevertheless, no substantial results have been produced to unveil the underlying mechanisms of acoustoelectric transport, considering a nonlinear dynamical framework. In this work, we theoretically investigate semiclassical dynamics of particles in a spatially periodic potential generated by a propagating plane wave. Therefore, our interest has focused primarily on the highlighted example of single miniband SL driven by an acoustic wave in the sub-THz frequency region [58]. To describe the interaction between electrons and acoustic wave in the strongly coupled superlattice, we employ the exact path integral solutions of the Boltzmann transport equation [66, 67]. In this case, further analysis of the Hamiltonian dynamics is addressed to afford a better overall picture of the single electron behaviour. Our study examines as well different possibilities to tackle the general matter of Bloch gain profile. Thus, we propose an approach for the generation and amplification of THz radiation in acoustically driven superlattice similar to the Bloch gain in electrically biased SLs [40, 68].

THz radiation and applications

The possibility of a semiconductor laser in THz region together with the intriguing optoelectronic properties of semiconductor superlattices (SSLs), have triggered the interest for fundamental development and study of semiconductor heterostructure elements. As was already mentioned, the related gain mechanisms in SL rely either on intersubband transitions of semiconductor structure or the second order processes attributed to inversionless lasing in dc biased SL. The realisation of these different approaches aiming to fill the so-called "THz gap" [69, 70] lying roughly between 300 GHz (0.3 THz) and 30 THz spectral range of electromagnetic radiation (see figure 1.1). Historically, the term "THz gap" was coined to refer to terahertz band, due to severe shortage of devices generating and detecting coherently the

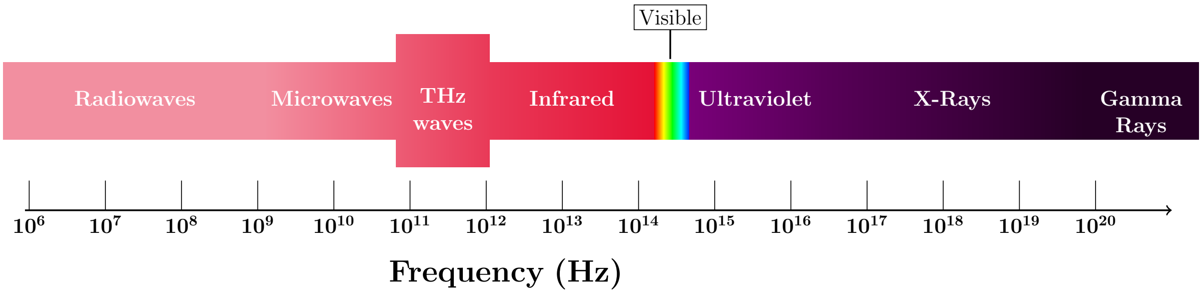

Figure 1.1: Spectrum of electromagnetic radiation, highlighting the terahertz spectral range.

radiation at these frequencies. In this section we review shortly the near-term practical applications of terahertz radiation, enabled by devices bridging the THz gap. The identified physical mechanisms of interactions between THz waves and matter then can be extensive involving molecular rotations, lattice vibrations, spin waves and internal excitations of bound electron-hole pairs [71–75]. It may, therefore, come as no surprise that the technology that can detect amplitude and phase of coherently generated electromagnetic radiation in the THz range is a precious spectroscopic tool, allowing investigations with very high spatial resolution [69, 74]. A rich variety of non-conducting materials can be penetrated by terahertz waves, including plastic, ceramics, wood, papers and clothing. However, penetration is limited in high-water contents or metal objects. These properties lend themselves to imaging systems alternative to mainstream solid-state analytical tools such as X-ray diffractions or thermal analysis. THZ waves have a great potential for security applications [76] and quality control [77] since THz spectroscopy can contribute to online measurement, remote sampling and three-dimensional imaging [78–80].

Terahertz radiation may be involved in biomedical imaging, offering a non-ionising alternative to X-rays [81]. Interestingly, the non-thermal effect of THz radiation on gene expression is negligible [82]. The terahertz technology has also attracted the interest of radio-astronomers because spectroscopy at THz frequency holds the key to our ability to remote sense emissions from molecular clouds in space, planet atmospheres and primaeval galaxies [70, 83].

An in-depth analysis of all the possible applications related to the control of THz pulses is beyond the scope of this work. Nevertheless, it is clear from our previous discussion, the importance of fine-tuning the electro-optical properties of semiconductor superlattices to obtain THz technology. In particular, this research investigates how SLs driven by acoustic wave can be used for the tunable generation of high-frequency (sub-terahertz and terahertz) electromagnetic waves.

Structure of this work

The present thesis has the following structure. Chapter 2 revisits the fundamental properties of semiconductor superlattices and discusses the mathematical formalism which is mainly involved in describing the miniband transport. Therefore, summarising the electron transport phenomena (i.e. Bloch oscillations, localisation, cyclotron oscillations) taking place in SL offers an physical insight into interaction of THz fields with transport through superlattices and miniband structure. Furthermore, the establishment of semiclassical Boltzmann approach that relies on the large band width, provides a powerful mathematical technique which is employed to study problems related to electron dynamics.

Chapter 3 is devoted to study the semiclassical dynamics of an electron, which tunnels through spatio-temporal potential of strongly-coupled superlattice driven by a plane acoustic wave. In particular, by extending the semiclassical formulation which was developed in the previous chapter, we characterise the charge transport in SL in the presence of scattering and identify the related dynamical regimes. To complete the picture in regard to charge oscillations induced by the acoustic wave, we examine the frequency characteristics of the ballistic electron transport. Chapter 4 following previously discussed concepts of the Bloch gain in dc-ac driven SLs or ac-driven SLs, develops an approach to study the possibility of amplification of THz signals for the acoustically pumped SL. Hence, in different limits we analyse the influence of the acoustoelectric field in Bloch gain. Chapter 5 considers the electron dynamics in SLs in the presence of a stationary potential wave and the implications on high-frequency gain. Eventually, the conclusions and the suggestions for future research are enclosed in the final chapter.

Chapter 2

Fundamental of superlattices: materials and physics properties

Superlattice structure

Let us take a closer look at superlattice structure. A typical semiconductor superlattice is schematically represented in figure 2.1. Following the original idea [10], this material grown by molecular epitaxy [84], consists of alternating layers of two semiconductor materials [1, 85]. Alternatively, this modulation can be achieved by related epitaxial growth techniques [86]. Conventionally, the growth direction of the SL layers is defined as x–axis whereas y– and z– directions are parallel to the plane of the layers. This semiconductor device encloses a superlattice region formed on a base layer that typically compromises a heavily doped GaAs substrate. On the outer surface of the substrate an additional highly doped GaAs layer is applied to attain the purpose of ohmic emitter contact (labelled in Fig. 2.1). This way, the metallised ohmic contact, would demonstrate the desirable low conducting resistance. The superlattice region, as was expected, consists of successive layers with moderate doping level of different type of semiconductor materials. The structure is sandwiched then between a highly doped emitter and collector region (labelled in Fig. 2.1). The topology of the device secures that electrons can be transferred from the contacts region to the lightly doped region of SL to evade electromigration failures [87]. This possibly can be achieved as well by increasing the carrier density within the superlattice but the practical implications would account for the suppression of electron mobility due to ionised dopants. In this work, we consider a superlattice of infinite length. Therefore, better consistency is achieved between the theoretical calculations and experimental characterizations if the device consists of at least ~ 10 layers [34, 46].

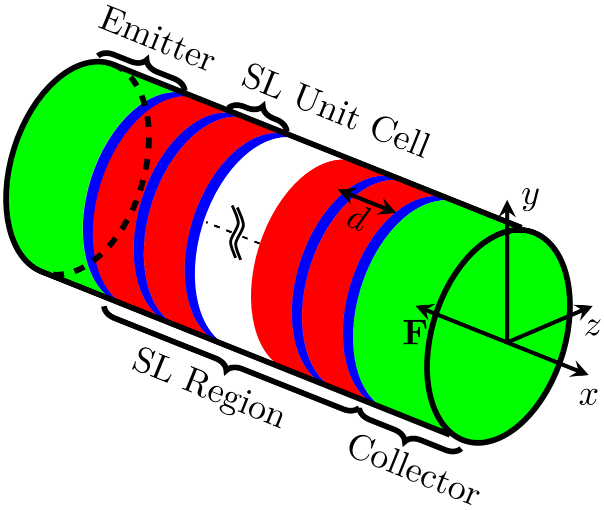

Figure 2.1: Schematic figure of a typical semiconductor superlattice. Emitter and Collector regions are shown by green regions. The superlattice unit cell is composed by a quantum well (red) embedded in barriers (blue). The device is biased by an electric field, $\mathbf{F} = (-E_{dc}, 0, 0)$, perpendicular to the layers of SL.

In the SL system, the layered arrangement of crystals induces discontinuities in the conduction and valence band, since each semiconductor material in the SL structure has its own band structure, which leads to spatial variations in the band structure perpendicular to heterolayer interface. More importantly, due to the conduction band discontinuity (see Fig. 2.2), the smaller energy gap layers behave as potential wells between larger energy gap layers. Therefore, the conduction band edge of an infinitely long ideal SL is modulated in such a way that in the vertical direction looks like one-dimensional crystal, which is shaped by alternating variation of a quantum well (A material) and a potential barrier (B material). In particular, this type of configuration is observable in the so-called type I SLs [see Fig. 2.2(a)], where the energy band gaps of the host materials are aligned but at the same time the size of the band gaps is different [88]. Furthermore, the modulation in the conduction-band remains indifferent to the modulation in the valence band. On the other hand, in the so-called Type-II SL the modulation of the valence band affects strongly the modulation of the conduction band [9]. In this case, the smaller-gap material might lie above that of the larger-gap material [see Fig. 2.2(b)]. In this thesis, we restrict our interest mainly to the type-I superlattices, where the lattice constants of the host materials demonstrate a very close match. As a result, the period d of the artificial superlattice structure is now significantly larger than a common semiconductor crystal.

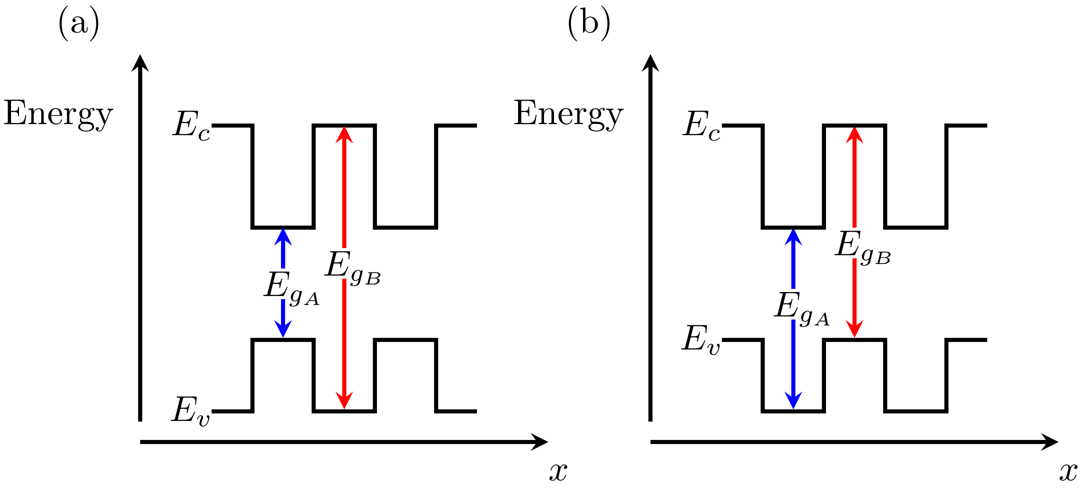

Figure 2.2: Sketches for (a) band alignment of type-I superlattice and (b) band alignment of type-II superlattice. E_{gA} and E_{gB} correspond to the energy gaps of material A and B respectively.

The enhancement of the lattice period has implications for the newly formed bands known as minibands which demonstrate a reduced magnitude in comparison with the conventional conduction bands. In a similar manner, the developed structure of Brillouin zone over $2\pi/d$ becomes much smaller and therefore the term minizone is introduced to describe the reciprocal lattice vectors.

The special design of a semiconductor superlattice affects the transport of the electron. This means that different approaches are applicable with the variation of the band structure. An important classification then emerges depending on the width of the barriers separating the quantum wells [34, 89]. If the SL structure consists of wells separated by relatively thick barriers (narrow minibands) then the electronic properties should be entailed on the subband structure which corresponds to the case of the so-called weakly coupled superlattices. In that case electron transport is feasible as a consequence of sequential tunnelling from well to well. In the opposite limit of the strongly coupled SL, the superlattice structure is formed by many identical quantum wells and thin barriers. Thus, the adjacent wells couple resulting to the transformation of resonant subbands into minibands with width Δ. Importantly, in this work we focus on carrier transport that involves the electronic properties efficiently described by systems of strongly coupled SL. In these terms, within the miniband transport scheme which is reviewed thoroughly in the following sections, the electron behaviour is pictured using an extended basis like the Bloch states.

The concept of energy band

The one-dimensional "mesoscopic" periodicity of crystal lattices is a recognised feature of superlattice structures, existing in both natural and artificial ones [90]. The mesoscopic scale of an artificial SL structure indicates that the newly formed lattice constant is larger than the period of constituent materials but smaller than mean free path of electrons [1]. In order to understand the properties of electron dynamics in crystalline solids with periodically varying potentials, the Kronig-Penney model [91] has been addressed which can additionally explain the origin of energy band structures. Nevertheless, different approaches have been developed to examine explicitly the characteristics of energy subbands of a SL [88].

In this section, initially, we construct the solution of one-dimensional Schrödinger equation in a generic periodic potential by employing the Floquet-Bloch treatment [92, 93]. This analysis would allow us to realise that the formation of energy spectrum in a periodic potential does not necessarily depend on the method of linear combination of atomic orbitals (LCAO[1]) but it is a mathematical consistency of Schrödinger equation. Subsequently, we will restrict our attention to the qualitative but more accurate description of the electronic band structures in SLs. For this aim, a formalism of Kronig-Penney model can be implemented, which explains the behaviour of electron in these periodic crystalline structures.

The behaviour of a single electron in a crystalline solid that demonstrates a periodic potential, can be given by the solutions of one-dimensional time-independent Schrödinger equation

$$-\frac{\hbar^2}{2m}\frac{d^2}{dx^2}\psi(x) + V(x)\psi(x) = E\psi(x) \tag{2.1}$$

where $\hbar = 6.626 \times 10^{-34}$ J s denotes the reduced Planck's constant, m is the mass of the quantum particle and $V(x) = V(x+d)$ is the periodic potential with d designating the lattice period. In this system, we have made a crude assumption that the effective mass is a constant as in SL structures, where the modifications in the conduction band edge position induce the periodic potential. For the further analytical studies of equation (2.1), it is more convenient to rewrite it in the dimensionless form

$$\frac{d^2}{dx^2}\psi(x) + (\epsilon - U(x))\,\psi(x) = 0 \tag{2.2}$$

Here $\epsilon = (2m/\hbar^2)E$ and $U = (2m/\hbar^2)V$. The necessity of employing the Bloch theory [93] emerges since we conceptualise the effect of a periodic potential on

---

[1] The periodic potential in a SL does not correspond to a real atomic potential, but a alternating repetition of different energy gap layers, the thickness of which is significantly larger than the period of the atomic potential [94].

the motion of electron. Remarkably, the Bloch electrons obey the single electron Schrödinger equation with a periodic potential, resulting to the so-called Bloch states that coincide with the eigenfunctions of the operator

$$L = -d^2/dx^2 + U(x) \tag{2.3}$$

Then according to Bloch's theorem, a complete set of solutions can be obtained in the form

$$\psi_{nk_x}(x) = e^{ik_x x} u_{nk_x}(x), \tag{2.4}$$

where k_x denotes the wavenumber of the particle and n a quantum number that corresponds to an individual band. The basic property of these eigenfunctions is that they change by a constant phase factor for a transverse displacement equal to an integer multiple of the lattice period

$$\psi_{nk_x}(x + Nd) = e^{ik_x Nd} u_{nk_x}(x) \tag{2.5}$$

It is important to note that the function $u_{nk_x}(x)$ also retains the periodicity of the potential and the eigenvalues ϵ_n designate the energies in different bands.

Analysis of energy band structure

By using the notation, $f(x) = \epsilon - U(x)$, equation (2.2) can be reformulated as

$$\frac{d^2\psi(x)}{dx^2} + f(x)\psi(x) = 0;\ \ f(x+d) = f(x), \tag{2.6}$$

which is known as the Hill equation [95]. Let us choose a basis $\psi_1(x)$, $\psi_2(x)$ of the solution space of the above Hill-equation, which are uniquely determined by initial conditions

$$\begin{pmatrix} \psi_1(0) & \psi_1'(0) \\ \psi_2(0) & \psi_2'(0) \end{pmatrix} = \begin{pmatrix} 1 & 0 \\ 0 & 1 \end{pmatrix}. \tag{2.7}$$

Equation (2.6) has stable solutions (corresponding to the energy bands) if Hill's discriminant [2]

$$\Lambda(\epsilon) = \psi_1(d,\epsilon) + \psi_2'(d,\epsilon) \tag{2.8}$$

is lying within the range $|\Lambda| \leq 2$, whereas the band gaps (unstable solutions) happen when $|\Lambda| > 2$. For completeness, it is possible to represent the general solution of (2.6), according to the Floquet-Bloch theorem, as a superposition of two Bloch waves

$$\psi(x) = c_1\psi_1(x) + c_2\psi_2(x), \tag{2.9}$$

---

[2] In literature it is also referred as Liapunov function [96].

where the Bloch waves satisfy the conditions

$$\psi_1(x+d) = \rho\psi_1(x),\ \psi_2(x+d) = \rho^{-1}\psi_2(x) \tag{2.10}$$

with ρ being either a pure phase factor, i.e. $\rho = e^{ik_x d}$ or a random complex number. There is a direct physical implication of the numerical form, which ρ takes, satisfying automatically the characteristic equation[3] associated with equation (2.6)

$$\rho^2 - \Lambda(\epsilon)\rho + 1 = 0. \tag{2.11}$$

By a simple investigation of trinomial (2.11), we can observe that if $\Lambda^2(\epsilon) \leq 4$ then its roots ρ_1, ρ_2, known as Floquet multipliers, will also be complex conjugate with $\rho_1 \cdot \rho_2 = 1$. In that case, $|\rho_1|$, $|\rho_2|=1$ and therefore the solutions of (2.6) become bounded. On the other hand, if $\Lambda^2(\epsilon) > 4$, at least one of the numbers $|\rho_1|$ or $|\rho_2|$ exceeds unity because $\rho_1 \cdot \rho_2 = 1$. Thus, the solutions of the Hill equation demonstrate an instability. Further investigation of the function $\Lambda(\epsilon)$ is feasible for $|\epsilon| >> 0$. For example, considering an $\epsilon = -\gamma^2$ for reasonably large real values of γ, equation (2.6) can be reduced to

$$\psi''(x) - \gamma^2\psi(x) = 0 \tag{2.12}$$

We see that this second order differential equation has a solution

$$\psi(x) = c_1\psi_1\cosh(\gamma x) + \frac{c_2}{\gamma}\psi_2\sinh(\gamma x) \tag{2.13}$$

Hereafter, the Hill's discriminant $\Lambda(\epsilon) = \psi_1(d) + \psi_2'(d)$ takes the form

$$\Lambda = 2\cosh(\gamma d), \tag{2.14}$$

for which, of course, $\Lambda > 2$, implying that these type of segments $\epsilon \in \Re$ would correspond to a forbidden band, or an energy gap. On the contrary, for $\epsilon >> 0$ ($\epsilon = k_x^2$), the Schrödinger equation in this region will be described by

$$\psi''(x) + k_x^2\psi(x) = 0, \tag{2.15}$$

which has a solution

$$\psi(x) = c_1\psi_1\cos(k_x x) + \frac{c_2}{k_x}\psi_2\sin(k_x x), \tag{2.16}$$

and therefore,

$$\Lambda(\epsilon) = 2\cos(k_x d). \tag{2.17}$$

---

[3] for complete derivation of the characteristic equation see appendix A.

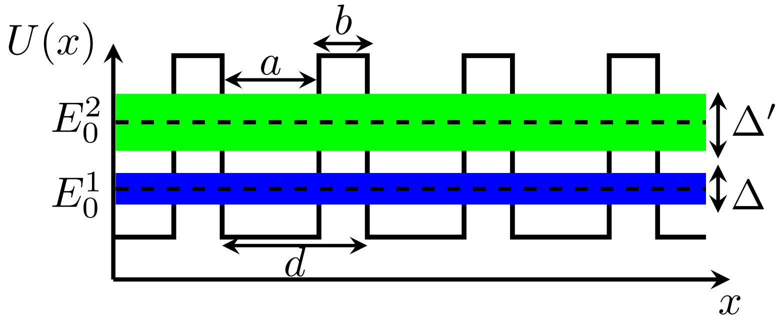

Figure 2.3: Schematic representation of the SL potential $U(x)$ and the conduction band with minibands $n = 1, 2$. The shaded regions indicate the first miniband (blue region) of width Δ and the second miniband (green region) of width Δ'.

The quantity $\Lambda(\epsilon)$ in this case will be certainly $|\Lambda(\epsilon)| \leq 2$, generating physical acceptable solutions that coincide with energy bands [98, 99]. The previously described theoretical framework has been used to determine the potential profiles that optimise the one-dimension energy bands such as in SL systems [99]. This method involves the minimising of effective mass at the bottom of the band and at the same time maintaining a gap between the first and second minibands that can suppress Zener interminiband tunnelling.

Miniband structure in a superlattice

Now let us consider specifically a periodic structure that can be described as a superlattice consisted by alternating layers of two materials with similar lattice constants resulting in the band-edge lineup for type-I superlattice [see Fig. 2.2(b)]. For example, such features may be present in a GaAs/AlGaAs structure making possible a formalism that employs the Kronig-Penney model and involves the effective mass jumps to determine the electronic band structures [85, 94, 100]. The material is assumed to represent a translation invariance in y and z directions, which are perpendicular to the growth direction, x, of the SL. The conduction band edge that includes the lowest point of the conduction band for each host material is delineated by

$$E_c(x) = \begin{cases} E_{cw} & \text{if x corresponds to a quantum well,} \\ E_{cb} & \text{if x corresponds to a barrier} \end{cases} \tag{2.18}$$

We have already discussed in Section 2.1, that depending on their relative bandgaps, the semiconductor materials form either a quantum well (e.g. GaAs) or a barrier region (e.g. AlGaAs). The corresponding effective mass of the electrons is space-dependent, and therefore is different in the well and barrier layers of SL structure

$$m_c(x) = \begin{cases} m_{cw} & \text{if x corresponds to a quantum well,} \\ m_{cb} & \text{if x corresponds to a barrier} \end{cases} \tag{2.19}$$

Thus, the envelope function of the superlattice potential, $\psi(\mathbf{r})$, satisfies the equation

$$\left[E_c(x) - E_{cw} - \frac{\hbar^2}{2m_c(x)}\nabla^2 + \frac{\hbar^2\mathbf{k}_\perp^2}{2m_c(x)}\right]\psi(\mathbf{r}) = E(\mathbf{k})\psi(\mathbf{r}), \tag{2.20}$$

where $\mathbf{k}_\perp = (k_y, k_z)$. The electron experiences an effective periodic potential associated with the periodic repetition of different gap layers. Therefore, we can define the effective potential of SL as $U(x) = E_c(x) - E_{cw}$ which exhibits no dependence on the directions perpendicular to x–axis. Figure 2.3 demonstrates this periodic square potential of a superlattice with well thickness a and barrier thickness b forming a lattice period $d = a + b$ and a potential barrier height $U_0 = E_{cb} - E_{cw}$. We can look for eigenfunctions which are separable in x,y and z directions since Hamiltonian is the sum of x,y and z contributions. In addition, the electron motion is free along y and z directions. Hence, the envelope function can be written as

$$\psi(\mathbf{r}) = \frac{1}{\sqrt{S}}e^{i(k_y y + k_z z)}\psi_{k_x}(x), \tag{2.21}$$

where S is the sample area. From the solution of Schrödinger equation, taking into account the Bloch theorem (2.5), the x–dependent envelope function, $\psi_{k_x}(x)$, within a single period may be represented as [85, 101]

$$\psi_{k_x}(x) = Ae^{ik_w x} + Be^{-ik_w x}, \qquad 0 \le x \le a \tag{2.22}$$

$$\psi_{k_x}(x) = Ae^{k_b x} + Be^{-k_b x}, \qquad -b \le x \le 0 \tag{2.23}$$

where A, B, C, D are constants, $k_w^2 = 2m_{cw}E_x/\hbar^2$ and $k_b^2 = 2m_{cb}(U_0 - E_x)/\hbar^2$ with E_x the given energy to the particle such that $0 < E_x < V$. If we employ the Bastard conditions [94] denoting the connection rules of the well-barrier interfaces

$$\begin{aligned}
\psi_{k_x}(x)|_{x\to 0^-} &= \psi_{k_x}(x)|_{x\to 0^+} \\
\psi_{k_x}(x)|_{x\to a^-} &= e^{ik_x d}\psi_{k_x}(x)|_{x\to -b^+} \\
\frac{1}{m_{cb}}\psi'_{k_x}(x)|_{x\to 0^-} &= \frac{1}{m_{cw}}\psi'_{k_x}(x)|_{x\to 0^+} \\
\frac{1}{m_{cb}}\psi'_{k_x}(x)|_{x\to a^-} &= \frac{e^{ik_x d}}{m_{cw}}\psi'_{k_x}(x)|_{x\to b^+}
\end{aligned}$$

then we end up with a system of linear equations which has a non-trivial solution of the form

$$\cos(k_x d) = \cosh(k_b b)\cos(k_w a) + \frac{1}{2}(\xi - \frac{1}{\xi})\sinh(k_b b)\sin(k_w a), \tag{2.24}$$

where

$$\xi = \frac{k_b m_{cw}}{k_w m_{cb}} = \sqrt{\frac{(U_0 - E_x) m_{cw}}{E_x m_{cb}}} \tag{2.25}$$

Provided that the barriers between the quantum wells in superlattice become sufficiently thin, the electronic states in the wells are coupled to form minibands. Therefore, the tuning of the band structure it is possible directly by the optimal choice of parameters a, b that determine the thickness of the alternating layers of SL. The allowed energy minibands and the related energy quasi-momentum dispersion relations can be obtained numerically by using equation (2.24). It is clear that if the absolute value of the right-hand side of the same equation is larger than one, the corresponding electron energy is prohibited. In this case, the energy values designate the unoccupied regions between the energy minibands known as energy gaps. From the previous analysis arises the importance of the parameters m_w, m_b, for the energy band structure of the SL, which characterise effective mass at wells and barriers respectively. Moreover, it is straightforward to observe that parameter ξ is reduced to the form of unscaled Kronig-Penney [91] model for $m_w = m_b$.

The energy bands $E^n(p_x)$ in general can be expanded in Fourier series as

$$E^n(p_x) = E_0^n + \sum_{l=1}^{\infty} 2T_l^n \cos\left(\frac{l p_x d}{\hbar}\right). \tag{2.26}$$

Here the constant E_0^n and the coefficients T_l^n represent the center of miniband and overlapping of the wavefunction respectively, at a given n–th band. A more transparent physical interpretation of coefficients T_l^n would suggest that they model the way that tunnelling couples the quantum mechanical states into Bloch waves [34]. Therefore, the summation over different l–lattice sites, indicates how electron travels through the effective periodic potential of the superlattice. By employing the energy levels of quantum wells, which are effectively isolated, we can identify the locations of energy bands E_0^n. In fact, bearing in mind that the energy bands arise due to coupling of the quantum mechanical states localised in the quantum wells, the energy spectrum of a particle in a single quantum well appears to be the limiting case of E_0^n

$$E_0^n = \frac{n^2 p^2 \hbar^2}{2 m_w a^2}. \tag{2.27}$$

Henceforth, increasing the width of the quantum well a would reduce the energy gap between the first and second energy minibands.

The energy dispersion relation of the first miniband, considering its center as the zero energy, it is outlined by

$$E(p_x) = \sum_{l=1}^{\infty} 2T_l^1 \cos\left(\frac{l p_x d}{\hbar}\right). \tag{2.28}$$

Depending on the parameters of superlattice, the short range interaction prevails and then only the nearest-neighbour terms need to be retained in equation (2.26), giving rise to the simplest case of tight-binding approach

$$E(p_x) = \frac{\Delta}{2}\left(1 - \cos\left(\frac{p_x d}{\hbar}\right)\right). \tag{2.29}$$

Equation (2.29) has been formulated by assuming that the width of the first miniband is $\Delta = 4T_1^1$ and the location of the energy band E_0^n at $\Delta/2$. The energy dispersion relationship can be redefined considering additionally the kinetic energy of the electron associated with the free particle motion with mass m^* in the y, z directions

$$E(\mathbf{p}) = \frac{\Delta}{2}\left(1 - cos\left(\frac{p_x d}{\hbar}\right)\right) + \frac{p_y^2}{2m^*} + \frac{p_z^2}{2m^*}, \tag{2.30}$$

where $\mathbf{p}(p_x, p_y, p_z)$ is the generalised momentum.

In concluding this section, we should take note that recognising the implications of the dispersive character of energy minibands, can provide the basis for further understanding of the literature and subsequent calculations of transport properties in SL.

Electron tranpsort in superlattices

The physical interpretation of the behaviour of electrons in crystalline potentials is evoked by recognising the dynamic significance of the translation symmetry of a periodic potential. By employing the semiclassical model, Bloch showed that a wave packet consisted of states from a single energy band, peaked around some crystal momentum, $\hbar\mathbf{k}$, propagates with group velocity determined by the gradient of energy dispersion with respect to $\mathbf{k}$ [93]. The force excreted on the electron due to an external field $\mathbf{F}$ is equal to the rate of change of quasimomentum $\hbar\mathbf{k}$. The Bloch states, which are eigenstates of the field-free Hamiltonian, allow to represent electrons occupying the lower part of energy band, and thus propagate freely in metals through the potential field induced by the ion cores. In fact, these localised wave packets arise as a consequence of the invariance properties of lattice periodicity. In addition, the dynamics of an electron in a natural solid are influenced by impurity scattering introducing strong decoherence of time-periodic oscillations. These semiclassical arguments comprise the standard approach to describe transport in solid-electron systems [102]. Remarkably, the same formulation is applicable on man-made superlattice structures with negligible interminiband tunnelling processes for which a electron localisation occurs in the higher range of static electric field amplitudes, being accompanied by Bloch oscillations. In general, when fields of finite magnitude are applied to SL is meaningless to employ a basis consisting of Bloch states, but it is preferable, as we will see later in this chapter, to consider the semiclassical distribution function $f(\mathbf{r}, \mathbf{p})$ instead, to describe the occupation of Bloch states in different time points. The latter dynamics description is desirable in the "real" case, when the oscillations of Bloch state are damped due to scattering processes. In the absence of scattering, the electron dynamics in the miniband of SL follow the the **k**-space form of Newton's law for Bloch waves [34, 103, 104], whereas the particle velocity is equal to the group velocity of its corresponding wave packet

$$\hbar \frac{d\mathbf{k}}{dt} = \mathbf{F} \tag{2.31}$$

$$\mathbf{v}(\mathbf{k}) = \frac{1}{\hbar} \nabla_{\mathbf{k}} E(\mathbf{k}) \tag{2.32}$$

Here **F** represents a constant force caused by some arbitrary energy potential. Given the tight-binding approach and by using the complete energy dispersion relationship (2.30), we obtain the miniband velocity for different directions

$$v_x(k_x) = \frac{\Delta d}{2\hbar} \sin(k_x d), \tag{2.33}$$

$$v_y(k_y) = \frac{\hbar k_y}{m^*}, \tag{2.34}$$

$$v_y(k_z) = \frac{\hbar k_z}{m^*}, \tag{2.35}$$

where m^* represents the effective mass of an electron in direction parallel to SL layers. Differentiating equation (2.32) with respect to t, we can obtain

$$\frac{dv(\mathbf{k})}{dt} = \hbar^{-1} \frac{dk}{dt} \frac{d^2 E(\mathbf{k})}{dk^2}. \tag{2.36}$$

Therefore, if we consider a external force F_i applied along one of the directions of

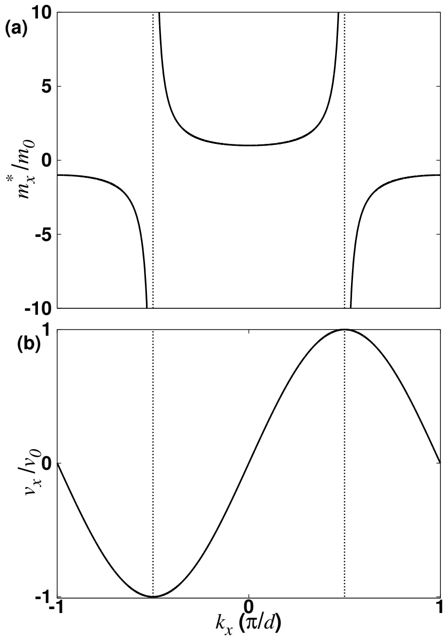

Figure 2.4: (a) Miniband velocity as a function of wave vector k_x. (b) Effective mass restricted to the first minizone of SL.

SL $i = x, y, z$, the effective mass taking into account an isotropic energy surface is defined as

$$\frac{1}{m_i^*} = \frac{1}{\hbar^2}\frac{d^2E(k_i)}{dk_i^2}. \tag{2.37}$$

Here, essentially we introduced the components of the diagonal effective mass tensor. According to equation (2.37) the reciprocal mass $1/m^*$ determines directly the curvature of E versus $\mathbf{k}$ in y, z directions, implying that the carrier is accelerated relative to the lattice in a applied magnetic or electric field but with a constant mass. For GaAs, as an example, the conduction band effective mass becomes simply a scalar for parabolic approximation with magnitude $0.067m_e$. This parameter is important because in this thesis one of the SL structures that we study is GaAs/AlAs, demonstrating effective masses for the chosen compounds $m_w = 0.067m_e$ and $m_b = 0.11m_e$ respectively. Considering actually that the unperturbed Bloch states have larger possibility to be occupied within the wells, we can assume the approximation $m^* = m_w$ [34, 105].

On the other hand, the effective mass in the growth direction is given by

$$\frac{1}{m_x^*} = \frac{1}{m_0}\cos(k_x d), \tag{2.38}$$

where $m_0 = 2\hbar^2/\Delta d^2$ is the effective mass at the bottom of the miniband. As it can be seen in figure 2.4(a), for a wide range of k_x the electron behaves as it carries mass in the centre of Brillouin zone. More importantly, the effective mass becomes negative at the upper part of the miniband, causing the suppresion of particle velocity [see Fig. 2.4(b)].

In this section, we will present the effect of different configurations of external fields on electron dynamics, gaining some physical insight in phenomena such as Bloch oscillations, Landau level spacings related to cyclotron frequencies and dynamic localisation.

Bloch oscillations

Now let us consider the influence of a static electric field applied along the SL direction. In this case the Hamiltonian for the electron in the first miniband reads

$$H = E(p_x) - eE_{dc}x. \tag{2.39}$$

In the single-particle picture, the semiclassical equations of motion for velocity v_x and crystal momentum of a wave packet $p_x = \hbar k_x$ in the electric field, then result in following set of equations

$$\frac{p_x d}{\hbar} = \omega_B t + \frac{p_x^0 d}{\hbar}, \tag{2.40}$$

$$v_x(t) = \sum_{l=1}^{\infty} v_l \sin\left(\frac{l p_x d}{\hbar} + l\omega_B t\right). \tag{2.41}$$

The equation (2.40) states clearly that the crystal momentum varies linearly with time. In turn, assuming that the particle is initially found at $k_x = 0$, the application of a constant electric bias will induce a positive change in k_x, and the Bloch electron, within the reduced-zone approximation discussed in the previous section, approaches the edge of the Brillouin zone $k_x = \pi/d$. It would be expected that an electron traverses the SL minizone to obtain the maximum miniband velocity [vertical line in Fig. 2.4(a) corresponding to $k_x = \pi/2d$] half way along the first Brillouin zone. In that case the dE_x/dk_x becomes maximal, whereas at the Brillouin zone boundary $dE_x/dk_x = 0$, implying that the velocity of the electron is zero. Here again we underline the physical significance of the fact that Bloch vectors are equivalent, if they differ by a reciprocal lattice vector. The idea of this approach is that the particle at $k_x = \pi/d$ undergoes the so-called Bragg reflection process that results in the reappearance of electron at the opposite edge of minizone $k_x = -\pi/d$, and hereafter the crystal momentum continues to increase. As a result, the electron trajectory in real space exhibits a negative drift with maximum negative velocity, when the norm of dE_x/d_k is maximal. From this point onwards, the electron starts to deaccelarate until its return to initial position $k_x = 0$ in quasimomentum space, where motion is temporarily suspended. This single Bloch period T_B, which was described above, constitutes a full cycle of motion in real space known as as Bloch oscillation with frequency

$$\omega_B = \frac{eE_{dc}d}{\hbar}. \tag{2.42}$$

In real space these periodic oscillations can be simply obtained by integrating equation (2.41)

$$x(t) - x(0) = \sum_{l=1}^{\infty} x_l \left[\cos\left(\frac{lp_x d}{\hbar} + l\omega_B t \right) - \cos\left(\frac{lp_x^0 d}{\hbar} \right) \right]. \tag{2.43}$$

Here $x(0)$ is the initial position and $x_l = 2T_l/eE_{dc}$ determines the span of oscillations in real space. The spatial extension of oscillations can be understood alternatively as the summation of the contributions of oscillations taking place in adjacent wells. This physical picture is consistent with the position of wave packet predicted analytically by solving Schrödinger equation [106] and more recently the spatially displacement of Bloch-oscillating electrons has been determined directly in experiments [107, 108] measuring a dipole field caused by the optical excitation of the wave packet. The dynamical description of Bloch oscillations implies that they could be observed in natural crystals. Actually, this was the initial prediction of Zener [35] following the work of Bloch [93], suggesting that electron wave packets do not delocalise but undergo high frequency oscillations. Nevertheless, in standard crystals the period of these oscillations is much greater than typical relaxation time causing the delocalisation of electron trajectories. The countereffect of SL structure that allows the realisation of Bloch oscillations is the enhanced length of its lattice period d. In particular, experimental confirmation of Bloch oscillations was provided by using a transient four-wave mixing signal that demonstrated a few Bloch cycles before the oscillations were restrained due to scattering events [12]. Alternatively, it was reported that coherent electromagnetic radiation can be directly associated with the manifestation of charge carriers performing Bloch oscillations [13]. SL structure, however, is not the only system that may provide conditions for coherent oscillations of the Bloch state. For example, an atom in a optical lattice in the absence of scattering events, can be also effectively tuned to exhibit multiple cycles of Bloch oscillations [109, 110].

Stark-cyclotron resonances

In order to investigate the dynamics of single-electron in the lowest miniband under the action of a static electric field, E_{dc}, perpendicular to the layers of SL and a constant arbitrary magnetic field $\mathbf{B} = (B_x, 0, B_z)$ that lies in x, z plane, where $B_z = Bsin\theta$ and $B_x = Bcos\theta$, it is feasible to tailor the Hamiltonian as follows

$$H = E(p_x) + \frac{(p'_y)^2}{2m^*} + \frac{p_z^2}{2m^*} - eE_{dc}x. \tag{2.44}$$

Here the dispersion relationship $E(p_x)$ for the electron is described by equation (2.28) and $\mathbf{p}(p_x, p_y, p_z)$ is the generalised momentum. To determine the equations of motion, H must be expressed solely in terms of coordinates and canonical momenta. Therefore, the canonical momentum is no longer simply given by a linear momentum ($m^*\mathbf{v}$) but there is additional term associated with vector potential [111]

$$p'_y = p_y + e\mathbf{A}. \tag{2.45}$$

Since kinetic energy in the y–direction corresponds to free particle motion, it is convenient to adopt the Landau gauge $\mathbf{A} = (0, xB_z - zB_x, 0)$ [112, 113]. In this case the related canonical momentum can be written as

$$p'_y = p_y + eB(x - z). \tag{2.46}$$

Now the motion of the single electron can be fairly described by employing equations of motion that arise from Hamiltonian. In general, the Hamilton's equations designating the equations of motion for a particle with generalised coordinates $\mathbf{r}(x, y, z)$ and momenta $\mathbf{p}(p_x, p_y, p_z)$ are given by

$$\begin{cases} \begin{pmatrix} \dot{x} \\ \dot{p}_x \end{pmatrix} = \begin{pmatrix} \dfrac{\partial H}{\partial p_x} \\ \\ -\dfrac{\partial H}{\partial x} \end{pmatrix}, \\ \\ \begin{pmatrix} \dot{y} \\ \dot{p}_y \end{pmatrix} = \begin{pmatrix} \dfrac{\partial H}{\partial p_y} \\ \\ -\dfrac{\partial H}{\partial y} \end{pmatrix}, \\ \\ \begin{pmatrix} \dot{z} \\ \dot{p}_z \end{pmatrix} = \begin{pmatrix} \dfrac{\partial H}{\partial p_z} \\ \\ -\dfrac{\partial H}{\partial z} \end{pmatrix}. \end{cases} \tag{2.47}$$

We can rewrite the system (2.47) in the more compact form

$$\begin{bmatrix} \dot{r}_i \\ \dot{p}_i \end{bmatrix} = \begin{bmatrix} \dfrac{\partial H(t, \mathbf{p}, \mathbf{r})}{\partial p_i} \\ \\ -\dfrac{\partial H(t, \mathbf{p}, \mathbf{r})}{\partial p_i} \end{bmatrix} \tag{2.48}$$

where the index $i = x, y, z$ signifies the degrees of freedom. In particular by using the Hamiltonian (2.44) and the Hamiltonian equations (2.47), we obtain the velocity elements in different directions

$$\begin{pmatrix} v_x = \dot{x} \\ v_y = \dot{y} \\ v_z = \dot{z} \end{pmatrix} = \begin{pmatrix} \sum_{l=1}^{\infty} v_l \sin\left(\dfrac{l p_x d}{\hbar}\right) \\ \dfrac{q_y}{m^*} \\ \dfrac{p_z}{m^*} \end{pmatrix} \tag{2.49}$$

Here $v_l = -2lT_l d/\hbar$ $(l = 2, 3, 4)$ constitutes the involvement of the remaining coupling between wells in electron transport by tunnelling processes through barriers of superlattice. In other words, the summation over different Fourier coefficients determines the velocity v_x in the direction of SL, which within the tight-binding approximation can be represented as

$$v_x = v_0 \sin\frac{p_x d}{\hbar}, \tag{2.50}$$

where $v_0 = \Delta d/2\hbar$ is the maximum miniband velocity, which is identical with $n = 1$ in equation (2.49). The canonical momenta can be found again by using the Hamilton equations

$$\begin{pmatrix} \dot{p}_x \\ \\ \dot{p}_y \\ \dot{p}_z \end{pmatrix} = \begin{pmatrix} eE_{dc} - \omega_c p'_y \\ \\ eB_z \sum_{l=1}^{\infty} v_l \sin\left(\frac{l p_x d}{\hbar}\right) - \omega_{c\perp} p_z \\ \omega_{c\perp}\, p'_y \end{pmatrix} \tag{2.51}$$

where $\omega_c = eB_z/m$ and $\omega_{c\perp} = eB_x/m$ are the frequencies of cyclotron oscillations in the corresponding directions. The latter frequency is associated with oscillations in the plane perpendicular to the SL axis, which are nonlinearly coupled with Bloch oscillations by the component of magnetic field along the z–axis. It has been shown that the semiclassical dynamics of miniband electron in a titled magnetic field corresponds to a harmonic oscillator with natural frequency $\omega_{c\perp}$ driven by a monochromatic plane wave, resulting in a resonantly enhanced self-induced dc current [113]. Exhibiting chaotic dynamics is an inherit property of this type of harmonic oscillator, which is driven by a single frequency plane wave. However, this behaviour is untypical for the dynamical systems that obey the KAM theorem, which implies the gradual disappearance of quasiperiodic orbits with increasing the amplitude of perturbation, and thus giving rise to chaotic motion [112, 114–116]. On the contrary, the "non-KAM" chaos [112, 113] in the tilted fields configuration is activated, when the Bloch frequency is commensurate with cyclotron frequency $\omega_B = n\omega_{c\perp}$, effect known as Stark-cyclotron resonances.

There is currently experimental evidence on how the Bloch oscillations and the in-plane cyclotron oscillations perform resonant mixing that results in a transient undirectional current [117]. In a different experimental scheme, it was shown that the specially extended character of the electronic states plays the same role in quantum mechanical picture as the delocalised semiclassical electron trajectories in tilted magnetic field [118]. In that case the coupling between Bloch and cyclotron oscillations generated a magnetic-field-induced miniband structure.

Dynamic localisation under the influence of multifrequency fields

We turn now to a short discussion of the noted features [119–123] of delocalisation of electrons in SL, applying solely an arbitrary alternating electric field in the direction of SL

$$E(t) = E_{dc} + \sum_{\nu=1}^{N} E_{\omega_\nu} \cos(\omega_\nu t + \phi_\nu), \tag{2.52}$$

where E_{ω_ν} and ω_ν constitute the amplitudes and frequencies respectively of N harmonics, and ϕ_ν the initial phases. This electric field can be induced by an electromagnetic wave propagating through the SL, if the wavelength of the wave is larger than the length of the superlattice. The equation of motion (2.31) can be simply integrated to yield the time dependence of crystal momentum

$$\frac{p_x(t)d}{\hbar} = \theta + \omega_B t + \sum_{\nu=1}^{N} \beta_\nu \sin(\omega_\nu t + \phi_\nu). \tag{2.53}$$

Here $\theta = \tilde{p}_0 - \sum_{\nu=1}^{N} \beta_\nu \cos(\phi_\nu)$ with $\tilde{p}_0 = p_x^0 d/\hbar$ designating the initial position of electron within the Brillouin zone and $\beta_n = eE_{\omega_\nu} d/(\hbar\omega_\nu)$. Therefore, for the tight-binding miniband, the time-dependent velocity is described by the following equation

$$\begin{aligned} v_x(t) &= v_0 \sin\left(\frac{p_x(t)d}{\hbar}\right) = v_0 \mathrm{Im}\left\{ e^{i(\theta+\omega_B t)} \prod_{\nu=1}^{N} e^{i\beta_\nu \sin(\omega_\nu t+\phi_\nu)} \right\} \\ &= v_0 \mathrm{Im}\left\{ e^{i(\theta+\omega_B t)} \sum_{n_1,\ldots,n_N} \prod_{\nu=1}^{N} J_{n_\nu}(\beta_\nu) e^{in_\nu(\omega_\nu t+\phi_\nu)} \right\} \\ &= v_0 \sum_{n_1,\ldots,n_N} \left[\prod_{\nu=1}^{N} J_{n_\nu}(\beta_\nu) \right] \sin\left[\theta + \omega_B t + \sum_{\nu=1}^{N} n_\nu(\omega_\nu t + \phi_\nu) \right] \end{aligned} \tag{2.54}$$

Here summation limits for $(n_1, \ldots n_N)$ are $\pm\infty$, $J_n(\beta)$ are the Bessel functions of the first kind, and we have employed the Jacobi-Anger identity [124]

$$e^{i\beta \mathrm{sinx}} = \sum_{n=-\infty}^{\infty} J_n(\beta) e^{inx}.$$

Considering now that the electric field contains only static bias and additionally biharmonic components $N = 2$, by using equation (2.54) we obtain

$$v_x(t) = v_0 \sum_{n_1,n_2=-\infty}^{\infty} J_{n_1}(\beta_1) J_{n_2}(\beta_2) \sin\left[\theta + \omega_\beta t + n_1(\omega_1 t + \phi_1) + n_2(\omega_2 t + \phi_2)\right]. \tag{2.55}$$

Given a non-periodic biharmonic field $(n_1\omega_1 \neq n_2\omega_2)$ without applying E_{dc}, the electrons can be localised after infinitely long period of time in SL miniband for the amplitudes of the harmonic fields satisfying the condition $J_0(\beta_1)J_0(\beta_2) = 0$ [120]. If the static field is involved with $\omega_B = n_1\omega_1 + n_2\omega_2$, the localisation emerges when $J_{n1}(\beta_1)J_{n2}(\beta_2) = 0$, becoming pronounced after the averaging over a long-time period. However, if the linear combination of the biharmonic frequencies do not match the Bloch frequency, then the localisation happens for arbitrary strengths of field components.

The localisation of electrons in a single miniband can be also realized with the assistance of a purely harmonic field $E(t) = E_{\omega_1}\cos(\omega_1 t)$. Therefore it can be easily derived from equations (2.53), (2.54) that

$$\frac{p_x(t)d}{\hbar} = \tilde{p}_0 + \beta_1\sin(\omega_1 t) \tag{2.56}$$

$$v_x(t) = v_0 \sum_{n_1=-\infty}^{\infty} J_{n_1}(\beta_1)\sin(\tilde{p}_0 + n_1\omega_1 t). \tag{2.57}$$

Hence, it is apparent that the particle returns periodically to its original state at the harmonic amplitude obeying the condition $J_0(\beta_1) = 0$ [122]. On the other hand, a theoretical analysis in the context of quasi-energy eigenstates instead of considering the time-dependent character of Bloch waves, it can identify the dynamic localisation as a result of miniband collapse [125].

Boltzmann transport equation and its solutions

The semiclassical approach considers that the Bloch wave vector becomes time-dependent under the influence of external fields and, therefore, the quasi-momentum follows the Newton law for Bloch waves. In the previous sections, we additionally introduced the dispersion relationship $E(\mathbf{p})$ to describe the dynamics of electron in SL. To complete the picture of miniband transport and essentially to include standard concepts arising from bulk transport such us scattering processes or thermal fluctuations, we introduce the semiclassical distribution function $f(\mathbf{r}, \mathbf{p}, t)$ that discloses the probability that a state $(\mathbf{r}, \mathbf{p})$ is occupied. In particular, $f(\mathbf{r}, \mathbf{p}, t)$, also known as phase space occupation number, quantifies the density of particles within the incremental volume $d\mathbf{r}d\mathbf{p}$

$$dN = \frac{2}{(2\pi\hbar)^3} f(\mathbf{r}, \mathbf{p}, t)d\mathbf{r}d\mathbf{p} \tag{2.58}$$

In the latter expression there is extra factor of two to account the spin degeneracy, stemming from Pauli principle.

Hence, the dynamical evolution of distribution function, which can be analysed by adopting the semiclassical theoretical framework, is governed by Boltzmann transport equation (BTE) [34, 126]

$$\frac{\partial f(\mathbf{r},\mathbf{p},t)}{\partial t}+\mathbf{v}(\mathbf{p})\frac{\partial f(\mathbf{r},\mathbf{p},t)}{\partial \mathbf{r}}+\mathbf{F}(\mathbf{r},t)\frac{\partial f(\mathbf{r},\mathbf{p},t)}{\partial \mathbf{p}}=\left(\frac{\partial f(\mathbf{r},\mathbf{p},t)}{\partial t}\right)_{\text{scatt}}, \tag{2.59}$$

where the right-hand side of the equation includes the collision integral. Once the Boltzmann equation (2.59) is solved, the density of electrons $N_e(\mathbf{r},t)$, the average electron velocity $v(\mathbf{r},t)$ and the average miniband energy $W(\mathbf{r},t)$ can be calculated as the zeroth, the first and the second momenta of the distribution function respectively

$$N_e(\mathbf{r},t)=\frac{2}{(2\pi\hbar)^3}\int_{-\infty}^{\infty}\int_{-\infty}^{\infty}dp_z dp_y\int_{-\pi\hbar/d}^{\pi\hbar/d}dp_x f(\mathbf{r},\mathbf{p},t), \tag{2.60}$$

$$v(\mathbf{r},t)=\frac{2}{(2\pi\hbar)^3 N_e}\int_{-\infty}^{\infty}\int_{-\infty}^{\infty}dp_z dp_y\int_{-\pi\hbar/d}^{\pi\hbar/d}dp_x\, v(\mathbf{p})f(\mathbf{r},\mathbf{p},t), \tag{2.61}$$

$$W(\mathbf{r},t)=\frac{2}{(2\pi\hbar)^3 N_e}\int_{-\infty}^{\infty}\int_{-\infty}^{\infty}dp_z dp_y\int_{-\pi\hbar/d}^{\pi\hbar/d}dp_x\, E_x(\mathbf{p})f(\mathbf{r},\mathbf{p},t). \tag{2.62}$$

The total current density given the expression of average velocity (2.61) is determined again by the distribution function

$$J(\mathbf{r},t)=\frac{2e}{(2\pi\hbar)^3}\int_{-\infty}^{\infty}\int_{-\infty}^{\infty}dp_z dp_y\int_{-\pi\hbar/d}^{\pi\hbar/d}dp_x\, v(\mathbf{p})f(\mathbf{r},\mathbf{p},t). \tag{2.63}$$

The distribution function in thermal equilibrium but at the absence of the external applied fields is described by Fermi-Dirac distribution

$$f_0(\mathbf{p})=\frac{1}{e^{[E(\mathbf{p})-\mu]/k_BT_e}+1}. \tag{2.64}$$

Here T_e is the temperature and μ is the chemical potential. For the case of electronic transport in single miniband of nondegenerate SL, the Fermi-Dirac energy distribution becomes the Maxwell-Boltzmann distribution $f_0(\mathbf{p})=e^{-[E(\mathbf{p})-\mu]/k_BT_e}$. By applying the relation

$$e^{y\cos x}=I_0(y)+2\sum_{n=1}^{\infty}I_n(y)\cos nx \tag{2.65}$$

we obtain the constant density of the electrons assuming the tight-binding dispersion relation (2.30)

$$N_e = \frac{m^* k_B T_e e^{\mu/k_B T_e} I_0(\Delta/2k_B T_e)}{d\pi\hbar^2}, \tag{2.66}$$

where $I_n(y)$ is the modified Bessel function of the fist kind. Hereinafter, the distribution function in the nondegenerate limit is described by the following expression if we substitute equation (2.66) into Maxwell-Boltzmann distribution

$$f_0(\mathbf{p}) = \frac{N_e d\pi\hbar^2}{m^* k_B T_e e^{\mu/k_B T_e} I_0(\Delta/2k_B T_e)} e^{\frac{\Delta}{2k_B T_e}(1-\cos(p_x d/\hbar))} e^{-\frac{(p_y^2+p_z^2)}{2m^* k_B T_e}}. \tag{2.67}$$

Mechanisms of electron scattering

The semiconductor crystal defects and the presence of impurities cause the disruption of periodicity of lattice, giving rise to localised scattering centres. Similar effects are exhibited by SLs with moderate doping, where the impurity scattering affects significantly the scattering processes [127]. Furthermore, the fabrication techniques for heterostructures are sufficiently mature to reduce the formation of imperfections or foreign atoms by employing modulation doping, a widespread technique for high mobility [128]. However, the interface roughness induced by misfit dislocations of neighbouring semiconductor materials, can evoke scattering events [1, 129].

It has already been shortly noted that when the electron collisions are highly important, an additional term is involved in the Boltzmann equation that can be treated by implementing the simplification of the relaxation-time approximation that transforms the BTE to linear partial differential equation. Thus, for a single constant scattering time τ this scattering term is described by

$$\left(\frac{\partial f(\mathbf{p},t)}{\partial t}\right)_{\text{scatt}} = \frac{f_0(\mathbf{p},t) - f((\mathbf{p},t)}{\tau}. \tag{2.68}$$

The latter equation implies that the distribution function without the presence of external fields would exponentially converge to the equilibrium distribution function. On the other hand, the impurity scattering that is associated with the occurrence of elastic scattering events does not change the energy of the particle, and therefore the thermal equilibrium is not restored. Here the inelastic scattering plays a significant role, since in that case both energy and momentum of electron are allowed to change, by transferring the energy to phonon systems as a consequence of electron-phonon scattering events. These events are triggered by thermal vibrations of the lattice causing deviations from the periodicity of the crystal structure. Following the above discussion, the scattering term that describes the relaxation-time approximation can be redefined as

$$\left(\frac{\partial f(\mathbf{p},t)}{\partial t}\right)_{\text{scatt}} = \frac{f_0(\mathbf{p},t) - f((\mathbf{p},t)}{\tau_{in}} + \frac{f(-p_x,p_y,p_z,t) - f(p_x,p_y,p_z,t)}{2\tau_{el}}, \quad (2.69)$$

where τ_{in} and τ_{el} denote the inelastic and elastic relaxation time respectively. In this thesis though we will simply adopt a single relaxation time approximation [10] that it could be treated as a single effective scattering time involving the scattering events reflecting the collision mechanisms due to impurities and electron-phonon interactions. In that case the effective scattering time is defined as

$$\tau_{eff} = \sqrt{\tau_e \tau_m} \quad (2.70)$$

Here τ_m is the relaxation time of average velocity that follows the Matthiessen's rule

$$\frac{1}{\tau_m} = \frac{1}{\tau_{in}} + \frac{1}{\tau_{el}} \quad (2.71)$$

A more generic treatment for scattering can be considered by describing the total rate, at which the distribution function is changing due to scattering processes including impurity centres or phonon scattering that preserve charge continuity

$$\left(\frac{\partial f(\mathbf{p},t)}{\partial t}\right)_{\text{scatt}} = \int_{-\pi\hbar/d}^{\pi\hbar/d} dp'_x \int_{-\infty}^{\infty}\int_{-\infty}^{\infty} dp'_z dp'_y \{W_{\mathbf{p},\mathbf{p}'}[1-(f(p'_x,p'_z,p'_z)]f(p_x,p_z,p_z) \\ -W_{\mathbf{p}',\mathbf{p}} f(p'_x,p'_z,p'_z)[1-(f(p_x,p_z,p_z)]\},$$

where $W_{\mathbf{p},\mathbf{p}'}$ designates the probability of scattering from Bloch state to another one. It is possible then following this description to address the scattering processes using Fermi's golden rule of evaluating the scattering rates [130, 131].

Chamber's path integral for a general excitation

If we adopt the single relaxation time approximation and a force field $\mathbf{F}(\mathbf{r},t)$ derived from a potential energy function $U(\mathbf{r},t)$, we can assign the distribution function to a particular energy band to find an explicit solution for Boltzmann equation of motion

$$\frac{\partial f(\mathbf{r},\mathbf{p},t)}{\partial t} + \mathbf{v}(\mathbf{p})\frac{\partial f(\mathbf{r},\mathbf{p},t)}{\partial \mathbf{r}} + \mathbf{F}(\mathbf{r},t)\frac{\partial f(\mathbf{r},\mathbf{p},t)}{\partial \mathbf{p}} = \frac{f_0(\mathbf{r},\mathbf{p},t) - f((\mathbf{r},\mathbf{p},t)}{\tau} \quad (2.72)$$

with initial condition $f(\mathbf{r},\mathbf{p},t_0) = f_0(\mathbf{r},\mathbf{p})$, assuming that no external forces are applied for $t < t_0$. The solution of the BTE may be represented by employing the solutions $r^*(t)$, $p^*(t)$ of semiclassical equations [67]

$$\frac{dr^*(t)}{dt} = v(\mathbf{p}) \quad (2.73)$$

$$\frac{dp^*(t)}{dt} = \mathbf{F} \tag{2.74}$$

Here the conjugate coordinates $\mathbf{r}$, $\mathbf{p}$ have been subjected to the following transformation $\mathbf{r} \to r^*(t)$ and $\mathbf{p} \to p^*(t)$. Considering the function $y(t) = f(\mathbf{r}^*(t), \mathbf{p}, t)$ and its derivative with respect to time, we get

$$\frac{dy}{dt} = \frac{\partial f}{\partial t} + \frac{\partial f}{\partial \mathbf{r}}\frac{d\mathbf{r}^*(t)}{dt} + \frac{\partial f}{\partial \mathbf{p}}\frac{d\mathbf{p}^*(t)}{dt}. \tag{2.75}$$

Therefore, the left-hand side of equation (2.75) is equal to the scattering term, giving rise to an ordinary differential equation

$$\frac{dy(t)}{dt} + \frac{y(t)}{\tau} = \frac{f_0(\mathbf{r}^*(t), \mathbf{p}^*(t))}{\tau} \tag{2.76}$$

with initial condition $y(t_0) = f_0(\mathbf{r}^*(t_0), \mathbf{p}^*(t_0))$. The solution of this equation in the limit $t_0 \to -\infty$, is given by the following expression

$$y(t) = \int_{-\infty}^{t} e^{-\frac{t-s}{\tau}} f_0(\mathbf{r}^*(s), \mathbf{p}^*(s))\frac{ds}{\tau}. \tag{2.77}$$

Now this solution can be implemented to find the stationary time-dependent value of some physical quantity $A = A(\mathbf{r}^*(t), \mathbf{p}^*(t), t)$

$$A(t) = \int\int d^3r d^3p \, A(\mathbf{r}, \mathbf{p}, t)\, \frac{1}{\tau}\int_{-\infty}^{t} ds\, e^{-\frac{t-s}{\tau}} f_0(\mathbf{r}^*(s), \mathbf{p}^*(s)). \tag{2.78}$$

Here the solutions of the system $r^*(t)$, $p^*(t)$ along the characteristics in phase space terminate at t with final conditions $\mathbf{r}^*(t) = \mathbf{r}$, $\mathbf{p}^*(t) = \mathbf{p}$ for the given $\mathbf{r}$ and $\mathbf{p}$. On the other hand, each pair of coordinates $(\mathbf{r}, \mathbf{p})$ corresponds to unique initial conditions $(\mathbf{r}_0, \mathbf{p}_0)$. Liouville's theorem though allows to replace the integration variables and thus integrate on "initial" coordinates instead of integrating on "final" coordinates [97]. In addition, if we assume that the "starting" coordinates are namely $\mathbf{r_s} = \mathbf{r}^*(s)$ and $\mathbf{p_s} = \mathbf{p}^*(s)$[4] then the physical quantity A and equilibrium distribution function f_0 that are involved in integration, transform into $\tilde{A}(\mathbf{r}_s^t, \mathbf{p}_s^t)$ and $\tilde{f}_0(\mathbf{r}_s, \mathbf{p}_s)$. Importantly the phase volume element according to Liouville's theorem

$$d^3r d^3p = d^3r_s d^3p_s \tag{2.79}$$

---

[4] the involvement of "starting" coordinates presupposes an intermediate transformation $(\mathbf{r}, \mathbf{p}) \xrightarrow{(\mathbf{r_0}, \mathbf{p_0})} (\mathbf{r_s}, \mathbf{p_s})$ that has been omitted in this derivation since we do not consider the transient dynamics $t_0 = -\infty$.

Therefore using equation (2.78), we obtain

$$A(t) = \int\int d^3r d^3p \; \tilde{f}_0(\mathbf{r}_s, \mathbf{p}_s) \, \frac{1}{\tau} \int_{-\infty}^{t} ds \, e^{-\frac{t-s}{\tau}} \tilde{A}(\mathbf{r}_s^t, \mathbf{p}_s^t). \tag{2.80}$$

In this thesis, it should be emphasized that we have assumed the initial state to be homogeneous, so that the charge density of electrons is constant across the device with $N_e(\mathbf{r}, t) = N_0$. In this instance, equations (2.61), (2.62), that represent the average electron velocity and average miniband energy, respectively, can be reformulated to describe their steady-state time-dependent value according to (2.80)

$$\mathbf{v}(t) = \frac{2}{(2\pi\hbar)^3 N_0 \tau} \int d^3p \; f_0(\mathbf{p}_s) \int_{-\infty}^{t} ds \, e^{-\frac{t-s}{\tau}} \mathbf{v}(\mathbf{p}_s^t) \tag{2.81}$$

$$W(t) = \frac{2}{(2\pi\hbar)^3 N_0 \tau} \int d^3p \; f_0(\mathbf{p}_s) \int_{-\infty}^{t} ds \, e^{-\frac{t-s}{\tau}} E(\mathbf{p}_s^t), \tag{2.82}$$

where the integration limits in both later equations for p_z and p_y are $\pm\infty$ whereas p_x is integrated over the Brillouin zone. In this subsection we have revisited the derivation of exact solution of the Boltzmann equation [97] employing the method of characteristics which has been previously used to obtain the same results [66, 67, 132]. A different approach that has been used to acquire the solution, is a generalised technique relied on the time-evolution operator [133, 134].

Solving the stationary Boltzmann equation for the energy dispersion relationship (2.29), it can provide the maximum miniband velocity v_0 or the maximum average miniband energy W_0 that the electron can obtain

$$v_0 = \frac{2}{(2\pi\hbar)^3 N_0} \frac{\Delta d}{2\hbar} \int d^3p \; f_0(\mathbf{p}) \, cos(p_x d/\hbar) \tag{2.83}$$

$$W_0 = \frac{2}{(2\pi\hbar)^3 N_0} \frac{\Delta}{2} \int d^3p \; f_0(\mathbf{p}) \, cos(p_x d/\hbar) \tag{2.84}$$

By assuming the limit of the non-degenerate case (2.67), the former equations can reveal the temperature dependency of kinetic transport

$$v_0 = \frac{\Delta d}{2\hbar} \frac{I_1(\Delta/2k_B T_e)}{I_0(\Delta/2k_B T_e)} \tag{2.85}$$

$$W_0 = \frac{\Delta}{2} \frac{I_1(\Delta/2k_B T_e)}{I_0(\Delta/2k_B T_e)}, \tag{2.86}$$

where I_0, I_1 are the modified Bessel functions of zeroth and first order respectively, T_e the lattice temperature and k_B the Boltzmann constant. The peak current density then can be simply determined by

$$j_p = N_0 e v_0 \tag{2.87}$$

This type of temperature dependence of current density has been verified experimentally in superlattices with narrow band widths [135–137]. These measurements also confirmed that electron dynamics is governed by miniband transport even at higher temperatures.

Simplified path-integral formulation

It is worth noting that in the case of a static electric or magnetic fields, the stationary drift velocity can be written in a simplified form introduced by Pippard [138]

$$v_d = \int_0^\infty v_x(t) e^{-\frac{t}{\tau}} \frac{dt}{\tau}. \tag{2.88}$$

This approach was used by Esaki and Tsu to calculate the drift velocity, taking into account the scattering time τ that affects the kinetic behaviour of the single electron in the miniband of SL. The relaxation time approximation [10] relies on the assumption that after scattering event the divergence from the unperturbed value of distribution function f_0 is $\delta f = 0$ due to the perturbation induced by the applied fields. This essentially means that the electron forgets the semiclassical path that it followed prior to collision event. The equation can be post-hoc justified as follows. The probability of a scattering event taking place in time dt is assumed to be dt/τ where τ is significantly larger than dt. The latter statement can be redefined by describing the dt as a time interval smaller than the duration of scattering-free motion. If the number of electrons that remain unscattered at time t is n(t), then following the previous arguments, the number of electrons scattered in time dt is described by

$$\frac{dt}{\tau} n(t) \tag{2.89}$$

Hereafter, the number of electrons that remain unscattered by the time t + dt is

$$n(t + \Delta t) = n(t)\left(1 - \frac{\Delta t}{\tau}\right) \tag{2.90}$$

The rate of the unscattered electrons can determined then by

$$\frac{dn}{dt} = \lim_{\Delta t \to 0} \frac{n(t + \Delta t) - n(t)}{\Delta t} = -\frac{n(t)}{\tau}. \tag{2.91}$$

Integrating equation (2.91) yields the the number of unscattered electrons at time t

$$n(t) = n_0 e^{-\frac{t}{\tau}}, \tag{2.92}$$

where $n_0 = n(t = 0)$ is the number of unscattered electrons at t=0. Thus, the probability of an electron to be scattered in time dt is:

$$p(t)dt = \frac{n(t)}{n(0)}\frac{dt}{\tau} \tag{2.93}$$

Substituting the number of unscattered electrons at time t into equation (2.93) we acquire

$$p(t)dt = \frac{1}{\tau}e^{-\frac{t}{\tau}}dt \tag{2.94}$$

Here $p(t)$ is actually a probability distribution that can reveal mean relaxation time

$$\int_0^\infty \frac{t}{\tau}e^{-\frac{t}{\tau}}dt = \tau. \tag{2.95}$$

The last relationship indicates that scattering time τ is equivalent to the average relaxation time $< \tau >= \tau$. This outcome is anticipated since according to our assumption every electron experiences the same scattering time. As we noted above, the electrons cannot recall their kinetic behaviour before the scattering events, and thus the velocity of electron is averaged over theoretically infinite time taking into account the probability of scattering addressed by equation (2.94). Within this theoretical context, the drift velocity can be defined as

$$v_d = \int_0^\infty v_x(t)p(t)dt = \int_0^\infty v_x(t)e^{-\frac{t}{\tau}}\frac{dt}{\tau}, \tag{2.96}$$

which is identical with the relationship (2.88) describing the stationary averaged velocity. Considering that electron propagates in the x–direction of the superlattice under the influence of a static electric field $\mathbf{E} = (-E_{dc}, 0, 0)$, and using equation (2.88), we obtain the following expression for drift velocity

$$v_d = \int_0^\infty \frac{\Delta d}{2\hbar}\sin\left(\frac{eE_{dc}d}{\hbar}t\right)e^{-\frac{t}{\tau}}\frac{dt}{\tau}. \tag{2.97}$$

The later equation indicates that for the particular case under study, the effect of the dc electric field on miniband transport is discussed for electrons starting at the bottom of the miniband $k_x(0) = 0$. An analytical expression of v_d can be obtained if we use the Laplace transform

$$\int_0^\infty \sin(at)e^{-st}dt = \frac{a}{s^2 + a^2}.$$

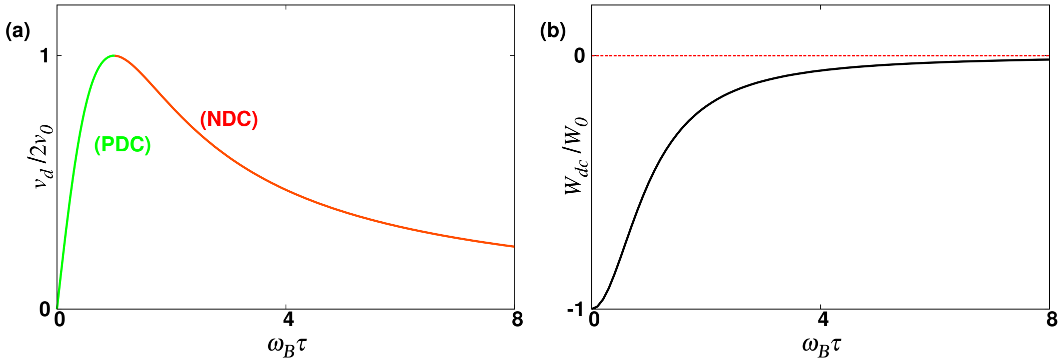

Figure 2.5: (a) Esaki-Tsu curve estimated using equation (2.98). (b) The average miniband energy dependence W_{dc} on Bloch frequency ω_B.

Then equation (2.97) becomes

$$v_d = v_0 \frac{\omega_B \tau}{1 + \omega_B^2 \tau^2}, \tag{2.98}$$

where $\omega_B = eE_{dc}d/\hbar$ is the frequency of Bloch oscillations and $v_0 = \Delta d/2\hbar$ designates the maximal change of electron velocity within the miniband. In a similar manner the average miniband energy can be obtained considering the Esaki-Tsu treatment

$$W = \int_0^\infty E(p_x(t)) e^{-\frac{t}{\tau}} \frac{dt}{\tau}, \tag{2.99}$$

and thus,

$$W_{dc} = -W_0 \frac{1}{1 + \omega_B^2 \tau^2}, \tag{2.100}$$

where $W_0 = \Delta/2$. The Esaki-Tsu curve corresponding to the analytical formula of drift velocity (2.98) is depicted in figure 2.5(a). The maximum drift velocity is obtained when $\omega_B = 1/\tau$, can be calculated by a simple differentiation of Esaki-Tsu relation. Thus, v_0 corresponds to the critical electric field

$$E_{dc} = E_{cr} \equiv \frac{\hbar}{ed\tau}. \tag{2.101}$$

If $\omega_B \tau << 1$, the drift velocity gets linearized $v_d \approx \Delta d^2/(2\hbar^2) eF\tau$ as seen in figure 2.5(a) where the curve exhibits almost linear behaviour for small Bloch frequencies. According to the Drude model [36], that describes the electron transport in isotropic crystalline solids in the presence of electric field, the averaged velocity is $< v_x >= eF\tau/m$. Both models converge to the same result for weak dc bias, the region, where the superlattice behaves as an ordinary conductor. Therefore, if in the Drude relationship we replace the mass of electron with the value of the effective mass at the bottom of the band where $m_0 = 2\hbar^2/(\Delta d^2)$ then the averaged velocity becomes $< v_x >= \Delta d^2/(2\hbar^2) eF\tau$. The electrons in this regime are scattered way before they have the chance to reach the boundary of the Brillouin zone. On the other hand, increasing the electric field beyond the point where the drift velocity obtains its maximum value, the electrons are allowed to progress far along the dispersion curve before they get scattered, and eventually to approach the edge of Brillouin zone. This results in the suppression of electron transport, which is reflected in the reduction of drift velocity with the increase of E_{dc} [see Fig. 2.5(a)]. On the contrary, average miniband energy [see Fig. 2.5(b)] continues to increase for large enough electric field $E_{dc} > E_{cr}$ $(\omega_B\tau > 1)$. In the region of negative differential velocity $\partial v_d/\partial E_{dc}$ <0, many electrons can perform effectively Bloch oscillations after being Bragg reflected. In the limit of a strong electric field $\omega_B\tau >> 1$ both v_d and W_{dc} disappear asymptotically implying that the electrons are homogeneously distributed within the Brillouin zone. Especially at high enough temperatures, the electrons obtain additional energy, since the non-degenerate electron gas is heated. Once the electrons get into the negative differential conductivity region, the energy attributed to thermal excitation is consumed by the formation of propagating high-field domains [36], making the transition to the population inversion $W_{dc} > 0$ inaccessible. The emergence of NDC triggers the formation of charge and field domains [41, 139] due to growth of space charge fluctuations that prevent the unswerving observation of Esaki-Tsu curve. However, seed of negative differential conductance was observed quite early after Esaki and Tsu predicted that its source is exactly what leads to Bloch oscillations [140]. In this work Esaki and Chang considering a weakly coupled SL with extremely narrow potential barriers, they reported domain formation induced by the appearance of NDC at an electric field beyond the critical point. The onset of space-charge fluctuations coincide with the threshold of localisation revealing multiple kinks in the conductance as the domains are fully developed. This system though behaved as multiple quantum well for a strong electric field associating the NDC effects with hopping conduction. Subsequently, a direct confirmation of negative differential conductance was observed by Beltram et al. in 1990 [141]. This experiment was an important confirmation of Stark quantization, indicating that the localisation of wavefunction is concurrent with the condition for NDC $\omega_B\tau > 1$. At the same time in France, Sibille et al. [142] using purely electrical techniques, were able to show that perpendicular NDC is feasible and an actual demonstration of the localisation of SL electronic states by Bragg reflection in the presence of electric bias. In the second experimental verification, transport processes through thin barriers were addressed making the semiclassical transport model adequately descriptive for miniband conduction. In recent years [137, 143–145], a series of experiments validated the picture of Esaki-

Tsu characteristic for the electric field-drift velocity dependence.

The different approaches to description of superlattice transport

In general, it is possible to distinguish the description of transport in SLs, in three complementary approaches, namely: miniband conduction, Wannier-Stark hopping (WSH), and sequential tunnelling [34, 89]. The ranges of validity of these different approaches have been addressed qualitatively [146, 147]. Moreover, specific calculations have been presented [148] to specify the borderlines between regimes of the different transport approaches by assembling a parameter space defined by energy scales $\Gamma = \hbar/\tau$, $eE_{dc}d$ and Δ. The semiclassical miniband transport model, which holds the main theoretical framework in this thesis becomes applicable when the energy miniband width is considerably larger than the rest of energy scales with $\Delta >> eE_{dc}d$ and $\Delta >> \Gamma$.

The transport model for Wannier-Stark hopping [149] can be applied to describe the transitions between the eigenstates of the Hamiltonian of a Bloch particle in the presence of an additional external field. These so-called Wannier-Stark states are metastable states with lifetime ascribed by scattering $\tau = \hbar/\Gamma$. Therefore, the scattering processes induce transitions between these states, accompanied by net current in the direction of the applied electric field. More importantly, the Wannier-Stark hopping approach is used to contribute supplementary to the interpretation of NDC region of drift velocity characteristic when spacing $eE_{dc}d$ is significantly larger than the energy scale Γ ($eE_{dc}d >> \Gamma$). However, Wannier-Stark hopping fails to describe the linear dependence of drift velocity on electric field as $E_{dc} \to 0$. To overcome this divergence, it was shown that WS hopping can be extended to lower field values for strongly coupled SLs by assuming that scattering times are much larger than tunneling times [150, 151].

The sequential tunnelling processes are feasible, when the barrier width of the superlattice is large enough to transform the structure into a series of decoupled quantum wells. In that case, a sequential resonant tunnelling of electrons between neighbouring wells of SL is possible if the relative height of the energy levels on each well is varied by a static electric field applied in the direction of growth of the SL. Thus, the transport process takes place from the first subband across the barrier into the second subband in the neighbouring well and subsequently rapid scattering of the electrons out the second subband into the first subband in the same well. These resonances cause strong nonlinearities in the local current-field relation. To calculate the drift velocity in this scheme, it is crucial to model accurately the scattering processes of the electrons within the wells, involving the scattering induced broadening of the states. The criteria for the validity of sequential tunnelling regime are reversed in comparison with semiclassical miniband scheme ($\Delta << eE_{dc}d$ and $\Delta << \Gamma$), implying the residual coupling between the wells. Interestingly though, both miniband transport and sequential tunneling model exhibit a drift velocity electric field dependence that fits the behaviour of Esaki-Tsu curve.

It was shown that the previously discussed approaches can be reproduced in the suitable limits from a quantum transport model by employing nonequilibrium Green functions [34, 148].

Fundamentals of charge domain formation in superlattices

In this section, we refer to the instability of the homogeneous electric field and how it affects the formation of charge domains in an infinite superlattice structure. This electric instability, which is manifested at NDC state, shares a lot of similarities with the regions of charge accumulations observed in the Gunn-effect despite the very different physical processes underlying the NDC itself. The case of instability development due to oscillatory character of charge transport in the SL narrow miniband was theoretically realised in [41] and then experimentally confirmed [152, 153].

To develop some understanding of the semiclassical miniband dynamics when the electron distribution is not spatially homogeneous, we will examine how domains grow and propagate in the SL under external applied voltage V, along the x-axis defined as being in the growth direction of the SL layers. In particular, considering that the drift velocity-field relation demonstrates a N-type shape induced by resonant tunneling at low fields, the electron dynamics can be described by the Boltzmann transport equation and Gauss' law, relating the distribution of electric charge $N_e(x)$ to the resulting electric field at position x, $\mathbf{F}(x)$

$$\nabla \cdot \mathbf{F}(x) = \frac{-e}{\epsilon_0 \epsilon_r} N_e(x), \tag{2.102}$$

where $\epsilon_0 = 8.8541 \times 10^{-12}$ F m^{-1} is the vacuum permittivity and ϵ_r is the relative permittivity of the material of the device. We suppose that the density of electrons is initially equal to the doping density N_0, implying that the equilibrium distribution function does not depend on the position. Therefore, the initial state of the system corresponds to a homogeneous field across the SL, whose value depends on

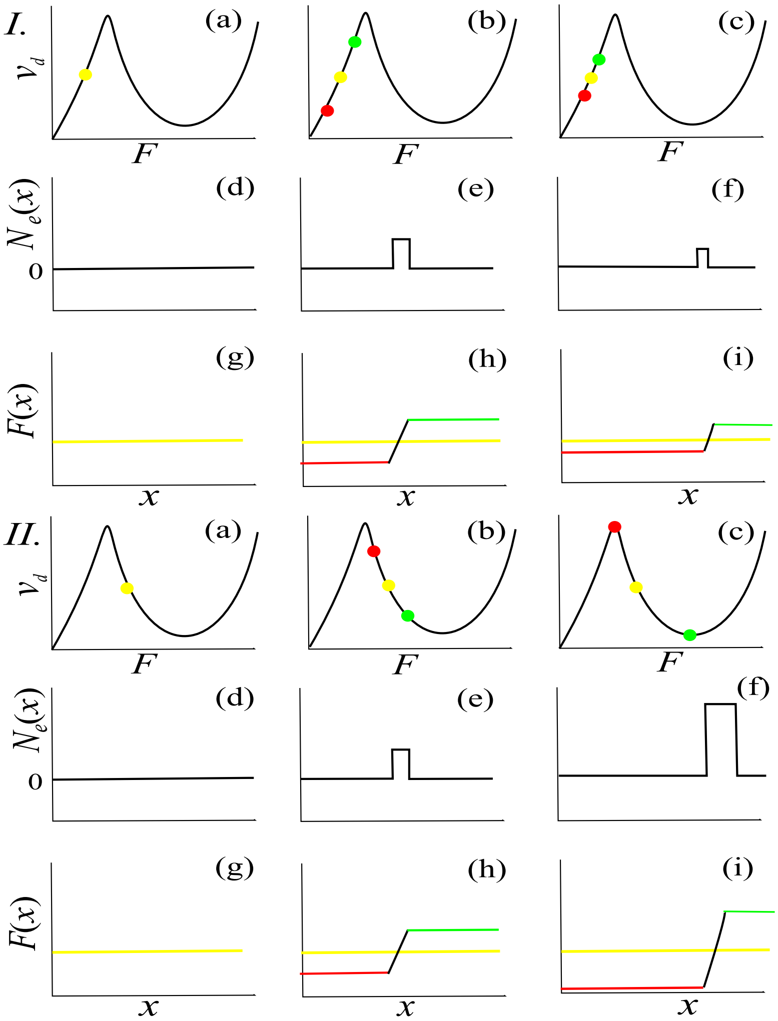

Figure 2.6: Schematic representation of domain formation in superlattice. Each column contains three different panels corresponding to $v_d(F)$, $N_e(x)$ and $F(x)$. Left-hand, centre and right hand columns, represent, respectively, the system in equilibrium, the behaviour of the system in response to a perturbation of local equilibrium caused by a small charge accumulation and the following evolution of that charge accumulation. Yellow dots and lines demonstrate the system in equilibrium. Green dots and lines show the high field regions. Red dots and line show the low field regions. *I.* The voltage applied to the superlattice is sufficient to access a region of PDV. *II.* The voltage is selected such that electric field lies initially in the negative differential region.

the electric potential according to

$$\mathbf{F}(x) = -\nabla\phi(x). \tag{2.103}$$

The latter equation indicates that for a potential that increases linearly through the device, the electric field remains constant along the x–direction [see Fig. 2.6 I(g)]. Controlling the voltage applied, V, which coincides with the total change of potential, we can optimally choose the field to stand at the PDV part of the drift velocity characteristic. It worth noting now the effect of a small perturbation of the charge density distribution induced by current injection into the device from the emitter. In that case, a small charge accumulation is formed [see Fig. 2.6 I(e)] with its initial location being assumed for simplicity, half way through the SL's extension. It is clear from equation (2.102) that the electron accumulation should introduce a jump in the electric field so that the right side of the device has higher field in comparison with left side. The value of drift velocity for the low field region is lower than the one for the high field region [see Fig.2.6 I(b)]. This allows the electrons to move away from the charge accumulation area faster than they enter in through the red region. Henceforth, the charge accumulation is shrinking [see Fig. 2.6 I(f)] as it moves along the SL, since the electrons that form the charge accumulation retain their mobility with the drift velocity determined by the value of local field. Let us consider now the effect of the same local perturbation in the net charge when the voltage applied to the superlattice is high enough to access the negative differential velocity region of drift velocity curve, as shown in figure 2.6 II(a). In the last-mentioned situation, the small charge accumulation continues to grow because the electrons approach the zone of charge accumulation faster than they leave. This picture is justified by the fact that low drift velocity v_d exhibits a higher value in the low field region and a lower v_d in the high field region [see Fig. 2.6 II(b)]. Here again, the charge accumulation can become effectively a charge domain and travel through the SL with its velocity depending on the local field value. If the difference in velocities of electrons passing into charge domain and moving out of the accumulation saturates, then the charge accumulation ceases to increase [see Fig. 2.6 II(c),(f)]. Charge domain exhibits then stability in the sense that electrons within the accumulation move approximately with the same speed along the axis of SL.

The simplified description above constitutes a crude explanation of the formation and the propagation of the electric domains within a dc biased SL. There has been though, consideration of electric stability in the presence of time-dependent electric field [34, 154, 155]. In addition, serious research efforts have been taken to study how a magnetic field can influence the dynamics of the charge domains in superlattices [113, 156, 157]. Lastly, the case of collective dynamics of electrons moving through periodic potential have been examined [47]. This theoretical research revealed that an acoustic wave causes the formation of nonlinear charge domains which relate to the onset of Bloch-type oscillations. Associating the spatio-temporal profile of charge domains with signatures of single-electron behaviour, as was reported in acoustically excited SL, it becomes of paramount importance for this thesis. The reason lies in the fact that we proceed by searching for regimes in the following chapters, where domains do not form under the influence of acousto-electric pump field.

Chapter 3

Band transport in a superlattice driven by a sound wave

Acoustoelectric effects in crystals

The interaction of high-frequency acoustic waves with electrons is strongly related with the kinetic effects and optoelectronic properties in crystals. Many techniques for the generation of coherent phonons in low-dimension semiconductor devices have relied on the development femtosecond pulsed lasers [158–160]. The standard method involves the pump pulse directly focused on a thin metallic film while a time-delayed probe monitors the changes in optical transmission. Then, a phononic wave induced by pump pulse generates a periodic change in the optical properties of the sample. Generation of incoherent phonons had been formerly achieved in the mid-1960s [161] by introducing heat pulses in dielectric materials. This was the milestone for a series of devices based on broadband phonons in lower frequencies [162–164]. The potential benefit of sources that operate in monochromatic-mode is that they would be allowed to reach the sub-THz range, making feasible the sound-microscopy of higher resolution [165]. Along with the research on opto-acoustic transduction, investigations have been made for surface acoustic waves (SAW) [166], and bulk acoustic waves (BAW) [167] in piezoelectric structures [166–169]. In this case the SAW which can be electrically excited, endorses an electric field that interacts with drifting carriers in the neighboring semiconductor. On the other hand, BAW are induced by means of thin-film transducers covering the excited part of a piezoelectric material. Although the acoustoelectric devices that engulf SAW and BAW are out of the scope of

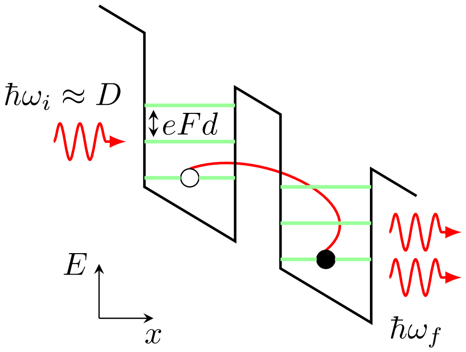

Figure 3.1: Figure adopted from citation [56], showing phonon-assisted hopping of electron between adjacent wells. The sinusoidal arrows illustrate the emitted or absorbed longitudinal acoustic (LA) phonons.

this work, their theoretical background is fundamentally connected with phenomena of electronic absorption and amplification of sound in semiconductor structures [170–173]. It was recently shown that acoustic excitation of a semiconductor heterostructure can induce measurable current pulses [61]. In particular, the optically generated thermoelastic deformation of an Al film which is deposited on bulk GaAs, creates a longitudinal strain pulse that propagates through the sample. The latter pulse is associated with a coherent acoustic wavepacket that interacts consistently with electrons by the deformation potential mechanism. In short, this concept reflects how the lattice vibration causes strain which induces a band edge shift. The phonon-generated strain is thus a wave that corresponds to the rate of change of a crystal's energy bands. Furthermore, the dynamic response of deformation potential couples different electronic states by a propagating periodic potential [49, 174, 175]. Therefore, electrons can be effectively trapped and dragged by the formulated traveling potential well. More importantly, it was demonstrated that this phonon drag of electron excited a current pulse in the absence of an electric field. Similar results were obtained using a semiconductor superlattice instead of GaAs epilayer sample between the contact layers in the experimental arrangement [61].

One of the most exciting developments in regard to high-efficiency materials harnessing acoustic waves is SASER (sound amplification by stimulated emission of acoustic radiation) device [56, 176]. It is considered to be the acoustic analogue to LASER. A weakly coupled SL, embedded in an acoustic cavity in the presence of electric field F, can function to provide coherent amplification of phonons (see Fig. 3.1). In the reference [56], it was reported the realisation of a such device based on a biased GaAs/AlAs SL with a period d that operates at sub-THz region (440 GHz).

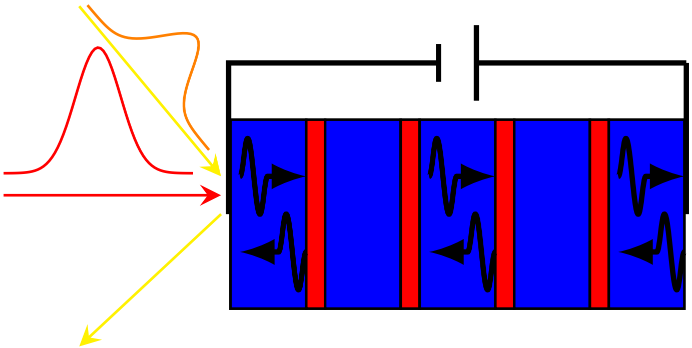

Figure 3.2: Figure modified from [58], demonstrating the schematic representation of SL structure in the presence of bias. The straight arrows indicate the pump-probe reflection geometry. The wavy arrows signify the generated LA phonons in SL.

The physical mechanism that describes the phonon amplification is based on the transition to a Wannier-Stark regime, where external field destroys the translational symmetry of the field-free Hamiltonian and results in the formation of a periodic sequence of energy levels (green horizontal lines in Fig. 3.1) separated by $D = eFd$ known as $Wannier-Stark\, ladder$ [149, 177]. The model of miniband electron transport is no longer applicable to Wannier-Stark regime. Hence, transport occurs by tunnelling between localised states in neighbouring quantum wells. Specifically, the electron perpendicular transport can be realised by inelastic phonon-assisted tunnelling or alternatively by an elastic process in-cooperating defect scattering with subsequent phonon or multiple phonons emission [178]. In the former case, the phonon-induced electron transition from a higher population to a lower population is indirect in momentum space due to low value of speed of sound. Thus, a phonon with energy $\hbar\omega_f < D$ can be emitted following the requirements for energy and momentum conservation. Subsequently, the phonon that was generated can be involved in other interwell transitions. Fine tuning of the phonons propagation at a relative angle to the normal of SL, would lead to coherent sound amplification of THz sound [56]. On the other hand, it was demonstrated experimentally that sound generation can occur due to intraminiband transport by involving the radiation of the so-called *Cherenkov* emission [58]. In this scheme, a GaAs/AlGaAs SL (see Fig. 3.2) excited by a picosecond optical pump in the presence of electric bias, generates coherent SL phonons at sub-THz frequencies. This mechanism involves a phonon wave propagating along with electric current, which can exchange energy through deformation potential. The piezoelectric coupling was weak in the experimental configuration due to lattice symmetry. The *Cherenkov* generation requires a component v_x of electron velocity to be greater that velocity of sound v_s, if the direction of sound is taken to be x-axis [172]. The population inversion of acoustic phonons is induced then because of electric momentum displacement. On the contrary, if the kinetic energy of the electrons is equal or less than the acoustic one, the net amplification of acoustic wave is attenuated.

It has been shown theoretically in relation to the above, how GHz acoustic waves can have a direct effect on electron transport in SL [47, 179]. In particular, it was demonstrated that the single electron dynamics are strongly depended on the sound wave amplitude. In addition, it was found that there exist different type of electron oscillations linked with distinct dynamical regimes, exhibiting THz frequencies far above the GHz frequency of the sound wave.

The results discussed above highlight the importance of phenomena associated with interaction of carriers with high-frequency phonons. Those effects unfold new possibilities especially for scrutinising electron dynamics in SL. Although a certain progress has been achieved in unscrambling the acoustoelectric transport, the underlying nonlinear dynamics can be still subjected to a thorough search. In this chapter, we will show how the kinetic behaviour is profoundly connected with real dynamic instabilities emerging with the modulation of acoustic wave properties.

Acoustic phonons in semiconductor superlattices

In the present work, we assume that the semiclassical particle transport is induced in a spatio-temporal potential of strongly coupled SL by a strain pulse similar to the one generated in the model considering intraminiband population inversion[1]. Here again, the acoustoelectric interaction is treated within the deformation potential framework. The acoustic wave can be represented as the atomic displacement within a unit cell

$$\begin{aligned}\mathbf{u}(\mathbf{r},t) = \frac{u_0}{2}\,\hat{e}_r[e^{i(\mathbf{k}\,\mathbf{r}-\omega_s t)} - e^{-i(\mathbf{k}\,\mathbf{r}-\omega_s t)}] \\ = u_0\,\hat{e}_r\,cos(\mathbf{k}\,\mathbf{r}-\omega_s t),\end{aligned} \tag{3.1}$$

---

[1] The existing model is applicable even for the sound generated by a saser device or using an ultrafast optical excitation of a metal film as it delivered in reference [61].

where u_0 is the maximum displacement and $\hat{e}_r$ is the unit vector along the principal growth axis [1 0 0]. The general form of the strain tensor as differential displacement of the atom site is described by

$$S_{ij} = \frac{1}{2}\left(\frac{\partial u_i}{\partial x_j} + \frac{\partial u_j}{\partial x_i}\right). \tag{3.2}$$

Here $x_j(x_i)$ constitute the components of vector $\mathbf{r}$ determining where a lattice point is located. The subscript i has value 1, 2 or 3, and for example x_j represents the Cartesian components of the vector $\mathbf{r}$. The change of the total energy of electron, induced due to elastic strain is given by [174]

$$\Delta E = \sum_{ij} \Xi_{ij} S_{ij}, \tag{3.3}$$

where Ξ is the deformation potential tensor. The summation can be reduced to a singular component $\Delta E = \Xi_d \, Tr(S)$, where Ξ_d is the hydrostatic deformation potential denoting the pure dilation[2] that unit cell undergoes. One of the underlining issues is the possible charge polarisation due to stress related effects. The piezoelectric coupling is outlined by a linear relationship between a second order tensor and a polarisation vector [180]

$$\delta P_i = \sum_j e_{ij} \epsilon_j. \tag{3.4}$$

Here e_{ij} determines the elements of piezoelectric tensor according to Voigt notation. If no shear strain is applied to a GaAs crystal, then there is only one non-vanishing element e_{14} which does not contribute to piezoelectricity [181, 182]. Therefore, considering a biaxial strain wave, the principal process of the effective electron-phonon interaction is the deformation potential without interference of piezo-electric effects [178, 183]. The potential energy due to the strain can be linked directly to the differential displacement

$$V(\mathbf{r}, t) = \Xi_d \cdot \nabla \mathbf{u} = -u_0 \Xi_d \hat{e}_r \mathbf{k} \sin(\mathbf{k}\mathbf{r} - \omega_s t). \tag{3.5}$$

Bearing in mind the one-dimensional character of miniband transport in superlattice and the longitudinal mode of phonon $\hat{e}_r \mathbf{k} = k_s$,we can acquire from equation (3.5)

$$V(x, t) = -u_0 \Xi_d k_s \sin(k_s x - \omega_s t) = -U \sin(k_s x - \omega_s t), \tag{3.6}$$

---

[2] the crystal dilation takes places in such a way that the internal reference points move uniformly without modifying the overall shape of the crystal.

where $U = ks\,u_0\,\Xi_d$ is the wave amplitude and $S_0 = k_s\,u_0$ the maximum strain induced by the lattice vibration. The other two traverse modes are orthogonal to the wave vector. The latter equations indicate the dependence of S_0 on phononic frequency $\omega_s = v_s\,k_s$, where $v_s = 5\,\times 10^3\,\mathrm{m/s}$ is the sound velocity in the medium. The linear frequency dispersion reflects a small–k group velocity which is considered for LA phonons that propagate in x-direction similar to zincblende structures [58, 59, 184].

With reference to S_0 which has been measured to be $\sim 10^{-4} - 10^{-2}$ and $\Xi_d \approx 10\,\mathrm{eV}$ [61, 174, 185, 186] designating the electron-phonon coupling constant, the maximum wave amplitude in this work is 50 meV. Nevertheless, it would be within reason if an enhanced high-field strain was assumed. This approach in order to be feasible presupposes an ultrafast laser excitation of a different thin metal film deposited on the substrate side [187, 188].

Effects of sound on miniband transport

To explain the effect of a plane wave that propagates along the SL's axis in x-direction in the previous section, we adopted the deformation potential mechanism. Therefore, the moving potential can be represented as

$$V(x,t) = -U\sin[(k_s(x+x_0)+\omega_s t)], \tag{3.7}$$

where displacement x_0 defines the initial phase of the driving wave. The electron transport is assumed only within the lowest miniband, and interminiband tunnelling is neglected. The same approach was also used in the Section 2.3. Then, within the tight-binding approximation, the kinetic energy of electron is defined as

$$E(p_x) = \Delta/2\left[1-\cos(p_x d/\hbar)\right], \tag{3.8}$$

where p_x is the electron quasi-momentum, Δ is the miniband width, and d is the period of SL. The semiclassical Hamiltonian $H(x,p_x) = E(p_x) + V(x,t)$ yields the following equations of motion:

$$\begin{aligned} v_x = \frac{dx}{dt} &= \frac{\partial H}{\partial p_x} = \frac{\Delta d}{2\hbar}\sin\frac{p_x d}{\hbar}, && (3.9)\\ \frac{dp_x}{dt} &= -\frac{\partial H}{\partial x} = k_s U\cos[(k_s(x+x_0)-\omega_s t)]. && (3.10) \end{aligned}$$

These equations were integrated numerically using a 4th order Runge-Kutta method [189] to find the electron trajectories.

Drift and mean velocity characteristics

In order to describe the dissipative electron dynamics in the presence of a spatial periodic potential, we use the well-established miniband transport model based on Boltzmann transport equation [102, 126], which was earlier outlined in Section 2.3. A different approach [47] was previously implemented to calculate drift velocity of electron v_d, based on Esaki-Tsu formalism [10]. The latter approach treats the electric field distribution along the SL being almost uniform, constant in time. It is worth noting that this formulation generates a drift velocity wave amplitude dependence that exhibits different behaviour for different initial conditions. Furthermore, this finding reveals additionally a connection between ballistic transport and conditions for the strong suppression of v_d. In order to improve the previous analysis and to take into account different initial conditions, we use the time-dependent path integral [133, 138, 190, 191] as a steady solution of the time-dependent Boltzmann transport equation. Therefore, for a constant relaxation time τ and a more general excitation, such as the one described by the model (3.9), (3.10), the drift velocity is determined by

$$v_d = \int_0^T \frac{dt}{T} \int_{-\infty}^{t} e^{\frac{-(t-t_0)}{\tau}} v_x(t, t_0) \frac{dt_0}{\tau}, \tag{3.11}$$

where t_0 is the moment of time, when the electron can be found at position x_0; and $T = 2\pi/\omega_s$ is the period of the acoustic plane wave. Equation (3.11) suggests that drift velocity can be calculated without further resorting to Boltzmann equation, but at the same time its formal solution requires the explicit description of nonlinear electron transport ruled by equations (3.9) and (3.10). The steady-state time-dependent drift velocity then can be fairly presented as the velocity of a single electron averaged over all initial moments t_0 after taking into account a probability of electron scattering within the time interval between $t - t_0$ and $t - t_0 + dt$. To evaluate the average drift velocity, it has to be averaged additionally over a time period commensurate with the period of sound wave. The problem of drift velocity calculation can be revisited by proposing a different approach that introduces averaging of electron velocities not over initial time t_0, but across the initial positions x_0 or, equivalently, across the initial phases of the acoustic wave. In this perspective, bearing in mind that Hamiltonian H is periodic in time, the velocity of electrons in the presence of scattering events $v(x, t)$ can be expanded in Fourier series [133] as

$$v(x, t) = \sum_n v_n e^{ink_s(x - v_s t)}$$

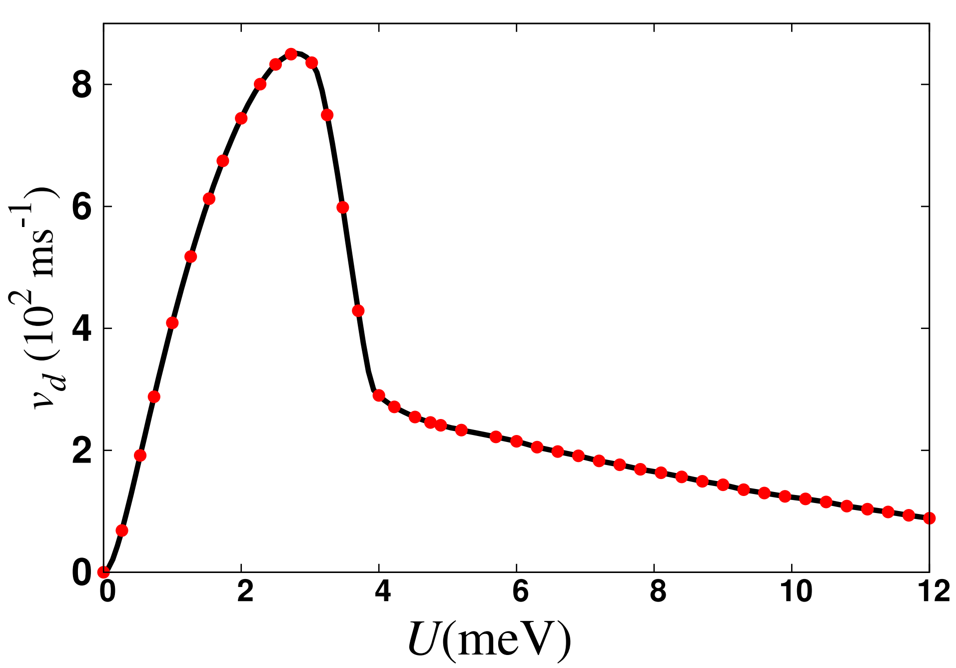

Figure 3.3: Solid curve: Drift velocity versus U calculated using the path-integral solution (3.11) of the Boltzmann equation. The red dots show the calculation of the v_d obtained with equation (3.12).

with

$$v_n = \frac{1}{\lambda}\int_0^{\lambda} dx_0 \int_0^{\infty} e^{\frac{-t'}{\tau}} v_x(x_0,t') \times e^{-ink_s(x_0+v_s t')}\frac{dt'}{\tau}, \tag{3.12}$$

where $\lambda = 2\pi/k_s$ represents the wavelength of the propagating wave. By applying Jacobian $J = \partial(tv_s, t-t_0)/\partial(t,t_0)$, the set of variables (x_0,t') can be substituted by (t_0,t), for which equation (3.12) takes the form

$$v_n = \frac{1}{T}\int_0^{T} dt \int_{-\infty}^{t} e^{\frac{-(t-t_0)}{\tau}} v_x(t,t_0) e^{-in\omega_s t}\frac{dt_0}{\tau}. \tag{3.13}$$

The zeroth Fourier component (for $n = 0$) of the velocity in (3.13) is of particular importance, so that v_0 is identical to the drift velocity v_d calculated with the time dependent path integral (3.11). The connection of these calculations suggests that integration over all initial starting times t_0 in (3.11) is equivalent to integration over all electron initial positions x_0 realized in (3.12). In this particular problem,

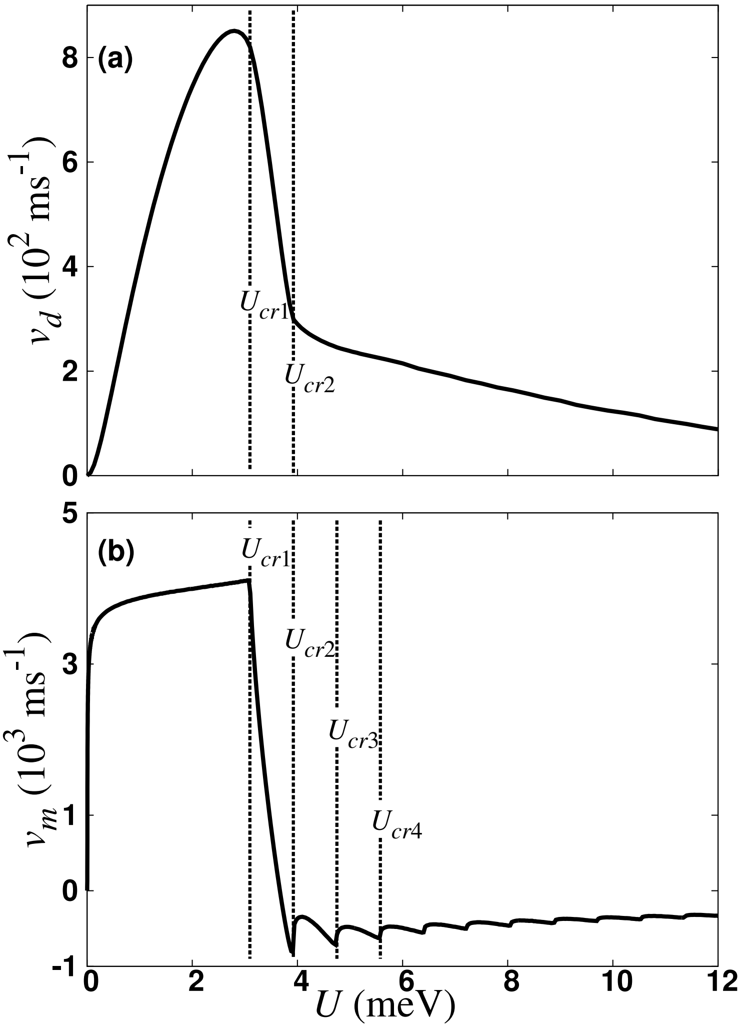

Figure 3.4: (a) The drift velocity v_d as a function of the acoustic wave amplitude U; (b) the dependence of the time–averaged electron velocity v_m upon U. The vertical lines correspond to the critical values of U.

with sound propagating through superlattice, it is possible to involve this equivalence to interpret the effect of electron trajectories with different dynamic properties on kinetic transport. Furthermore, the latter approach is implemented for efficient optimization of v_d calculation, since the direct averaging over the initial positions is a easier numerical task. This method can be considered as an effective alternative for the path-integral solution of Boltzmann equation used for arbitrary time-dependent electric and static magnetic field applied in SLs [192–194]. In the simulations of the present chapter produced for $v_0 > v_s$, we consider a strongly coupled SL outlined in 2.1, with a set of realistic parameters: $\Delta = 7$ meV, $d = 12.5$ nm, $\omega_s = 4 \times 10^{11}$ rad/s, $v_s = 5000$ m/s and $\tau = 250$ fs. Assuming that v_0 is determined by (2.85), we get using the latter SL parameters $v_0 \approx 6.65 \times 10^4$ m/s ($v_0 \approx 13.3\, v_s$). Larger maximum miniband velocities can be obtained by using SL structures with wider minibands or superlattice periods. The variation of drift velocity v_d with the increase of the acoustic wave amplitude U is demonstrated in figures 3.3 and 3.4(a). In particular, figure 3.3 shows an excellent agreement between the path-integral approach based on equation (3.11) and the drift velocity calculated [see Eq. (3.12)] by averaging the electron velocities across the different initial phases x_0 of the driving wave. Although the conduction electron temperature may affect the electron transport [195], for simplicity we consider that electrons initial momentum is p_0=0 that corresponds to $T_e \to 0$. One can see that $v_d(U)$ characteristic demonstrates a strongly non-monotonic dependence which manifested itself with a dramatic suppression of drift velocity that it would appear at a characteristic value U_{cr1} [see Fig. 3.4(a)]. Subsequently, the curve exhibits an observable change in slope at U_{cr2}. The appearance of a prominent peak for the former value of wave amplitude resembles Esaki-Tsu $v_d(E_{dc})$ curve [10]. In that case, if the electric field is large enough ($E_{dc} > E_{cr}$) electrons can reach the edge of Brillouin zone before scattering, and the drift velocity decreases with the increase of electric field. However, it has been found that driving electrons with sub-THz waves can induce a sudden onset of Bloch-type oscillations when U exceeds a critical threshold, thereby causing negative differential velocity [47, 196]. The non-monotonic dependence illustrated in figure 3.4(a) as follows can be associated either with changes in dynamics or scattering events. To find which mechanism prevails we calculate the mean velocity of electrons v_m averaged over the time:

$$v_m = \frac{1}{\lambda}\int_0^{\lambda} dx_0 \int_0^{\Delta t} v_x(t+t_0, t_0)\frac{dt}{\Delta t}. \tag{3.14}$$

Actually, mean velocity can be thought as finite time version of the equation (3.12) where the effect of scattering is negligible ($\tau \to \infty$). In these calculations, v_m was averaged over a period Δt=2 ns equivalent with a large number of periods of acoustic wave oscillations. Determining the averaged velocity is considered to be a significant process to reflect the measured transport characteristics of cold atoms in optical lattices. Given the dispersive energy-quasimomentum relation of the optical lattice, we expect that ultracold atoms exhibit similar dynamics to acoustically driven electrons in superlattice, using a sound wave in high-frequency $\omega_s\tau > 1$ for the acoustic excitations.

Figure 3.4(b) illustrates the dependence of $v_m(U)$. Here, the curve again demonstrates a non-monotonic character. Remarkably, it presents its pronounced features at almost the same values [U_{cr1},U_{cr2}-dashed lines in Fig. 3.4(b)] as the drift velocity-wave amplitude characteristic [see Fig. 3.4(a)]. In contrast to the latter, the graph shown in figure 3.4(b) reveals the emergence of multiple maxima and that the electron can access a region of negative velocity. On the other hand, if we would had only a dc electric field applied, the Bloch oscillations would lead to the localisation of electrons in the absence of scattering and thus to the suppression of mean velocity [197]. The dynamic localisation occurs since the electron periodically returns to its initial state after a single Bloch period.

Dynamical regimes and their phase portraits

The description of electron motion within a co-moving frame can follow a transformation from the inertial frame at rest (lab frame) with coordinates (x, t) to the propagating frame of acoustic wave determined by the coordinates (x', t). In order to understand how dynamics of electrons affects v_m and v_d,we can analyse the equations of motion (3.9) and (3.10) in the moving reference frame

$$x'(t) = x(t) + x_0 - v_s t \tag{3.15}$$

Using this canonical substitution, it is easy to prove that the system is completely integrable. This could give rise to a new Hamiltonian that appears to be time-invariant. To deliver this canonical transformation[3] we introduce the Lagrangian function $L(x, \dot{x}, t)$ of the system concerned, with x and $\dot{x}$ being the generalised coordinate and generalised velocity respectively. If those two kinematic parameters are concurrently determined then the transport state of the particle can be estimated for any given instant. The Lagrangian L under Legendre's transformation can be expressed

$$L(x, \dot{x}, t) = p_x \dot{x} - H(x, p_x, t), \tag{3.16}$$

whereas the canonically transformed Lagrangian L' is

$$L(x'(t), \dot{x}') = p'_x \dot{x}' - H'(x', p'_x, t). \tag{3.17}$$

Here H' is the Hamiltonian and p'_x the generalised momentum, both in the moving frame. If we engage a generating function approach, the *action integral* over the latter Lagrangians can provide the following canonical transformation

$$d\Phi = p_x dx + x' p'_x + (H' - H)dt \tag{3.18}$$

---

[3] For further guidance consult L.D. Landau and E.M. Lifishitz [198], they provide a good introduction in canonical transformations.

Therefore we can obtain

$$p_x = \frac{\partial \Phi}{\partial x}; \quad x' = \frac{\partial \Phi}{\partial p'_x}; \quad H' = H + \frac{\partial \Phi}{\partial t} \tag{3.19}$$

From here one can deduce that the generating function is a given function of *type two* that depends only on the old coordinate and the new momentum

$$\Phi(x, p'_x, t) = p'_x(x - v_s t) \tag{3.20}$$

Given that Φ is represented by equation (3.20), the relation between the generalised momentum in the moving frame and p_x follows from the formula (3.19)

$$p_x = \frac{\partial \Phi}{\partial x} = p'_x \tag{3.21}$$

obtaining that the canonical momentum is a translational invariant. The electron in the moving frame is subjected to a time-independent potential, and therefore the potential energy in equation (3.7) turns into

$$V(x') = -U \sin(k_s x') \tag{3.22}$$

Now the semiclassical Hamiltonian in the moving frame can be generated again by implementing equation (3.19), noting that the generalised momentum is the same in both frames

$$H'(x', p_x) = H(x, p_x) + \frac{\partial \Phi(x, p_x, t)}{\partial t} = E(p_x) - v_s p_x + V_s(x'). \tag{3.23}$$

Thus, the new Hamiltonian has a constant of motion, since there is no explicit time dependence. The kinetic energy versus crystal momentum dispersion relation in the moving reference frame can be described by a modified dispersion curve

$$E'(p_x) = E(p_x) - v_s p_x \tag{3.24}$$

New equations of motion should correspond to the Hamiltonian $H' = E'(p_x) + V(x')$. In that case the model has the form

$$\dot{x}' = v_0 \sin \frac{p_x d}{\hbar} - v_s, \tag{3.25}$$

$$\dot{p}_x = k_s U \cos(k_s x'), \tag{3.26}$$

which, in contrast to equations (3.9) and (3.10), does not explicitly depend on the time, and thus simplify analysis. Here, $v_0 = \Delta d/(2\hbar)$ characterises the maximal possible change of electron velocity within the miniband. For both numerical and analytical studies it is more convenient to rewrite equations (3.25) and (3.26) in a dimensionless form

$$\frac{d\tilde{x}}{d\tilde{t}} = \frac{v_0}{v_s}\sin\tilde{p} - 1, \tag{3.27}$$

$$\frac{d\tilde{p}}{d\tilde{t}} = \frac{Ud}{\hbar v_s}\cos\tilde{x}, \tag{3.28}$$

where, $\tilde{x} = k_s x'$, $\tilde{p} = p_x d/\hbar$, and $\tilde{t} = \omega_s t$. These normalized quantities have clear physical interpretations. Namely, $\tilde{p}$ corresponds to the phase of the de Broglie wave characterising a position of the electron within the first Brillouin zone, whereas $\tilde{x}$ and $\tilde{t}$ are associated with the phase and time component of the total phase of the acoustic wave, respectively.

Linear stability analysis of the dynamical system

For any conservative system, the determination of the equilibrium points plays a significant role for the construction of the global phase portrait[4]. Therefore, identifying the local behaviour around the equilibria, which comprise stable and unstable fixed points, can provide a tool to shed light on the phase-space dynamics. Here, we can extract the nature of phase trajectories near the fixed points in a model that describes a typical SL driven by an acoustic wave. Let us consider a simple stability analysis, which involves a 2D dynamical system in the form

$$\dot{\tilde{x}} = f_1(\tilde{x}, \tilde{p}), \tag{3.29}$$

$$\dot{\tilde{p}} = f_2(\tilde{x}, \tilde{p}). \tag{3.30}$$

The fixed points $(\tilde{x}_c, \tilde{p}_c)$ are held responsible for stationarising phase flow since $f_1(\tilde{x}_c, \tilde{p}_c) = 0$ and $f_2(\tilde{x}_c, \tilde{p}_c) = 0$. Let us represent a small perturbation from the fixed point as

$$\begin{cases} \epsilon_{\tilde{x}} = \tilde{x} - \tilde{x}_c \\ \epsilon_{\tilde{p}} = \tilde{p} - \tilde{p}_c \end{cases}$$

Expanding f_1, f_2 around the points $\tilde{x}_c, \tilde{p}_c$, we can obtain the evolution of disturbance according to

$$\frac{d}{dt}\begin{pmatrix} \epsilon_{\tilde{x}} \\ \epsilon_{\tilde{p}} \end{pmatrix} = \hat{C}\begin{pmatrix} \epsilon_{\tilde{x}} \\ \epsilon_{\tilde{p}} \end{pmatrix} + \tilde{O}(\epsilon_{\tilde{x}}^2, \epsilon_{\tilde{p}}^2, \epsilon_{\tilde{x}}\epsilon_{\tilde{p}}) \tag{3.31}$$

---

[4] For more details in phase plane analysis see the well-written textbook of J.M.T. Thompson and H.B. Stewart [199].

where $\tilde{O}(.)$ denotes the quadratic terms in $\epsilon_{\tilde{x}}$ and $\epsilon_{\tilde{p}}$ which are negligible since the terms $\epsilon_{\tilde{x}}$,$\epsilon_{\tilde{p}}$ are already small. Here $\hat{C}$ represents the Jacobian matrix at the fixed point $(\tilde{x}_c, \tilde{p}_c)$

$$\hat{C} = \begin{pmatrix} \dfrac{\partial f_1}{\partial \tilde{x}} & \dfrac{\partial f_1}{\partial \tilde{p}} \\ \\ \dfrac{\partial f_2}{\partial \tilde{x}} & \dfrac{\partial f_2}{\partial \tilde{p}} \end{pmatrix}_{(\tilde{x}_c, \tilde{p}_c)} \tag{3.32}$$

Henceforth, the dynamical system under discussion demonstrates a countable set of equilibrium points, which satisfy the following conditions

$$v_0 \sin \tilde{p} = v_s, \tag{3.33}$$

$$\cos \tilde{x} = 0. \tag{3.34}$$

Equations (3.33) and (3.34) evidence that a steady state corresponds to the situation, when an electron moves with the velocity of the acoustic wave v_s being at the position coinciding with one of extrema of the potential wave $V(x, t)$. This yields the following coordinates of the fixed points on the phase plane $(\tilde{x}, \tilde{p})$:

$$\tilde{x}_c = \frac{\pi}{2} + m\pi, \tag{3.35}$$

$$\tilde{p}_c = (-1)^n \sin^{-1}(\frac{v_s}{v_0}) + n\pi, \tag{3.36}$$

where n and m are arbitrary integer numbers. To classify them, we have to calculate the characteristic equation

$$det[\hat{C} - \lambda I] = 0 \tag{3.37}$$

where $\hat{C}$ is the Jacobian matrix and I is the identity matrix of identical dimension. Using (3.37) we can find the eigenvalues from the characteristic polynomial

$$\lambda^2 = \pm\mu \tag{3.38}$$

where $\mu = \frac{Ud}{\hbar v_s}\sqrt{\left(\frac{v_0}{v_s}\right)^2 - 1}$. In the present work we mostly focus on the realistic case $v_0 > v_s$, which conforms to the sole existence of saddle or centre points in accordance with equation (3.38). Thus, the general solutions to (3.31) are the following linear combinations

$$\begin{cases} \vec{\epsilon}_1 = \vec{c}_1 e^{\sqrt{\mu} t} + \vec{c}_2 e^{-\sqrt{\mu} t} \\ \vec{\epsilon}_2 = \vec{c}_3 e^{\sqrt{i\mu} t} + \vec{c}_4 e^{-i\sqrt{\mu} t} \end{cases} \tag{3.39}$$

Denoting $\vec{c_i}$ $(i = 1..4)$ as the eigenvectors associated with the eigenvalues. For the first part of equation (3.39) the flow is locally pure rotation around the fixed point whereas the second generates incoming and outgoing manifolds connected with the hyperbolic (saddle) point. The very existence of the fixed points can be interpreted as effective reduction of sound absorption and eventually transition to a transport regime where miniband velocity overreaches sound velocity. Other treatments of sound-electron interaction in crystals that consider the linearised Boltzmann transport equation, present the electron drift excess over v_s as a condition for sound amplification [171, 200].

For the sake of completeness, it is critical to consider as well the implication of maximum miniband velocity being less than v_s and the limiting case where the sound velocity coincides with v_0. If v_0/v_s=1 or equivalently when the critical equilibrium has eigenvalue $\mu = 0$, then the equilibria generated by the autonomous ODEs (3.29), (3.30) collide and form saddle-neutral stable node equilibriums

$$\tilde{x}_c = \frac{\pi}{2} + m\pi, \tag{3.40}$$

$$\tilde{p}_c = (-1)^n \frac{\pi}{2} + n\pi, \tag{3.41}$$

where n and m are integer numbers. This phenomenon can be associated with the so-called saddle-neutral stable node bifurcation or also known as fold bifurcation [201, 202]. Kinetics in this case have been studied for different dynamics scenarios in SL [203, 204]. In our system it reflects the minimum attenuation of sound or the efficient trapping of electrons in the moving potential of the sound wave. On the contrary, $v_0 < v_s$ causes the enhancement of wave attenuation, where the electron cannot find itself travelling with the trailing slope. In either of the two latter cases, the transport mechanism can be directly linked with the acousto-electric phenomena, where the effective electric field $E_s = k_s U/e$, induced by the

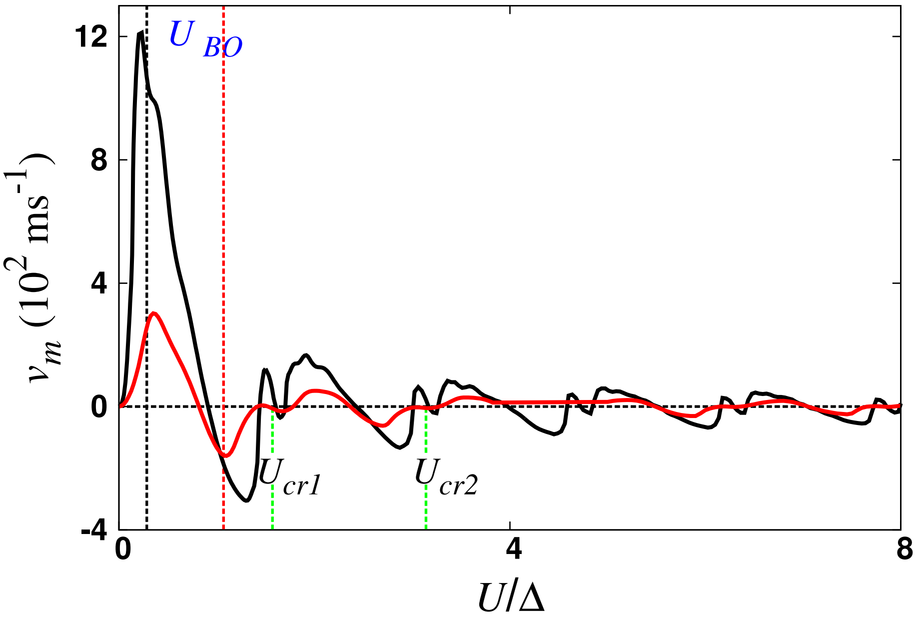

Figure 3.5: Mean velocity v_m versus U characteristics. Black curve shows mean velocity calculated using $v_0/v_s = 1$ whereas red curve for $v_0/v_s = 0.5$. Black and red vertical dashed lines show the onset of Bloch oscillations for $v_0 = v_s$ and $v_s = 2v_0$ respectively. The vertical green lines correspond to the critical values U. For advice, the horizontal dashed line indicates $v_m = 0$.

sound wave, can assemble electrons in bunches that interact with the propagating potential [170, 205]. This phenomenological approach is valid only for $k_s l \ll 1$ where k_s is the wave number of the sound and l is electron mean free path. On the other hand, in the short-wavelength limit, when the particle moves in the direction of the wave propagation with a velocity less than the wave's phase velocity, the wave will give up energy to the particle. In this picture, if the sound wave vector has the same direction as the velocity of electron and $v_0 > v_s$, then there is a net gain of energy from carriers to sound wave. This description encloses the possibility of phonon quantum emission following the Cherenkov-like radiation [171, 172]. Therefore, the energy that is absorbed by electrons can be modified under momentum displacement induced by electron-sound interaction. In order to realise how the electron transport is influenced by reducing the the maximal miniband velocity v_0, we calculate numerically the averaged velocity v_m as a function of U using equation (3.14). The same approach is used in regard to initial conditions of electron, considering $p_x(t_0) = 0$. In our calculation, we considered two values, the resonant case $v_0 = v_s$ and v_s having twice the magnitude of v_0. This subsonic motion is apparently slower than speed of sound for the particular substance. Figure 3.5 reveals how v_m varies as the amplitude of acoustic wave U increases. It can be observed that $v_m(U)$ for both values of v_0 preserve the non-monotonic character of transport, typical for an electron driven by a static electric field of magnitude k_sU/e [10]. However, in comparison with the maximum value of $v_m(U)$ that is attained for $U = U_{cr1}$ in figure 3.4(b), the overall electron transport is significantly suppressed. Both velocity profiles exhibit multiple peaks and they can obtain negative values. In figure 3.5 $v_m(U)$ for $v_0 = v_s$ shows a pronounced peak at $U = U_{BO}$ which is connected with the onset of Bloch oscillations as will be explained in detail in Section 3.3.6. On the other hand, when $v_s = 2v_0$ the characteristic of mean velocity attains a minima at $U = U_{BO}$, which is again associated with the initiation of the Bloch oscillations. When actually $U = U_{cri}$, it is possible to comprehend the transition from positive to negative velocity within the framework of analysing the phase space dynamics and their effects on kinetic properties of electron. Similar crossover occurs for the non-trivial parameters $v_0 = 2v_s$. Note that after this point, the mean velocity quickly vanishes.

Ballistic transport in phase space

We now restrict ourselves to the second-order autonomous system (3.27), (3.28) and represent the possible motions of electron transport by a diagram on the phase plane known as a phase portrait. As we discussed in the previous section, the fixed points can be classified according to their stability properties. The points, which are determined by equations (3.35), (3.36), are periodically spread in the phase space as illustrated in figure 3.6, where the black circles denote the centres, and the red crosses indicate positions of the hyperbolic fixed points (saddles).

Now dividing equation (3.28) by equation (3.27) we obtain the equation

$$\frac{d\tilde{p}}{d\tilde{x}} = \frac{Ud}{\hbar v_s} \frac{\cos \tilde{x}}{\frac{v_0}{v_s} \sin \tilde{p} - 1}, \tag{3.42}$$

which still describes the phase trajectories. This can be integrated to return the general solution that represents a phase trajectory, starting from the initial condition ($\tilde{x}_0$,$\tilde{p}_0$), as a function $\tilde{x}(\tilde{p})$

$$\tilde{x} = (-1)^n \sin^{-1} \left\{ \sin \tilde{x}_0 - \frac{\hbar v_s}{Ud} \left[\frac{v_0}{v_s} (\cos \tilde{p} \right. \right. \\ \left. \left. - \cos \tilde{p}_0) + \tilde{p} - \tilde{p}_0 \right] \right\} + n\pi, \tag{3.43}$$

where n is an integer number. The characteristic phase portraits of the dynamical system (3.27), (3.28) are shown in figure 3.6. In fact, they are produced using equations (3.35), (3.36) and (3.43) for different values of the acoustic wave amplitude: (a) $U < U_{cr1}$, (b) $U_{cr1} < U < U_{cr2}$, (c) $U_{cr2} < U < U_{cr3}$. The dynamical system under study can be equally analysed either on the plane ($-\infty < \tilde{x}, \tilde{p} < \infty$), or on the cylinder ($-\infty < \tilde{x} < \infty, -\pi \leq \tilde{p} < \pi$) or on the torus ($-\pi \leq \tilde{x}, \tilde{p} < \pi$). The phase space of the system, for small $U < U_{cr1} \approx 3.1$ meV [Fig. 3.6(a)], contains periodic "islands" of localized trajectories (blue and yellow closed orbits), which surround the corresponding centres. The fixed centres, as discussed previously, coincide with the lowest possible energy of periodic potential. Now, there is a distinction between localised trajectories which rotate clockwise (blue orbits) and those that rotate anticlockwise (yellow orbits), contingent on the position in the phase space. To fill the picture, regions of unbounded trajectories, which propagate either to positive or negative direction along the $\tilde{x}$–axis, interrupt the islands of the bounded trajectories. The positive or negative drift of these trajectories again depends on the initial value $\tilde{p}_0$. To be more specific, for the unbounded trajectories involved in figure 3.6(a), the ones (green lines) below the islands of the clockwise

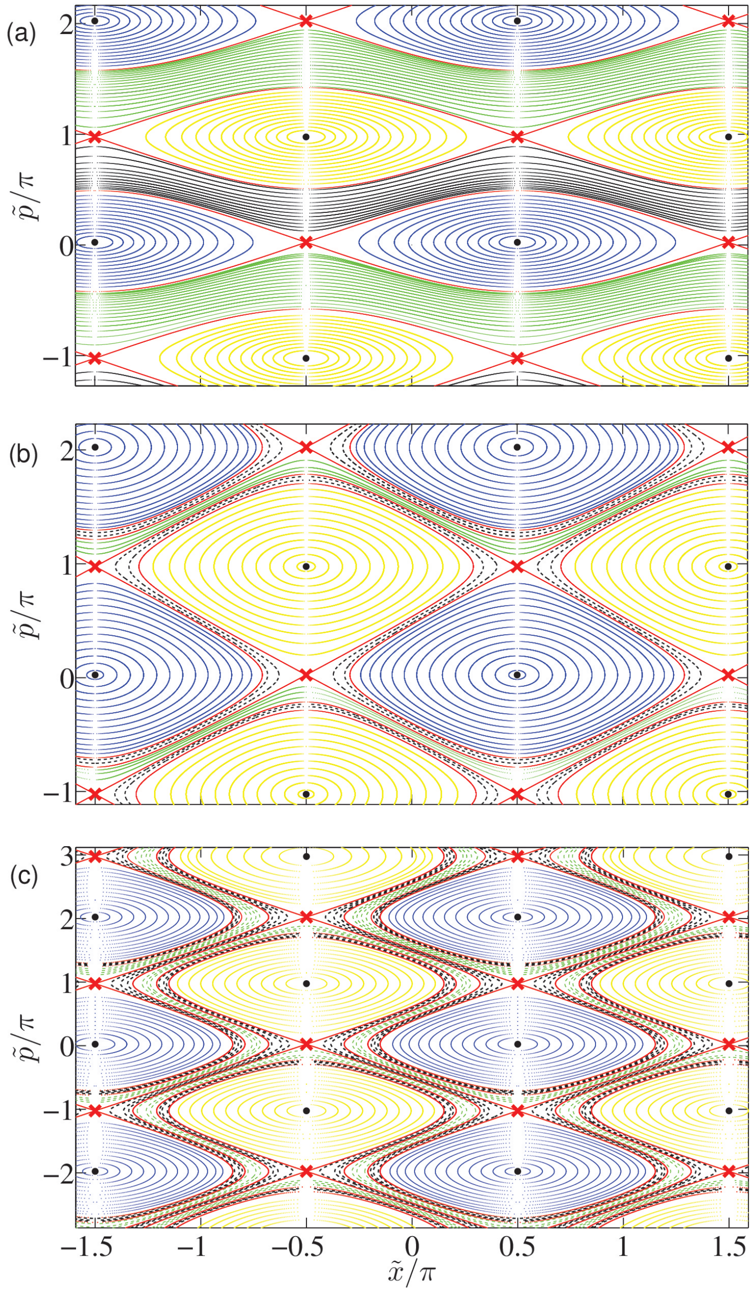

Figure 3.6: Phase portraits of the dynamical system (3.27), (3.28) for (a) $U = 1.5$ meV; (b) $U = 3.45$ meV and (c) $U = 4.25$ meV. The positions of equilibrium points are indicated by black solid circles (centres) and red crosses (saddles). The localized orbits are represented by blue and yellow dots. Smooth solid curves correspond to the unbounded trajectories, dashed curves mark the meandering trajectories, and red curves denote the separatrices.

orbits move in the negative direction of $\tilde{x}$, whereas the trajectories (black lines) above these islands propagate in the positive direction of $\tilde{x}$. The saddle points (red crosses) represent the electron at rest on the top of the potential well; hence the heteroclinic trajectories (red curves) segregate the areas of different trajectories. This heteroclinic structure comprise the separatrix, formed by manifolds of the saddle points with the same coordinate $\tilde{p}$. In a following section, we will show that for $\tilde{p} << 1$ such dynamics can be undestood in terms of the librations and rotations of a nonlinear pendulum. The regions of the localised trajectories grow with the increase of U. On the other hand, the areas of unbounded trajectories diminish and after the critical value U_{cr1}, the ones that propagate in positive direction they disappear completely, making evident a drastic change in the topology of phase portrait. This dynamic scenario engenders a new type of phase trajectories, which manifest a meandering behaviour [black dashed curves in Fig. 3.6(b)] that is delivered by the trajectories propagating around the islands of localised orbits. Note that these meandering trajectories drift always to the negative direction of $\tilde{x}$ regardless the initial conditions. Increasing U beyond $U_{cr2} \approx 3.92$ meV eliminates utterly the unbounded trajectories (the remaining ones which were moving in the negative direction), but at the same time new meandering trajectories emerge that exhibit enhanced complexity [black dashed curves in Fig. 3.6(c)]. This new type of meandering trajectories encompass more islands of localised orbits and they are extended in $\tilde{p}$-direction. The trajectories [green dashed curves in Fig. 3.6(c)] which were born when U overreached U_{cr1} survive, but they are less elongated in comparison with the previous ones. It is worth noting that similar appearance of new meandering trajectories takes place for other critical values of U ($U_{cr3} \approx 4.75$ meV and $U_{cr4} \approx 5.58$ meV) as shown in figure 3.4(b). Therefore, these trajectories envelope a larger number of islands of the localised orbits along $\tilde{p}$ − direction.

Similar meandering trajectories have been also observed in other Hamiltonian systems where the larger canonical momentum does not necessarily imply larger velocity, known as the violation of twist condition. In this case, the hyperbolic points can be joined in different ways either with heteroclinic or homoclinic connections [206]. These type of Hamiltonians have been studied with respect to different applications in plasma physics, fluid dynamics and condensed matter physics [206–208].

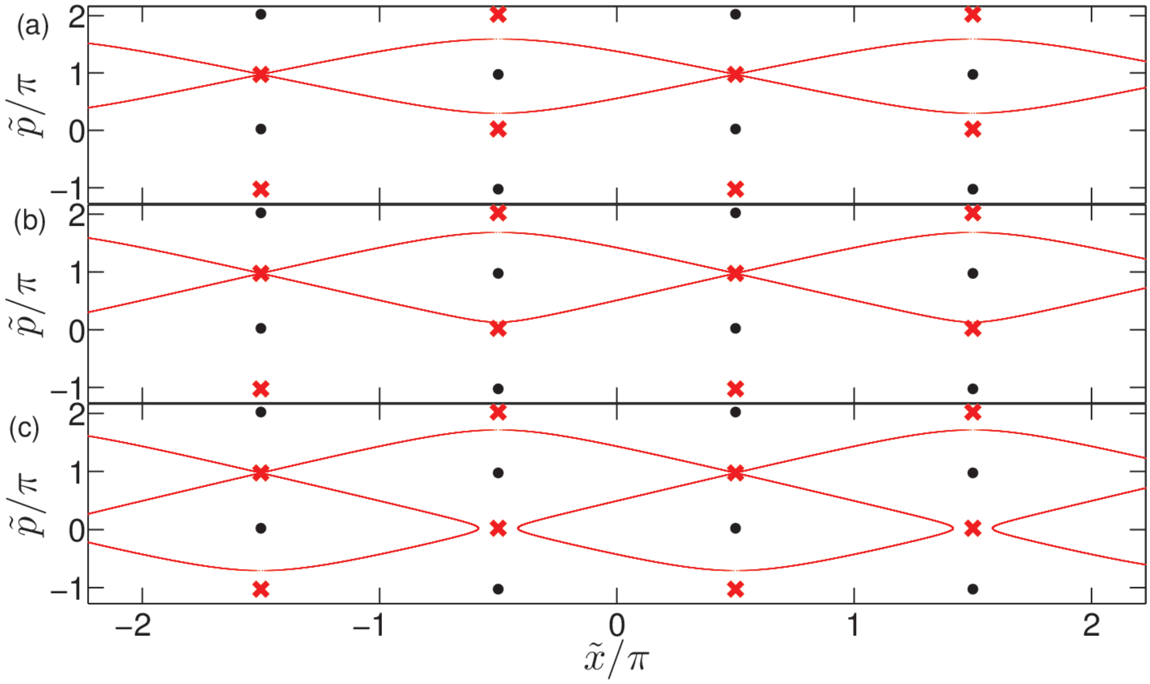

Figure 3.7: Separatrix structure for (a) $U = 2.5$ meV; (b) $U = 3$ meV; (c) $U = 3.15$ meV. The positions of the centres are indicated by black solid circles and the saddles – by red crosses.

The restructuring of the phase portraits in general displays structural instabilities of the system that can induce global bifurcations [209]. A detailed investigation of the global bifurcations that are involved in our problem can reveal the particular mechanisms underlying the dynamic instabilities and the related sound-induced kinetic properties. Hence, we scrutinise the development of separatrices in the vicinity of critical values U. The separatrix structures which are displayed in figure 3.7 consisted of manifolds of the hyperbolic points with the same coordinate $\tilde{p}_1 = -\sin^{-1}(v_s/v_0) + \pi$ for three values representing the bifurcation transition nearby U_{cr1}. Figure 3.6(a) illustrates a separatrix structure composed by heteroclinic orbits when $U < U_{cr1}$, that separates the areas of localised trajectories. The manifolds of the saddles with coordinate $\tilde{p}_1$ approach the saddles with coordinate

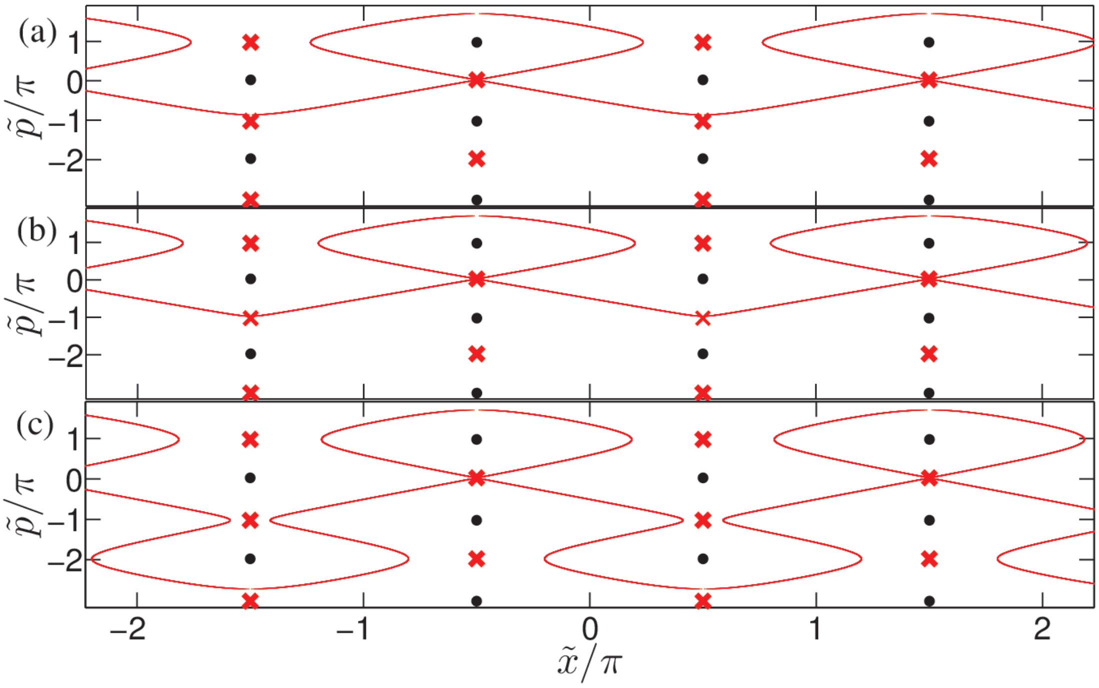

Figure 3.8: Separatrix structure for (a) $U = 3.7$ meV; (b) $U = 3.9$ meV; (c) $U = 4$ meV. The positions of the centres are indicated by black solid circles and the saddles – by red crosses.

$\tilde{p}_2 = \sin^{-1}(v_s/v_0)$ [see Fig. 3.7(b)] as U grows, and at exactly U_{cr1} meet them, therefore inducing a global bifurcation. With a further increase of U the manifolds undergo a separatrix reconnection, that leaves each heteroclinic orbit with a homoclinic and a heteroclinic manifold [see Fig. 3.7(c)]. This separatrix structure joins the adjoint saddle points having the same coordinate $\tilde{p}_1$. Moreover, the island of localised trajectories rotating clockwise around the centers with the coordinate $\tilde{p}_2$, it is delimited by a homoclinic loop that is formed by the manifolds of each saddle with the coordinate $\tilde{p}_1$. The latter separatrix structure is sufficient condition for the existence of the meandering trajectories illustrated in figure 3.6(b) by dashed curves.

We can extend the previous analysis of the restructuring of the phase space occurring close to other critical values of U. Hence, the topological rearrangement nearby U_{cr2} with the change of U is presented in figure 3.8. When $U < U_{cr2}$, before the global bifurcation per se, the separatrix in figure 3.8(a) is composed of homoclinic and heteroclinic structures such as the ones illustrated in figure 3.7 (c). For this particular evolution of separatrix though, we will consider the saddles with coordinate $\tilde{p}_2$. Therefore, increase of U towards U_{cr2} will force the heteroclinic connections of the separatrix to approach nearer to the saddle points with $\tilde{p}_3 = -\sin^{-1}(v_s/v_0) - \pi$ [see Fig. 3.8(b)]. These points will be incorporated into heteroclinic parts at U_{cr2} which is the value that signifies the second bifurcation. However, this structure is not robust and with further increase of U, is disengaged to form a supplementary lap around the island of localised orbits that rotate around the centres with coordinate $\tilde{p}_4 = \sin^{-1}(v_s/v_0) - 2\pi$ [see Fig. 3.8(c)]. In this way the meandering trajectories that emerge after each bifurcation and demonstrate complex behaviour can envelope additional regions of localised trajectories in a similar manner to that shown in figure 3.6 (c) by dashed curves. The structure of the separatrix is the one that enforces these complex trajectories to follow a specific path when drifting to the negative $\tilde{x}$-direction. Note that after the second global bifurcation ($U > U_{cr2}$) there are always two types of the meandering trajectories that encompass areas of the localised orbits. Their difference lies in whether they round even or odd number of islands of localised trajectories. For example, black and green dashed curves in figure 3.6(c) have a complex shape encompassing two and three islands of stability, respectively. Then the additional bifurcations are triggered when extra saddle points are involved in the heteroclinic parts. In connection with the calculation of $v_m(U)$ characteristic [see Fig. 3.4(b)], the critical values of U related to other local extrema in the curve concur with the new global bifurcations.

Since the global bifurcations are attributed to the situations, when a manifold of one saddle touches another saddle, equation (3.43) can be used for finding the critical values of U analytically. For this aim, we substitute the coordinates of the saddles involved into (3.43) and get

$$U_{cr} = \frac{\hbar v_s}{d} \frac{\frac{v_0}{v_s}[\cos\tilde{p}_{s1} - \cos\tilde{p}_{s2}] + \tilde{p}_{s1} - \tilde{p}_{s2}}{\sin\tilde{x}_{s2} - \sin\tilde{x}_{s1}},$$

where $(\tilde{x}_{s1}, \tilde{p}_{s1})$ and $(\tilde{x}_{s2}, \tilde{p}_{s2})$ are the coordinates of two saddles involved in the bifurcation. Next, using these coordinates from equations (3.35) and (3.36) we obtain the following explicit expression[5] for all critical U_{cr_n}:

$$\begin{aligned} U_{cr_n} &= \frac{\hbar v_s}{d}\left[\sqrt{\left(\frac{v_0}{v_s}\right)^2 - 1}\right. \\ &+ \left.\sin^{-1}\left(\frac{v_s}{v_0}\right) + \left(n - \frac{3}{2}\right)\pi\right]. \end{aligned} \tag{3.44}$$

According to (3.44) the four first critical values of U are U_{cr1}=3.1 meV, U_{cr2} = 3.92 meV, U_{cr3} = 4.75 meV, and U_{cr4}=5.58 meV. These values are in an excellent

---

[5] A more complete formulation of U_{cr} is included in Appendix B.

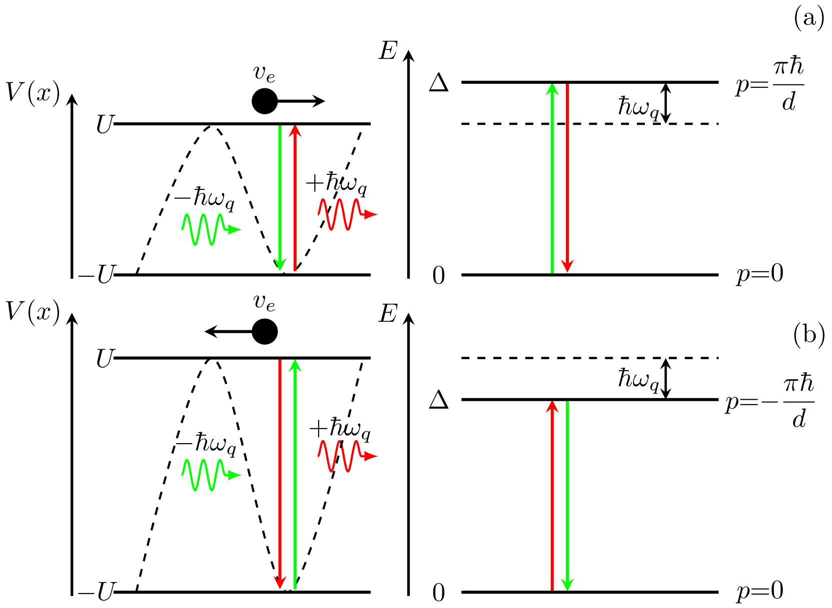

Figure 3.9: Diagrams of electron trasitions within the potential of acoustic wave $V(x)$ (left panel) and within the energy miniband (right panel) in conditions of the first (a) and second (b) bifurcations.

agreement with critical values found in numerical simulations and shown in figure 3.4(b).

Bifurcations in terms of waves and quanta

The aim of this subsection is to reveal physical meaning of the analytical criterion (3.44) and gain deeper insight into the physical processes behind the bifurcations in terms of waves and quanta.

Consider the limit $v_0/v_s \gg 1$ which is well satisfied for typical semiconductor SLs. Physically, it guarantees that the miniband electron speed $v = v_0|\sin\tilde{p}|$ exceeds the speed of sound v_s almost for all momenta. In this limit the hyperbolic points (3.36), involved in the derivation of (3.44), are located at $p_s \approx 0$ and very close to the boundaries of the first and successive Brillouin zones. In terms of electron de Broglie wavelength $\lambda_{dB} = h/p$ it corresponds to the Bragg resonances $l\lambda_{dB} = 2d$, l being an integer. The criterion of bifurcations (3.44) itself is simplified to the form

$$U_{cr_n} = \frac{\Delta}{2} + \hbar\omega_q\left(n - \frac{3}{2}\right), \tag{3.45}$$

where $\hbar\omega_q$ might be considered as the energy of an acoustic phonon with the wavelength equals twice the period of the superlattice $\lambda_q = 2d$. In what follows, we will mainly focus on the first two major bifurcations, for which

$$U_{cr_{1,2}} = \frac{\Delta}{2} \mp \frac{\hbar\omega_q}{2}. \tag{3.46}$$

It is easy to see that the relative contribution of the terms $\Delta/2$ and $\hbar\omega_q/2$ to the value U_{cr} in equation (3.46) is controlled by the ratio $|v_e|/v_s$, where $v_e = 2v_0/\pi$ is the effective electron speed. Therefore, in the physically interesting limit $v_e/v_s \gg 1$ the critical wave amplitude U_{cr} asymptotically approaches the half of the miniband width $\Delta/2$. The limit $v_e/v_s \to \infty$ itself can be reached either by increasing Δ, or by slowing down the speed of sound $v_s \to 0$. The latter demonstrates that the appearance of the quantum in criterion (3.46) is directly related to the propagation effects.

Now we turn to the discussion of the origin of the first and second terms in equation (3.46). Consider an electron that absorbs or emits a phonon with the quasi-momentum $\hbar q = \hbar 2\pi/\lambda_q = h/2d$. As a result of the radiation act, the electron momentum becomes $p_f = p_i \pm \hbar q$, where p_f (p_i) stands for the final (initial) momentum and upper (lower) sign refers to the process of the phonon absorption (emission). Next, a variation of the electron kinetic energy in the moving reference frame is $\delta E' = \delta E - v_s \delta p$, where $\delta E = E(p_f) - E(p_i)$ and $\delta p = p_f - p_i$. Assuming the electron is initially at the center of Brillouin zone $p_i = p_0 = 0$, it is easy to find both the variation of the electron kinetic energy $\delta E = \Delta$ and the variation of its momentum $\delta p = \mp\hbar\omega_q/v_s$. Finally, equating $\delta E'$ to the corresponding variation of the electron potential energy $\delta V = V_f - V_i$, we get the condition of energy conservation in the moving frame as

$$\delta V = -\Delta \pm \hbar\omega_q. \tag{3.47}$$

Now consider an electron transition from the top ($\tilde{x}_s = -\pi/2$) of the potential $V(\tilde{x})$ to its bottom ($\tilde{x}_s = \pi/2$) for which $\delta V = -U - (+U) = -2U$. Substituting this δV in (3.47) we immediately get equation (3.46). Therefore, the values of the critical amplitudes $U_{cr_{1,2}}$ follow from a delicate energy balance in distribution of the acoustic wave energy ($2U$) between an excitation of the electron within the miniband ($E_i = 0 \to E_f = \Delta$) and absorption (first bifurcation) or emission (second bifurcation) of the quantum $\hbar\omega_q$. While the energy of the quantum is relatively small $\hbar\omega_q/\Delta \ll 1$, it brings a large momentum linked to the inverse superlattice constant. Thereby this inelastic scattering event is able to kick the electron from the bottom of the miniband directly to its upper edge, giving rise to the electron Bragg reflections. The condition of energy conservation in the moving frame can be rewritten in the alternative form

$$\delta V = \hbar\omega_q \left(-\frac{v_e}{v_s} \pm 1 \right), \tag{3.48}$$

where v_e is the effective electron speed. Let us assume that the shifted frequency of the corresponding quantum transition is close to one harmonic, for example

$$-\hbar\omega_1 = \hbar(-qv_e \pm \omega_q). \tag{3.49}$$

Equation (3.49) has then a profound similarity with the general expression for the dispersion relation of the Doppler effect

$$n\hbar\omega_1 = \hbar(\omega - ku). \tag{3.50}$$

where $n = 0, \pm 1, \pm 2, ..$, $\hbar k$ is the momentum related to quantum and u the velocity of the particle. The latter description is applicable for a charged particle behaving as oscillator possessing kinetic energy and internal potential energy [210–212]. In particular, the case $n > 0$ corresponds to the normal Doppler effect, where the radiation frequency $\omega - ku$ in the oscillator's reference frame is equivalent with the frequency of the corresponding quantum transition. If $n < 0$, we obtain the anomalous Doppler effect, $\hbar ku = \hbar\omega + \hbar|n|\omega_1$. Finally, the case $n = 0$ is associated to the Vavilov-Cerenkov effect [212]. This type of behaviour has been observed in an oscillator moving in a magnetoactive plasma with superluminal velocity [213, 214]. The same concept is involved to describe negative energy waves in fluid [215] and plasma media [211]. In our system the first bifurcation is associated with the case of the anomalous Doppler effect. Therefore, the condition $-\omega_1 = \omega_q - qv_e$ is analogous to the dispersion relation (3.50) for $n < 0$. The anomalous character of the process lies in that electron absorbs (emits) the phonon $\hbar\omega_q$ and makes a transition from the bottom (top) of the potential to its top (bottom) [see figure 3.9 (a)]. Thus, the absorption (emission) of a quantum happens at the expense of potential energy (kinetic energy). In the second bifurcation which corresponds to normal Doppler effect, the realisation of electronic transition from the bottom to the top of the potential [green arrow, left panel Fig. 3.9(b)] is assisted by an absorption of a phonon. That, however, makes the electron to jump down [green arrow, right panel Fig. 3.9(b)] within the miniband.

Electron motion in real space and related transport in phase space

The previous discussion with regard to phase space dynamics and the related topological rearrangements induced with the variation of U, enable us to identify three different type of phase orbits that are associated with the properties of kinetic transport in real space. Figure 3.10 demonstrates representative electron trajectories in real space and the corresponding trajectories in phase space. The localised trajectories which can rotate either clockwise (trajectory 1 in the left panel) or counterclockwise (trajectory 2 in the left panel) around the centres are depicted in figure 3.10(a) correspondingly to different initial conditions. It might seem that the direction of rotation has an effect on the way that electron propagates in real space, but both of the trajectories exhibit a positive drift with speed v_s. The electron apart from the drift, experiences periodic oscillations for the motion to and fro across the potential as shown in the right panel of figure 3.10(a). The latter description corresponds to propagation of the periodic potential dragging the electron with v_s velocity through the superlattice [47, 196]. Since the electron is localised in x–space, we can consider a single well moving in the lattice. The unbounded trajectories, which are portrayed in the left panel of figure 3.10(b), can coexist with localised phase orbits for a relatively small U ($U < U_{cr2}$). Here again the direction of the unbounded trajectories along $\tilde{x}$-axis depends on the initial conditions. To highlight this symmetry, in the left panel of figure 3.10(b) are demonstrated the blue trajectories (curves 1) that move towards the positive direction of $\tilde{x}$ whereas the yellow trajectories (curves 2) designate the motion in the negative direction along $\tilde{x}$. As one can notice, $\tilde{p}$ in this dynamical regime barely oscillates around a definite mean value. In this case following from equation (3.9), the time-averaged velocity of the electron can be determined by the product αv_0, where α is a constant representing the averaged value of $\sin\tilde{p}$, being either positive or negative. The right panel of figure 3.10(b) displays the corresponding electron trajectories to phase space dynamics which are not trapped by acoustic wave, and can travel in positive or negative directions in real space, depending on the initial value of $\tilde{p}$. On the other hand, the Bloch-like (frequency-modulated) oscillations emerge with the increase of the wave amplitude. This mean that with variation of U, the amplitude of $\tilde{p}$ - oscillations becomes larger and eventually cannot be restricted in the first Brillouin zone. The aforesaid oscillations are resonantly interacting with phonons having the wave-length twice as much as the superlattice period. This Bragg resonance coincides with the global bifurcation that is associated with the rise of meandering trajectories which are depicted in the left panel of figure 3.10(c) for comparison. We have already mentioned in the previous section that a meandering trajectory dependent on the initial state $\tilde{p}_0$ which round along $\tilde{p}$–direction either odd (yellow curve 2) or even (blue curve 1) number of islands of the localised orbits. Despite having different amplitude of $\tilde{p}$ - oscillations, the meandering trajectories propagate en route to the negative direction of $\tilde{x}$. The related electron trajectories shown in the right panel of figure 3.10(c), exhibit high-frequency fluctuations (Bloch-like oscillations) driven in the negative

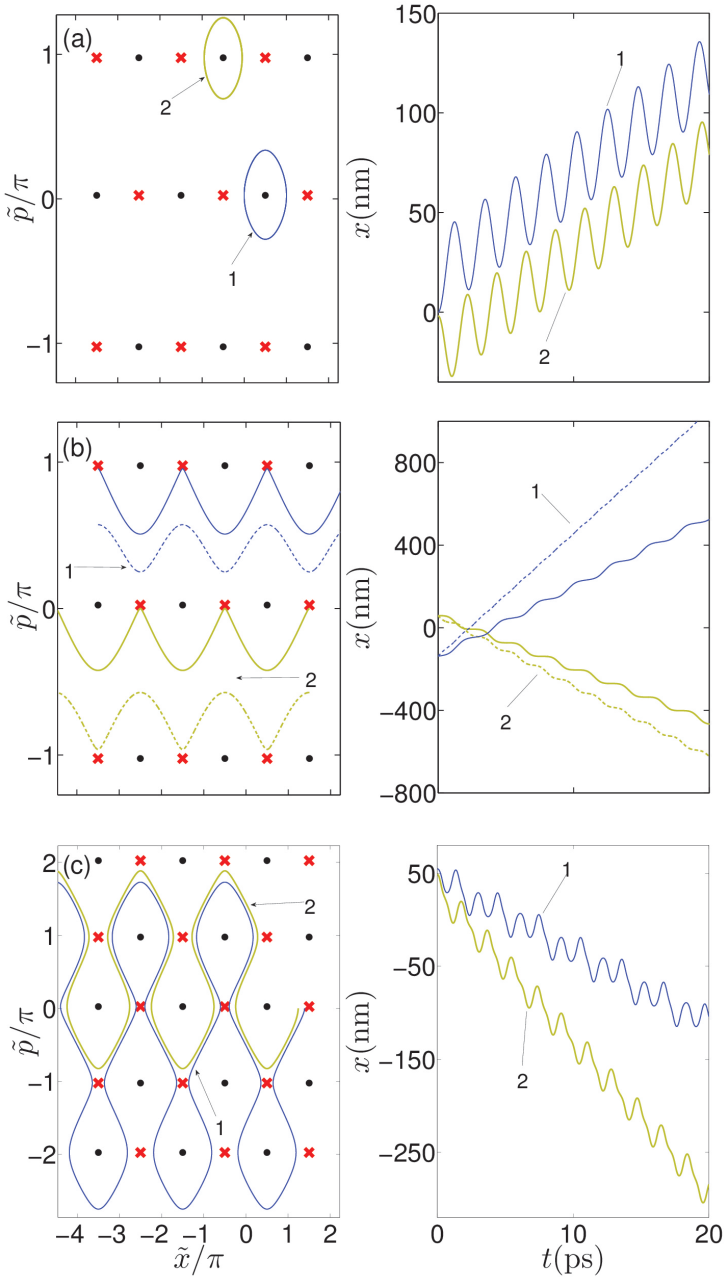

Figure 3.10: Three distinct types of the phase trajectories (left panels) and the corresponding electron trajectories in the real space (right panels) for (a) $U = 1.5$ meV; (b) $U = 2.5$ meV; (c) $U = 4.2$ meV.

direction. This negative drift reflects effect of the resonant scattering of electrons on phonons, which is translated into the changes of the momentum of electrons and their direction of motion on the opposite one. The profile of $v_m(U)$ and $v_d(U)$ characteristics in figure 3.4 can interpreted on the basis of different phase trajectories and how they determine the behaviour of ballistic transport. We have seen in Section 3.2.1 that v_m can be explained as the time-averaged electron velocity additionally averaged over initial positions x_0. This approach is efficient at any temperature, but for simplicity we assume $T_e \to 0$, which is reflected in zero initial momentum $\tilde{p}_0$ for every trajectory under consideration. To see the implications of the considering temperature close to zero, one should exclude from the calculation of v_m the contribution of counterclockwise trajectories (yellow curve 2) and unbounded trajectories (blue curve 1) in figures 3.10(a) and 3.10(c) respectively. For small $U < U_{cr1}$ then only localised trajectories [curve 1 Fig. 3.10(b)] and unbounded trajectories [curve 2 Fig. 3.10(b)] contribute to the estimation of value v_m. Therefore, the unbounded trajectories exhibiting negative drift compete with the localised trajectories, for which the electrons are trapped by the acoustic wave and driven towards to the positive direction of x. Since for the system under study $v_0 \gg v_s$, the positions of saddles, according to (3.36), are very close to $\tilde{p} = 0$. With this, the area of the unbounded trajectories with zero momenta is significant less than the one of the bounded trajectories that rotate clockwise around centres. This leads to a positive value of v_m. As U grows though, the regions of the islands of the localised trajectories increases, whereas the area of the unbounded trajectories shrinks. In other words the increase of U causes the enhancement of effective localisation of electron within the potential well that initially results in the rapid growth of v_m and subsequently to its saturation for a range of the U up to U_{cr1}. Increasing U beyond the first global bifurcation gives birth to the meandering trajectories [black dashed curves in Fig. 3.6(b)] that move apace in the negative direction of $\tilde{x}$, assisting the backward motion of electrons. Hence, the increase of U starts to affect v_m and further growth would result in rapid suppression of mean velocity as shown in figure 3.4(b). The homoclinic loop [see Fig. 3.7(c)] that bounds the localised trajectories can be expanded after the second bifurcation with the increase of U, delimiting the region for propagation of meandering trajectories. These topological rearrangement instantly increases the v_m. The additional minima and maxima in figure 3.4(b) are produced with further global bifurcations that they replicate the previously described dynamic scenario. Similarly, the dependence of $v_d(U)$ can be associated with the development of the global bifurcations and the corresponding contribution of phase trajectories to electron transport. On the other hand, as equations (3.11) and (3.12) suggest the scattering events weaken the influence of trajectories that contribute to the drift velocity and hence suppress the miniband velocity. This is observed in figure 3.4(a) where only two kinks survive that correspond to global bifurcations. The co-existence of these effects are possible due to the austere condition of supersonic motion of the system ($v_e > v_s$). In the opposite case of the subsonic motion ($v_e < v_s$), only the normal Doppler effect is possible. As we have seen, the initial conditions have an effect on constant α and thus exert influence on mean velocity. Figure 3.10(b) compares different ways that initial conditions may affect the real trajectories.

Interpretation of electron trajectories using kinetic and potential profiles

There are evidently two distinct issues raised in Sections 3.3.2 and 3.3.4 in relation to the behaviour of the meandering trajectories. First, these complex trajectories always drift in the negative direction of $\tilde{x}$. Second, two different types of the phase trajectories coexist for $U > U_{cr2}$, which demonstrate meandering behaviour across the phase plane. Their difference lies in the number (odd or even) of the islands of the localised orbits, around which they propagate in $\tilde{p}$–direction. In order to understand better these issues, let us now consider two meandering trajectories, which are triggered at $(\tilde{x}_1, \tilde{p}_1) = (\pi/2, -\pi)$ [green dashed curve in Fig. 3.11(a)] and $(\tilde{x}_2, \tilde{p}_2) = (\pi/2, -\pi/1.3)$ [black dashed curve in Fig. 3.11(a)], when $U = 4.25$ meV. The latter trajectory can encompass three islands of the localised trajectories before its orbit is reversed along $\tilde{p}$–direction. On the other hand, the former complex trajectory meanders just along two. The intersections of the vertical dash-dotted line with the phase trajectories indicate the initial positions in figure 3.11(a). To explain the characteristics of the meandering trajectories, we can employ a description in terms of energy balance, between potential energy and kinetic energy in the moving frame. The variation of the electron kinetic energy in the moving frame is $\delta E' = \delta E - v_s \hbar \delta\tilde{p}/d$, where $\delta E = E(\tilde{p}_f) - E(\tilde{p}_i)$, and $\delta\tilde{p} = \tilde{p}_f - \tilde{p}_i$. In general, the $\delta E'$ corresponds to the variation of the electron potential energy $\delta V = V(\tilde{x}_f) - V(\tilde{x}_i)$. This satisfies the condition of energy conservation

$$\delta V = -\delta E'. \tag{3.51}$$

Note that p_i (p_f) stands for the initial (final) momentum whereas x_f (x_i) represents the initial (final) position of the electron. Here, we modify the dispersion relationship $E'(\tilde{p})$ [see Eq.(3.24)] to include a change in the initial conditions of the electron so that

$$\tilde{E}(\tilde{p}, \tilde{p}_i, \tilde{x}_i) = \delta E' - V(\tilde{x}_i) = -V(\tilde{x}), \tag{3.52}$$

where $\tilde{E}$ can only take values between $\pm U$, controlled by the variation of $V(\tilde{x})$. Thus, we examine the variation of $\tilde{E}(\tilde{p})$ and $V(\tilde{x})$, illustrated respectively in figures

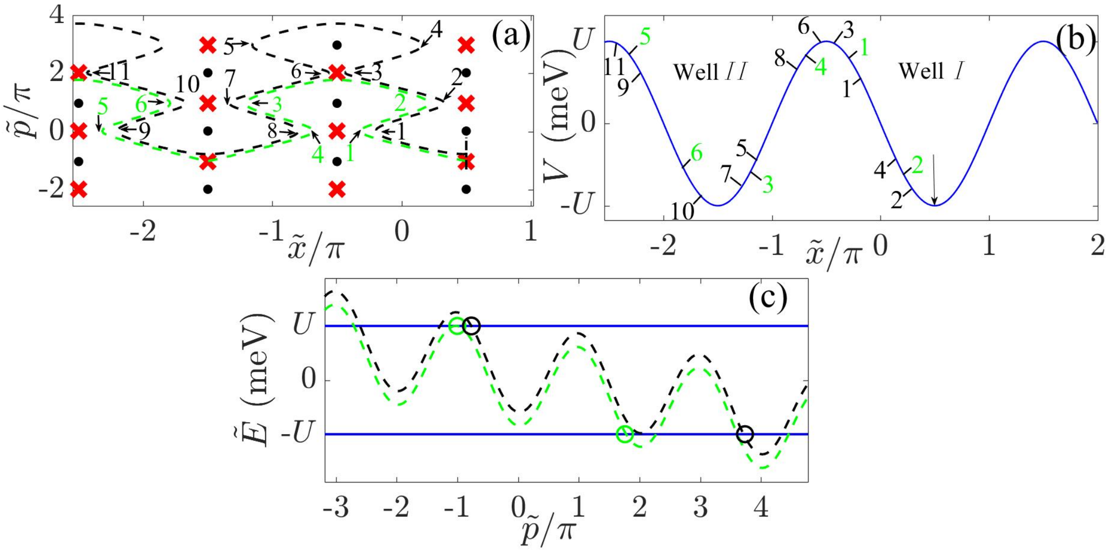

Figure 3.11: (a) Green dashed curve: Meandering trajectory calculated for $(\tilde{x}_1, \tilde{p}_1) = (\pi/2, -\pi)$, Black dashed curve: Meandering trajectory calculated for $(\tilde{x}_2, \tilde{p}_2) = (\pi/2, -\pi/1.3)$. Vertical dashed line is discussed in the text. (b) Acoustic wave potential $V(\tilde{x})$ with black [black curve] and green [green curve] numbers labelling the sequence of electron position within the SL according to orbits in panel (a). Arrow is discussed in the text. (c) Effective kinetic energy $\tilde{E}(\tilde{p}, \tilde{p}_i, \tilde{x}_i)$ [Eq. (3.52)], where horizontal blue lines denote $\pm U$. The green (black) dispersion curve corresponds to the phase trajectory of the same colour in (a) panel. The left and right open green (black) circles mark where $\tilde{E}(\tilde{p}) = U$ and $-U$ respectively. The wave amplitude is considered to be U=4.25 meV.

3.11(b) and 3.11(c), corresponding to the trajectories in figure 3.11(a). The numbers in figure 3.11 designate a sequence of inflection points on the meandering trajectories, which occur to be at close proximity to the saddle points. In addition, they represent the turning points in $\tilde{x}$–direction as the electron Bloch-oscillates within Well I and II [see Fig. 3.11(b)]. The initial acoustic force $k_s U \cos\tilde{x}_i$, for both sets of the initial conditions, is negligible because the electron is found at the bottom of the Well I [arrow in Fig. 3.11(b)]. It is important to understand that in this case the electron will not be just dragged by the acoustic wave. Instead, it is momentarily forced in the negative direction in $\tilde{x}$–space since according to (3.52) $\tilde{E}(\tilde{p}_i) > 0$. As the electron moves up the left-hand side of Well I, it experiences a positive force where the gradient of $V(\tilde{x}) > 0$, thus reversing v_x. This implies that the electron is forced in the positive direction in momentum space, which results in a reduction of the velocity $\tilde{v} = dE'(\tilde{p})/d\tilde{p} = v_x - v_s$. The particle has zero velocity ($\tilde{v} = 0$, labelled 1 in figure 3.11 (b)), within the potential, if its momentum attains a value of $\tilde{p} = \tilde{p}_{s1}$ which is the $\tilde{p}$–coordinate of the hyperbolic point $(\tilde{x}_{s1}, \tilde{p}_{s1}) = (-\pi/2, \sin^{-1}(v_s/v_0))$. In this case, the electron is de-accelerated up to the centre of the Brillouin zone where the gradient of the $\tilde{E}(\tilde{p})$ becomes zero. Now, the electron experiences a downward displacement at the left-hand side of Well I due to the positive force, and thus the value of $\tilde{E}(\tilde{p})$ decreases. Here the particle is accelerated in momentum space ($\tilde{v} > 0$) until $\tilde{p} = \pi/2$ ($\tilde{v} = \tilde{v}_{max}$). At this point, the high gradient of $V(\tilde{x})$ causes $\tilde{p}$ to quickly increase almost up to the edge of the first Brillouin zone. In this case, the corresponding position within the potential $V(\tilde{x})$ is labelled 2 in figure 3.11(b). Moreover, the momentum coordinate of this inflection point in phase space coincides with the coordinate of the saddle point $(\tilde{x}_{s2}, \tilde{p}_{s2}) = (\pi/2, \pi - \sin^{-1}(v_s/v_0))$. Then, the electron velocity v_x is again reversed with $\tilde{v} = 0$. According to equation (3.51), the variation of the electron potential energy, δV_1, between the inflection points (labelled 1, 2 in Fig. 3.11(b)) should be equated to the variation of the electron kinetic energy in the moving frame $\delta E'_1 = E'(\tilde{p}_{s2}) - E'(\tilde{p}_{s1})$. Therefore, the condition of energy conservation takes the form

$$\delta V_1 = -\frac{\hbar v_s}{d}\left[\sqrt{\left(\frac{v_0}{v_s}\right)^2 - 1} + \sin^{-1}\left(\frac{v_s}{v_0}\right) - \frac{\pi}{2}\right]. \tag{3.53}$$

Considering the limit $v_0 >> v_s$ and provided that the Bragg resonance $\lambda_{dB} = 2d$, where $\lambda_{dB} = h/p$, the condition (3.53) can be further simplified to the form

$$\delta V_1 = -\Delta + \hbar\omega_q. \tag{3.54}$$

This description suggests that the reversing of $\tilde{v}$ is associated with the jump of electrons within the miniband. Thereby this electronic transition is assisted by the absorption of the quantum $\hbar\omega_q$. As a result of the radiation act, the electron is prevented to move up the right hand side of the Well I. Instead, after crossing the boundary of the first Brillouin zone, the electron moves up again the left-hand side Well I in figure (3.11)(b). We see in figures (3.11)(b) and (c) that as $\tilde{p}$ increases due to a large positive force, the value of $E'(\tilde{p})$ decreases and therefore $V(\tilde{x})$ increases. Note, however, that a profound difference emerges between the meandering trajectories depicted in figure 3.11(a), after they reach the border of the first Brillouin zone [labelled 2 in Fig. 3.11(b)]. On the one hand, the electron reaches the top of the Well I if it follows the trajectory encompassing just one island of stability. In this case, $V(\tilde{x}) = -U$ and $\tilde{E}(\tilde{p})$ obtains its lowest possible value of $-U$ [lower horizontal line in Fig. 3.11(c)] and therefore $\tilde{p}$ ceases to increase. On the other hand, considering the meandering trajectory which is more elongated in $\tilde{p}$–direction, the electron continues to experience a large positive force, which increases $\tilde{p}$ throughout the second Brillouin zone. In addition, close to the boundary of the second Brillouin zone exists an inflection point, which is characterised by the coordinate $\tilde{p}_{s3} = 2\pi + \sin^{-1}(v_s/v_0)$ so that induces the reverse of $\tilde{v}$. Hereafter, the electron remains confined within the potential and moves down again the left-hand side of Well I. It is easy to see that the variation of the electron potential energy between inflection points [(labelled 2, 3 black colour in Fig 3.11(b)] is described by equation

$$\delta V_2 = \frac{\hbar v_s}{d}\left[\sqrt{\left(\frac{v_0}{v_s}\right)^2 - 1} + \sin^{-1}\left(\frac{v_s}{v_0}\right) + \frac{\pi}{2}\right]. \tag{3.55}$$

In the physical limit $v_0 >> v_s$ and if $\lambda_{dB} = 2d$, the expression (3.55) is reduced to

$$\delta V_2 = \Delta + \hbar\omega_q. \tag{3.56}$$

Here the transition between the inflection points, within the potential, is assisted by the emission of $\hbar\omega_q$, which makes the electron to jump down within the miniband. The emission of this quantum brings a large momentum, so that the electron remains confined within the potential and moves down the left-hand side of Well I. Thereafter, the velocity in moving frame will be again reversed at a new inflection point due to absorption of an acoustic phonon. The variation of the potential energy between points 3, 4 is $\delta V = \delta V_1$ where $\delta V = E'(\tilde{p}_{s4}) - E'(p_{s3})$ and $\tilde{p}_{s4} = 3\pi - \sin^{-1}(v_s/v_0)$. This excitation of the electron within the miniband is the final act before it can reach the crest of the potential. On the top of the well, the electron is shoved to make a jump to the left due to the high negative velocity. The magnitude of the velocity $\tilde{v}$ at the crest of the potential wave depends on the initial conditions $(\tilde{x}_i,\tilde{p}_i)$. Thus, when $(\tilde{x}_i,\tilde{p}_i)$=$(\tilde{x}_1,\tilde{p}_1)$ we find that the electron obtains velocity $\tilde{v}_1 \approx -4.73\times10^4$ m s^{-1} whereas when $(\tilde{x}_i,\tilde{p}_i)$=$(\tilde{x}_2,\tilde{p}_2)$ then $\tilde{v}_2 \approx -5.71\times10^4$ m s^{-1}. The jump from the top of the potential transfers the electron to different positions marked by numbers 3 (green colour, $\tilde{v} = v_1$) and 5 (black colour, $\tilde{v} = v_2$) in potential well II [Fig. 3.11(b)]. At these positions, the acoustic force which is negative now, will generate a rapid decrease of $\tilde{p}$ inducing a new cycle of Bloch-type oscillation. This cycle involves the successive transitions between the inflection points $[3 \to 4\ (-\delta V_1)]$ and $[5 \to 6\ (-\delta V_1), 6 \to 7(-\delta V_2), 7 \to 8\ (-\delta V_1)]$ which are related to the meandering trajectories [green dashed curve in Fig. 3.11(a)] and $(\tilde{x}_2, \tilde{p}_2) = (\pi/2, -\pi/1.3)$ [black dashed curve in Fig. 3.11(a)] respectively. After these transitions, the force exerted on the electron continues to be negative due to the negative gradient of $V(\tilde{x})$ [right-hand side of Well II in Fig. 3.11(b))]. Thus, $\tilde{p}$ rapidly decreases, until $E'(\tilde{p})$ reaches its maximum value [upper horizontal line in Fig. 3.11(c)] and $V(\tilde{x})$ obtains its minimum value of $-U$. This allows the electron to perform a transition from the right- to the left-hand side of the Well II. Here, a positive force causes $\tilde{p}$ to increase, and thus an excitation of Bloch oscillation. Next, the electron is allowed to jump again backwards to a adjacent well by repeating the mechanism described above.

This analysis implies that both effects (normal Doppler and anomalous Doppler) analysed in Section 3.3.3 are possible for the meandering trajectory that encompasses two islands of the localised orbits [black orbit, Fig. 3.11(a)] . On the other hand, only the anomalous Doppler effect is feasible for the meandering trajectory (green orbit) depicted in figure 3.11(a). In either case, by pumping energy to the system (i.e. increasing the amplitude U of the acoustic wave), the electron in the moving frame is transformed by the anomalous Doppler effect to a higher excitation state, having higher kinetic energy. The enhanced kinetic energy allows the particle to counter-propagate with respect to the predominant direction of sound propagation. Therefore, for considerably large values of the wave amplitude U, the mean velocity [see Fig. 3.4(b)] is reversed due to area widening of the meandering trajectories on the phase plane. This effect can be explained as counter-dragging that results from acoustic phonon emission. Further increase of U above U_{cr2} is accompanied by a development of the system instabilities, giving rise to more complex trajectories. As a result, the area of the meandering trajectories which can encompass odd number of localised trajectories narrows. This explains the reduction of the absolute value of the mean velocity.

Electron trajectories in the subsonic limit

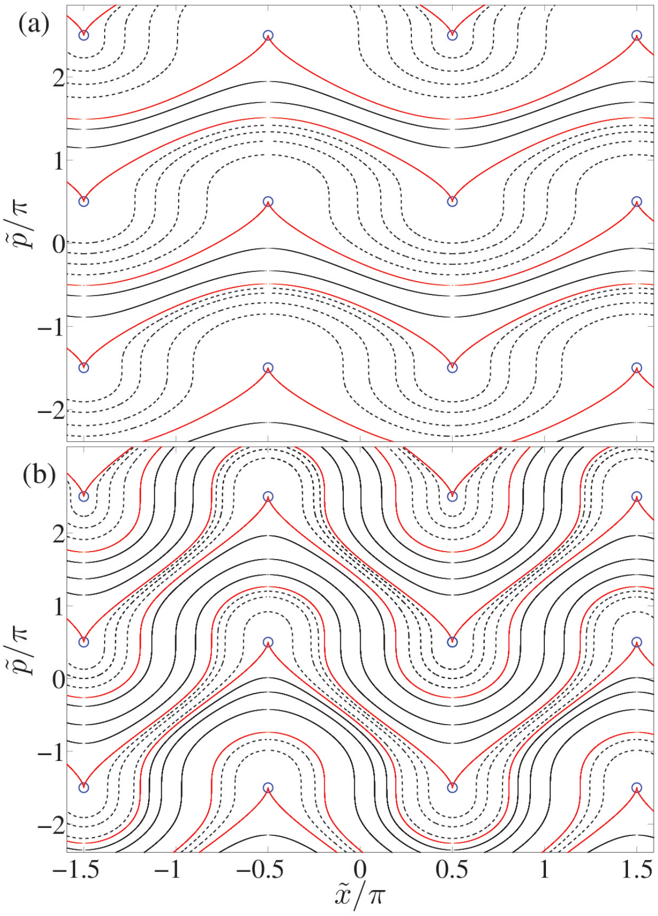

Figure 3.12: Phase trajectories of the dynamical system (3.27), (3.28) for $v_0 = v_s$ and different values of wave amplitude U=: 0.8 Δ (a) and 2 Δ (b). The positions of equilibrium points are indicated by blue empty circles. Smooth solid curves correspond to the unbounded trajectories, dashed curves mark the meandering trajectories, and red curves denote the separatrices.

As mentioned in Section 3.3.1, for the case $v_0 \leq v_s$ the dependence $v_m(U)$ (Fig. 3.5) demonstrates prominent features in a similar manner as figure 3.4 (b). The reduction of maximum miniband velocity to the limit of v_s

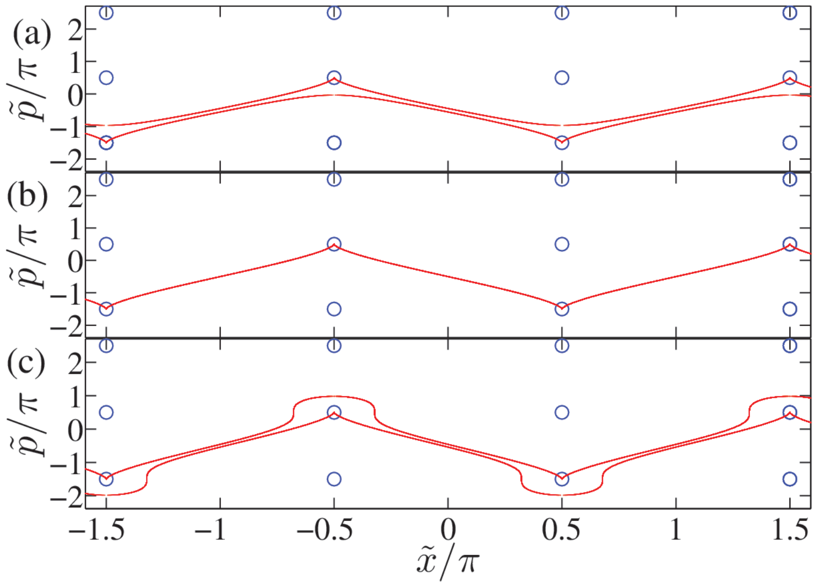

Figure 3.13: Separatrix structure for $v_0 = v_s$ and different values of acoustic wave amplitude U=: 1.4 $\Delta < U_{cr1}$ (a), $\Delta\pi/2 = U_{cr1}$ (b) and 1.7 $\Delta > U_{cr1}$ (c). The positions of equilibrium points are depicted by blue empty circles.

induces the collision of fixed points and the formation of new equilibrium points (saddle-nodes represented by the empty circles) that are spread in figure 3.12. These topological changes in the phase portrait can be associated with characteristic alterations in the miniband transport. Figure 3.12 exhibits the phase portraits of the model generated by equations (3.40), (3.41) and (3.43) for two different values of the sound wave amplitude. Considering U being less than U_{cr1} [see Fig. 3.12(a)], the phase space trajectories can be divided into areas of unbounded trajectories (black solid curves) and meandering trajectories (dashed curves). Common attribute of these trajectories is that they move towards to the negative direction of $\tilde{x}$-axis. The different regions of motion then are segregated by separatrix (red curves) consisted of unstable manifolds connecting the equilibrium points (blue open circles). This separatrix is structurally unstable because a really small reduction of v_0 could cause the annihilation of fixed points and therefore resulting in collapse of manifolds. Increasing the wave amplitude U has an immediate impact on the regions of unbounded trajectories by diminishing them. This has a direct effect on v_m by causing a rapid increase of averaged velocity to its maximum value (black curve Fig. 3.5). As U overreaches the critical value U_{cr1} the unbounded trajectories are eliminated and they give their place to meandering trajectories. The newly born meandering trajectories follow the new shape of the separatrix and therefore become more stretched in $\tilde{p}$–direction.

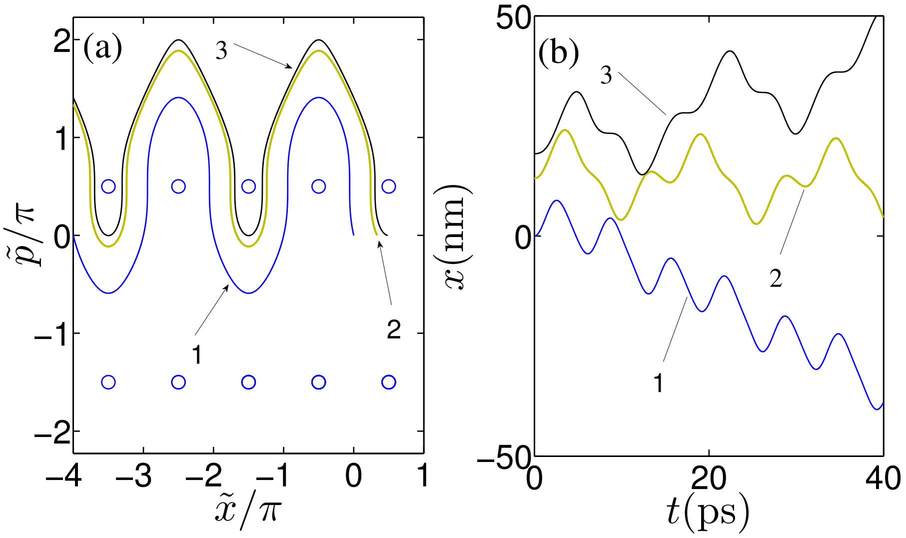

Figure 3.14: ((α) Phase trajectories and (β) the corresponding electron trajectories in the real space for $U = U_{cr1}$ and $v_0 = v_s$.

The rise of the new meandering trajectories and the enhancement of the old ones lies in the separatrix reconnection that starts to take place at $U = U_{cr1}$. The topological structure of the phase portrait is sensitive to the variation of U. Then, the phase space can be drastically restructured when global bifurcations occur near other values of U_{cr_i} $(i = 2, 3, ..)$. To explain the mechanism of these bifurcations, we employ a similar approach as one we used in Section 3.3.2. Figure 3.13 shows the separatrices consisted by manifolds of equilibrium points with coordinates $\tilde{p}_1 = \pi/2$ and $\tilde{p}_2 = -3\pi/2$. These unstable structures for $U < U_{cr1}$ [see Fig. 3.13(a)] initially allow the existence of the unbounded trajectories. However, increasing U makes the manifolds to incline toward each other and at the limit $U = U_{cr1}$ simultaneously touch the same saddle-node points [see Fig. 3.13(b)]. Just above U_{cr1} [see Fig. 3.13(c)] the manifolds are being reconnected, thus evincing the realisation of the global bifurcation. In this case, the manifold of the equilibrium point with coordinate $\tilde{p_1} = \pi/2$ can twist around the fixed point at $\tilde{p}_2 = -3\pi/2$. After the critical values of U can be found analytically considering that the global bifurcations are caused when a manifold of one saddle-neutral stable node touches another one. Therefore, after substituting into equation (3.43) the coordinates of the equilibrium points that take part in the bifurcation, we obtain the formula

$$U_{cr_n} = \frac{\Delta}{2} n\pi \tag{3.57}$$

There is a fundamental difference between the meandering trajectories in the current case and the one realised for $v_0 > v_s$, and illustrated in figure 3.6. In the latter case for a fixed value of U, the phase trajectories can move around islands, that enclose localised trajectories corresponding to the dragging regime. However, it turns out that in the former case no dragging exists and at each new bifurcation only one type trajectory is generated. The occurrence of the first bifurcation, coincides with meandering trajectories, which can exceed the first Brillouin zone [curves 1, 2 of Fig. 3.14(a)] or reach the edge of the second one [curve 3 left panel of Fig. 3.14(a)]. All these meandering phase trajectories move towards the negative direction of $\tilde{x}$ [see Fig. 3.14(a)]. However, despite of the same $\tilde{x}$–direction for all phase trajectories, the related electron trajectories in the real space can travel in any direction from the following [see Fig. 3.14(b)] : negative (blue curve 1), performing small oscillations around $x = 0$ (yellow curve 2) and demonstrating positive drift (black curve 3). One can notice that a real trajectory become less harmonic as the corresponding meandering trajectory approach the fixed point (black trajectories 3 in Fig. 3.14). The degeneracy of meandering trajectory with respect to existence of different electron orbits in real space affects directly the product αv_0 where a, as it was mentioned in the previous section, determines the mean velocity. Here, $\alpha \approx 0$ which is reflected on the characteristic of the mean velocity at the crossover points (green vertical lines Fig. 3.5). This behaviour suggests that bifurcations in the current system ($v_0 = v_s$) lead to zero kinetic gain for the particle. Referring back to the discussion over the bifurcations in terms of waves and quanta, the equation (3.47), which describes the condition of energy conservation in the moving frame, holds in the form $\delta V = -\delta E \pm \hbar\omega_q$. This condition is still valid in the limit $v_0 \to v_s$. As result, in this case both the energy of the quantum $\hbar\omega_q$ and the variation δE of the kinetic energy approach zero, and thus $\delta V = 0$. The latter case suggests that the variation of the potential energy of the system stays practically unaffected by the emission of a quantum. Consequently, the Vavilov-Cerenkov radiation can be emitted similar to a free charged particle having no internal degrees of freedom [210].

The system triggers an acoustic charge transport for $v_o < v_s$, where the fixed points collide and disappear. This comes in contrast to the degenerate case $v_0 = v_s$ or the effective localisation of electron within the periodic potential that happens for $v_0 > v_s$. Figure 3.15 demonstrates that the only type of trajectories that can be observed are the ones associated with unbounded electron transport. For small U the unbounded trajectories, which are depicted in figure 3.15(a), appear to have almost harmonic behaviour. In this instance, if the initial momenta is $\tilde{p}_0 = 0$, the $\tilde{p}$-oscillations never exceed the boundary of first Brillouin zone, see figure (3.5). However, one can see that with a further increase of U, the oscillations are enhanced, inducing Bloch-like oscillations.

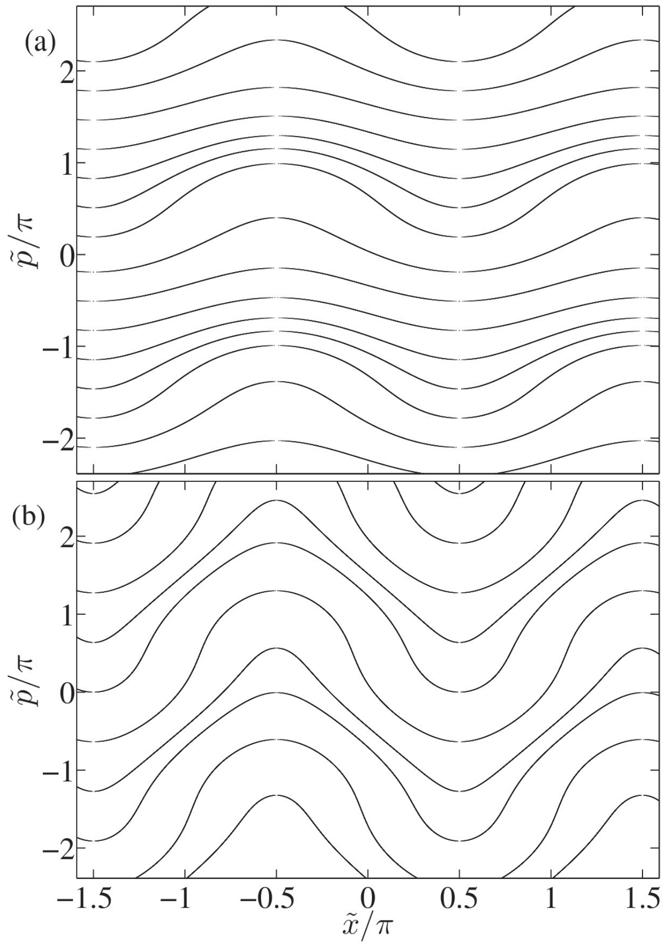

Figure 3.15: Phase trajectories of the dynamical system (3.27), (3.28) for $v_0 = v_s/2$ and different values of acoustic wave amplitude U: 0.04 (a) and 0.15 (b). Smooth solid curves represent the unbounded trajectories.

The condition that describes the sufficient amplitude of acoustic wave U for which the electron performs Bloch oscillations in momentum space can be derived from equation (3.43). Actually, substituting the coordinates of the point[6]

---

[6] This point represents one of the potential crests. The particle is no more effectively trapped and it can propagate across the potential. From the energy preservation the minimum kinetic energy $E'_{min} = \Delta - v_s\pi$ determined by $\tilde{p} = \pi$ corresponds to a maximum potential energy U for $\tilde{x}_0 = \pi/2$.

$(\tilde{x}, \tilde{p})$=$(-\pi/2, \pi)$ into (3.43), we acquire

$$U_{BO} = \frac{\Delta}{2v_0} \frac{\pi v_s - 2v_0}{\sin x_0 + 1}, \tag{3.58}$$

where x_0 is the position of electron whilst it is found at the bottom of the miniband at the initial moment. The last equation is generic and applicable for $v_0 \leq v_s$. If we consider only one cell of periodic phase space $(-\pi, \pi]$, the least sufficient wave amplitude for $\tilde{p}$-oscillations to touch the first Brillouin zone $|\tilde{p}| = \pi$ is acquired for $\tilde{x}_0 = n\pi$, where $n = 0, 1$, which triggers the Bragg reflections of electron. Noticeably, this value produces the maximum value in figure 3.5 for the resonant case $v_0 = v_s$. From then onwards, the increase of U enhances the area including meandering trajectories that can manifest Bloch-like oscillations. The emergence of these quasi-periodic orbits (curve 1 in right panel of Fig. 3.14) can explain the rapid decrease of mean velocity. On the contrary, the onset of Bloch oscillations for $v_0 = v_s/2$ coincides with the minimum value of v_m.

Note here that the coherent interaction of an electron with the acoustic wave cannot be established due to the absence of phonon drag that can contribute to the drift of the electrons towards the positive direction of x. On the contrary, v_0 is quite small and the electron can be thought practically immobilised at the bottom of the miniband. For $v_s >> v_0$ the equations of motion (3.25), (3.26) become analytically solvable as

$$x' = -v_s t + x_0 \tag{3.59}$$

$$k_x d = \frac{\omega_B^{max}}{\omega_s} \cos(\omega_s t + x_0) \tag{3.60}$$

Here ω_B^{max}=$k_s U d/\hbar$ corresponds to the maximal frequency of frequency-modulated Bloch oscillations discussed in references [47, 179] and the following Section 3.5. One can see that according to equation (3.60) the phase space trajectories becomes completely periodic with frequency of motion the ω_s. In the limit $\omega_{fm} \to \omega_s$, $k_x d \to 1$, which means that the Bragg reflections of the electron become feasible. We have to underline here though that for most electrons their component of velocity is much smaller than the speed of sound wave. Therefore, the time average over their trajectories is zero, and these electrons are essentially unaffected by the presence of the acoustic wave.

Non-linear pendulum approximation of ballistic electron dynamics

The semiclassical equations of motion in the moving frame (3.27), (3.28), describing phase trajectories for the limiting case $\tilde{p} \ll 1$, can be transformed under the translation $\hat{T}\tilde{x} = \tilde{x} + \pi/2$ into

$$\begin{aligned} \frac{d\tilde{x}}{d\tilde{t}} &= \frac{v_0}{v_s}\tilde{p} - 1, & (3.61)\\ \frac{d\tilde{p}}{d\tilde{t}} &= -\frac{Ud}{\hbar v_s}\sin\tilde{x}. & (3.62) \end{aligned}$$

The ballistic transport regime of electrons before the first bifurcation, as we discussed in Section 3.3.2, can be decomposed into the localised and unbounded motion. The trajectories that constitute this motion and assume a small variation of $\tilde{p}$, satisfy the pendulum equation

$$\frac{d^2\tilde{x}}{d\tilde{t}^2} + \Omega_{\tilde{x}}^2 \sin\tilde{x} = 0 \tag{3.63}$$

Here $\Omega_{\tilde{x}} = (U\Delta/2)^{1/2}(d/\hbar v_s)$. The total energy of the pendulum manifests its conservation in the form of an integral of motion

$$H = \frac{1}{2}\dot{\tilde{x}}_0^2 - \Omega_{\tilde{x}}^2 \cos\tilde{x}_0, \tag{3.64}$$

where $\tilde{x}_0$, and $\dot{\tilde{x}}_0$, the initial values of $\tilde{x}$ and $d\tilde{x}/d\tilde{t}$, respectively. If a constant $m^2 = 1/2 + H/(2\Omega_{\tilde{x}}^2)$ is involved then the integral of motion can be alternatively expressed as

$$\frac{1}{2}\dot{\tilde{x}}^2 - \Omega_{\tilde{x}}^2 \cos\tilde{x} = 2m^2\Omega_{\tilde{x}}^2 - \Omega_{\tilde{x}}^2 \tag{3.65}$$

Designating $\omega_\dagger = 2m\Omega_{\tilde{x}}$ and using equation (3.61), the last equation can be modified to determine the semiclassical phase-space dynamics

$$\left(\frac{v_0}{v_S}\frac{1}{\Omega_{\tilde{x}}}\tilde{p} - \frac{1}{\Omega_{\tilde{x}}}\right)^2 + 4\sin^2\frac{x}{2} = \left(\frac{\omega_\dagger}{\Omega_{\tilde{x}}}\right)^2 \tag{3.66}$$

where $\omega_\dagger$ depends on the initial conditions and intensity of the acoustic wave.
The pendulum can swing over only if its initial energy is greater than maximum potential energy, being obtained when the mass reaches the unstable fixed point. Indisputably, if the kinetic energy is not sufficient enough, the pendulum will perform oscillations around the stable equilibrium point. On the other hand, if the

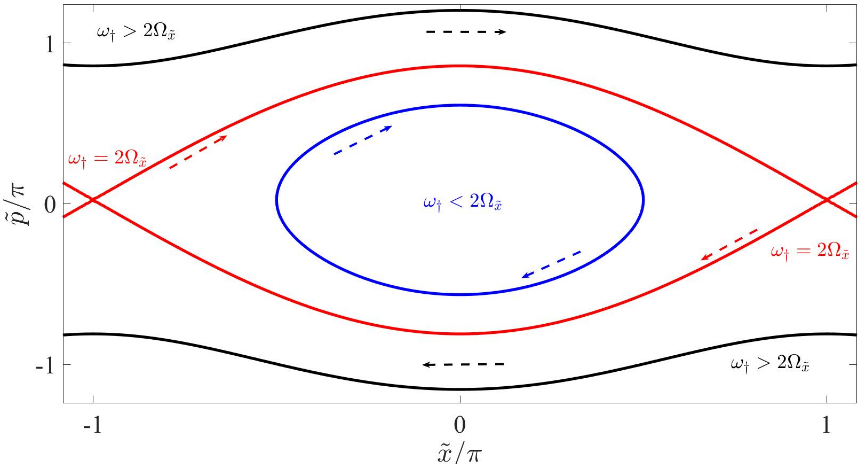

Figure 3.16: Characteristic types of ballistic electrons' trajectories in $(\tilde{x}, \tilde{p})$ plane. The localised trajectory represented by blue curve corresponding to $\omega_\dagger/\Omega_{\tilde{x}} < 2$. Unconfined electron motion for $\omega_\dagger/\Omega_{\tilde{x}} > 2$ displayed by black rotational orbits of the pendulum. The two transport regimes are set apart by separatrix (red curve) at $\omega_\dagger/\Omega_{\tilde{x}} = 2$.

pendulum has just right kinetic energy to reach the unstable equilibrium, it will approach it asymptotically and all oscillations are suppressed. Similarly, dealing with the pendulum formulation for an acoustically excited SL, one can find that for $\omega_\dagger < 2\Omega_{\tilde{x}}$ the electrons perform bounded oscillations within potential wells, whereas for $\omega_\dagger > 2\Omega_{\tilde{x}}$ they demonstrate delocalised motion. The latter types of motion, which can be seen in figure (3.16) are set aside by a seperatrix for $\omega_\dagger = 2\Omega_{\tilde{x}}$. The ballistic trajectories under this classification can be described analytically involving the Jacobi elliptic functions and hyperbolic functions

$I.\ \omega_\dagger < 2\Omega_{\tilde{x}}$

$$\begin{pmatrix} x \\ p_x\, d/\hbar \\ v_x \end{pmatrix} = \begin{pmatrix} 1/k_s \left\{ 2 \arcsin \left[\frac{\omega_\dagger}{2\Omega_{\tilde{x}}} \operatorname{sn} \left(\Omega_{\tilde{x}} \omega_1 t + \theta, \frac{\omega_\dagger}{2\Omega_{\tilde{x}}} \right) \right] + \pi/2 \right\} + v_s t \\ vs/vo \left[1 + \omega_\dagger \operatorname{cn} \left(\Omega_{\tilde{x}} \omega_1 t + \theta, \frac{\omega_\dagger}{2\Omega_{\tilde{x}}} \right) \right] \\ vs \left[1 + \omega_\dagger \operatorname{cn} \left(\Omega_{\tilde{x}} \omega_1 t + \theta, \frac{\omega_\dagger}{2\Omega_{\tilde{x}}} \right) \right] \end{pmatrix} \tag{3.67a}$$

II. $\omega_\dagger = 2\Omega_{\tilde{x}}$

$$\begin{cases} \begin{pmatrix} x \\ p_x\, d/\hbar \\ v_x \end{pmatrix} = \begin{pmatrix} 2\arcsin\left[\tanh\left(\Omega_{\tilde{x}}\omega_1 t+\theta\right)\right] \\ v_s/v_0\left[1+2/\Omega_{\tilde{x}}\,\mathrm{sech}\left(\Omega_{\tilde{x}}\omega_1 t+\theta\right)\right] \\ v_s\left[1+2/\Omega_{\tilde{x}}\,\mathrm{sech}\left(\Omega_{\tilde{x}}\omega_1 t+\theta\right)\right] \end{pmatrix}, p_0 d/\hbar > v_s/v_0 \\ \begin{pmatrix} x \\ p_x\, d/\hbar \\ v_x \end{pmatrix} = \begin{pmatrix} 2\arcsin\left[\tanh\left(-\Omega_{\tilde{x}}\omega_1 t+\theta\right)\right] \\ v_s/v_0\left[1-2/\Omega_{\tilde{x}}\,\mathrm{sech}\left(-\Omega_{\tilde{x}}\omega_1 t+\theta\right)\right] \\ v_s\left[1-2/\Omega_{\tilde{x}}\,\mathrm{sech}\left(-\Omega_{\tilde{x}}\omega_1 t+\theta\right)\right] \end{pmatrix}, p_0 d/\hbar < v_s/v_0 \end{cases} \tag{3.67b}$$

III. $\omega_\dagger > 2\Omega_{\tilde{x}}$

$$\begin{cases} \begin{pmatrix} x \\ p_x\, d/\hbar \\ v_x \end{pmatrix} = \begin{pmatrix} 2\,\mathrm{am}\left(\omega_\dagger\omega_1 t+\theta, \frac{2\Omega_{\tilde{x}}}{\omega_\dagger}\right) \\ v_s/v_0\left[1+\omega_\dagger\,\mathrm{dn}\left(\Omega_{\tilde{x}}\omega_1 t+\theta, \frac{2\Omega_{\tilde{x}}}{\omega_\dagger}\right)\right] \\ v_s\left[1+\omega_\dagger\,\mathrm{dn}\left(\Omega_{\tilde{x}}\omega_1 t+\theta, \frac{2\Omega_{\tilde{x}}}{\omega_\dagger}\right)\right] \end{pmatrix}, p_0 d/\hbar > v_s/v_0 \\ \begin{pmatrix} x \\ p_x\, d/\hbar \\ v_x \end{pmatrix} = \begin{pmatrix} 2\,\mathrm{am}\left(-\omega_\dagger\omega_1 t+\theta, \frac{2\Omega_{\tilde{x}}}{\omega_\dagger}\right) \\ v_s/v_0\left[1-\omega_\dagger\,\mathrm{dn}\left(-\Omega_{\tilde{x}}\omega_1 t+\theta, \frac{2\Omega_{\tilde{x}}}{\omega_\dagger}\right)\right] \\ v_s\left[1-\omega_\dagger\,\mathrm{dn}\left(-\Omega_{\tilde{x}}\omega_1 t+\theta, \frac{2\Omega_{\tilde{x}}}{\omega_\dagger}\right)\right] \end{pmatrix}, p_0 d/\hbar < v_s/v_0 \end{cases} \tag{3.67c}$$

The different initial conditions $x(0) = x_0$ and $p_x(0) = p_0$ are included in the equations in the form of a phase

$$\theta = \begin{cases} F\left(\mathrm{atan2}\left[\frac{2\Omega_{\tilde{x}}}{\omega_\dagger}\sin\left(\frac{\tilde{x}_0}{2}\right), \frac{1}{\omega_\dagger}\left(\frac{v_0}{v_s}\tilde{p}_0 - 1\right)\right], \frac{\omega_\dagger}{2\Omega_{\tilde{x}}}\right), & \omega_\dagger < 2\Omega_{\tilde{x}} \\ \mathrm{arctanh}\ \left[sin\left(\frac{\tilde{x}_0}{2}\right)\right], & \omega_\dagger = 2\Omega_{\tilde{x}} \\ F\left(\frac{\tilde{x}_0}{2}, \frac{2\Omega_{\tilde{x}}}{\omega_\dagger}\right), & \omega_\dagger > 2\Omega_{\tilde{x}} \end{cases} \tag{3.68}$$

In this inscription $F(.)$ constitutes the non-complete elliptic integral of the first kind

$$F(z,k) = \int_0^z \frac{dt}{\sqrt{1-k^2\sin^2(t)}} \tag{3.69}$$

and atan2[.] is the four-quadrant inverse tangent indicating the polar angle from the ellipse center. Note, we prefer to express the solutions of (3.61), (3.62) in the real space notation that provides the ground for comparison with the numerically

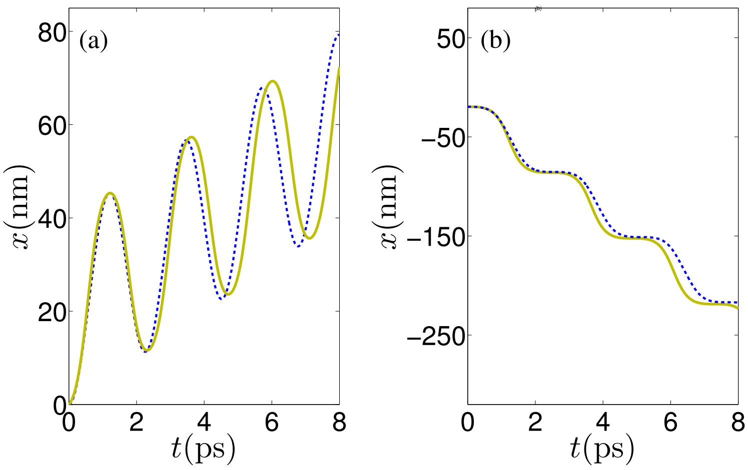

Figure 3.17: (a) Electron trajectories in real space for U=1.5 meV, $x_0 = 0$ and initial momentum $p = 0$. (b) Backward motion generated for U=1.5 meV, $x_0 = -19.635$ nm and $p = 0$. The dashed blue curves are electron trajectories described by Eqs. (3.9), (3.10) and the yellow solid curves are within pendulum approximation (3.63).

produced results by the holistic treatment of the problem. The semiclassical trajectories (dashed blue curves, Fig. 3.17) generated by equations (3.67a), (3.67c), in retrospect, exhibit considerably good agreement for U=1.5 meV with the numerical solution of equations (3.9), (3.10) (yellow curves, Fig. 3.17). The frequency of the first harmonic describing the nonlinear oscillations can be calculated as

$$\omega_1 = \begin{cases} \dfrac{\pi \Omega_{\tilde{x}} \omega_s}{2K\left(\omega_\dagger / 2\Omega_{\tilde{x}}\right)}, & \omega_\dagger < 2\Omega_{\tilde{x}} \\[2ex] \dfrac{\pi \omega_\dagger \omega_s}{2K\left(2\Omega_{\tilde{x}} / \omega_\dagger\right)}, & \omega_\dagger > 2\Omega_{\tilde{x}} \end{cases} \tag{3.70}$$

Here $K(.)$ is the complete elliptic integral of the first kind defined as $F(\pi/2, k)$ [124] from equation (3.69). In the limit $\omega_\dagger << 2\Omega_{\tilde{x}}$ the electron trajectories would be described by the characteristic frequency $\omega_1 = \Omega_{\tilde{x}}\, \omega_s$ of a harmonic oscillator. In that instance, the electron will be confined close to the bottom of the potential well, performing a quasi-harmonic motion. Henceforth, the frequency of motion to and fro across the well becomes tunable accordingly to the parameters of superlattice, bearing in mind $\Omega_{\tilde{x}}$ analytical form. Now if $\omega_\dagger >> 2\Omega_{\tilde{x}}$, we obtain $\omega_1 = \omega_\dagger\, \omega_s$ corresponding to the unbounded motion, which can be considered to be uniform and self-sustained as long as miniband velocity is large enough to neglect the potential energy.

Spectral analysis of semi-classical trajectories

Fourier analysis over the time-dependent x_0-averaged velocity of electrons $v_a(t) = \langle \dot{x} \rangle_{x_0}$ for different values of U can help to determine the frequency characteristics of non-dissipative electron dynamics. In this way, we may reveal connection between the drift and frequency properties of each transport regime realised in the system. For this aim we utilise the Fast Fourier Transform technique [216]. Subjecting the time-dependent $\langle x \rangle_{x_0}$ to signal analysis could provide information for the same non-zero Fourier components since $\langle x \rangle_{x_0} \leftrightarrow V(\omega_v)/j\omega_v$ where $V(\omega_v)$ is the Fourier transform pair of averaged velocity. We prefer performing Fourier transform of $v_a(t)$ since no drift components are involved in the realisation of this signal.

The left panels of figures 3.18 and 3.19 illustrate the temporal evolution $v_a(t)$ considering a typical response time and different values of the wave amplitude U. The $\langle \dot{x} \rangle_{x_0}$ represents an ensemble average over different x_0 that covers all the values for a range $[-\lambda/2, \lambda/2)$ but with the same initial momentum $p_0 = 0$. The effects of acoustic wave on the typical time realisation of $v_a(t)$ and the corresponding spectra are demonstrated in figure 3.18, near the point of the first bifurcation. The left panel of figure 3.18(a) exhibits a realisation of $v_a(t)$ calculated for $U = 1.5$ meV $< U_{cr1}$. One can see that the oscillations amplitude vary in an irregular, seemingly chaotic way. The middle panel of figure 3.18(a) reveals that these oscillations are associated with a broadband spectrum, which is centred around frequency $\omega_v = 2.5 \times 10^{12}$ rad/s^{-1}. The broadband character of this spectrum can be explained by the fact that for the given value of U, the main contribution to transport is provided by localised and unbounded trajectories in figure 3.6(a). A description within a pendulum approximation is applicable for these trajectories as we showed in Section 3.4. Equations (3.27) and (3.28) can be simplified to the undamped pendulum differential equation (3.63) under the assumption that the ballistic electron dynamics is characterised by a narrow range of modulation for $\tilde{p}$. The integral of motion (3.64) is noted that determines the spectrum of oscillations of the model (3.63) [217].

In the right panel of figure 3.18(a), we see how the spectrum $S(\omega_v)$ of oscillations $\dot{x}(t)$ varies with the change of initial condition $\tilde{x}_0$. The dot-dashed lines display the frequency ω_1 estimated analytically using equation (3.70), whereas the color map designates the different values of $S(\omega_v)$ calculated numerically using equations (3.9) and (3.10). It can be observed that the most pronounced spectral peak and the related frequency strongly depends on the initial position x_0. Furthermore, the

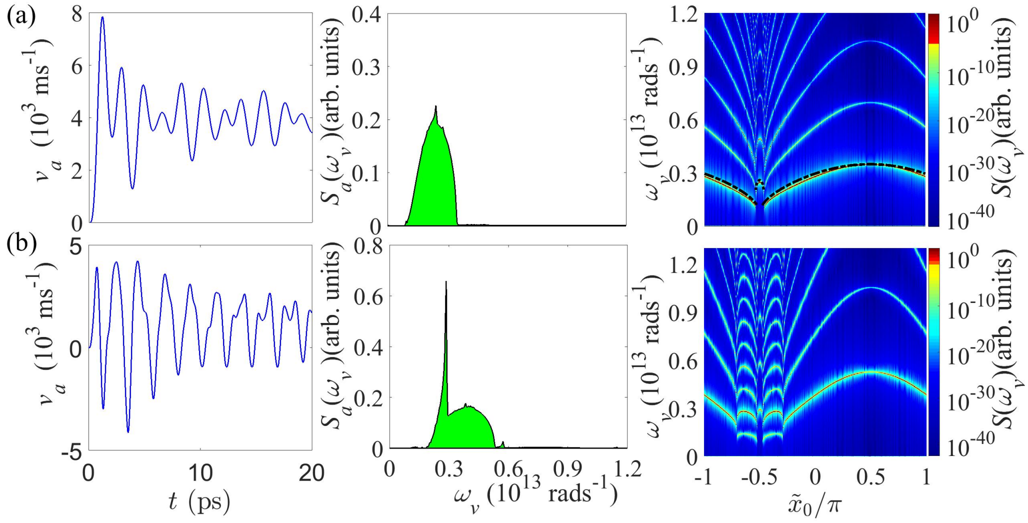

Figure 3.18: A typical time-realization of $v_a(t)$ (left panel), its Fourier spectrum $S_a(\omega)$ (middle panel) and the dependence of the spectrum $S(\omega)$ on the initial position of the particle x_0 (right panel) calculated for (a) $U = 1.5$ meV and (b) $U = 3.45$ meV. Dot-dashed lines mark the dependence $\omega_1(x_0)$ calculated analytically (see the text for details). Hereafter $p_0 = 0$.

average value of these spectral peaks seems to have high degree of proximity to the centre of the spectral band of S_a [cf. middle panel of Fig. 3.18 (a)]. This can be verified directly by the dependence $\omega_1(x_0)$ [Eq. 3.70] which is shown in the right panel of figure 3.18(a) by dot-dashed line.

The emergence of a prominent peak in $S_a(\omega_v)$ [middle panel of Fig. 3.18(b)] when U slightly overreaches U_{cr1} is reflected in the regularisation of oscillations $v_a(t)$ in the left panel of figure 3.18(b). This spectrum modification can be attributed to the appearance of meandering trajectories [see Fig. 3.6(b)], which can be understood as frequency-modulated (FM) Bloch oscillations with the maximal frequency $\omega_B^{max} = k_s U d/\hbar$ [47]. The frequency of the dominant peak of the frequency-modulated oscillations is weakly depended on the initial conditions which is accompanied by regularization of average velocity oscillations $v_a(t)$. The dependence of the spectrum $S(\omega_v)$ of $\dot{x}(t)$ on the initial position x_0 is shown in the right panel of figure 3.18(b). The right panel of figure 3.18 (b) displays how the spectrum $S(\omega_v)$ of $\dot{x}(t)$ varies with the change of initial position x_0. In particular, it is shown that for meandering trajectories initiated nearby $\tilde{x}_0 = -\pi/2$ [see Fig. 3.6(b)], the location of the dominant peak in $S(\omega_v)$ changes weakly. Furthermore, the position of this dominant peak in $S_a(\omega_v)$ (middle panel) is in agreement with the locations of the most prominent peaks in spectra $S(\omega_v)$ (right panel) linked to

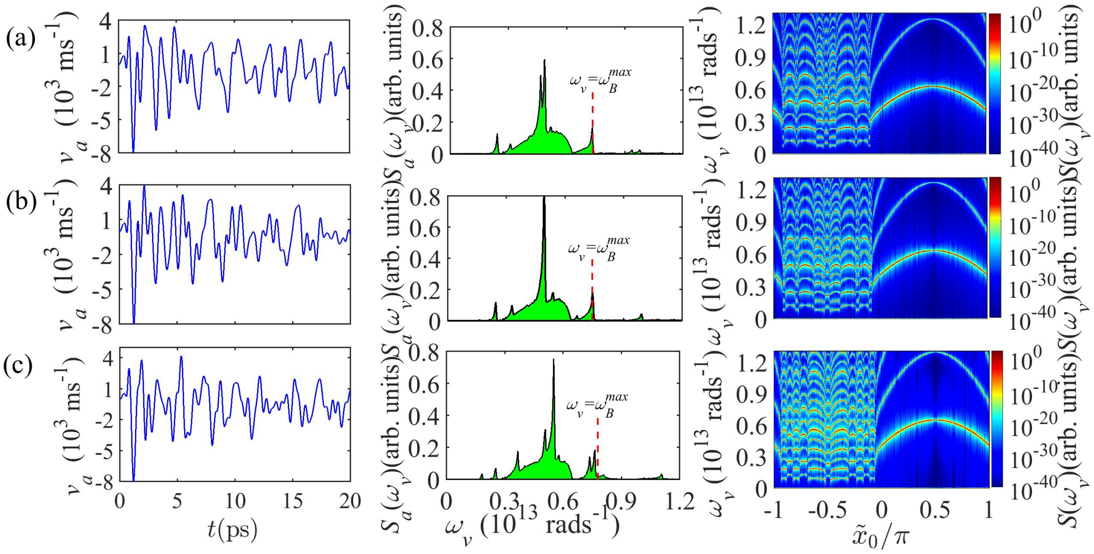

Figure 3.19: A typical time-realization of $v_a(t)$ (left panel), its Fourier spectrum $S_a(\omega_v)$ (middle panel) and the dependence of the spectrum $S(\omega_v)$ on the initial position of the particle x_0 (right panel) calculated for (a) $U = 4.85$ meV, (b) $U = 4.932$ meV, and (c) $U = 5.2$ meV. The vertical dashed line in the middle panel corresponds to maximal FM Bloch oscillations.

different meandering trajectories. On the other hand, the broadness of the spectrum $S_a(\omega_v)$ featured in the middle panel of figure 3.18(b) can be associated with the frequency characteristics of localised trajectories.

The averaged velocity $v_a(t)$ and corresponding spectra dependence on the value of U among two subsequent global bifurcations is demonstrated in figure 3.19. Therefore, we consider three values U from the range between third and fourth bifurcation, more precisely, $U = 4.85$ meV (a), $U = 4.932$ meV (b) and $U = 5.2$ meV (c). In this case the characteristics of electron transport is determined by the contribution of meandering and localised trajectories. It is important to note that the range of initial x_0 that trigger meandering trajectories becomes comparable with interval of initial conditions that generate localized trajectories. However, the former follow a more complex pattern enveloping three or four islands of stability. The enhancement of meandering trajectories involvement in electron motion is present in the time realisations of $v_a(t)$ (left panels), which demonstrate a far more complicated response under the action of sound wave. Henceforth, the related spectrum of v_a oscillations is enhanced and spread over a wider bandwidth since new different spectral components may appear, comparing second panels of figures 3.18 and 3.19. In addition, for these three values of the wave amplitude

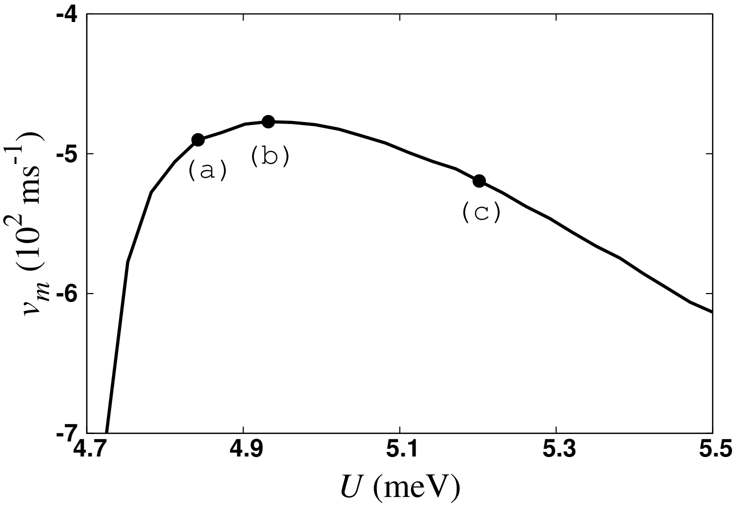

Figure 3.20: v_m versus U calculated for an electron driven by an acoustic wave. The labels (a)-(c) show the values on drift velocity characteristic used to produce the spectra $S_a(\omega_v)$ and $S(\omega_v)$ in Fig. 3.19

[see figure 3.18(b)], a dominant peak always emerges in the Fourier spectrum, which is apparently located at a higher frequency comparing with the one in figure 3.18(b) which represents the spectrum for value of U between U_{cr1} and U_{cr2}. A closer look at the dependency of velocity spectrum $S(\omega_v)$ on the initial position $\tilde{x}_0$ displayed in the right panel of figure 3.19 reveals more information about spectral content of $S_a(\omega_v)$. In particular, as we discussed above a greater interval of initial conditions are associated with meandering trajectories which, due to their frequency modulated characteristics, assist in the formation of multiple peaks in $S_a(\omega_v)$ which is known as a direct consequence of FM signals. The vertical dashed lines in the middle panel of figure 3.19 demonstrate the peak frequency deviation according to value ω_B^{max} which also reveal an remarkable agreement with numerical calculations. This estimation arises from $Carson's\ rule$ [218] that is often used to determine the frequency modulated signal bandwidth

$$\Delta\omega_v = 2(\omega_B^{max} + \omega_s) \tag{3.71}$$

where ω_s in this case is the maximum baseband message frequency component. In this context, the right panel of figure 3.19 suggests that frequency components are weakly dependent on initial conditions. At the same time, the contribution of localised trajectories yields a broad band background positioned in the frequency range 3×10^{12} – 6×10^{12} rad/s. With increasing U from U_{cr1} to U_{cr2}, we find that the dominant peak in $S_a(\omega_v)$ shifts moderately to higher frequencies. Nevertheless, the power at these frequencies behaves non-monotonically obtaining the maximum at the value of $U \approx 4.93$ meV corresponding to the local maximum of v_m in figure 3.20.

We conclude that the phonon propagation after the first bifurcation U_{cr1} generates high-frequency oscillations of ballistic electron orbits. In this regime, the rise of meandering trajectories, which can be understood as frequency-modulated Bloch oscillations, leads to the formation of a pronounced spectral peak. Therefore, the frequency of this peak is roughly one order of magnitude higher than the frequency of the sound wave. Moreover, by changing U, one can tune the frequency of the dominant peak as well as control its height.

Summary

In summary, we investigate how the bifurcation mechanisms affect the miniband electron transport in a superlattice driven by a plane wave. The analysis of the related phase portraits in the moving reference frame reveals the specific bifurcations, which are triggered with the variation of the acoustic wave amplitude. In addition, we calculated the electron drift velocity v_d and the time averaged velocity v_m in order to characterise the transport of electrons in the SL. The drastic changes in both $v_d(U)$ and $v_m(U)$ characteristics are directly associated with the restructuring of phase space caused by the global bifurcations. The critical values of wave amplitude U, which correspond to these bifurcations, were determined analytically by the conditions for separatrix reconnection. We found out that averaged velocities exhibit pronounced maxima, followed by a dramatic drop. Interestingly, the critical values of U estimated analytically coincide with the values of U for which $v_d(U)$ and $v_m(U)$ dependencies present the latter prominent features.

The study of ballistic transport allowed to reveal three characteristic types of electron trajectories produced by the propagating acoustic wave. They can be directly associated with typical acousto-electric effects which involve (i) carriers that are effectively trapped and move within the moving potential wave (localised trajectories in the moving reference frame) and (ii) ineffective interaction of carriers with potential wave (unbounded trajectories in the moving reference frame). On the other hand, frequency-modulated Bloch oscillations might emerge as U increases and is reflected by the existence of meandering trajectories in the moving reference frame. We additionally considered the limiting case $v_0 \leq v_s$ which reveals similar kinetic effects on the electron transport due to topological rearrangements of the phase space.

The wave amplitude influences the partial contribution of each type of trajectories to electron transport. Therefore, for each transport regime, the directed transport is associated with particular drift and spectral characteristics. This description is verified by the ultrasonic oscillations of the averaged electron velocity, which are induced by selecting a suitable value of U. These oscillations demonstrate either a broadband spectrum or a spectrum with a prominent peak. Furthermore, the velocity spectrum is consistently centred around a frequency which surpasses the frequency of the acoustic wave ω_s and can be tuned by its magnitude.

The previously discussed results indicate strongly that acoustically excited semiconductor superlattices may be used for the tunable generation of electromagnetic waves. In particular, the frequency properties of the averaged velocity reveal a possibility for using a SL driven by an acoustic wave for amplification of THz signals. Thus, in the following chapters our theoretical study is focused on the ways which can mimic mechanisms similar to the Bloch gain observed in an electrically pumped SL [40, 219, 220].

Chapter 4

Amplification of EM signals in a superlattice driven by an acoustic pump

Broadband Bloch gain and its modifications

In standard crystals the strong impurity scattering in the lattice, prevents the electron to complete even one full cycle of the Bloch oscillation, and thus the electron motion exhibits Drude-like conductivity. This restriction in superlattices is waived, since the lattice constant of the man-made SL can be fabricated to maintain the coherence of electron oscillations in the presence of scattering events [1]. In this instance, the drift velocity versus an applied dc bias E_{dc}, reaches a maximum value and beyond this point the slope is negative (see Section 2.3 for further discussion). Consequently, we expect the driven electrons, as they approach the Brillouin zone edge, to turn around because of Bragg reflection. Without scattering, the localisation of the electron trajectories, due to Bloch oscillations, results in zero drift velocity. On the other hand, a constant drift velocity appears in the presence of scattering but decreases with increase of E_{dc}, beyond a certain critical value E_{cr}. Such nonlinear transport property was first considered by Esaki and Tsu in their pioneering paper which addressed the feasibility of self-sustained oscillations and hence the generation of electromagnetic radiation in SL [9, 10]. Subsequently, the problem of how the Bloch oscillations would provide amplification of an electromagnetic wave was treated theoretically by Ktitorov et al [40], who calculated high-frequency conductivity of SL from the Boltzmann equation. In particular, it was shown that the real part of the dynamical conductivity $\mathrm{Re}[\sigma(\omega)]$ of Bloch oscillating electrons which becomes dispersive [Fig. 4.1, line (iv)]. On the other hand, the imaginary part of the dynamical conductivity $\mathrm{Im}[\sigma(\omega)]$ demonstrates a Lorentzian shape. In the former case, $\mathrm{Re}[\sigma(\omega)]$ exhibits negative values below the frequency ω_B of the Bloch oscillating electrons, and thus the SL oscillators can demonstrate the so-called THz Bloch gain. In the latter case, the peak in the imaginary part appears at $\omega = \omega_B$, emphasising that the system is oscillating at the Bloch frequency. Further theoretical studies on the realisation of Esaki-Tsu superlattice oscillator have been carried out to investigate the particular dispersive gain property [30, 219–224]. These efforts are ultimately aiming to design a frequency-tunable source of electromagnetic radiation which is able to work in the range of a few hundred GHz to several THz at room temperature. However, the existence of static NDC induces space-charge instabilities and the formation of electric domains. The existence of these electric domains acts destructively upon the Bloch gain [43]. Therefore, it is important to find alternative ways of suppressing the electric domains, while preserving the high-frequency gain in SLs. The main idea in the different schemes for achieving the so-called stable gain is that the electric instability can be avoided if the SL system demonstrates positive dynamical conductivity at low frequencies, whereas the high-frequency conductivity is still negative corresponding to the amplification of electromagnetic field. In principle, to analyse whether energy is transferred or absorbed from an alternating field (probe field) $E_{pr}(t) = E_\omega \cos(\omega t)$ in the presence of an electric pump field $E_P(t)$ [e.g. $E_{dc} + E_\Omega \cos(\Omega t)$], the time-dependent drift velocity $v(t)$ has to be determined under the action of the electric field

$$E(t) = E_P(t) + E_{pr}(t). \tag{4.1}$$

The frequency ω of the probe field can be favourably tuned by an external resonant cavity [44, 225]. If the time-dependent pump field is not uniform, but varies spatially as well, the path-integral solution of Boltzmann transport equation can again be addressed to calculate the time-dependent current. Within the semiclassical approach, the absorption of the probe ac field $E_\omega \cos(\omega t)$ in SL miniband is defined as

$$A(\omega) = \langle v(t) \cos(\omega t) \rangle_t \,, \tag{4.2}$$

where $v(t)$ [see Eq. 2.81] is the stationary time-dependent velocity of the electron accelerated by simultaneous action of pump and probe fields [220, 222, 226]. The brackets $\langle ... \rangle$ designate the time-average that is performed in general over infinite time. The absorption can equivalently be represented using the current density $j(t)$ induced in the SL by the total field (4.1)

$$\mathrm{Re}[\sigma(\omega)] = \frac{2 \langle j(t) \cos(\omega t) \rangle_t}{E_\omega}. \tag{4.3}$$

Here absorption ($\mathrm{Re}[\sigma(\omega)] > 0$) and gain ($\mathrm{Re}[\sigma(\omega)] < 0$), are determined by the real part of the dynamical conductivity, see appendix C. For the calculations in this work, we consider a period of time that is determined by the common period of both fields $T = 2\pi n/\omega = 2\pi m/\Omega$, where n, m are integers. Therefore, the frequencies are commensurate $\omega = n\Omega/m$ with n, m being relative primes [227]. However, we should emphasise here that coherent effects may emerge from the commensurability of the frequencies, if m and n are small integers. These effects are related to coherent interaction of alternating fields, which are realised under the conditions of parametric resonance [44, 228]. The physical interpretation of parametric resonances then relates to the instant values of electron effective mass that varies periodically with the frequency of energy oscillations in the presence of a strong ac field. The dynamical conductivity is always scaled with the Drude conductivity $\sigma_0 = eN_0v_0/E_{cr} = j_p/E_{cr}$ which is demonstrated in figures of this dissertation. The magnitude of absorption in real units cm^{-1} has the following relationship[1] with the scaled dynamical conductivity [229, 230]

$$\alpha(\omega) = \sqrt{2\epsilon_r}\,\frac{\omega}{c}\left[\left(1 + \frac{(\mathrm{Re}[\sigma(\omega)])^2}{\omega^2\epsilon_0^2\epsilon_r^2}\right)^{1/2} - 1\right]^{1/2} \mathrm{sgn}\left(\mathrm{Re}[\sigma(\omega)]\right). \tag{4.4}$$

Here ϵ_r is the relative permittivity of SL material, c is the speed of light in the vacuum and ϵ_0 is the permittivity in the vacuum. Importantly, the skin depth which is the distance that takes to reduce the amplitude of probe field by a factor $1/e$ is determined by

$$\delta(\omega) = \frac{2}{\alpha(\omega)}. \tag{4.5}$$

In the limit $\mathrm{Re}[\sigma(\omega)] << \omega\epsilon_0\epsilon_r$ and probe field with frequency $\omega\tau > 0.01$ the magnitude of absorption (gain) is reduced to

$$\alpha(\omega) = \alpha_0\frac{\mathrm{Re}[\sigma(\omega)]}{\sigma_0}, \tag{4.6}$$

where

$$\alpha_0 = \frac{2}{\epsilon_0\sqrt{\epsilon_r}c}\frac{j_p}{E_{cr}}. \tag{4.7}$$

This limit has important implications for the study of the behaviour of dynamical conductivity in the presence of high-frequency electric field. Since we consider the nondegenerate equilibrium distribution the peak current j_p is given by equations

---

[1] For a more general discussion on plane monochromatic waves in conducting media and the derivation of equations (4.2), (4.3) see appendix C.

(2.85), (2.87). As a result the parameters of SL determine j_p, and therefore a_0 which is the coefficient that relates scaled dynamical conductivity with the magnitude of absorption.

The behaviour of Bloch gain [220] for a SL under the sole action of a monochromatic field $E(t) = E_{dc} + E_\omega \cos\omega t$ can be determined analytically [134, 220, 231]

$$\mathrm{Re}[\sigma(\omega)] = \frac{1}{E_\omega} \sum_{n=-\infty}^{\infty} J_n(\beta)\left[J_{n+1}(\beta) + J_{n-1}(\beta)\right] j_{dc}(eE_{dc}d + n\hbar\omega). \tag{4.8}$$

Here $\beta = eE_\omega d/\hbar\omega$ and j_{dc} is the dc current density given by

$$j_{dc}^{\omega} = \sum_{n_1=-\infty}^{\infty} J_n^2(\beta) j_{dc}(eE_{dc}d + n\hbar\Omega), \tag{4.9}$$

where $J_n(\beta)$ are the Bessel functions of the first kind. It can be seen from the latter equation that the VI characteristic in the presence of ac field is given by a sum of shifted Esaki-Tsu characteristics. In the limit of weak probe field $\beta << 1$, the Tucker difference formula can evaluate the dynamic conductivity without further recourse to equation (4.8) as [220, 232, 233]

$$\mathrm{Re}[\sigma(\omega)] = \frac{j_{dc}(eE_{dc}d + \hbar\omega) - j_{dc}(eE_{dc}d - \hbar\omega)}{2\hbar\omega} ed \tag{4.10}$$

Now note that if we consider the limit of low frequency $\omega\tau << 1$, the dynamical conductivity reduces to dc differential conductivity $\sigma_{dc} = eN_0 \partial v_{dc}/\partial E_{dc}$ at the given operational point E_{dc}, which behaves as the free-electron absorption for extremely weak dc bias

$$\frac{\mathrm{Re}[\sigma(\omega)]}{\sigma_0} = \frac{1}{1 + \omega^2\tau^2} \tag{4.11}$$

As follows from equation (4.11), the free-electron absorption [Fig. 4.1, line (i)] is always positive with a maximum value $\mathrm{Re}[\sigma(\omega)]/\sigma_0 = 1$ while it exhibits a power-like decay ($\sim 1/\omega^2\tau^2$) in the high frequency limit $\omega\tau >> 1$. As dc bias increases the absorption profile is modified and at low-frequencies the absorption is suppressed to become $\mathrm{Re}[\sigma(\omega)] = 0$ for $\omega_B\tau = 1$ [Fig. 4.1, line (ii)]. When ω_B exceeds slightly $1/\tau$, Bloch gain emerges, and thus Esaki-Tsu characteristic demonstrates NDC, since $\partial v_{dc}/\partial E_{dc} < 0$. The derivative of dc differential conductivity $\partial\sigma_{dc}/\partial\omega_B\tau$, when equates to zero, can determine the point where the Esaki-Tsu characteristic demonstrates the most negative slope (green inclined segment in the inset of Fig. 4.1). By using the geometric interpretation of the Tucker formula the maximum gain [Fig. 4.1, line (iii)] in the limit of low frequency

$$\omega_B\tau = \sqrt{3}\ ;\ \min\{\mathrm{Re}[\sigma(\omega)]\} = -0.125$$

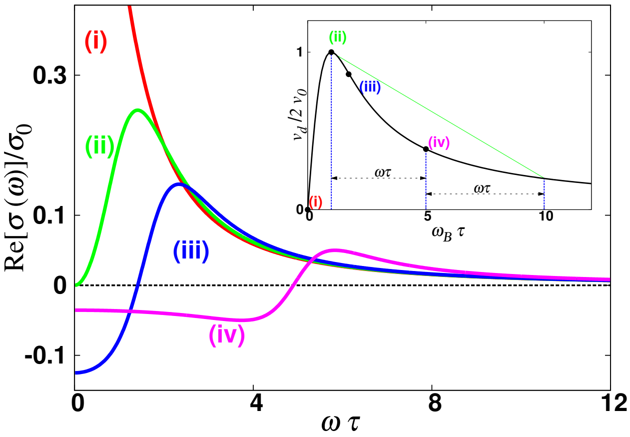

Figure 4.1: Absorption and gain profiles obtained using the Tucker relation (4.10) at the operation points marked in the Esaki-Tsu curve (i) $\omega_B\tau = 0$, (ii) $\omega_B\tau = 1$, (iii) $\omega_B\tau = \sqrt{3}$ and (iv) $\omega_B\tau = 5$. Inset: The Esaki-Tsu characteristic and illustration of the geometrical meaning of the Tucker formula. Figure adapted from [134, 220].

The familiar Bloch gain profile [Fig. 4.1, line (iv)] is obtained with increasing dc bias above $\omega_B\tau = \sqrt{3}$, when the electron is able to oscillate before scattering. This gain profile as it is described by equation (4.10) demonstrates a crossover from gain to loss at the resonance $\omega = \omega_B$. The shaping of dispersive Bloch gain profile in the proximity of frequency $\omega{=}\omega_B$ has been associated with the formation of momentum bunching of electron distribution for a SL in the presence of a static and THz electric field [68]. The time-dependent drift velocity can be then synchronous with the terahertz field due to periodic motion of electron bunch in k–space with period $T = 2\pi/\omega_B$. The physical interpretation k–space bunching allows the consideration of large-signal differential conductivity, since for the large signals the bunch becomes more pronounced and therefore the understanding of arising domain instabilities [219]. The concept of Bloch gain has additionally explained on the basis of quantum effects introduced by scattering processes that cause transitions between Wannier-Stark states [34, 224, 229].

The principal objective to obtain conditions for stable THz gain becomes streneous for NDC state which induces space-charge instabilities resulting in reduction of gain. The development of space-charge instabilities generates spatial domains of different electric fields that violate the assumption of homogeneous electric field used to uphold the negative dynamical conductivity of the device. One of the basic approaches to suppress the formation of charge domains is to apply suitable electric fields under which the dc drift velocity would perform a steep positive slope

[43]. This can be achieved by increasing the amplitude of ac drive that stimulates a time-dependent drift velocity, which has notably quasi-periodic behaviour and involves an enhanced dc component. Thus, the travelling-wave package becomes weaker as it reflected in momentum space electron bunching [68].

If the SL length is adequately short, this prevents the formation electric domains because the space-charge fluctuations are not sufficient enough to give rise to an electrically unstable state [235]. In particular, the diminishing of static or dynamic electric field domains was achieved by engineering a "super-superlattice" composed by short sections of superlattice, which are seperated by heavily doped $III - V$ compounds [42]. Nonetheless, this type of electrically biased superlattice cannot guarantee a net Bloch gain, since the THz transmission has a sharp change at the Bloch frequency.

The modulation of spectral shape of the dynamical conductivities concerning electrons experiencing Bloch oscillations, was considered as evidence of dispersive Bloch gain in SLs [236]. In experiments with undoped SLs, it was demonstrated that the information about the dependence of $\mathrm{Re}[\sigma(\omega)]$ can be obtained with the help of time domain spectroscopy [236, 237]. This information can be used to suppress high-field domains. On the other hand, semiclassical and quantum calculations showed that the terahertz-field transient cannot clearly indicate existence of the gain, whereas for long-duration pulses it was ruled out that the former experimental evidence is consistent with steady-state Bloch gain [238, 239]. To achieve tunable terahertz gain, the carrier dynamics of an optically excited SL in the presence of THz pulse should demonstrate an excitonic absorption asymmetry of the Wannier-Stark transitions as has been discussed in the references [240, 241].

More recently, using a quantum transport formulation relied on nonequilibrium Green functions it has also been shown, that the gain profile emerges for an operation point within the positive differential conductivity (PDC) region [245]. The gain in this case is affected by scattering parameters and the doping of a SL structure [246] should be designed in such a way to allow stimulate emission at transition between Wannier-Stark ladders.

The theoretical treatment of electron dynamics in the presence of an external magnetic field predicted notable modification of the gain profiles which leads to a dramatic increase of the magnitude of THz gain in SLs [45]. In this work investigations were performed to explain the behaviour of dissipative electron dynamics in the presence of crossed electric and magnetic fields. More importantly, an appropriate choice of the operation point at PDC part of VI characteristic eliminates electric instabilities, and also a tunable gain is found which is attributed to nonlinear cyclotron oscillations. On the other hand, the Bloch-like regime emerges with further increase of E_{dc}. This takes place when an operating point corresponds to the NDC part of VI curve. Interestingly, there is a direct connection of ballistic dynamics, which are equivalent to nonlinear pendulum, to the different type of gain profiles. In this case, the amplification is revealed by the sign of effective mass that becomes negative as a result of strongly nonlinear oscillations [247].

The feasibility of amplification and generation of high-frequency radiation in dc-ac-driven SSLs in the absence of electric domains was discussed in references [134, 220]. In these works amplifications was studied by analysing the Bloch gain in the presence of high-frequency pump field $E_p(t) = E_{dc} + E_\Omega \cos(\Omega t)$, when the pump and the probe frequencies, Ω and ω, are incommensurate. In this case, the use of the exact solution of the Boltzmann equation and an extended formalism [134, 231] for the stationary time-dependent current leads to the following expression

$$\mathrm{Re}[\sigma(\omega)] = \frac{1}{E_\omega} \sum_{n=-\infty}^{\infty} J_n(\beta) \left[J_{n+1}(\beta) + J_{n-1}(\beta)\right] j_{dc}^{\Omega}(eE_{dc}d + n\hbar\omega). \tag{4.12}$$

Here where $J_n(\beta)$ are the Bessel functions of the first kind, $\beta = eE_\omega d/\hbar\omega$ and j_{dc}^{Ω} is the dc current density modified solely by the pump field, which can be calculated as

$$j_{dc}^{\Omega} = \sum_{n_1=-\infty}^{\infty} J_{n_1}^2(\beta_1) j_{dc}^{\Omega}(eE_{dc}d + n_1\hbar\Omega), \tag{4.13}$$

with $\beta_1 = eE_\Omega d/\hbar\Omega$. Then again, the dc current modified by simultaneous action of the pump and probe field, is obtained by the following expression

$$j_{dc}^{\Omega,\omega} = \sum_{n=-\infty}^{\infty} J_n^2(\beta) j_{dc}^{\Omega}(eE_{dc}d + n\hbar\omega). \tag{4.14}$$

The modification of voltage-current characteristic by pump field conceivably describes the changes in absorption as noted above and can be attributed to the physical meaning of Tucker relation [234]. The modified drift-velocity-field curve then exhibits photon-assisted peaks at dc bias values $eE_{dc}d = n\hbar\Omega + \Gamma$, where $\Gamma = \hbar/\tau$ and n corresponds to number of photons that electrons absorb to experience a potential difference $eE_{dc}d + n\hbar\Omega$ across the potential barrier. The realisation of these new transport channels is associated with the coefficients $J_n(\beta)$ that represent the probability amplitude of a transition with n-photon emission or absorption within the framework of the semiclassical approach. Interestingly, a high-frequency gain is achievable at regions of VI characteristics with positive slope, which is modified because of the action of an auxiliary ac pump [220]. Also, it has been observed that dc bias is not strictly connected with a stable Bloch gain [134]. Thus, from the analysis of the Bloch gain only in the presence of a high-frequency pump field, a small-signal dispersive gain profile (e.g. green curve Fig. 4.10) can also be obtained.

A different approach was developed to suppress the instability of a homogeneous electric field in negative differential conductivity conditions by implementing low-frequency modulation of the dc bias applied to a long SL [15]. This approach involved two different parts in the waveform of the modulation, namely: a short time-interval when the bias is switched off, during which the free-carrier absorption prevails inducing suppression of space-charge instabilities, and a longer fraction of each period of modulation that allows the excitation of Bloch oscillations. This modulation in the applied bias makes possible the shaping of a desirable gain profile. Alternatively, this process of fast switching bias can be replicated by polychromatic modulation which suppresses instabilities and demonstrates a distinct gain profile [15, 248]. This gain profile can be controlled by variation of the different amplitudes of polychromatic drive components and due to the mixing of harmonics with the frequencies Ω, $n\Omega$.

This latter work focused especially on the use of a bichromatic microwave field for achieving the stable Bloch gain. However, the expense has to be paid in this approach is the use of a low-frequency auxiliary pump field. Therefore, in this work we suggest a scheme that relies solely on acoustically pumped SLs for an amplification of electromagnetic signals. In addition, our approach for achieving stable high-frequency gain, can be distinguished from those employing ac pump field or the polychromatic scheme, since we consider a pump which varies spatially as well as temporally. To understand the implications of our main idea, let us consider the influence of a strong phononic pump $E_s(x,t) = k_s U/e \cos(k_s x - \Omega_s t)$ on electron dynamics. This pump is induced by an acoustic wave with frequency Ω_s that propagates along SL's axis in x–direction. In such system the nonlinear particle dynamics sensitively depends on the amplitude of the propagating wave. As it is already hinted in the previous chapter, the SLs driven by acoustic wave provide the media for the generation of high-frequency electromagnetic waves. Consequently, we assume the additional action of a weak ac field $E_{pr}(t) = E_\omega \cos\omega t$ on SL (see Fig.4.2). To find the absorption or the gain of this probe field $E_{pr}(t)$, we have to compute the time-dependent drift velocity in a manner similar to those used in the ac-driven SL, but now the total effective electric field in the form

$$E(x,t) = E_{\Omega_s} \cos(k_s x - \Omega_s t) + E_\omega \cos\omega t. \tag{4.15}$$

Here $E_{\Omega_s} = k_s U/e$ is the amplitude of an effective acoustoelectric field. The latter term is introduced to allow the comparison with the previous obtained results on electron accelerated by a static electric field or in the presence of a strong high-frequency ac field. By considering a total field (4.15), the ballistic electron dynamics in tight-binding SLs is determined by equations

$$v_x = v_0 \sin \frac{p_x d}{\hbar}, \tag{4.16}$$

$$\frac{dp_x}{dt} = eE_{\Omega_s} \cos(k_s x - \Omega_s t) + eE_\omega \cos\omega t. \tag{4.17}$$

In this work, we assume that the frequencies Ω_s and ω are incommensurate. To gain a more general overview of how the parameters which determine v_0 can influence the electron dynamics and the attenuation of the electromagnetic waves, we will consider more than one superlattice structures. The different sets of parameters, which are experimentally obtained and verified in references [45, 179, 249, 250] and the corresponding a_0 are summarised in the table 4.1 both for almost zero temperature, and room temperature.

Parameter SL structure		Δ (meV)	d (nm)	τ (fs)	N_0 (cm^{-3})	ϵ_r	T_e=0,300 K a_0 (cm^{-1})
I.	[179]	7	12.5	250	10^{16}	12.5	536.76, 272.6
II.	[45]	60	6	200	10^{16}	13	831.54, 422.3
III.	[249]	120	4.6	150	8×10^{16}	13.5	5756, 2923
IV.	[250]	146	5.3	100	10^{17}	13.88	7747, 3934

Table 4.1: Parameters of different SL structures determining a_0.

The main question that now arises here is how a phononic wave will alter the shapes of the gain profiles and the magnitude of THz gain in SLs. In addition, we are interested to find whether it can provide the conditions for suppression of electric instability. Hence, in order to determine whether the probe field (red-Fig.4.2) is attenuated or amplified (green-Fig.4.2) in the presence of a pump field (blue-Fig.4.2) , we employ an exact solution of the Boltzmann equation [Eq. (3.13)].

Weak-signal gain in the quasistatic limit

The influence of a pure ac pump field on the absorption of weak probe field in the quasistatic limit $\omega\tau < 0.1$ has been analysed in detail [44, 251, 252]. It was shown that in this scheme the dominant physical processes, associated with the net gain in SL, are the effect of spontaneous frequency multiplication and parametric amplification of the probe field due to coherent interaction of the pump and probe

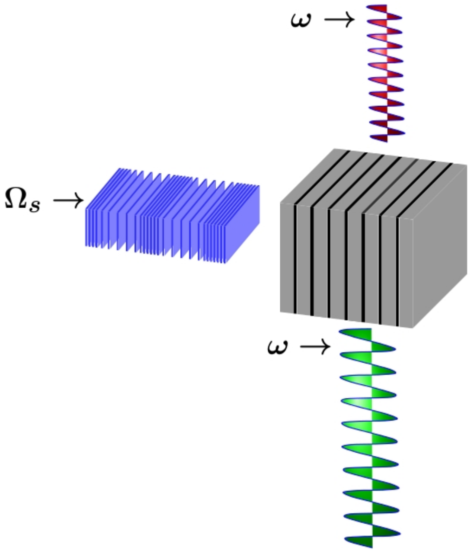

Figure 4.2: Schematic structure of an acoustically pumped semiconductor SL with frequency Ω_s. Gain occurs in the case of weak ω probe field is incommensurate with pump frequency.

fields together and non parametric-absorption. Therefore, in the case $\omega = n\Omega$ the weak signal absorption can be represented as a sum of three terms

$$A_\omega = A_\omega^{harm} + A_\omega^{coh} + A_\omega^{incoh}, \tag{4.18}$$

where

$$A_\omega^{harm} = \langle v(E_\Omega(t)) cos\omega t \rangle \,, \tag{4.19}$$

$$A_\omega^{coh} = \langle v'(E_\Omega(t)) cos2\omega t \rangle \, \frac{E_n}{2}, \tag{4.20}$$

$$A_\omega^{incoh} = \langle v'(E_\Omega(t)) \rangle \, \frac{E_n}{2} = \frac{\tilde{E}_\omega}{(1+\tilde{E}_\Omega^2)^{3/2}}. \tag{4.21}$$

Here prime denotes the derivation with respect to E, $\tilde{E}_\omega = E_\omega/E_{cr}$ and $\tilde{E}_\Omega = E_\Omega/E_{cr}$. In general, incoherent absorption A_ω^{incoh} describes the free carrier absorption modified by the pump field. Hence, if the SL is additionally biased ($E_{dc} \neq 0$), the incoherent absorption can become negative related to the slope in the dependence of v_{dc} on dc bias at a specific working point E_{dc}. Now, by choosing the working point at the PDC one can prevent the space-charge instability arising in

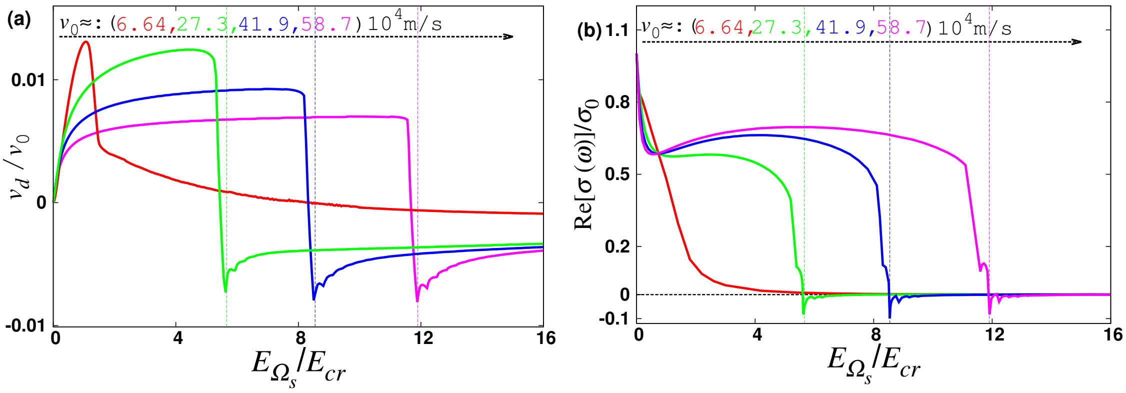

Figure 4.3: (a) Acoustoelectric-drift velocity characteristics for $\Omega_s\tau = 0.1$ and $v_0 \approx$(6.64, 27.3, 41.9, 58.7)10^4 m/s. (b) Absorption dependencies on E_{Ω_s}/E_{cr} for $v_0 \approx$(6.64, 27.3, 41.9, 58.7)10^4 m/s. The vertical lines identically correspond to the reversal of drift velocity and the maximum values of gain. The horizontal dashed line in the right panel signifies the zero absorption.

the SL. On the other hand, the incoherent component [Eq. (4.21)] of total absorption [Eq. (4.18)] shows that it is independent from n and always positive. An alternative approach to an ac pump might be undertaken if we consider a sound wave in the quasistatic limit. Therefore, in the presence of an arbitrary phonon pump $E_{\Omega_s}(x,t)$, we need again to calculate the time-dependent drift velocity under the effective electric field $E(x,t)$. It is worth mentioning that in order to obtain the incoherent absorption in the latter scheme, for reasons related to the optimisation of numerical solving, we considered commensurate frequencies [2] $\omega = n\Omega_s/m$ with $m \geq 7$. In this limit, the parametric effects become negligible, and gain can only take place due to the incoherent component of the small-signal absorption. Figure 4.3 demonstrates how the drift velocity v_d and the related absorption change with the variation of the amplitude of the pump field E_{Ω_s}, for the different parameters which can be found in table 4.1. We can see that the red curve in figure 4.3(a) corresponds to the typical profile of $v_d(U)$ dependence, which was discussed in Section 3.2.1. On the other hand, the other drift velocity characteristics in figure 4.3(a) have multiple maxima and they can attain negative values. This behaviour is caused by the increase of maximum miniband velocity v_0 that enhances the length of the trajectories contributing to the drift velocity. Essentially, the growth of v_0 results in trajectories that fluctuate faster, allowing the electron to perform several cycles of localised oscillations between the scattering events. Thus, the change

---

[2] The specific ratio assumed for m, n in all calculations was the fifth convergent of the golden ratio reciprocal, namely: $n/m = 5/8$.

of v_0 can strengthen the effects of phase portraits restructuring, making visible a series of successive global bifurcations (U_{cr_n}, $n > 2$) discussed in Section 3.3.2 and reflected in the profile of $v_d(E_{\Omega_s}/E_{cr})$ [see Fig. 4.3 (a)]. This type of behaviour of drift velocity bears close resemblance with averaged velocity shown in figure 3.4(b). Figure 4.3 (b) reveals that incoherent absorption remains always positive for $v_0 \approx 6.64 \times 10^4$ m/s (red curve) with the increase of E_{Ω_s}. Nevertheless, as v_0 grows, the profiles of absorption (green, blue and magenta curves) demonstrate correlation with $v_d(E_{\Omega_s})$ dependences. This becomes apparent by comparing figures 4.3(a) and (b) that $\mathrm{Re}[\sigma(\omega)]$ starts to exhibit negative values with the appearance of negative drift velocity. The latter implies a sensitive dependence of gain on the sign of drift velocity. Moreover, after the first bifurcation with increase of the pump field, the emergence of Bloch-type oscillations [meandering trajectories, Fig. 3.6(b)] coincides with the sharp drop of the absorption and the dynamical conductivity practically exhibits negative values when $v_d < 0$. We underline here that the maximal value of the gain occurs right at the onset of the second bifurcation, as illustrated in figure 4.3 (b) (vertical lines). This observation is in excellent agreement with the following equation

$$e[E_{\Omega_s}]_2 d \;=\; \hbar\omega_s\left[\sqrt{\left(\frac{v_0}{v_s}\right)^2 - 1} + \sin^{-1}\left(\frac{v_s}{v_0}\right) + \frac{\pi}{2}\right] \quad . \tag{4.22}$$

This potential drop corresponds to the condition for the second global bifurcation determined by the explicit expression (3.44) for the given value U_{cr2}. In the previous analysis of phase space dynamics for $v_0 >> v_s$, it was pointed out that the Bragg reflections of the electron from the edges of the Brillouin zone result in nonlinear phonon-assisted Bloch oscillations. Hence, in this case the excitation of electron within the miniband ($\Delta/2$) is accompanied by the emission of the quantum $\hbar\omega_q$ for U_{cr2}, giving rise to an amplification. Thereafter, the homoclinic loop that bounds the localised trajectories [see Fig. 3.6(c)] is expanded with the increase of U, while the region of meandering trajectories is reduced, thus inducing increase of drift velocity and positive crossover for dynamical conductivity. Further global bifurcations will enforce the reappearance of amplification and for the limiting case $E_{\Omega_s} >> E_{cr}$ the complete attenuation of the probe field.

Stable gain in the presence of sub-THz acoustic pump wave

In this section, we describe the influence of sub-THz acoustic wave ($\Omega_s\tau = 0.1$) on the profile of absorption, and under which conditions it is possible that the high-

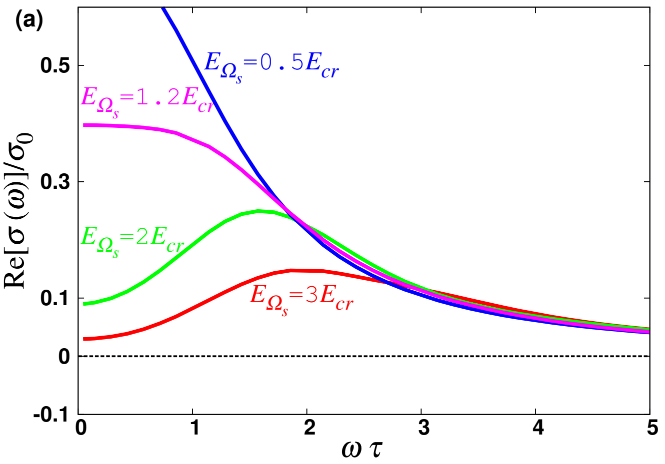

Figure 4.4: Absorption profiles for $\Omega_s\tau$=0.1 and estimated for E_{Ω_s}/E_{cr}=: 0.5, 1.2, 2, 3. $\sigma(\omega)$ is scaled by the $\sigma_0 = 5.0409\ (\Omega\ \mathrm{cm})^{-1}$ for the parameters of the SL structure (I, table 4.1). The dashed-curve signifies the free-carrier absorption whereas the horizontal dashed line marks the zero absorption.

frequency response of electrons in the single miniband can prevent the formation of space-charge instability. The study of the Bloch gain profile under the action of high-frequency electric pump field suggests that the small-signal dispersive gain profile is realisable even without application of dc bias. In particular, there has been some work on the demonstration of a stable THz gain in superlattice using a strong ac pump field in the absence of dc bias [134]. On the contrary, at low frequencies $\omega\tau << 1$ the small-signal dispersive gain profile does not exist anymore [251]. The latter can be well (4.10). In fact, if the quasistatic approximation is not applicable then the absorption profile follows the free-carrier absorption exhibiting the power-like decay as probe frequency ω increases.

Figure 4.4 illustrates how the absorption profiles are affected by the variation of pump field E_{Ω_s} with individual values ranging from substantially smaller to considerably larger than the critical field E_{cr}. The absorption profile behaves similarly to free-carrier absorption for $E_{\Omega_s} << E_{cr}$, being consistent with power-like decay for frequencies $\omega\tau >> 1$. As E_{Ω_s} grows, the area of unbounded trajectories [smooth solid curves in Fig. 3.6(a), (b)] shrinks as we saw previously in the discussion on phase space dynamics. When E_{Ω_s} exceeds $1.2E_{cr}$ ($\sim U_{cr_1}$), the absorption profile changes sharply its slope in the vicinity of $\omega = k_s U_{cr1} d/\hbar$ (magenta curve, Fig. 4.4). This frequency corresponds to the maximal frequency, ω_B^{max}, of frequency modulated Bloch oscillations. Therefore, the modification of absorption profile

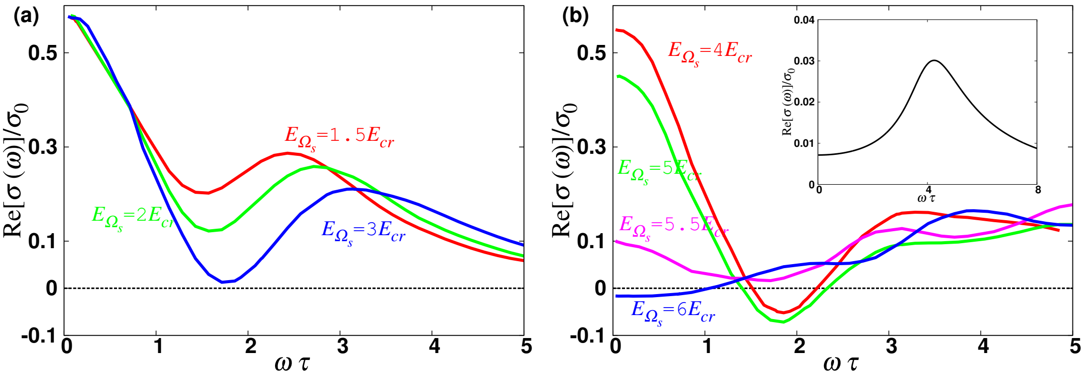

Figure 4.5: (a) Absorption profiles calculated for $\Omega_s\tau = 0.1$ and different values of pump amplitude E_{Ω_s}/E_{cr}=: 1.5, 2, 3. (b) Gain and absorption profiles in the presence of pump field with magnitude E_{Ω_s}/E_{cr}=: 4, 5, 5.5, 6 and frequency $\Omega_s\tau = 0.1$. Inset: Small-signal absorption as a function ω for pure ac pump $E_\Omega = 4E_{cr}$. $\sigma(\omega)$ is scaled by the $\sigma_0 = 7.964$ $(\Omega\ \text{cm})^{-1}$ for the parameters of the SL structure (II, table 4.1).

relates to the rise of meandering trajectories manifesting the excitation of electron within the miniband and the simultaneous absorption of phonon. With further increase of the pump field, $\text{Re}[\sigma(\omega)]$ demonstrates resonant features (green and red curve in figure 4.4) again nearby $\omega = \omega_B^{max}$. Specifically, the pump amplitude several times the critical field, $E_{\Omega_s} \approx 3E_{cr}$, causes reduction in absorption for $\omega\tau \to 0$. This value of the pump field corresponds with a value of U well beyond the sixth global bifurcation, and, according to our numerical calculations, the crossover from loss to gain in the limit of low probe frequency is approached asymptotically with the increase of E_{Ω_s} [see Fig. 4.3(b)]. In addition, for such a strong acoustic pump, the interval of the initial conditions $\tilde{x}_0$ for meandering trajectories becomes comparable with the range of initial conditions for the localised trajectories [see discussion in Section 3.5]. Therefore, the robustness of electrical stability $[\text{Re}[\sigma(\omega)] > 0, \omega\tau \to 0]$, in this case, can be associated with the contribution of the localised trajectories. On the contrary, the emergence of more complex meandering trajectories, and thus of oscillations with higher frequency components cannot assist in the avoidance of destructive electric domains. In a similar way, the electric instability exists in SLs due the synchronized Bloch oscillations in the presence of dc bias [68]. We now turn to the consideration of electron dynamics within the same theoretical framework, but for a different SL structure [II, table 4.1]. For this choice of SL parameters $v_0 \approx 27.3 \times 10^4$ m/s and the

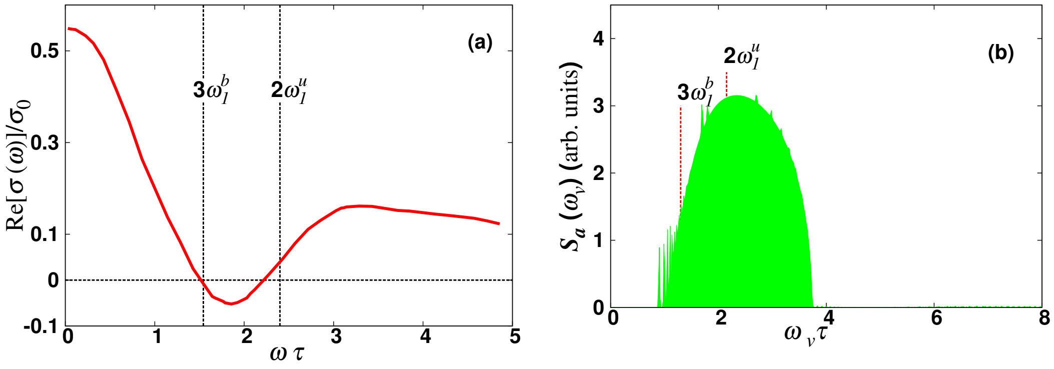

Figure 4.6: (a) Gain profiles calculated for $\Omega_s\tau = 0.1$ and pump strength E_{Ω_s}/E_{cr}=4. (b) Fourier spectrum $S_a(\omega_v)$ for a typical time-realisation of $v_a(t)$ corresponding to ballistic motion, calculated using the same E_{Ω_s} as (a). The vertical lines correspond to the harmonics of nonlinear oscillations, where ω_1^b, ω_1^u are the frequencies associated with localised and unbounded motion respectively. $\sigma(\omega)$ is scaled by the $\sigma_0 = 7.964$ $(\Omega \text{ cm})^{-1}$ for the parameters of the SL structure (II, table 4.1).

key ratio $v_0/v_s \approx 54.65$. Figure 4.5 (a) demonstrates the absorption profile with moderate field strengths E_{Ω_s} far away from the first bifurcation that takes place at $E_{\Omega_s} \approx 5.31E_{cr}$. Nevertheless, additional structures arise, dispersive sub-profiles, which are centred at a frequency in the vicinity of $\omega = \tilde{\Omega} = (2U/\Delta)^{1/2}v_0/v_s\Omega_s$. This frequency $\tilde{\Omega} = \Omega_{\tilde{x}}\Omega_s$ corresponds to the motion of electron, when almost periodic oscillations appear about the bottom of a single potential well. Note that the absorption is always positive and the minimum detectable absorption of the probe field can be also observed at the frequency, ω_1^u, of an unbounded trajectory for initial condition $\tilde{x}_0$=-$\pi/2$. To determine $\omega_1^u = \omega_1[\tilde{x}_0 = -\pi/2]$ we use the analytical expression (3.70) derived to estimate the frequency components of the electron trajectories within a pendulum approximation in the previous chapter. Increasing E_{Ω_s} above $3E_{cr}$, can generate dispersive gain profiles [red and green curves in Fig. 4.5(b)] that correspond to the saturation of drift velocity v_d which follows its rapid growth [green curve Fig. 4.3(a)]. It is important to note that in this case, the emergence of high-frequency gain can be associated with the nonlinear oscillations in the proximity of separatrix. In contrast, the inset of figure 4.5(b) shows that the dynamical conductivity remains positive under the action of a moderate ac pump $E_\Omega = 4E_{cr}$ and the dispersive profile of absorption arises near a frequency determined by the amplitude of pump field $\omega = eE_\Omega d/\hbar$. This picture reminds us of the one that we obtained for phononic pump, but in the case of smaller v_0. This suggests that absorption profile would converge asymptotically to the one for ac-driven SL for pump frequencies $\Omega_s\tau << 0.1$. Given that gain appears for pump field values essentially smaller than U_{cr1}, we further assume the validity of pendulum approximation (see Section 3.4). Remarkably, the frequency, $\omega_1^b = \omega_1[\tilde{x}_0 \to -\pi/2]$, of the nonlinear oscillations which correspond to localised trajectories, signifies the position of a resonant crossover from loss to gain. In particular, the appearance of dispersive gain profile at odd harmonics of ω_1^b is related to the anharmonicity of the ballistic oscillations. However, the signatures of ballistic motion in the response of miniband electrons to a weak ac field cannot be limited to confined electron motion [localised trajectories in Fig. 3.6(a)]. Moreover, we consider an ensemble of electron trajectories with different $\tilde{x}_0$, and thus the frequency of the nonlinear unbounded oscillations determine the position of a resonant crossover from loss to gain. These crossover conditions, $\omega = 3\omega_1^b$ (loss→gain) and $\omega = 2\omega_1^u$ (gain→loss), manifest the importance of higher harmonics nearby the separatrix [253]. In addition, the scattering events weaken the effects of phase space dynamics on dynamical conductivity, and therefore the amplitudes of pump field are optimally chosen to allow several cycles of oscillations $\omega_v\tau > 1$. Figure 4.6(b) illustrates the spectrum of $\tilde{x}_0$–averaged velocity of electrons, reflecting the frequency characteristics of the ballistic electron transport for E_{Ω_s}/E_{cr}=4. The broadband character of this spectrum is consistent with the picture which was obtained in Section 3.5 and it was associated with localised and unbounded trajectories contributing to carrier transport.

For $E_{\Omega_s} > 5.31E_{cr}$ ($\sim U_{cr2}$) and between the first two global bifurcations, the dynamical conductivity is always positive [magenta curve, Fig. 4.5(b)] and an amplification of probe field is not feasible. Here the emergence of meandering trajectories cause the dramatic reduction of absorption for lower frequencies. In this absorption profile, the frequency of Bloch-like oscillations corresponds to phonon-mediated Bloch oscillations. This high-frequency response of SL to supersonic excitation is associated with an electron absorbing an phonon that results in $\tilde{p}$–oscillations exceeding the size of the first Brillouin zone. The abrupt transition from the gain to loss coincides with the regularisation of time-dependent x_0–averaged velocity of electrons as noted in the previous chapter. Interestingly, an additional bifurcation will implicate negative dynamical conductivity extended at low frequencies presented in figure 4.5(b) for $E_{\Omega_s} = 6E_{cr}$. In addition, the coexistence of two type of meandering trajectories introduce multiple peaks even for the low frequency components revealing strong anharmonicity.

Having performed the previous calculations, let us be even more realistic by considering the targeted frequency of the probe field that allows the suppression of the skin effect in a SL. The dynamical conductivity at low frequencies $\omega\tau << 1$ and for small values of pump field is dominated by free carrier absorption $\mathrm{R}[\sigma^{\mathrm{free}}(\omega)]$.

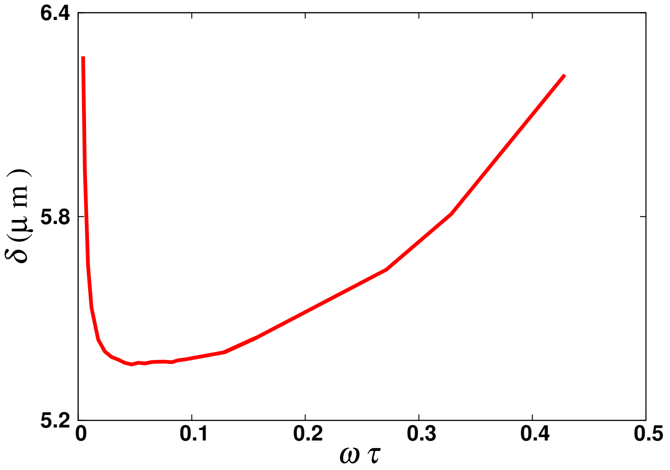

Figure 4.7: Penetration depth of the incident probe field related to its frequency ω for acoustic pump frequency $\Omega_s\tau = 0.1$ and pump amplitude $E_{\Omega_s}/E_{cr} = 5$. The superlattice parameters used correspond with the SL structure (II, table 4.1).

In this limit the dispersion relationship that describes the skin depth becomes

$$\delta = \sqrt{\frac{2}{\mu_0\sigma_0\omega}}. \tag{4.23}$$

Here μ_0 is the permeability of free space. The value of skin depth can be used to estimate the cut-off frequency for a superlattice device with superlattice mesa structure of diameter D_{SL}. Making the substitution $\delta = D_{SL}$ in equation (4.23) and rearranging we find that

$$\omega_{co} = \frac{2}{\mu_0\sigma_0 D_{SL}^2}. \tag{4.24}$$

In the case of a superlattice mesa of circular shape, having a diameter $D_{SL} = 4\,\mu\text{m}$, and in order to avoid the skin effect, the frequency of the probe field should be $\omega\tau < \omega_{co}\tau \approx 0.32$ which is not within the frequency range that we have assumed for the expression (4.23) to be valid. Since there is not a limit in the frequency ω to be considered, the penetration depth, showing how deep the electric probe field can penetrate the material, is estimated by equation (4.5). Figure 4.7 demonstrates how penetration depth varies with increasing ω. This dependence was calculated using equations (4.4), (4.5), for an acoustic pump field of the amplitude E_{Ω_s}/E_{cr} =5, the same pump frequency $\Omega_S\tau = 0.1$ and the parameters used to produce the absorption profiles in figure 4.5. It turns out that corresponding to low frequencies ($\omega\tau << 0.1$) the penetration depth displays a rapid decrease,

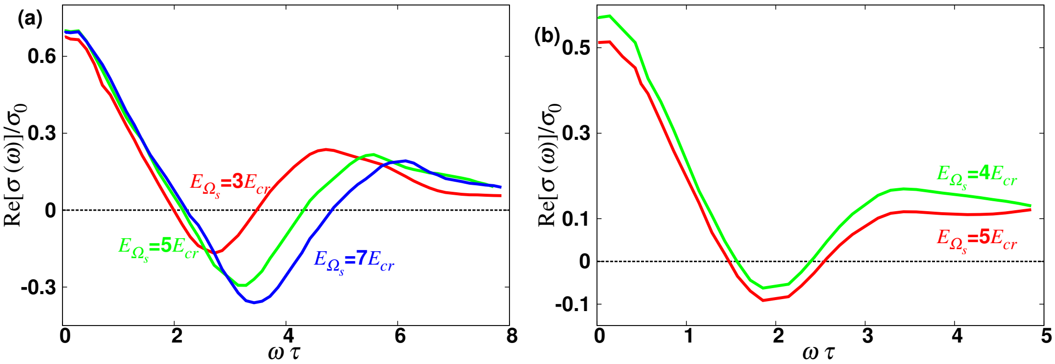

Figure 4.8: (a) Gain profiles in the presence of pump field with magnitude E_{Ω_s}/E_{cr}=: 3, 5, 7 and frequency $\Omega_s\tau = 0.1$. (b) Gain profiles in the presence of pump field with magnitude E_{Ω_s}/E_{cr}=: 4, 5 and frequency $\Omega_s\tau = 0.05$. $\sigma(\omega)$ is scaled by the $\sigma_0 = 7.5607$ $(\Omega \text{ cm})^{-1}$ for the parameters of the SL structure (IV, table 4.1).

while it remains approximately constant until frequency exceeds Ω_s. Note that, the penetration depth at any frequency range, is always larger than D_{SL} for the given SL structure, implying that the specific parameters are suitable for the efficient detection of weak sub-THz signals. Our results distinctly indicate the influence of maximal miniband velocity on gain profiles corresponding to high-frequency response of SLs to supersonic excitations ($v_0 >> v_s$). Further increase of v_0 results in more effective trapping of electrons by the propagating potential and an enhanced frequency response. This can be described using the parameters of SL structure IV (see table 4.1). Figure 4.8(a) demonstrates the gain profiles for different field strengths having the desirable shape Re[$\sigma(\omega)$] >0. In contrast to the results displayed in figure 4.5, small signal gain is even obtained when $E_{\Omega_s} < 3E_{cr}$. By numerically solving the dissipative dynamics using equations (4.16) and (4.17), the maximum gain observed is increased by almost three times while a strong enough pump field can provide the conditions for a stable gain profile [blue curve, Fig. 4.8(a)]. This can be seen as an inherent characteristic due to the strong confinement of electrons within the potential, inducing localisation in momentum space. The realisation of Bloch-like oscillations and the suppression of absorption at very low frequencies can be determined again by the behaviour of v_d characteristic [Fig. 4.3(a)]. Increasing the pump strength above the critical value 11.6 E_{cr} ($\sim U_{cr1}$), leads to a rapid drop of drift velocity [magenta curve, Fig. 4.3(a)] and a drastic change in the phase space dynamics. However, the corresponding value of the wave amplitude that evokes the birth of the meandering trajectories is $U_{cr1} \approx$72.03 meV, which is far beyond the realistic limit determined by the maximum strain (see Section

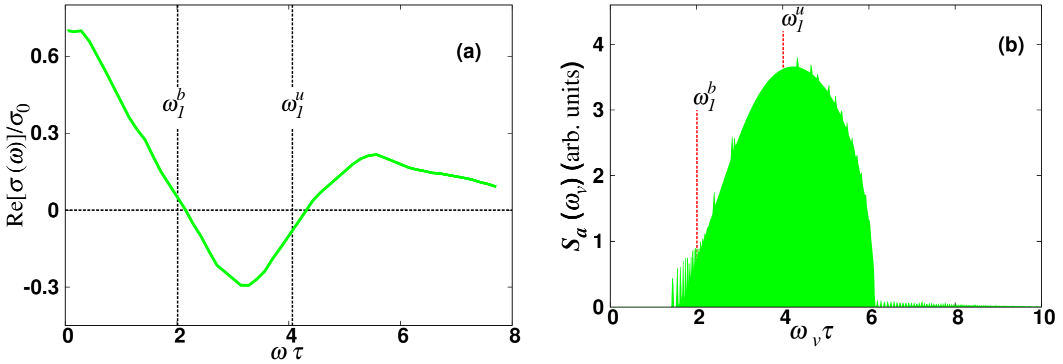

Figure 4.9: (a) Gain profiles calculated for $\Omega_s\tau = 0.1$ and pump strength E_{Ω_s}/E_{cr}=5. (b) Fourier spectrum $S_a(\omega_v)$ for a typical time-realisation of $v_a(t)$ corresponding to ballistic motion, calculated using the same E_{Ω_s} as (a). The vertical lines correspond to the harmonics of nonlinear oscillations, where ω_1^b, ω_1^u are the frequencies associated with localised and unbounded motion respectively. $\sigma(\omega)$ is scaled by the $\sigma_0 = 7.5607$ $(\Omega\ \mathrm{cm})^{-1}$ for the parameters of the SL structure (IV, table 4.1).

3.1.1). Despite the increase of v_0/v_s, our results confirm the picture that THz gain profile appears due to nonlinear localised oscillations induced by the acoustic wave. This characteristic shape of gain profile has also been depicted in figure 4.9. Here the frequency of the nonlinear localised oscillations ω_1^b, determines the resonant frequency of the crossover from absorption to gain, whereas the complementary unbounded oscillations with frequency ω_1^u can reveal when the real part of dynamical conductivity becomes again non-negative with the increase of ω. We see that a large THz gain can be obtained at frequencies $\omega\tau > 2$, if the frequency of nonlinear oscillations is to a moderate extent larger than the scattering rate $\omega_1^b\tau > 1$. The Fourier spectrum $S_\alpha(\omega)$ [see Fig. 4.9(b)] that examines the frequency characteristics of the ballistic electron transport, retains the spectral broadness associated with the localised trajectories for these parameters and strength of pump field $E_{\Omega_s} = 5E_{cr}$. Nevertheless, the beginning of the spectral continuum almost coincides with the first harmonic of nonlinear localised oscillations, while $S_\alpha(\omega_v)$ is centred in the vicinity of the first harmonic of unbounded oscillations. The latter suggests that the additional harmonics of nonlinear oscillations play significant role in dissipative dynamics and, therefore, in shaping of gain profiles only if $\omega_1^b\tau < 1$.

Figure 4.8(b) demonstrates the gain profiles for the same key ratio v_0/v_s but for acoustic wave frequency $\Omega_s\tau$=0.05. Comparing these profiles with the ones previously obtained for higher pump frequency [see Fig. 4.5(a) and Fig. 4.8(a)], it is possible to observe similar behaviour in dynamical conductivity. Re[$\sigma(\omega)$] is

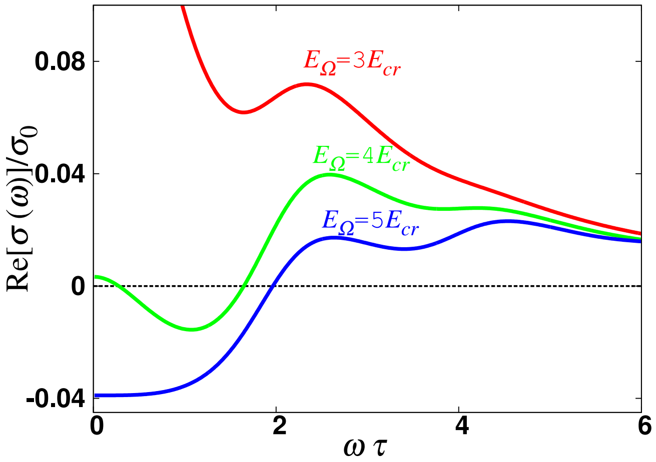

Figure 4.10: Absorption and gain profiles for ac pump frequency $\Omega\tau = 2$ and different pump amplitudes $E_{\Omega_s}/E_{cr} =: 3, 4, 5$. $\sigma(\omega)$ is scaled by the $\sigma_0 = 7.964$ (Ω cm)$^{-1}$ for the parameters of the SL structure (II, table 4.1).

positive at low frequencies whereas close to the frequency of nonlinear unbounded oscillations $\omega = \omega_1^u$; it has the usual shape of the dispersive Bloch gain. In addition, the acoustically driven SL provides a reduced magnitude of small-signal gain for the same values of the pump field used to produce the profiles in figure 4.8(a). On the other hand, since the frequencies of nonlinear localised oscillations close to the separatrix $\omega_1^b\tau \gtrsim 1$, the resonant crossover from loss to gain occurs at lower frequencies. More significantly, the acoustic pump itself can be quasistatic $\Omega_s\tau <$ 0.1. Since the scattering rate in this SL structure has been considered $\tau \approx$100 fs, the $\Omega_s\tau$=0.05 corresponds to the frequency $\Omega_s/2\pi \approx$0.8 THz.

Bloch gain in superlattice driven by THz acoustic wave

As already mentioned in the previous sections, the small-signal dispersive gain profile is obtainable for ac-driven SL in the absence of dc bias. The feasibility of such a Bloch gain that is acquired in PDC state, is strongly depended on the frequency of the ac pump field. Therefore, at sub-terahertz frequencies, the Bloch gain may arise, but the main problem here is the destructive low frequency electric instability. Figure 4.10 demonstrates how the absorption profiles change with the variation of the ac pump field amplitude, E_Ω, assuming that the frequency Ω belongs to the terahertz frequency domain ($\Omega\tau = 2$). The dynamical conductiv-

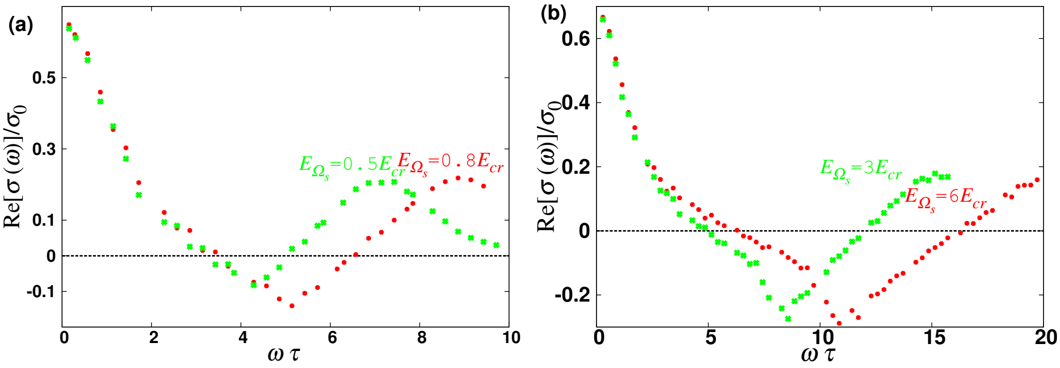

Figure 4.11: (a) Gain as a function of the probe frequency ω under the influence of high-frequency pump field $\Omega_s\tau = 2$ for fixed E_{Ω_s}/E_{cr}=0.5,0.8. (b) Gain dependence on small-signal probe frequency ω in the presence of pump field for fixed E_{Ω_s}/E_{cr}=3, 6 and $\Omega_s\tau = 2$. $\sigma(\omega)$ is scaled by the $\sigma_0 = 7.964$ $(\Omega\ \mathrm{cm})^{-1}$ for the parameters of the SL structure (II, table 4.1).

ity as a function of frequency ω in this case has been calculated using equation (4.10). Given moderate pump amplitude $E_\Omega = 3E_{cr}$ the absorption profile does not resemble the typical free-carrier absorption, but rather looks like a modified dispersion profile with a additional structure in the proximity of the pump field frequency $\omega = \Omega$. Stable high-frequency gain can be obtained with increase of pump strength $E_\Omega = 4E_{cr}$ for frequencies lower than the pump frequency. In particular, the gain resonance is associated with the behaviour of high-frequency dynamical conductivity at $\omega\tau = \Omega - 1$ (Fig. 4.10, green curve). On the other hand, the low frequency dynamical conductivity becomes negative with further increase of the pump field strength $E_\Omega = 5E_{cr}$ giving rise to electric instability. One of the interesting features of the ac-driven superlattice is the tunability of small-signal gain profile by using different frequencies Ω of pump field, which contradicts to the usual way of obtaining the Bloch gain in a superlattice excited by dc bias. The electric stability might be actually enhanced for larger ac pump frequencies and at the same time a notable THz gain can be obtained. The explanation of the formation of dispersive gain profile arises from the geometric interpretation VI characteristic for an operation point at PDC region incorporating the Tucker formulas.

Let us now reconsider an acoustic phononic pump and how it affects the shapes of the gain profiles and the magnitude of THz gain in SLs. Here, though, the frequencies Ω_s and ω are incommensurate, but both belong to the terahertz frequency domain. Figures 4.11(a), (b) show the the gain profiles, calculated using equations (4.2), (4.3) for different values of E_{Ω_s} and frequency $\Omega_s\tau = 2$ for an acoustically pumped SL. Furthermore, we have a dispersive gain profiles demonstrating the desirable characteristics of the dynamical conductivity being positive at $\omega\tau << 1$ and $\mathrm{R}[\sigma(\omega)] < 0$ for higher frequencies. The peculiarity of using a THz acousto-electric field as pump is that even a relatively weak pump strength E_{Ω_s}/E_{cr}=0.5 can provide small-signal gain [see Fig. 4.11(a)]. With further increase of pump field, the gain profiles become more pronounced [see Fig. 4.11(b)] and achieves significant values $\mathrm{R}[\sigma(\omega)]/\sigma_0 \approx -0.25$.

Our results show that we obtain a different situation in regard to appearance of gain profile at frequencies, which are not related directly to the nonlinear localised oscillations, as it is seen for a sub-THz pump field. In fact the linear response corresponding to frequency $\tilde{\Omega} = \Omega_{\tilde{x}}\Omega_s$ can be used to estimate the position of a resonant crossover from loss to gain. In this case, the scattering events do not significantly limit the length of the different trajectories contributing to the drift velocity. Therefore, even the oscillations with frequencies that belong to the far-end of the broadband spectrum play a significant role in the formation of the gain profile. Note, however, the wider frequency range that gain is demonstrated with the growth of pump strength [Figs. 4.11(a) and (b)]. The latter effect is associated with the enhanced role of nonlinear electron oscillations since with increase of the pump strength the islands of the localised trajectories increase as well [see figures 3.6(a), (b)]. Moreover, as E_{Ω_s} grows, the separatrix approaches the saddle point that is found at the end of Brillouin zone [see figures 3.7(a), (b)], thus allowing the electrons to visit the upper part of miniband, where their effective masses are negative. In spite of the fact that the response of SL to the ac probe fields relates to far more complicated nonlinear electron dynamics, the phase space dynamics is becoming of increased importance in the origin of the notable THz gain. The impact of the related electron trajectories on electron transport is enhanced, especially, if we consider the substantial weakening of scattering influence at higher frequencies of acoustic pump field. Importantly, additional harmonics that come to into play, producing parametric effects reflecting possibly the coherent amplification of half-harmonics [228, 254]. This is highlighted by the points that describe the dynamical conductivity in figure 4.11 in comparison with smooth curves demonstrating the absorption as a function of probe frequency (see Fig. 4.4).

Conclusively, the gain dispersive profiles for an acoustically pumped SL are tunable by changing the pump field strength which prompts a dependence similar to the mechanism of Bloch gain in dc biased SL. The latter scheme though enfolds the destructive electric instabilities for low frequencies of the probe field. In addition, it easy to notice that the maximum values of gain are considerably larger than the ones achieved for ac pump field (see Fig. 4.10) at the same pump frequency.

Summary

In conclusion, we have theoretically shown that THz gain is feasible for acoustically pumped SL. In the quasistatic picture, the gain appears with the change of the direction of the electron motion whereas in the vicinity of gain extrema, events of spontaneous phonon emissions take place. The dependence of the gain on the miniband electron-transport characteristics was shown by comparing dependences $v_d(E_s/E_{cr})$ and $\mathrm{R}[\sigma(\omega)]$. Depending on the particular value of v_0, the structural rebuilding of the phase space induces different changes in the drift velocity characteristics. For higher values of maximal miniband velocity, the behaviour of $v_d(E_s)$ converges to the one of averaged velocity $v_m(E_s)$. We also described how the ballistic dynamics directly affect the shapes of the gain profiles, with a crossover from loss to THz gain at the frequencies of nonlinear localised oscillations. The latter indicates the importance of the motion near the separatrix similar to cyclotron gain [45, 247]. The transition from supersonic to hypersonic electron velocities can additionally modify the dispersive profiles and tune the magnitude of THz gain. The broadness of spectrum that characterise the oscillations of the averaged electron velocity, can be tuned by the features of the SL structure. For the realistic parameters of the SL structure IV [table 4.1] and using the value α_0 at low temperature, the magnitudes of gain reaching values above $\alpha = 2324$ cm^{-1} [see Fig. 4.8(a)]. The smooth temperature dependence results in significant gain, $\alpha = 1180$ cm^{-1} at room temperature. For a high-frequency (THz) acoustic wave, the undesirable low-frequency instabilities can again be suppressed for nominal values of pump field strength, while an enhanced broadband terahertz gain persists at frequencies incommensurate with the pump frequency. The transition from loss to gain in the last case, however, does not depend on the initial position, x_0, of electron but is associated with the frequency $\tilde{\Omega}$. This frequency can be directly controlled by the variation of U. Finally, we have identified, the important role of the frequency of acoustic wave in the realisation of the acoustically driven Bloch gain. In the following chapter we consider the effects of a stationary plane wave on miniband electron transport, and the tunability of the gain of electric probe field.

Chapter 5

Influence of a slow acoustic wave

For a slow potential wave, when $v_0 >> v_s$, the Hamiltonian (3.23) describing the nonlinear dynamics in the moving frame of the wave, can be rewritten in the form

$$H = -\alpha \text{cos} \tilde{p} - \beta \text{sin} \tilde{x}. \tag{5.1}$$

Here $\beta = \alpha \, 2U/\Delta$ and $\alpha = v_0/v_s$, where the maximum miniband velocity is scaled with v_s to provide a unitless constant complied with the previous model. The equation (5.1) naturally appear in many problems as a simplified two-wave Hamiltonian [256–258]. In particular, the related dynamics is investigated in the context of a tight-binding electron in the Hall configuration known as the classical Harper model [259], and for representing non-interacting cold atoms in the driven one-dimensional optical lattice [260]. Furthermore, experimental realisation of the Harper model has occurred for a metal-insulator transition at the critical value $\alpha = \beta$ [261].

In this chapter we consider the electron dynamics in SL in the presence a potential wave that is uniform in time, and thus can be defined by the following equation

$$V_z = -\beta \text{sin} \tilde{x} \tag{5.2}$$

We are especially interested in charge transport and how the related dynamical regimes affect absorption and gain as a response to a weak ac field. From the view point of the critical limit $\alpha = \beta$, we contemplate separately the implications emerging for semiclassical motion. The parameters (see II, table 4.1 in Chapter 4) in this model correspond with the physical structure of superlattice in reference [220].

Generalisation of Zaslavsky Hamiltonian

The critical value $\alpha = \beta$ corresponds to the situation, where the maximal value of kinetic energy $K = -\alpha\text{cos}\tilde{p}$ is equal to the potential barrier $V_z = -\beta\text{sin}\tilde{x}$. The spatial structures arising from this symmetrical potential have been extensively discussed by GM Zaslavksky to describe Hamiltonian dynamics of a particle moving in a periodic two-dimensional potential [115, 256, 262]. In this case, the symmetrical (egg-crate) structure [see figure 5.1(b)] makes the dynamics of the particle nonlinear. Intuitively, one might assume that motion in a analytic two-dimensional periodic potential should be simple. However, even in the integrable case of (5.1) for $\alpha = \beta$, a potential perturbation can induce chaotic dynamics and potentially delocalised particle motion [263, 264]. In Chapter 3, we identified that the variation of wave amplitude U results in different types of trajectories. Therefore, it seems natural to consider the variation of parameters α, β directly in the Hamiltonian (5.1). This could possibly affect the way that electron ballistically propagates along $\tilde{x}$–direction or the conditions for excitation of the Bloch oscillations in momentum space. Let us consider again a set of variables $\tilde{y} = \tilde{x} - \pi/2$, $\tilde{p}$ similar with the one introduced in the case of pendulum approximation (see section 3.4) and retrieve the corresponding equations of motion:

$$\frac{d\tilde{y}}{d\tilde{t}} = \alpha sin\tilde{p}, \tag{5.3}$$

$$\frac{d\tilde{p}}{d\tilde{t}} = -\beta\sin\tilde{y}. \tag{5.4}$$

It follows that the above system of equations can be expressed in a form of a second order differential equation

$$\ddot{\tilde{y}} + \beta^2\left(\tilde{H}\text{sin}\tilde{y} - \frac{1}{2}\text{sin}2\tilde{y}\right) = 0, \tag{5.5}$$

where $\tilde{H} = -H/\beta$ is a dimensionless constant of motion. Thus, the electron trajectories for $\beta << 1$ can be described by $\ddot{\tilde{y}} + \beta H\text{sin}\tilde{y} = 0$. The latter equation corresponds to the pendulum approximation and is a reduced form of equation (5.5). For $\beta \leq \alpha$ which designates that the maximum value of kinetic part is smaller or equal than potential barrier, a simple stability analysis yields a countable set of the equilibrium points. This set contains the elliptic fixed (centres) points described by

$$\mid \tilde{H} \mid= \frac{\alpha}{\beta} + 1; \;\; \tilde{p} = n\pi; \;\; \tilde{y} = m\pi; \;\; m + n = 2k; \;\; k = 0, \pm1, \pm2.. \tag{5.6}$$

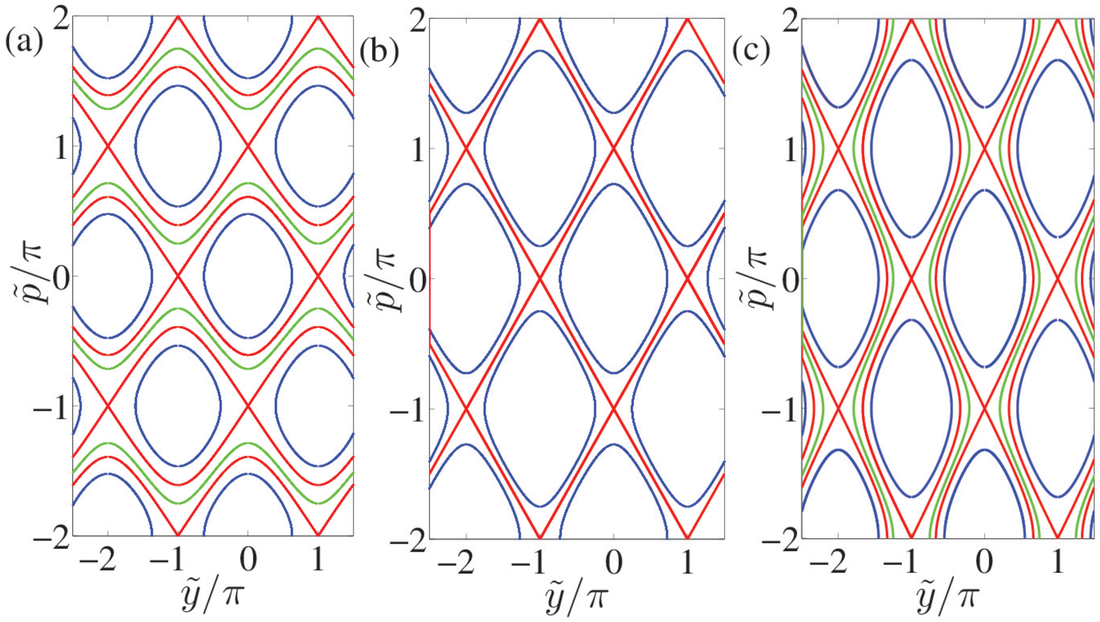

Figure 5.1: Phase trajectories of the dynamical system (5.3), (5.4) at (a) $U < \Delta/2$ ($\beta < \alpha$), (b) $U = \Delta/2$ ($\beta = \alpha$) and (c) $U > \Delta/2$ ($\beta > \alpha$). The localised orbits correspond to blue dots. Red curves demonstrate the separatrices and green curves denote the rotational trajectories.

and hyperbolic fixed points (saddles) that characterise the unstable equilibria

$$\mid \tilde{H} \mid= \frac{\alpha}{\beta} - 1; \;\; \tilde{p} = n\pi; \;\; \tilde{y} = m\pi; \;\; m + n = 2k + 1; \;\; k = 0, \pm 1, \pm 2.., \tag{5.7}$$

where n and m are arbitrary integer numbers. The electron motion described by the dynamical system (5.3), (5.4) can be represented as a set of distinct regimes. These dynamical regimes depend on whether amplitude of the potential U is greater than, less than, or equal to the half of miniband width $\Delta/2$. To describe the electron trajectories that correspond to these different cases, we produced the phase portraits demonstrated in figure 5.1. The phase trajectories were calculated using equations (5.3), (5.4). For $U < \Delta/2$ ($\beta < \alpha$) [see Fig. 5.1(a)], the phase portrait of the system is represented by periodic "islands" of localised trajectories (blue orbits). These localised trajectories are associated with the motion of electrons confined within the potential wells. In the same dynamical regime, unbounded trajectories [green trajectories Fig. 5.1(a)] do exist which describe the ballistic propagation of electron across x–space. Thus, the "islands" of localised trajectories

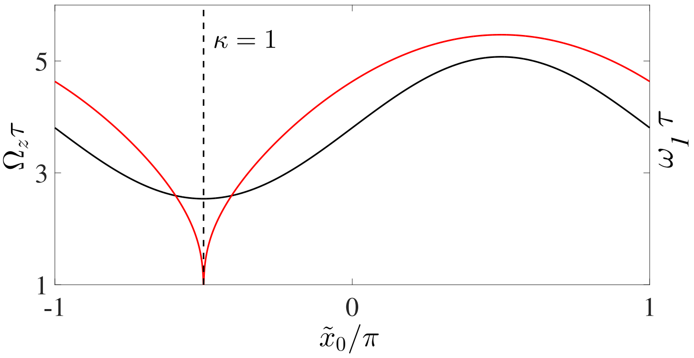

Figure 5.2: Frequency of the nonlinear oscillations as a function of initial position of the particle. The black curve shows the frequency Ω_z versus initial position $\tilde{x}_0$ [Eq. (5.10)]. The red line exposes the latter dependence, $\omega_1(\tilde{x}_0)$, within the pendulum approximation [Eq. (3.70)] calculated for $\alpha = \beta$. The dashed line reveals the point that corresponds to oscillations in the vicinity of unstable equilibrium.

are intermitted by areas of unbounded trajectories. The heteroclinic structure (red curves) segregates those two different regions of motion. The topology of the phase space in figure 5.1(b) suggests that the unbounded trajectories for $U = \Delta/2$ ($\alpha = \beta$) are eliminated completely. Such restructuring of phase space indicates that the electron cannot propagate across multiple potential wells. The localised trajectories [blue curves Fig. 5.1(b)] can be found for the limited case $U = \Delta/2$ ($\alpha = \beta$) by integrating equation (5.5). Thus, for $\mid \tilde{H} \mid \leq 2$ we can acquire

$$\cos\tilde{p} = \frac{1}{2}\tilde{H} + \left(1 - \frac{1}{2}\tilde{H}\right)\ \mathrm{cd}\left[\left(1 + \frac{1}{2}\tilde{H}\right)\beta t, \kappa\right] \tag{5.8}$$

$$cos\tilde{y} = \frac{1}{2}\tilde{H} - \left(1 - \frac{1}{2}\tilde{H}\right)\ \mathrm{cd}\left[\left(1 + \frac{1}{2}\tilde{H}\right)\beta t, \kappa\right] \tag{5.9}$$

Here $\kappa = (2-\tilde{H})/(2+\tilde{H})$ and $\mathrm{cd}(.)$ is the elliptic Jacobian function [124, 265]. The frequency of nonlinear oscillations in the latter case can be represented as [115]

$$\Omega_z = \frac{\pi\beta\left(1 + \dfrac{\tilde{H}}{2}\right)}{4K(\kappa)}, \tag{5.10}$$

where $K(.)$ is the complete elliptic integral of the first kind as a function of elliptic modulus κ (see Section 3.4). Figure 5.2 demonstrates the effect of initial position on the frequency of the localised oscillations. Now it follows from equation (5.10), that in the limit $\tilde{H} \to 2$ the electron trajectories are eventually confined to a small region near the bottom of potential well, experiencing small oscillations of frequency $\Omega_z = \beta$. By adding the solutions (5.8), (5.9) and then integrating, one can find a phase trajectory, starting from the initial conditions $(\tilde{y}_0, \tilde{p}_0)$, as a function $\tilde{p}(\tilde{y})$. Thus, the separatrix [red curves, Fig. 5.1(b)] meeting the hyperbolic fixed points along the phase portrait can be described by the following equation

$$\tilde{p} = \pm(\tilde{y} + \pi) + 2\pi k \;\; (k = 0, \pm 1, \pm 2). \tag{5.11}$$

The existence of this infinite web [red curves, Fig. 5.1(b)] has some implications for the electron transport. In particular, considering the effect of a perturbation on the whole pattern of the phase space, would result in the formation of a stochastic web. Hence, if the initial position, $\tilde{x}_0$, of the particle corresponds to the used web, the related phase trajectories will undertake a random walk along the web's network [115]. Our model allows to implement the perturbation via weak probe field, which agitates the phase dynamics and could result in the formation of a stochastic web as result of the destruction of separatrix. The generation of a stochastic web permits the electron to undergo rapid diffusion similarly as in the periodic potential of superlattice with an applied DC-voltage and tilted magnetic field [113]. This type of global diffusion can be produced also by a linear oscillator perturbed by periodic δ–function which represents the gyration of a charged particle in a magnetic field crossed with a plane wave [115, 266].

The study of electron transport reveals that the localised trajectories [blue curves in Fig. 5.1(c)] survive even if U exceeds the critical value ($\beta = \alpha$) which corresponds to the generation of periodic web across the phase space [see Fig. 5.1(b)]. The robustness of localised dynamics is a result of separatrix reconnection that leads to the formation of heteroclinic cycles [red curves in Fig. 5.1(b)] joining equilibrium points that can only be found at the same $\tilde{p}$-coordinate. In addition, this simple analysis of the separatrix structure with respect to the Brillouin zone boundaries provides a single critical value $U_{cr} = \Delta/2$ for triggering nonlinear Bloch oscillations. Hence, the behaviour of the system exposes a transition from localised phase trajectories in momentum space to confined motion in coordinate space since the particle cannot escape from the potential well. A closer look at the amplitude of $\tilde{p}$-oscillations [green curves in Fig. 5.1(c)], when U exceeds U_{cr} shows that the particles can reach the border of the Brillouin zone, and they can be effectively Bragg reflected. Remarkably, instead of different type of meandering trajectories [cf. Fig. 3.10(c)] as seen for the system (3.27), (3.28) here we got only one type of electron orbits extended in the $\tilde{p}$–direction.

Dissipative electron dynamics and gain in slow wave potential

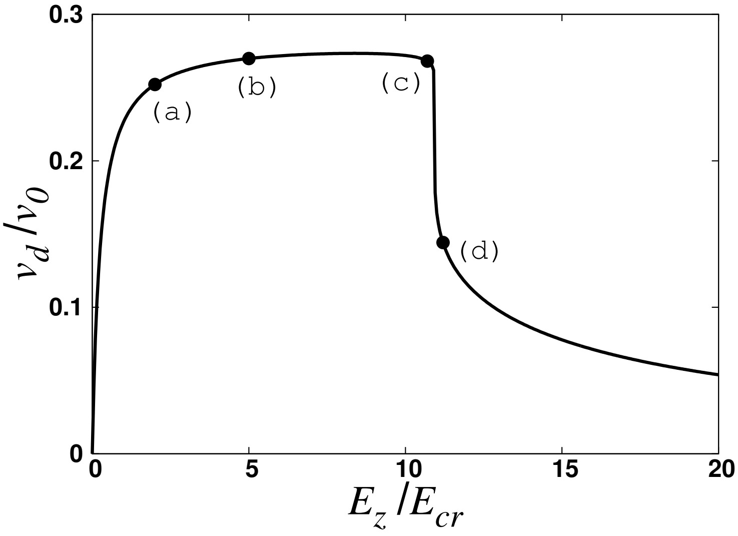

Figure 5.3: v_d dependence on E_s for miniband electrons driven by an acoustic wave in the limit $v_0 \gg v_s$. The labels (a)-(d) signify the positions on the characteristic of E_z values used to calculate the phase trajectories and absorption in Fig. 5.4 and Fig. 5.5 respectively. The acoustoelectric-drift velocity v_d is scaled by the maximum miniband velocity v_0 ≈27.3×10^4 m/s for the parameters of the SL structure (*II*, table 4.1) .

The system under study should satisfy a Hamiltonian which varies slowly not with the time, but with the coordinate. For this problem, we, for example, may consider a mechanism similar to one used for the deceleration of light pulses in optical dense crystals [267] or the periodically loaded waveguides, enabling the slow-wave propagation of microwave field [268]. However, fabrication of the superlattice with a higher miniband velocity, appears to be a more realistic solution, for producing a plane wave which demonstrates just x–dependence. Clearly, it would allow to neglect the term, -$v_s p$, that emerges in Hamiltonian (3.23) in the moving frame after the canonical transformation. Alternatively, a standing phonon wave can be created due coherent superposition of anti-propagating waves [58]. We now turn our attention to a superlattice under the action of a moving potential given in equation (5.2) and a time-dependent electric field $E_{pr}(t)$. The probe field $E_{pr} = E_\omega \cos\omega t$ is involved to examine the influence of the potential

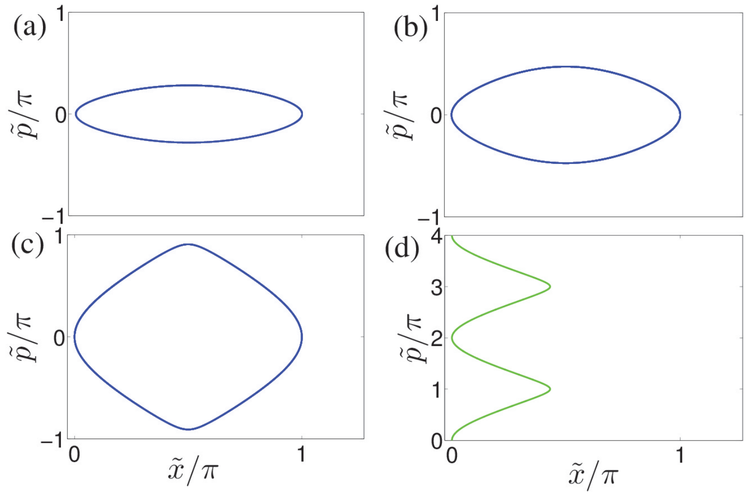

Figure 5.4: Different types of phase trajectories. Localised orbits for different values of pump amplitude E_z/E_{cr} =:2 (a), 5 (b) and 10.7 (c). Trajectory extended in $\tilde{p}$–space that corresponds to the non-linear Bloch oscillations for pump amplitude. E_z/E_{cr} =11.2 (d)

wave on the small signal absorption. This approach is essentially different than the one studied in the previous Chapter 3. The difference lies in the fact, that we consider a pump field of the form $E_z\cos(\tilde{x})$, for the present calculations. In this section, we simulate the electron trajectories starting at the centre of one from subsequent potential wells which corresponds to the condition $\tilde{x}(t_0) = \tilde{x}_0 = 0$. Changing the $\tilde{x}_0$ (see the following section) will have an effect not only on the ballistic dynamics but on the formation of different type of gain profiles as well. In addition, the drift velocity and the gain profiles were calculated again for electrons starting at the t_0 with $\tilde{p}_0 = 0$, which corresponds to the experimental conditions of the non-degenerate electron gas close to zero temperature $T_e \to 0$. The approach which is based on path-integral solution of the Boltzmann equation (see Eq. 2.59), is most efficient at low temperatures, because otherwise, we should additionally take into accound a thermal distribution of the electrons. Thus, the steady-state drift velocity (see Eq. 2.81) is determined by the ballistic trajectories starting at $\tilde{p}_0 = 0$. The velocity of electrons at the presence of scattering can be estimated by the simplified Chamber's path integration method (see Eq. 2.88). The latter approach is feasible, because in our approximation the effective electric field $E_z(x)$ that has emerged for $v_s \to 0$ is free from explicit time dependence. The curve in figure 5.3 shows the variation of drift velocity as an function of the amplitude of the pump field E_z. Comparing the $v_d(E_z)$ curve with the results discussed in section 3.2.1, we note that drift velocity still has a pronounced negative differential

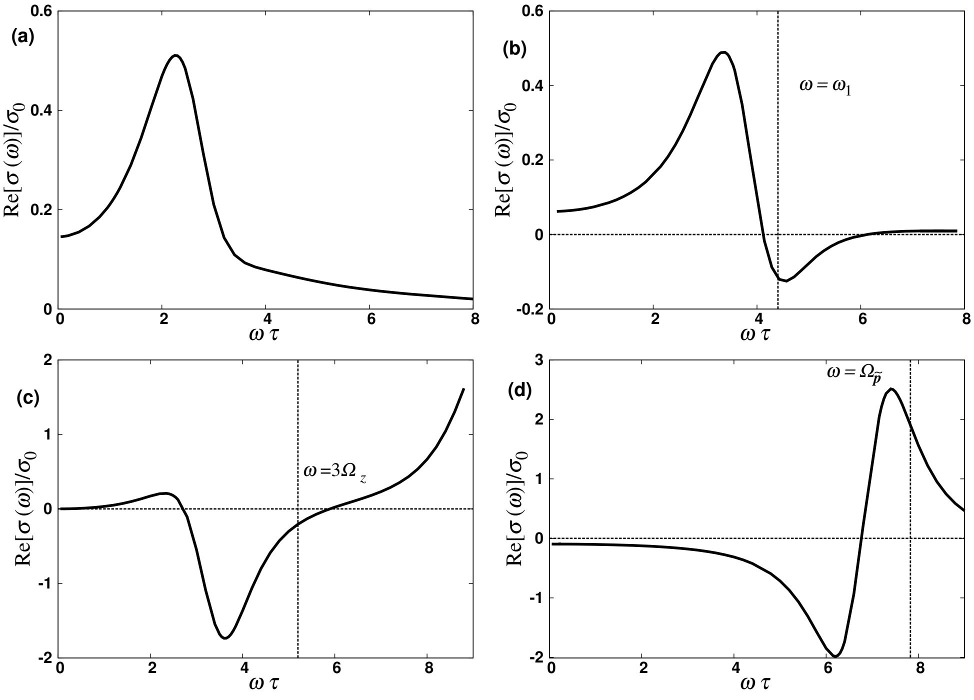

Figure 5.5: Absorption and gain profiles for $(\tilde{x}_0, \tilde{p}_0) = (0, 0)$ and values of E_z/E_{cr} =:2 (a), 5 (b), 10.7 (c) and 11.2 (d). $\sigma(\omega)$ is scaled by the $\sigma_0 = 7.964$ $(\Omega\ \mathrm{cm})^{-1}$ for the parameters of the SL structure (*II*, table 4.1).

velocity region. However, previously the abrupt suppression of electron transport in $v_d(U)$ (see Fig. 3.4) is associated with a global bifurcation. In the present model we consider a single ballistic trajectory starting from the same initial position x_0. Therefore, the influence of E_z on v_d should not attributed directly to the restructuring of phase space, but to the type of trajectories in the different dynamical regimes. In particular, the localised orbits [blue curves in figures 5.4(a)-(c)], for the same initial conditions, stretch in the momentum space as U increases. Figure 5.4(c) demonstrates a trajectory that approaches, but it does not reach the edge of the first Brillouin zone. This explains a rapid growth of v_d (see Fig. 5.3) followed by its saturation within the range of these values. With E_z increasing further, the electron trajectory [green curve in Fig. 5.4(d)] can be elongated in p–direction and thus to Bloch-oscillate. The different behaviour of electron transport in momentum space coincides with an abrupt drop of $v_d(E_z)$ dependence. Our results suggest then that the critical behaviour of drift velocity is related to the manifestation of Bloch oscillations. In a similar manner, the miniband transport under the influence of a weak probe field implies the drastic effect of transition between different types of ballistic motion. Specifically, distinct profiles of absorption and gain are produced for a set of values of E_z [see Fig. 5.5(a-d)]. These profiles were obtained by using equation (4.3). For a relatively weak pump field, the dissipationless dynamics can be represented by a pendulum driven by AC bias

$$\frac{d^2\tilde{x}}{dt^2} - \Omega_{\tilde{x}}^2 \mathrm{cos}\tilde{x} = -\gamma\omega^2 \mathrm{sin}\omega t, \tag{5.12}$$

where $\Omega_{\tilde{x}} = \dfrac{v_0}{v_s}\sqrt{\dfrac{2U}{\Delta}}$, and $\gamma = \dfrac{eE_\omega d}{\hbar\omega}$. Equation (5.12) is a valid approximation that follows from equation (5.5) for $\beta << 1$ and the substitution $\tilde{x} = \tilde{y} + \pi/2$. Hereafter, using equation (4.3), we acquire the distinguishing Lorentzian-like absorption profile [see Fig. 5.5(a)] which is centred at $\Omega_{\tilde{x}}/2 < \omega < \Omega_{\tilde{x}}$. The sub-harmonic resonance of the absorption is invoked since the system is driven strongly enough to induce the non-linear effects in pendulum oscillations [269]. The amplification of the probe field for this case is not feasible, which is highlighted by Re$[\sigma(\omega)]$ [see Fig. 5.5(a)] that remains positive with the increase of probe frequency ω. It is noticeable that the increase of E_z affects electron transport in a way, which leads to gain in high-frequency range [see Fig. 5.5(b)]. The emergence of gain can be attributed to nonlinear oscillations [see Fig. 5.5(b)] that represent the localised motion of electron. Here, large enough of E_z results in a growth of the maximal crystal momentum towards the brillouin zone boundary. The Brillouin zone boundary at $\tilde{p} = \pi$ coincides with the saddle points described by equation (5.7). The non-linearities become more dominant when the system trajectory draws closer to the saddle points separatrix. As mentioned in the previous chapter, the separatrix plays a significant role in the realisation of the gain, as one can deduce from analysis of figure 5.4(b). Given that the pendulum approximation is still reliable, the frequency of these localised oscillations, ω_1 (see Eq. 3.70), can point the transition between loss and gain for a small-signal. This particular gain profile [see Fig. 5.5(b)] is an inverse of the usual dispersive Bloch gain profile [see Fig. 4.1 (iii)-(iv), resonant frequency ω_B], in the sense that the maximum values of the absorption occur at frequencies smaller than the resonant frequency ω_1. In addition, the gain in Fig. 5.5(b) takes place at frequencies somewhat above the resonant frequency. On the other hand, approaching the critical value of E_z which determines the maximal value of v_d would have a direct effect on the gain [see Fig. 5.5(c)] by inverting the dispersion profile shown in figure 5.5(b). Since the necessity of the condition $\beta << 1$ for the pendulum approximation is obvious, now the electron dynamics are governed instead by equations (5.8), (5.9). Thus, the crossover frequency Ω_z in this case is appointed by equation (5.10). It can be observed that gain in this case is magnified and the reason of that lies in the highly nonlinear oscillations that closely approach the seperatrix. With $E_z/E_{cr} > 2\alpha$, electrons experience Bragg reflections [green curves in figures 5.1(c) and 5.6(d)] which contribute to low-frequency instability of gain [see Fig. 5.5(d)]. The vertical dashed line in Figure 5.6 (d) indicates the natural frequency, $\omega = \Omega_{\tilde{p}}$, of a harmonic oscillator in $\tilde{p}$-space, where, in the vicinity of which the maximum absorption is realised. In the Bloch-like regime, the electrons are prevented from unbounded motion, which makes the dynamical behaviour of the system concede to a pendulum approximation for $E_z/E_{cr} >> 2\alpha$ but in momentum space

$$\frac{d^2\tilde{p}}{dt^2} + \Omega_{\tilde{p}}^2 \sin\tilde{p} = -\gamma\omega^2 \sin\omega t. \tag{5.13}$$

Here $\Omega_{\tilde{p}} = \dfrac{v_0}{v_s}\sqrt{\dfrac{2U}{\Delta}}$. The previous analysis reveals that existence of two limits for the single particle dynamics described by the system (5.3), (5.3), namely one reduced to $\tilde{x}$–pendulum and one described by $\tilde{p}$–pendulum with $\alpha \gg \beta$ and $\beta \gg \alpha$ respectively. Inherently, the gain profile changes as we sweep from a extreme localisation within the first Brillouin zone to a strongly bounded state of single-electron in the potential wells.

Effect of initial phase on small signal-gain

The restructuring of the phase space can have multiple implications on the kinetic properties, and particularly on the THz dynamics of electrons. In the view that ballistic trajectories are strongly depended on the initial conditions, it is important to take into account the effect of initial phase of electron $\tilde{x}_0$ on the gain of terahertz radiation in SLs. Therefore, the consideration of the change of the initial position $\tilde{x}_0$, modifies accordingly the constant of the motion of the $\widetilde{H}$, and is given by

$$\frac{\alpha}{\beta}(1 - cos\tilde{p}) + sin\tilde{x} = sin\tilde{x}_0 \tag{5.14}$$

In the previous section, we illustrated that the drift velocity becomes dramatically suppressed at a value close to $E_z/E_{cr} = 10.9$ ($U = \Delta$) for $\tilde{x}_0$=0. Of course, this behaviour is vigorously linked to the condition for a trajectory to exhibit Bloch oscillations. The question that follows is whether it can be generalised for a phase shift in the range $-\pi < \tilde{x}_0 < \pi$. To deliver this objective, one has to substitute into equation (5.14) the coordinates of any saddle point and the corresponding initial phase. Indeed, the Bloch oscillations occur at the critical value of the acoustic wave amplitude U_{BO}, satisfying the following equation.

$$U_{BO} = \frac{\Delta}{1 - 2sin\tilde{x}_0} \tag{5.15}$$

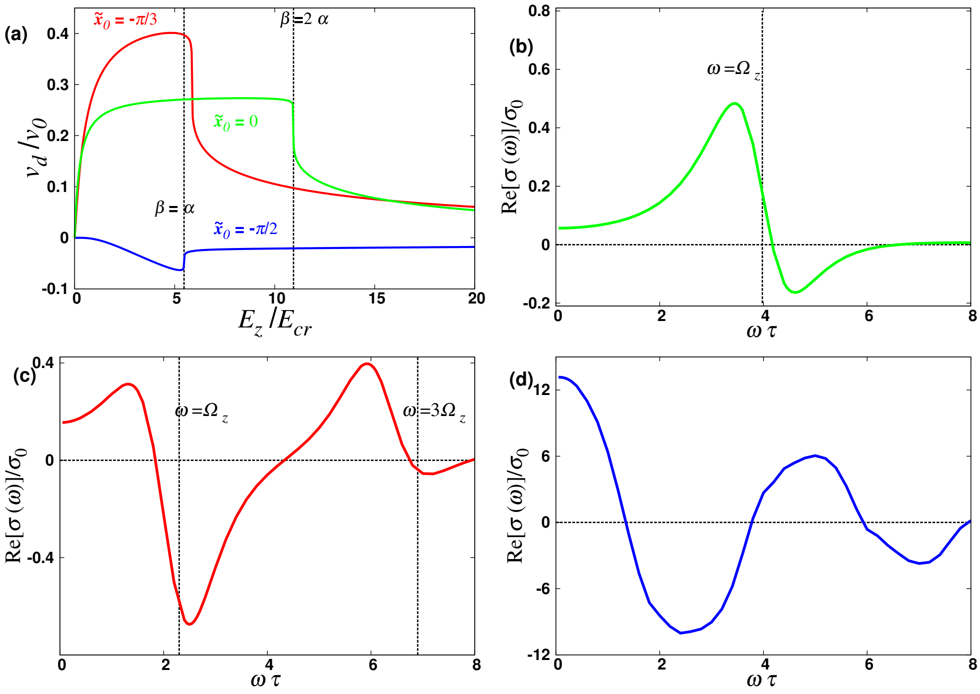

Figure 5.6: (a) Drift velocity versus effective field E_z characteristics.(b)-(d) Gain profiles for different values of initial positions $\tilde{x}_0$ =:0 (i),$-\pi/3$ (ii),$-\pi/2$ (iii). $\sigma(\omega)$ is scaled by the $\sigma_0 = 7.964$ $(\Omega \text{ cm})^{-1}$ for the parameters of the SL structure (II, table 4.1).

The critical difference between this formula and the one that describes the implications on miniband transport for a moving potential wave [see Eq.3.7], is that the latter is connected with specific instabilities responsible for the dramatical change in the topology of the phase space. Here we acknowledge that for $U = \Delta/2 + \epsilon$ (where $\epsilon \ll$) the islands of localised orbits, which are periodically spread around corresponding centres become larger with growth of U, allowing the $\tilde{p}$-oscillations eventually to reach the border of the first Brillouin zone.

Figure 5.6(a) illustrates how the dependence $v(E_z)$ changes with the variation of initial position $\tilde{x_0}$. In particular, we consider three values of $\tilde{x}_0$, scilicet, (i) $\tilde{x}_0$=0, (ii) $\tilde{x}_0$=$-\pi/3$ and (iii) $\tilde{x}_0$=$-\pi/2$. We are able to recognise that the common pattern of drift velocity characteristics is that they demonstrate non-monotonic behaviour. As it was expected, the locations of the prominent extrema coincide with $U = U_{BO}$. Now, the sudden change of the drift velocity can be generally connected with the existence of Bragg reflections. Noticeably, for $\tilde{x}_0 = -\pi/2$, v_d (blue curve) becomes increasingly negative as E_z/E_{cr} grows from 0 to 5. Entering the Bloch-like regime has an interesting consequence for the particle motion, since the drift velocity can perform a relative increase in comparison with the v_d minima.

The high-frequency gain response to the ac field appears to be linked to the same complicated nonlinear dynamics, with many respects predefined by the motion near the separatrix. To examine explicitly the involvement of phase in shaping the gain profiles, we hand-pick the special case of $E_z = 2Uv_0/(\Delta v_s)$, where $U = \Delta/2$, which is interesting from viewpoint of electron dynamics, since the $\mathrm{Re}[\sigma(\omega)]$ dependence indicates significant amplification of a range of $\tilde{x}_0$ as shown in figure 5.6[(b)-(d)]. It is evident that there is a variation of dispersive gain profile with simulating ballistic trajectories at different initial positions. In particular, the characteristic shape of gain profile for $\tilde{x}_0 = 0$ [see Fig. 5.6(b)] and $\tilde{x}_0 = -\pi/3$ [see Fig. 5.6(c)] appears to be an inverse of the usual dispersive Bloch gain profile [e.g. Fig. 4.1 (iii)-(iv)]. On the other hand, figure 5.6(d) demonstrates a Bloch-like gain profile. This difference arises because of the anharmonicity of ballistic oscillations when we are approaching the separatrix $\tilde{x}_0 = -\pi/2$. In addition, the electron oscillations near the separatrix cause a significant enhancement of the magnitude of the gain. For example, the maximal observed gain in figure 5.6(d) is boosted by more than a order of magnitude, in comparison with the one in figure 5.6(d). Similarly with the previous section, we can determine the crossover frequency Ω_z [see Fig. 5.6(b)-(c)] using equation (5.10). The predictions for zero absorption can be slightly detuned from the actual value due to dissipation effects. Hence, we choose optimally the size of effective electric field that it will enable electrons to perform several cycles of oscillations $\Omega_z\tau > 1$ before scattering occurs.

Summary

By exploring the response of dynamical model to a weak probe field $E_{pr}(t)$ in the presence of scattering, we realised that triggering different dynamical regimes significantly affect the conversion of energy electrons to high-frequency radiation. Our results show that localised oscillations are associated with a dynamical regime, where SL operates in conditions of PDC. It is known that PDC should be considered as one of the conditions for electric stability of the superlattice system [43]. Therefore, the stable gain profiles, which correspond to the localised trajectories in phase space, demonstrate desirable tunability of the magnitude of the gain. This can be achieved either by changing the initial position of the electron or the magnitude of the pump field. In contrast, as electrons perform Bloch-like oscillations, the problem of electric instability persists, in the same way as in the case of the usual Bloch gain in SLs. The preceding discussion raises the question, whether a static plane wave influences the small-signal absorption and gain in a similar fashion as in a SL under the action of an electric field and a tilted static magnetic field (for further discussion over this arrangement see Section 2.3.2). In the latter case, the mechanisms of the gain can be attributed to two different dynamical regimes [45, 247]. On the one hand, cyclotron gain which is associated with nonlinear cyclotron oscillations. On the other hand, a Bloch-like regime, where the Bloch-like oscillations provide THz gain. For a realistic SL parameters $\Delta = 60$ meV, $d = 6$ nm and $\tau = 200$ fs, we obtain the value of critical electric field $E_{cr} \approx 5.5$ kV/cm. Considering moderate doping $N = 10^{16}$ cm^{-3} and relative permittivity $\epsilon = 13$ (GaAs) at really low temperature, the gain α is divided [see Eq. 4.6] by the constant $a_0 = 831.5$ cm^{-1} to determine the scaled dynamical conductivity $\mathrm{Re}[\sigma(\omega)]/\sigma_0$. We found that when such SL pumped by a slow wave is tuned into regime when electron oscillates in the vicinity of the separatrix, α attains the colossal value of $\approx$ 8315 cm^{-1} [see Fig. 5.6(d)].

Conclusively, the Bloch-line oscillations produce dynamical conductivity exhibiting negative sign at low frequencies, whereas, the localised trajectories secure the problems arising from space-charge fluctuations. Thus, in case of a propagating potential wave of the form given in equation (3.7), the stability of the THz gain will be determined by a particular collective contribution of topologically different electron trajectories starting from a range of the initial conditions.

Chapter 6

Conclusions

This study was dedicated to the semiclassical dynamics of particles in periodic potentials induced by a propagating plane wave. In particular, we focused on the interaction between a coherent acoustic wave and miniband electrons in a semiconductor superlattice. We began with the investigation of Hamiltonian dynamics of electrons, which in our case of the propagating wave is strongly nonlinear. We calculated the acoustically induced electron current, which is connected with electron transitions between specific states within the energy miniband. Subsequently, we investigated the possibility to reach inversionless Bloch gain in an acoustically driven superlattice. By extending this approach, we also examined the influence of a slow acoustic wave on small-signal absorption and gain in the superlattice in the presence of scattering.

The first part of results (Chapter 3) highlights the effects of the acoustic wave on the nonlinear electron dynamics. Here the wave amplitude plays a role of control parameter determining abrupt transitions between different dynamical regimes. To understand fully the mechanisms which govern the miniband electron transport, we analysed the related phase portraits in the moving reference frame. We discovered that global bifurcations, triggering dramatic transformations of the system phase space, affect significantly the electron transport process. The drift velocity v_d and the averaged velocity v_m of the charge carriers were calculated by applying approaches based on the exact path-integral solutions of Boltzmann transport equation. Importantly, both velocity characteristics exhibit non-monotonic dependence with prominent maxima, followed by a sudden drop. We derived analytical conditions for the development of the dynamic instabilities and showed how these relate to the characteristic features of miniband electron transport. In particular, heteroclinic-homoclinic seperatrix topologies are observed for specific values of the wave amplitude U. By using nonlinear dynamics techniques we described and classified three distinct types of ballistic electron trajectories, generated by the propagating wave. These trajectories are associated with three different types of motion, namely: (i) motion of electrons confined by a moving potential (localised trajectories in the moving reference frame), (ii) unconfined electron motion (unbounded trajectories in the moving reference frame) and (iii) Bloch-like electron oscillations (meandering trajectories in the moving reference frame). Each type of the trajectory contributes differently to the electron transport which can change significantly with the variation of U. Thus, the enhancement or the suppression of different types of motion predetermine the electron drift and spectral properties of the transport regime realised in the system. Changes in the amplitude of the acoustic wave can generate oscillations of the averaged electron velocity, the spectrum of which exhibits broadband features or a well-pronounced peak. Herewith, the central frequency of the velocity spectrum was found to notably surpass the frequency of the sound wave ω_s and can be tuned favourably by the amplitude U.

In Chapter 4, we demonstrated the feasibility of a stable THz gain in a acoustically pumped SL. We examined the conditions, under which the energy of moving electrons is converted to a high-frequency radiation. Our analysis has shown that this acousto-electrical conversion is possible in the regime when the SL is stable against the formation of high field domains. In the case of a quasistatic acoustic pump, it was shown that the incoherent absorption is negative as long as the electrons attain a negative drift velocity. This finding strongly implies the underlying connection between nonlinear dynamics and the appearance of the high-frequency gain. Consequently, the crossover from the gain to loss approximately coincides with the emergence of meandering trajectories, in the same way as the sharp transitions between different dynamical regimes cause sudden change in averaged velocity of the carriers. For the same type of sub-THz acoustic pump wave, we also showed how an appropriate tuning of the wave parameters can lead to a particular profile of the dynamical conductivity: the low-frequency dynamical conductivity is positive, whereas the high-frequency dynamical conductivity is negative, providing a stable THz gain. The high-frequency gain is attributed to non-linear oscillations, which correspond to the localised trajectories in the moving reference frame. These electron trajectories in the vicinity of the separatrix were found to enhance the response of the miniband electrons to a weak ac field. On the other hand, after the first global bifurcation, a sufficient part of the electrons perform frequency-modulated Bloch oscillations. We found that the excitation of these strongly nonlinear oscillations result in the extension of the gain profile to the lower frequencies. Here the electric instability can appear in the long sample similar to the case of Bloch gain in dc biased SL. By using a high-frequency acoustic pump, we showed that the small-signal dispersive gain profile still exists. One of the interesting consequences of this scheme is that the gain-bandwidth demonstrates significant broadening.

In Chapter 5, it was shown that the nonlinear character of the dynamics of the miniband electrons in the presence of a slow acoustic wave, can provide the conditions for strong THz gain. We showed that the topological rearrangement of the phase space, which takes place for a single critical value U, allows the transition from the localised oscillations to the Bloch-like oscillations. In this respect, the problem of electric instability in the Bloch-like regime exists similarly as in the case of the usual Bloch gain in superlattices. In contrast, before the global bifurcation the superlattice is in a electrically stable state due to the sole contribution of nonlinear localised trajectories.

Outlook

Our study of nonlinear electron dynamics in a miniband SL driven by a plane wave not only provides new perspectives to obtain an in-depth understanding of acoustoelectronic phenomena in SL, but also raises many intriguing possibilities for further research. It was shown that the increase of the electron and lattice temperatures, has strong influence on charge transport in the superlattice [195, 270]. This effectively alters the shape of current-voltage characteristics and the collective behaviour of electrons in SL [195]. Therefore, by taking into account a thermal distribution of the electrons, it would be interesting to study the way that temperature affects the measured kinetic properties of the acoustically induced electron transport. In this case, it would be critical to get a deeper insight into the influence of temperature on the specific bifurcations which are developed with the variation of the wave amplitude. In addition, from the perspective of possible applications, it would be intriguing to investigate the temperature dependence of the gain profile, when electron heating effects become important.

The non-linear dynamics in a miniband SL driven by a plane wave in the presence of a constant electric field have been studied in [271]. That work, however, focused primarily on the case of a very high-frequency wave. Thus, it would be interesting to consider the propagation of a low-frequency acoustic pulse through a superlattice within the negative differential conductivity regime. Possible modifications of the voltage-current characteristic could be explained with further recourse in the phase space dynamics.

There has been some work focused on how the acoustic wave can affect the collective behaviour of electrons, inducing self-sustained current oscillations in SSLs [47]. Here, we could utilise the exact path integral solutions of the transport equations to determine the global current density and extend the previous studies which were developed, based on a quasi-static approximation.

The Hamiltonian in our model bears strong resemblance to the one that entails the cold atoms dynamics in the optical lattices [272, 273]. On this basis, the discussed results in this thesis have a potential in applications involving cold atom manipulations within the emerging field of atomtronics [274, 275]. In particular, it is possible to consider the approach taken in Section 3.3.6, assuming that the maximal velocity of the cold atom is comparable or smaller than the velocity of the moving optical lattice. Therefore, the analysis undertaken to explain the ballistic dynamics of electrons can be used to determine the conditions for effective trapping of cold atoms by the moving optical lattice. On the other hand, it was shown that a directed current of ultracold fermionic atoms under static forcing can be generated by collisional interaction with bosons [276, 277]. In this case, the ultracold fermions in one-dimensional optical lattice demonstrate similar dissipative dynamics as the electrons in SLs. Given an fermionic transport model described by semi-classical Boltzmann approach [278], there is a possibility to calculate induced gain phenomena [279, 280] similar to the theoretical scheme studied in Chapter 4.

Appendix A

Floquet theorem and its characteristic equation

Considering a basis of space solution which satisfy the conditions (2.7), the general solution of equation (2.2) is described by

$$\psi(x) = c_1\psi_1(x) + c_2\psi_2(x) \tag{A.1}$$

In addition, we assume now that the general solution satisfies the condition (2.10)

$$c_1\psi_1(x+d) + c_2\psi_2(x+d) = \rho(c_1\psi_1(x) + c_2\psi_2(x)). \tag{A.2}$$

Since $\psi_1(x+d)$ and $\psi_2(x+d)$ are also solutions of (2.2) due to the symmetric displacement d, they can be written as linear combination of $\psi_1(x)$, $\psi_2(x)$, and hence

$$\psi_1(x+d) = c_{11}\psi_1(x) + c_{12}\psi_2(x) \tag{A.3}$$

$$\psi_2(x+d) = c_{21}\psi_1(x) + c_{22}\psi_2(x). \tag{A.4}$$

It follows that for $x = 0$ and substituting the initial conditions (2.7) into equations (A.3), (A.4) and their derivatives, we obtain

$$\begin{pmatrix} c_{11} & c_{12} \\ c_{21} & c_{22} \end{pmatrix} = \begin{pmatrix} \psi_1(d) & \psi_1'(d) \\ \psi_2(d) & \psi_2'(d) \end{pmatrix} \tag{A.5}$$

Therefore, we find easily that the equations (A.3), (A.4) may be rewritten as

$$\psi_1(x+d) = \psi_1(d)\psi_1(x) + \psi_1'(d)\psi_2(x) \tag{A.6}$$

$$\psi_2(x+d) = \psi_2(d)\psi_2(x) + \psi_2'(d)\psi_2(x) \tag{A.7}$$

Then, after inserting the expressions (A.6), (A.7) for $\psi_1(x+d)$, $\psi_2(x+d)$ into equation (A.2), we obtain

$$\begin{aligned} c_1(\psi_1(d)\psi_1(x) + \psi_1'(d)\psi_2(x)) + c_2(\psi_2(d)\psi_1(x) + \psi_2'(d)\psi_2(x)) \\ = \rho(c_1\psi_1(x) + c_2\psi_2(x)) \end{aligned} \tag{A.8}$$

Thus, by equating the coefficients of $\psi_1(x)$ and $\psi_2(x)$ in the latter equation, a linear homogeneous system is produced

$$\begin{pmatrix} \psi_1(d) - \rho & \psi_2(d) \\ \psi_1'(d) & \psi_2'(d) - \rho \end{pmatrix} \begin{pmatrix} c_1 \\ c_2 \end{pmatrix} = 0 \tag{A.9}$$

To obtain the non-trivial solution of the system (A.9), we employ the necessary and sufficient condition

$$\det \begin{pmatrix} \psi_1(d) - \rho & \psi_2(d) \\ \psi_1'(d) & \psi_2'(d) - \rho \end{pmatrix} = 0, \tag{A.10}$$

resulting in the equation

$$\rho^2 - (\psi_1(d) + \psi_2'(d))\rho + W(d) = 0. \tag{A.11}$$

where $W(d) = \psi_1(d)\psi_2'(d) - \psi_2(d)\psi_1'(d)$ is the Wronskian of the two independent solutions $\psi_1(x)$ and $\psi_2(x)$, calculated at $x = d$. However, the Wronskian of an equation of the form (2.2) is always constant, and thus according to initial conditions (2.7), $W(d) = 1$.

By setting $\Lambda = \psi_1(d) + \psi_2'(d)$, we can now determine the final expression of Hill's discriminant

$$\rho^2 - \Lambda\rho + 1 = 0. \tag{A.12}$$

Appendix B

Generic expression for critical wave amplitude

The development of the instability and the realisation of the first bifurcation at U_{cr1} generates two different transport channels. What channel will be active depends on the initial conditions. Let denote $\mathcal{E}$ and $\mathcal{O}$ sequential even and odd numbers respectively. Therefore, considering the electron found at position $\tilde{x}_0$ with $\tilde{p}_0 = 0$, we get the following representation for critical U

$$U_{cr_n} = -\frac{\hbar}{d\sin\tilde{x}_s}\left[\frac{v_0}{v_s}\cos\tilde{p}_s + \tilde{p}_s - (\mathcal{E} - n + 3/2)\pi\right]. \tag{B.1}$$

Here $(\tilde{x}_s, \tilde{p}_s)$ is any saddle point found at $\tilde{x}_s = -\pi/2 + 2\pi\eta \ \{\eta \in \mathbb{Z}\}$ and $\tilde{p}_s = (-1)^{\mathcal{E}} \sin^{-1}\left(\frac{v_s}{v_0}\right) + \mathcal{E}\pi$. If electrons are out of the thermal equilibrium at the initial time t_0 then the critical wave amplitude takes the form

$$U_{cr_n} = -\frac{\hbar}{d\sin\tilde{x}_s}\left[\frac{v_o}{v_s}\cos\tilde{p}_s + \tilde{p}_s - (\mathcal{O} + n - 3/2)\pi\right], \tag{B.2}$$

where $(\tilde{x}_s, \tilde{p}_s)$ is any saddle point located at $\tilde{x}_s = \pi/2 + 2\pi\eta \ \{\eta \in \mathbb{Z}\}$ and $\tilde{p}_s = (-1)^{\mathcal{O}} \sin^{-1}\left(\frac{v_s}{v_0}\right) + \mathcal{O}\pi$. Note, that the separatrix reconnection at $U = U_{cr1}$ involves saddle points which differ by $|\Delta\tilde{p}| = sin^{-1}\left(\frac{v_s}{v_0}\right) + \pi$. This way, the electron moves all along the distance between two adjacent wave crests. In the limit $v_0 >> v_s$, the electron under the action of sound wave for $U = U_{cr1}$ can reach the boundary of first Brillouin zone $|\Delta\tilde{p}| \rightarrow \pi$. Figure B.1 describes the possible transitions to the subsequent Brillouin edges corresponding to the realisation of bifurcations determined by equations (B.1), (B.2) for different U_{cr}. It is worth to note that we may treat though the particle motion over the "elementary cell" $-\pi \leq \tilde{p} < \pi$. Suppose the node "0" lies at the center of Brillouin zone then subtracting the integral multiple of 2π from the group of nodes with values $\{2\pi, 4pi, .., \mathcal{E}\pi\}$ gives again the same point inside the first zone. On the other hand, "π" standing on the location in momentum space for which the Bragg condition is satisfied, it is physically identical with the values $\{-\mathcal{O}\pi, ..., -3\pi, -\pi\}$. Therefore, for the latter case every U_{cr} will coincide with excitation of the electron at the upper half of the miniband whereas for the former, with suppression to its bottom.

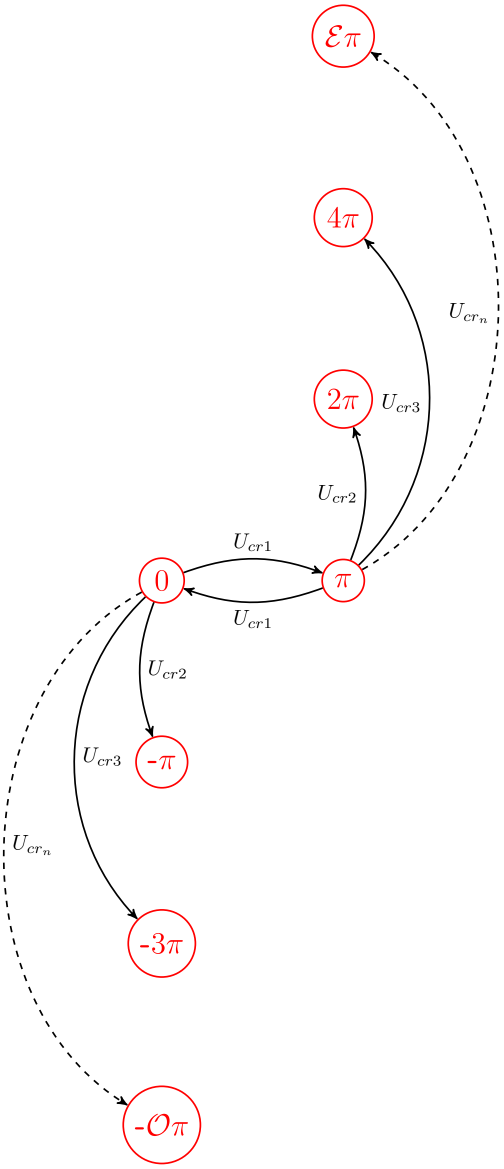

Figure B.1: Graphical representation of the two possible electron's transport paths in momentum space, when the system undergoes a sequence of global bifurcations.

Appendix C

Propagation of an Electromagnetic Wave in Conductor

We consider the propagation of an EM wave through a linear conducting medium, neglecting the transient effects related to the migration of free charge to the surface of the conductor. With this, we assume the free charge density to be zero $\rho_f = 0$. Maxwell's equations describing such a conductor are represented by

$$\nabla \cdot \mathbf{E} = 0, \tag{C.1}$$

$$\nabla \cdot \mathbf{B} = 0, \tag{C.2}$$

$$\nabla \times \mathbf{E} = -\frac{\partial \mathbf{B}}{\partial t}, \tag{C.3}$$

$$\nabla \times \mathbf{B} = \mu_0 \mathbf{J} + \epsilon_0 \mu_0 \epsilon_r \frac{\partial \mathbf{E}}{\partial t}. \tag{C.4}$$

Within the conductor with conductivity σ, the Ohm's law can be written as

$$\mathbf{J} = \sigma \mathbf{E}. \tag{C.5}$$

Applying the curl to equation (C.3) and by using equations (C.5), (C.1) we obtain the wave equation for $\mathbf{E}$

$$\nabla^2 \mathbf{E} - \mu_0 \sigma \frac{\partial \mathbf{E}}{\partial t} - \epsilon_0 \mu_0 \epsilon_r \frac{\partial^2 \mathbf{E}}{\partial t^2} = 0, \tag{C.6}$$

The latter equation has a solution similar to the one of an ordinary wave equation

$$\tilde{\mathbf{E}}(\mathbf{r}, t) = \tilde{E}_0 e^{i(\mathbf{kr} - \omega t)}\, \hat{\nu}, \tag{C.7}$$

where $\hat{\nu}$ is the polarization vector, $\hat{k}$ is the propagation vector, $\tilde{E}_0$ is the complex amplitude and the real part of $\tilde{\mathbf{E}}$ satisfies equation (C.6). Assuming now a plane wave, which is polarised in $\hat{x}$ direction and that travels along z-axis, from the equation (C.6) we obtain

$$\frac{d^2\tilde{E}}{dz^2} + \frac{n^2\omega^2}{c^2}\tilde{E} = 0, \tag{C.8}$$

where $\tilde{n} = n_0\left(1 + i\frac{\sigma}{\omega\epsilon_0\epsilon_r}\right)^{\frac{1}{2}}$ is the complex refractive index with $n_0 = \sqrt{\epsilon_r}$ for a weakly magnetic substance ($\mu_r \approx 1$) and c is the speed of light in the vacuum. The existence of a complex factor in the refractive index will implicate the involvement of a complex wave number $\hat{K}$ in the space-dependent part of the plane wave. Hence, substituting $\tilde{E}(z) = \tilde{E}_0 e^{i\hat{K}z}$ in equation (C.8) produces

$$\hat{K} = n_0\frac{\omega}{c}\left(1 + \frac{\sigma^2}{\omega^2\epsilon_0^2\epsilon_r^2}\right)^{1/4} e^{i\frac{\theta}{2}} \tag{C.9}$$

$$\theta = \tan^{-1}\left(\frac{\sigma}{\omega\epsilon_0\epsilon_r}\right) + n\pi,\ n \in \mathbb{Z} \tag{C.10}$$

Given the Euler formula $e^{i\frac{\theta}{2}} = \cos\frac{\theta}{2} + i\sin\frac{\theta}{2}$, the cosine function in terms of tangent $\frac{1}{\sqrt{1+\tan^2\theta}}$ and the trigonometric half angle formulas $\cos\frac{\theta}{2} = \sqrt{(1+\cos\theta)/2}$, $\sin\frac{\theta}{2} = \sqrt{(1-\cos\theta)/2}$ we obtain

$$\begin{aligned} \cos\frac{\theta}{2} &= \frac{1}{\sqrt{2}}\left[1 + \left(1 + \frac{\sigma^2}{\omega^2\epsilon_0^2\epsilon_r^2}\right)^{-1/2}\right]^{1/2} \\ \sin\frac{\theta}{2} &= \frac{1}{\sqrt{2}}\left[1 - \left(1 + \frac{\sigma^2}{\omega^2\epsilon_0^2\epsilon_r^2}\right)^{-1/2}\right]^{1/2} \end{aligned} \tag{C.11}$$

Now, if we substitute these analytical forms of $\cos\frac{\theta}{2}$ and $\sin\frac{\theta}{2}$ into equation (C.9) we find

$$\hat{K} = k_r + ik_i \tag{C.12}$$

with

$$\begin{pmatrix} k_r \\ k_i \end{pmatrix} = n_0\frac{\omega}{\sqrt{2}c}\left[\left(1 + \frac{\sigma^2}{\omega^2\epsilon_0^2\epsilon_r^2}\right)^{1/2} \pm 1\right]^{1/2} \tag{C.13}$$

The existence of the imaginary part in $\hat{K}$ causes the attenuation of the wave with the increase of z:

$$\tilde{E}(z,t) = \tilde{E}_0 e^{-k_i z} e^{i(k_r z - \omega t)}. \tag{C.14}$$

The distance it takes to reduce the amplitude of the wave by a factor 1/e is called skin depth

$$\delta(\omega) = 1/k_i(\omega). \tag{C.15}$$

For $\sigma << \omega\epsilon_0\epsilon_r$, known as the case of the bad conductor, the imaginary part of complex wave number becomes frequency independent and therefore δ describes the penetration length. Using (C.13) in this limit, δ can be written as

$$\delta = \frac{2\epsilon_0\epsilon_r c}{\sigma n_0}. \tag{C.16}$$

It becomes clear that for high-frequency fields the dielectric properties of the conductor determine the attenuation of the wave. In general, the average power per unit area transported by an electromagnetic wave is called intensity

$$I = \frac{1}{2}c\epsilon_0\tilde{E}_0^2. \tag{C.17}$$

Because the intensity is proportional to the square of the amplitude of wave [see Eqs. (C.17),(C.14)] and therefore to $e^{-2k_i z}$, the absorption coefficient of the EM wave is defined as

$$\alpha = 2k_i. \tag{C.18}$$

It is easy to see from equation (C.13), (C.18) that if we know the value of the real part of the dynamical conductivity $\sigma(\omega)$, we can determine the coefficient of absorption. To calculate the absorption of an electric field in a conductor (see also in Chapter 4), we use equation

$$\mathrm{Re}[\sigma(\omega)] = \frac{2\left\langle j(t)\cos(\omega t)\right\rangle_t}{E_\omega}. \tag{C.19}$$

At this point, it is useful to revisit the Drude model of high-frequency conduction. In the Drude theory, the response of the carriers, having charge e and mass m, to a spatially uniform electric field, is described by the equation of motion

$$m\dot{\mathbf{v}}(t) = -\frac{m}{\tau}\mathbf{v}(t) + e\mathbf{E}(t), \tag{C.20}$$

where $\mathbf{v}$ is the velocity of the particle and τ is a phenomenological relaxation time. The general solution to equation (C.20) can be found by first rewriting it as

$$\frac{d}{dt}\left[e^{\frac{t}{\tau}}\mathbf{v}(t)\right] = \frac{e}{m}e^{\frac{t}{\tau}}\mathbf{E}(t) \tag{C.21}$$

and then by integrating from $t' = -\infty$ (denoting a time before any field has been applied) to t (the time we make the measurement of drift velocity), we obtain

$$\mathbf{v}(t) = \frac{e}{m} \int_{-\infty}^{t} dt' e^{\frac{-(t-t')}{\tau}} \mathbf{E}(t'). \tag{C.22}$$

Equation (C.22) indicates that electron velocity at any given time t, depends on the response of the system to the external electric field at a prior time. Given that the density of conduction electrons, n, is constant and the electric field demonstrates harmonic variation, the current density is represented by

$$\begin{aligned} \mathbf{J}(t) &= \mathrm{Re}\left[\frac{ne^2\tau}{m}\mathbf{E}(\omega) \int_{-\infty}^{t} dt' e^{\frac{-(t-t')}{\tau}} e^{-i\omega t'}\right] \\ &= \mathrm{Re}\left[\frac{\sigma_0}{1 - i\omega\tau}\mathbf{E}(\omega)e^{-i\omega t}\right], \end{aligned} \tag{C.23}$$

where $\sigma_0 = ne^2\tau/m$. The time dependent current density has a complex amplitude defined by the following dispersion relationship

$$\mathbf{J}(\omega) = \sigma(\omega)\mathbf{E}(\omega). \tag{C.24}$$

Using equations (C.24) and (C.23), the Drude frequency-dependent complex conductivity can be obtained as

$$\sigma(\omega) = \mathrm{Re}[\sigma(\omega)] + i\,\mathrm{Im}[\sigma(\omega)] = \frac{\sigma_0}{1 + \omega^2\tau^2} + i\omega\tau\frac{\sigma_0}{1 + \omega^2\tau^2}. \tag{C.25}$$

The in-phase component [this can be obtained by multiplying $J(t)$ with $\cos(\omega t)$] to the frequency, ω, of the dynamic electric field is

$$J(t)\cos(\omega t) = \mathrm{Re}\left[\frac{\sigma_0}{1 - i\omega\tau}E_\omega e^{-i\omega t}\right]\cos(\omega t). \tag{C.26}$$

By integrating equation (C.26) over a period $T = 2\pi/\omega$, it is easy to see that

$$\langle j(t)\cos(\omega t)\rangle_t = \frac{\mathrm{Re}[\sigma(\omega)]E_\omega}{2}, \tag{C.27}$$

which is equivalent with equation (C.19).

A more direct way, to observe that the gain or the absorption of an alternating field in a conductor is consistent with equation (C.27), it is to calculate the output power per electron. This can be simply done by determining the energy that the wave gives to the particle or the energy that the particle loses to damping and radiation. Only the electric field does work on the electron. And since the electric force is $eE_\omega \cos\omega t$, the amount of work done on the particle in time dt is

$$dW = \mathbf{F}_{E_\omega} d\mathbf{x} = eE_\omega \cos\omega t \; v dt \tag{C.28}$$

The instantaneous power and the averaging power over a complete cycle are given by

$$P(t) = \frac{dW}{dt} \tag{C.29}$$

and

$$P_{avg} = \frac{1}{T} \int_0^T P(t) dt. \tag{C.30}$$

respectively. Therefore, combining equations (C.28), (C.29), (C.30) and if the space charge effects are neglected, the dissipated power turns out to be

$$P_{avg} = \frac{1}{T} \int_0^T eE_{pr}(t) v(t) dt = \frac{eE_\omega}{T} \int_0^T v(t) \cos\omega t \; dt. \tag{C.31}$$

Considering a semiconductor superlattice oscillator, the way that energy is transferred between the electron and the electric field $E(t)$ is hidden in the sign of the power P_{avg}. Hence, if $P_{avg} > 0$ energy of the alternating field is absorbed by the superlattice. On the other hand, if $P_{avg} < 0$ energy is transferred to the alternating field and thus $E(t)$ is amplified, making possible the oscillation of the system.

References

[1] Raphael Tsu. *Superlattice to nanoelectronics.* Elsevier, 2005.

[2] Ernest Braun and Stuart MacDonald. *Revolution in miniature: The history and impact of semiconductor electronics.* Cambridge University Press, 1982.

[3] Lawrence E Larson, RH Hackett, and RF Lohr. Microactuators for GaAs-based microwave integrated circuits. In *Solid-State Sensors and Actuators, 1991. Digest of Technical Papers, TRANSDUCERS'91., 1991 International Conference on*, pages 743–746. IEEE, 1991.

[4] Susumu Noda, Katsuhiro Tomoda, Noritsugu Yamamoto, and Alongkarn Chutinan. Full three-dimensional photonic bandgap crystals at near-infrared wavelengths. *Science*, 289(5479):604–606, 2000.

[5] James Meindl. Special issue on limits of semiconductor technology. *Proceedings of the IEEE*, 89(3):223–226, 2001.

[6] Mark Lundstrom. Moore's law forever? *Science*, 299(5604):210–211, 2003.

[7] Steven H Gold and Gregory S Nusinovich. Review of high-power microwave source research. *Review of Scientific instruments*, 68(11):3945–3974, 1997.

[8] JR Pierce and Lester M Field. Traveling-wave tubes. *Proceedings of the IRE*, 35(2):108–111, 1947.

[9] Raphael Tsu. Applying the insight into superlattices and quantum wells for nanostructures: Low-dimensional structures and devices. *Microelectronics Journal*, 38(10):959–1012, 2007.

[10] Leo Esaki and Ray Tsu. Superlattice and negative differential conductivity in semiconductors. *IBM Journal of Research and Development*, 14(1):61–65, 1970.

[11] Anatoly A Ignatov, EP Dodin, and VI Shashkin. Transient response theory of semiconductor superlattices: connection with Bloch oscillations. *Modern Physics Letters B*, 5(16):1087–1094, 1991.

[12] Karl Leo, Peter Haring Bolivar, Frank Brüggemann, Ralf Schwedler, and Klaus Köhler. Observation of Bloch oscillations in a semiconductor superlattice. *Solid State Communications*, 84(10):943–946, 1992.

[13] Christian Waschke, Hartmut G Roskos, Ralf Schwedler, Karl Leo, Heinrich Kurz, and Klaus Köhler. Coherent submillimeter-wave emission from Bloch oscillations in a semiconductor superlattice. *Physical Review Letters*, 70(21): 3319, 1993.

[14] VI Sankin, AV Andrianov, AG Petrov, and AO Zakhar'in. Terahertz emission from SiC natural superlattices in strong electrical field. *Applied Physics Letters*, 108(21):211108, 2016.

[15] Timo Hyart, Natalia V Alexeeva, Jussi Mattas, and Kirill N Alekseev. Terahertz Bloch oscillator with a modulated bias. *Physical Review Letters*, 102 (14):140405, 2009.

[16] Heribert Eisele, Suraj P Khanna, and Edmund H Linfield. Superlattice electronic devices as high-performance oscillators between 60–220 Ghz. *Applied Physics Letters*, 96(7):072101, 2010.

[17] VV Makarov, Alexander E Hramov, Alexey A Koronovskii, KN Alekseev, VA Maximenko, MT Greenaway, TM Fromhold, Olga I Moskalenko, and Alexander G Balanov. Sub-terahertz amplification in a semiconductor superlattice with moving charge domains. *Applied Physics Letters*, 106(4): 043503, 2015.

[18] MI Ovsyannikov, Yu A Romanov, VN Shabanov, and RG Loginova. Periodic semiconductor structures. *SOVIET PHYSICS SEMICONDUCTORS-USSR*, 4(12):1919, 1970.

[19] Yu A Romanov. Nonlinear effects in periodic semiconductor structures (frequency multiplication due to nonparabolicity of dispersion law in semiconductor structure subbands, noting electromagnetic signal transformation). *Optika i Spektroskopiia*, 33:917–920, 1972.

[20] JB Gunn. The discovery of microwave oscillations in gallium arsenide. *IEEE Transactions on Electron Devices*, 23(7):705–713, 1976.

[21] Herbert Kroemer. Theory of the Gunn effect. *Proceedings of the IEEE*, 52 (12):1736–1736, 1964.

[22] Luis L Bonilla and Stephen W Teitsworth. *Nonlinear wave methods for charge transport*. John Wiley & Sons, 2009.

[23] Viktor Leopoldovich Bonch-Bruevich, Igor Petrovich Zviagin, and Aleksandr Grigorevich Mironov. *Domain electrical instabilities in semiconductors*. Consultants Bureau, 1975.

[24] R Tsu and Leo Esaki. Tunneling in a finite superlattice. *Applied Physics Letters*, 22(11):562–564, 1973.

[25] LL Chang, Leo Esaki, and R Tsu. Resonant tunneling in semiconductor double barriers. *Applied Physics Letters*, 24(12):593–595, 1974.

[26] TCLG Sollner, WD Goodhue, PE Tannenwald, CD Parker, and DD Peck. Resonant tunneling through quantum wells at frequencies up to 2.5 THz. *Applied Physics Letters*, 43(6):588–590, 1983.

[27] ER Brown, TCLG Sollner, CD Parker, WD Goodhue, and CL Chen. Oscillations up to 420 GHz in GaAs/AlAs resonant tunneling diodes. *Applied Physics Letters*, 55(17):1777–1779, 1989.

[28] Jerome Faist, Federico Capasso, Deborah L Sivco, Carlo Sirtori, Albert L Hutchinson, Alfred Y Cho, et al. Quantum cascade laser. *Science*, 264 (5158):553–556, 1994.

[29] Claire Gmachl, Federico Capasso, Deborah L Sivco, and Alfred Y Cho. Recent progress in quantum cascade lasers and applications. *Reports on Progress in Physics*, 64(11):1533, 2001.

[30] RF Kazarinov and RA Suris. Possibility of amplication of electromagnetic waves in a semiconductor with a superlattice. *Fiz. Tekhn. Poluprov*, 5(4): 797–800, 1971.

[31] Benjamin S Williams. Terahertz quantum-cascade lasers. *Nature photonics*, 1(9):517–525, 2007.

[32] Yu Yao, Anthony J Hoffman, and Claire F Gmachl. Mid-infrared quantum cascade lasers. *Nature Photonics*, 6(7):432–439, 2012.

[33] Jérôme Faist. Quantum cascade lasers. *OUP Oxford*, 2013.

[34] Andreas Wacker. Semiconductor superlattices: a model system for nonlinear transport. *Physics Reports*, 357(1):1–111, 2002.

[35] Clarence Zener. A theory of the electrical breakdown of solid dielectrics. *Proceedings of the Royal Society of London. Series A, Containing Papers of a Mathematical and Physical Character*, 145(855):523–529, 1934.

[36] Paul Drude. Zur elektronentheorie der metalle. *Annalen der Physik*, 306(3): 566–613, 1900.

[37] Karl Leo. Interband optical investigation of Bloch oscillations in semiconductor superlattices. *Semiconductor Science and Technology*, 13(3):249, 1998.

[38] J Feldmann, K Leo, Jagdeep Shah, DAB Miller, JE Cunningham, T Meier, G Von Plessen, A Schulze, P Thomas, and S Schmitt-Rink. Optical investigation of Bloch oscillations in a semiconductor superlattice. *Physical Review B*, 46(11):7252, 1992.

[39] Thomas Dekorsy, R Ott, Heinrich Kurz, and Klaus Köhler. Bloch oscillations at room temperature. *Physical Review B*, 51(23):17275, 1995.

[40] SA Ktitorov, GS Simin, and VY Sindalov. Bragg reflections and high-frequency conductivity of an electronic solid-state plasma. *SOVIET PHYSICS SOLID STATE, USSR*, 13(8):1872, 1972.

[41] M Büttiker and H Thomas. Current instability and domain propagation due to Bragg scattering. *Physical Review Letters*, 38(2):78, 1977.

[42] Pavlos G Savvidis, Borys Kolasa, G Lee, and SJ Allen. Resonant crossover of terahertz loss to the gain of a bloch oscillating InAs/AlSb superlattice. *Physical review letters*, 92(19):196802, 2004.

[43] Herbert Kroemer. Large-amplitude oscillation dynamics and domain suppression in a superlattice Bloch oscillator. *arXiv preprint cond-mat/0009311*, 2000.

[44] Kirill N Alekseev, Maxim V Gorkunov, Natalia V Demarina, Timo Hyart, Natalia V Alexeeva, and Aleksey V Shorokhov. Suppressed absolute negative conductance and generation of high-frequency radiation in semiconductor superlattices. *EPL (Europhysics Letters)*, 73(6):934, 2006.

[45] Timo Hyart, Jussi Mattas, and Kirill N Alekseev. Model of the influence of an external magnetic field on the gain of terahertz radiation from semiconductor superlattices. *Physical Review Letters*, 103(11):117401, 2009.

[46] Mark Thomas Greenaway. *Single particle and collective dynamics in periodic potentials*. PhD thesis, University of Nottingham, 2010.

[47] MT Greenaway, Alexander G Balanov, D Fowler, AJ Kent, and TM Fromhold. Using acoustic waves to induce high-frequency current oscillations in superlattices. *Physical Review B*, 81(23):235313, 2010.

[48] CL Poyser, AV Akimov, AG Balanov, RP Campion, and AJ Kent. A weakly coupled semiconductor superlattice as a harmonic hypersonic-electrical transducer. *New Journal of Physics*, 17(8):083064, 2015.

[49] John M Ziman. *Electrons and phonons: the theory of transport phenomena in solids*. Oxford University Press, 1960.

[50] I Tamm. Über die quantentheorie der molekularen lichtzerstreuung in festen körpern. Zeitschrift für Physik, 60(5-6):345–363, 1930.

[51] Martin Maldovan. Sound and heat revolutions in phononics. *Nature*, 503 (7475):209–217, 2013.

[52] Taras Gorishnyy, Chaitanya K Ullal, Martin Maldovan, G Fytas, and EL Thomas. Hypersonic phononic crystals. *Physical Review Letters*, 94 (11):115501, 2005.

[53] Hong-xiang Sun, Shu-yi Zhang, and Xiu-ji Shui. A tunable acoustic diode made by a metal plate with periodical structure. *Applied Physics Letters*, 100(10):103507, 2012.

[54] Steven A Cummer and David Schurig. One path to acoustic cloaking. *New Journal of Physics*, 9(3):45, 2007.

[55] SA Cavill, LJ Challis, AJ Kent, FF Ouali, AV Akimov, and M Henini. Acoustic phonon-assisted tunneling in GaAs/AlAs superlattices. *Physical Review B*, 66(23):235320, 2002.

[56] RP Beardsley, AV Akimov, M Henini, and AJ Kent. Coherent terahertz sound amplification and spectral line narrowing in a stark ladder superlattice. *Physical Review Letters*, 104(8):085501, 2010.

[57] W Maryam, AV Akimov, RP Campion, and AJ Kent. Dynamics of a vertical cavity quantum cascade phonon laser structure. *Nature Communications*, 4, 2013.

[58] Keisuke Shinokita, Klaus Reimann, Michael Woerner, Thomas Elsaesser, Rudolf Hey, and Christos Flytzanis. Strong amplification of coherent acoustic phonons by intraminiband currents in a semiconductor superlattice. *Physical Review Letters*, 116(7):075504, 2016.

[59] C Colvard, TA Gant, MV Klein, R Merlin, R Fischer, H Morkoc, and AC Gossard. Folded acoustic and quantized optic phonons in (GaAl)As as superlattices. *Physical Review B*, 31(4):2080, 1985.

[60] HE Bömmel and K Dransfeld. Excitation and attenuation of hypersonic waves in quartz. *Physical Review*, 117(5):1245, 1960.

[61] DR Fowler, AV Akimov, Alexander G Balanov, MT Greenaway, M Henini, TM Fromhold, and AJ Kent. Semiconductor charge transport driven by a picosecond strain pulse. *Applied Physics Letters*, 92(23):232104, 2008.

[62] C Brüggemann, AV Akimov, AV Scherbakov, M Bombeck, C Schneider, S Höfling, A Forchel, DR Yakovlev, and M Bayer. Laser mode feeding by shaking quantum dots in a planar microcavity. *Nature Photonics*, 6(1):30–34, 2012.

[63] GM Shmelev, SY Mensah, and GI Tsurkan. Hypersound amplification by a superlattice in a nonquantised electric field. *Journal of Physics C: Solid State Physics*, 21(33):L1073, 1988.

[64] Nguyen Quang Bau and Nguyen Van Hieu. The quantum acoustoelectric current in a doped superlattice GaAs:Si/GaAs:Be. *Superlattices and Microstructures*, 63:121–130, 2013.

[65] FG Bass, AP Panchekha, and AE Zhukov. Electronic properties of semiconductor superlattices in high-frequency electromagnetic fields. *Physical Review B*, 51(12):7640, 1995.

[66] RG Chambers. The kinetic formulation of conduction problems. *Proceedings of the Physical Society. Section A*, 65(6):458, 1952.

[67] Herbert F Budd. The generalized path variable method. *J. Phys. Soc. Japan*, 18, 1963.

[68] Ekkehard Schomburg, NV Demarina, and Karl Friedrich Renk. Amplification of a terahertz field in a semiconductor superlattice via phase-locked k-space bunches of Bloch oscillating electrons. *Physical Review B*, 67(15):155302, 2003.

[69] Masayoshi Tonouchi. Cutting-edge terahertz technology. *Nature Photonics*, 1(2):97–105, 2007.

[70] Eric R Mueller. Terahertz radiation: applications and sources. *Industrial Physicist*, 9(4):27–30, 2003.

[71] Matthew C Beard, Gordon M Turner, and Charles A Schmuttenmaer. Terahertz spectroscopy. *The Journal of Physical Chemistry B*, 106(29):7146–7159, 2002.

[72] Ronald Ulbricht, Euan Hendry, Jie Shan, Tony F Heinz, and Mischa Bonn. Carrier dynamics in semiconductors studied with time-resolved terahertz spectroscopy. *Reviews of Modern Physics*, 83(2):543, 2011.

[73] Sergey Ganichev and Willi Prettl. *Intense terahertz excitation of semiconductors*. Number 14. Oxford University Press on Demand, 2006.

[74] P Uhd Jepsen, David G Cooke, and Martin Koch. Terahertz spectroscopy and imaging–modern techniques and applications. *Laser & Photonics Reviews*, 5 (1):124–166, 2011.

[75] Tobias Kampfrath, Koichiro Tanaka, and Keith A Nelson. Resonant and nonresonant control over matter and light by intense terahertz transients. *Nature Photonics*, 7(9):680–690, 2013.

[76] John F Federici, Brian Schulkin, Feng Huang, Dale Gary, Robert Barat, Filipe Oliveira, and David Zimdars. Thz imaging and sensing for security applicationsexplosives, weapons and drugs. *Semiconductor Science and Technology*, 20(7):S266, 2005.

[77] Frank Rutz, Martin Koch, Shilpa Khare, Martin Moneke, Heike Richter, and Uwe Ewert. Terahertz quality control of polymeric products. *International Journal of Infrared and Millimeter Waves*, 27(4):547–556, 2006.

[78] K Lien Nguyen, Tomislav Friščić, Graeme M Day, Lynn F Gladden, and William Jones. Terahertz time-domain spectroscopy and the quantitative monitoring of mechanochemical cocrystal formation. *Nature Materials*, 6(3): 206–209, 2007.

[79] B Fischer, M Hoffmann, H Helm, G Modjesch, and P Uhd Jepsen. Chemical recognition in terahertz time-domain spectroscopy and imaging. *Semiconductor Science and Technology*, 20(7):S246, 2005.

[80] K Lien Nguyen, Michael L Johns, Lynn Gladden, Christopher H Worrall, Paul Alexander, Harvey E Beere, Michael Pepper, David A Ritchie, Jesse Alton, Stefano Barbieri, et al. Three-dimensional imaging with a terahertz quantum cascade laser. *Optics Express*, 14(6):2123–2129, 2006.

[81] AJ Fitzgerald, E Berry, NN Zinovev, GC Walker, MA Smith, and JM Chamberlain. An introduction to medical imaging with coherent terahertz frequency radiation. *Physics in Medicine and Biology*, 47(7):R67, 2002.

[82] AN Bogomazova, EM Vassina, TN Goryachkovskaya, VM Popik, AS Sokolov, NA Kolchanov, MA Lagarkova, SL Kiselev, and SE Peltek. No Dna damage response and negligible genome-wide transcriptional changes in human embryonic stem cells exposed to terahertz radiation. *Scientific Reports*, 5:7749, 2015.

[83] Craig Kulesa. Terahertz spectroscopy for astronomy: From comets to cosmology. *IEEE Transactions on Terahertz Science and Technology*, 1(1):232–240, 2011.

[84] Leroy L Chang and Klaus Ploog. *Molecular beam epitaxy and heterostructures*, volume 87. Springer Science & Business Media, 2012.

[85] Gerald Bastard. Wave mechanics applied to semiconductor heterostructures. 1990.

[86] Holger T Grahn. *Semiconductor superlattices: growth and electronic properties*. World Scientific, 1995.

[87] Herbert Kroemer. The effect of band filling on the width of the minigaps on long period one-dimensional superlattices. *Colorado Univ. Boulder Technical Report*, 1, 1974.

[88] DL Smith and C Mailhiot. Theory of semiconductor superlattice electronic structure. *Reviews of Modern Physics*, 62(1):173, 1990.

[89] Luis L Bonilla and Holger T Grahn. Non-linear dynamics of semiconductor superlattices. *Reports on Progress in Physics*, 68(3):577, 2005.

[90] AA Lebedev. Heterojunctions and superlattices based on silicon carbide. *Semiconductor science and technology*, 21(6):R17, 2006.

[91] R de L Kronig and WG Penney. Quantum mechanics of electrons in crystal lattices. In *Proceedings of the Royal Society of London A: Mathematical,*

Physical and Engineering Sciences, volume 130, pages 499–513. The Royal Society, 1931.

[92] Gaston Floquet. Sur les équations différentielles linéaires à coefficients périodiques. In *Annales scientifiques de l'École normale supérieure*, volume 12, pages 47–88, 1883.

[93] Felix Bloch. Über die quantenmechanik der elektronen in kristallgittern. *Spendthrift für Physik*, 52(7-8):555–600, 1929.

[94] G Bastard. Superlattice band structure in the envelope-function approximation. *Physical Review B*, 24(10):5693, 1981.

[95] Wilhelm Magnus and Stanley Winkler. *Hill's equation.* Courier Corporation, 2013.

[96] Evgeni Korotyaev. Characterization of the spectrum of Schrödinger operators with periodic distributions. *International Mathematics Research Notices*, 2003(37):2019–2031, 2003.

[97] MA Pyataev. Solution of the Boltzmann equation in the relaxation time approximation (personal communication). 2016.

[98] Peter Kuchment. An overview of periodic elliptic operators. *Bulletin of the American Mathematical Society*, 53(3):343–414, 2016.

[99] David E Rourke, Larisa A Khodarinova, and T Mark Fromhold. Band structure engineering: A simple way to optimize key features of one-dimensional energy bands. *Physical Review B*, 72(15):155334, 2005.

[100] Hung-Sik Cho and Paul R Prucnal. New formalism of the Kronig-Penney model with application to superlattices. *Physical Review B*, 36(6):3237, 1987.

[101] Bernhard Rieder. *Semiclassical transport in semiconductor superlattices with boundaries.* PhD thesis, 2004.

[102] Neil W Ashcroft and N David Mermin. Solid state physics. *Saunders College, Philadelphia*, 2005.

[103] Herbert Kroemer. On the derivation of $\hbar\cdot\, dk/dt = F$, the k–space form of Newtons law for Bloch waves. *American Journal of Physics*, 54(2):177–178, 1986.

[104] E Brown. Bloch electrons in a uniform magnetic field. *Physical Review*, 133 (4A):A1038, 1964.

[105] T Ando and S Mori. Effective-mass theory of semiconductor heterojunctions and superlattices. *Surface Science*, 113(1-3):124–130, 1982.

[106] AM Bouchard and Marshall Luban. Bloch oscillations and other dynamical phenomena of electrons in semiconductor superlattices. *Physical Review B*, 52(7):5105, 1995.

[107] VG Lyssenko, G Valušis, F Löser, T Hasche, K Leo, MM Dignam, and K Köhler. Direct measurement of the spatial displacement of Bloch-oscillating electrons in semiconductor superlattices. *Physical Review Letters*, 79(2):301, 1997.

[108] M Sudzius, VG Lyssenko, G Valusis, F Löser, T Hasche, MM Dignam, K Köhler, and K Leo. Direct measurement of the spatial displacement of Bloch-oscillating electrons in semiconductor superlattices. *Physica E: Low-dimensional Systems and Nanostructures*, 2(1):437–440, 1998.

[109] Maxime Ben Dahan, Ekkehard Peik, Jakob Reichel, Yvan Castin, and Christophe Salomon. Bloch oscillations of atoms in an optical potential. *Physical Review Letters*, 76(24):4508, 1996.

[110] M Gustavsson, Elmar Haller, MJ Mark, JG Danzl, G Rojas-Kopeinig, and H-C Nägerl. Control of interaction-induced dephasing of Bloch oscillations. *Physical review letters*, 100(8):080404, 2008.

[111] Lev Davidovich Landau. *The classical theory of fields*, volume 2. Elsevier, 2013.

[112] TM Fromhold, AA Krokhin, CR Tench, S Bujkiewicz, PB Wilkinson, FW Sheard, and L Eaves. Effects of stochastic webs on chaotic electron transport in semiconductor superlattices. *Physical Review Letters*, 87(4): 046803, 2001.

[113] TM Fromhold, A Patane, S Bujkiewicz, PB Wilkinson, D Fowler, D Sherwood, SP Stapleton, AA Krokhin, L Eaves, M Henini, et al. Chaotic electron diffusion through stochastic webs enhances current flow in superlattices. *Nature*, 428(6984):726–730, 2004.

[114] VV Beloshapkin, AA Chernikov, M Ia Natenzon, BA Petrovichev, and RZ Sagdeev. Chaotic streamlines in pre-turbulent states. *Nature*, 337:133–137, 1989.

[115] Georgin Moiseevich Zaslavskiî, RZ Sagdeev, and DA Usikov. *Weak chaos and quasi-regular patterns*. Cambridge University Press, 1992.

[116] Michael F Shlesinger, George M Zaslavsky, and Joseph Klafter. Strange kinetics. *Nature*, 363(6424):31–37, 1993.

[117] Yuriy A Kosevich, Anne Beate Hummel, Hartmut G Roskos, and Klaus Köhler. Ultrafast Fiske effect in semiconductor superlattices. *Physical Review Letters*, 96(13):137403, 2006.

[118] Daivid Fowler, David PA Hardwick, Amalia Patanè, Mark T Greenaway, Alexander G Balanov, Timothy M Fromhold, Laurence Eaves, Mohamed Henini, Nadezda Kozlova, Jens Freudenberger, et al. Magnetic-field-induced miniband conduction in semiconductor superlattices. *Physical Review B*, 76 (24):245303, 2007.

[119] Yu A Romanov and Yu Yu Romanova. Bloch oscillations in superlattices: The problem of a terahertz oscillator. *Semiconductors*, 39(1):147–155, 2005.

[120] Yu A Romanov, J Yu Romanova, and LG Mourokh. Electron Bloch oscillations and electromagnetic transparency of semiconductor superlattices in multi-frequency electric fields. *Physical Review B*, 79(24):245320, 2009.

[121] Kirill A Pronin, Peter Reineker, and Andre D Bandrauk. Control of field-induced localization in superlattices: Coherence and relaxation. *Physical Review B*, 71(19):195311, 2005.

[122] DH Dunlap and VM Kenkre. Dynamic localization of a charged particle moving under the influence of an electric field. *Physical Review B*, 34(6): 3625, 1986.

[123] DH Dunlap and VM Kenkre. Effect of scattering on the dynamic localization of a particle in a time-dependent electric field. *Physical Review B*, 37(12): 6622, 1988.

[124] Milton Abramowitz and Irene A Stegun. *Handbook of mathematical functions: with formulas, graphs, and mathematical tables*, volume 55. Courier Corporation, 1964.

[125] Martin Holthaus. Collapse of minibands in far-infrared irradiated superlattices. *Physical Review Letters*, 69(2):351, 1992.

[126] Mark Lundstrom. *Fundamentals of carrier transport*. Cambridge University Press, 2009.

[127] Andreas Wacker, Antti-Pekka Jauho, Stefan Zeuner, and S James Allen. Sequential tunneling in doped superlattices: Fingerprints of impurity bands and photon-assisted tunneling. *Physical Review B*, 56(20):13268, 1997.

[128] R Dingle, HL Störmer, AC Gossard, and W Wiegmann. Electron mobilities in modulation-doped semiconductor heterojunction superlattices. *Applied Physics Letters*, 33(7):665–667, 1978.

[129] Andreas Wacker and A-P Jauho. Impact of interface roughness on perpendicular transport and domain formation in superlattices. *Superlattices and microstructures*, 23(2):297–300, 1998.

[130] I Dharssi and PN Butcher. Interface roughness scattering in a superlattice. *Journal of Physics: Condensed Matter*, 2(20):4629, 1990.

[131] G Etemadi and JF Palmier. Effect of interface roughness on non-linear vertical transport in GaAs/AlAs superlattices. *Solid State Communications*, 86 (11):739–743, 1993.

[132] Herbert Budd. Chamber's solution of the Boltzmann equation. *Physical Review*, 127(1):4, 1962.

[133] FG Bass, VV Zorchenko, and VI Shashora. Theory of galvanomagnetic and high-frequency phenomena in super-lattice semiconductors. *SOVIET PHYSICS SEMICONDUCTORS-USSR*, 15(3):263–266, 1981.

[134] Timo Hyart. *Tunable Superlattice Amplifiers Based on Dynamics of Miniband Electrons in Electric and Magnetic Fields.* PhD thesis, University of Oulu, Finland, 2009.

[135] G Brozak, M Helm, F DeRosa, CH Perry, M Koza, R Bhat, and SJ Allen Jr. Thermal saturation of band transport in a superlattice. *Physical Review Letters*, 64(26):3163, 1990.

[136] HT Grahn, K Von Klitzing, K Ploog, and GH Döhler. Electrical transport in narrow-miniband semiconductor superlattices. *Physical Review B*, 43(14): 12094, 1991.

[137] A Sibille, JF Palmier, M Hadjazi, H Wang, G Etemadi, E Dutisseuil, and F Mollot. Limits of semiclassical transport in narrow miniband GaAs/AlAs superlattices. *Superlattices and Microstructures*, 13(2):247, 1993.

[138] Alfred Brian Pippard. *The dynamics of conduction electrons.* Gordon and Breach, 1965.

[139] J Kastrup, R Hey, KH Ploog, HT Grahn, LL Bonilla, M Kindelan, M Moscoso, A Wacker, and J Galán. Electrically tunable GHz oscillations in doped GaAs-AlAs superlattices. *Physical Review B*, 55(4):2476, 1997.

[140] L Esaki and LL Chang. New transport phenomenon in a semiconductor" superlattice". *Physical Review Letters*, 33(8):495, 1974.

[141] Fabio Beltram, Federico Capasso, Deborah L Sivco, Albert L Hutchinson, Sung-Nee G Chu, and Alfred Y Cho. Scattering-controlled transmission resonances and negative differential conductance by field-induced localization in superlattices. *Physical Review Letters*, 64(26):3167, 1990.

[142] A Sibille, JF Palmier, H Wang, and F Mollot. Observation of Esaki-Tsu negative differential velocity in GaAs/AlAs superlattices. *Physical Review Letters*, 64(1):52, 1990.

[143] M Hadjazi, JF Palmier, A Sibille, H Wang, E Paris, and F Mollot. 60 GHz reflection gain based on superlattice negative differential conductance. *Electronics Letters*, 29(8):648–649, 1993.

[144] JF Palmier, JC Harmand, C Minot, H Le Person, E Dutisseuil, H Wang, and G Leroux. Microwave miniband NDC in GaInAs/AlInAs superlattices. *Solid-State Electronics*, 37(4-6):697–700, 1994.

[145] E Schomburg, T Blomeier, K Hofbeck, J Grenzer, S Brandl, I Lingott, AA Ignatov, KF Renk, DG Pavelev, Yu Koschurinov, et al. Current oscillation in superlattices with different miniband widths. *Physical Review B*, 58(7):4035, 1998.

[146] Raphael Tsu and L Esaki. Stark quantization in superlattices. *Physical Review B*, 43(6):5204, 1991.

[147] B Laikhtman and D Miller. Theory of current-voltage instabilities in superlattices. *Physical Review B*, 48(8):5395, 1993.

[148] Andreas Wacker and Antti-Pekka Jauho. Quantum transport: The link between standard approaches in superlattices. *Physical Review Letters*, 80(2): 369, 1998.

[149] Markus Glück, Andrey R Kolovsky, and Hans Jürgen Korsch. Wannier–Stark resonances in optical and semiconductor superlattices. *Physics Reports*, 366 (3):103–182, 2002.

[150] S Rott, P Binder, N Linder, and GH Döhler. Combined description for semiclassical and quantum transport in superlattices. *Physical Review B*, 59 (11):7334, 1999.

[151] S Rott, N Linder, and GH Döhler. Field dependence of the hopping drift velocity in semiconductor superlattices. *Physical Review B*, 65(19):195301, 2002.

[152] J Kastrup, R Klann, HT Grahn, K Ploog, LL Bonilla, J Galán, M Kindelan, M Moscoso, and R Merlin. Self-oscillations of domains in doped GaAs-AlAs superlattices. *Physical Review B*, 52(19):13761, 1995.

[153] KK Choi, BF Levine, RJ Malik, J Walker, and CG Bethea. Periodic negative conductance by sequential resonant tunneling through an expanding high-field superlattice domain. *Physical Review B*, 35(8):4172, 1987.

[154] OM Bulashenko, MJ Garcia, and LL Bonilla. Chaotic dynamics of electric-field domains in periodically driven superlattices. *Physical Review B*, 53(15): 10008, 1996.

[155] E Schomburg, K Hofbeck, R Scheuerer, M Haeussler, KF Renk, A-K Jappsen, A Amann, A Wacker, E Schöll, DG Pavelev, et al. Control of the dipole domain propagation in a GaAs/AlAs superlattice with a high-frequency field. *Physical Review B*, 65(15):155320, 2002.

[156] Baoquan Sun, Jiannong Wang, Weikun Ge, Yuqi Wang, Desheng Jiang, Haijun Zhu, Hailong Wang, Yuanming Deng, and Songlin Feng. Current self-oscillation induced by a transverse magnetic field in a doped GaAs/AlAs superlattice. *Physical Review B*, 60(12):8866, 1999.

[157] T Schmidt, AGM Jansen, RJ Haug, K v Klitzing, and K Eberl. Magnetic control of electric-field domains in semiconductor superlattices. *Physical Review Letters*, 81(18):3928, 1998.

[158] C Thomsen, Holger T Grahn, Humphrey J Maris, and Jan Tauc. Surface generation and detection of phonons by picosecond light pulses. *Physical Review B*, 34(6):4129, 1986.

[159] J. Tauc, H.J. Maris, and C. Thomsen. Optical generator and detector of stress pulses, December 1 1987. URL `https://www.google.com/patents/US4710030`. US Patent 4,710,030.

[160] SA Akhmanov, VE Gusev, and AA Karabutov. Pulsed laser optoacoustics: Achievements and perspective. *Infrared Physics*, 29(2-4):815–838, 1989.

[161] RJ Von Gutfeld and AH Nethercot Jr. Heat pulses in quartz and sapphire at low temperatures. *Physical Review Letters*, 12(23):641, 1964.

[162] Dvira Segal and Abraham Nitzan. Spin-boson thermal rectifier. *Physical review letters*, 94(3):034301, 2005.

[163] Baowen Li, Lei Wang, and Giulio Casati. Negative differential thermal resistance and thermal transistor. *Applied Physics Letters*, 88(14):143501, 2006.

[164] Lei Wang and Baowen Li. Thermal logic gates: computation with phonons. *Physical Review Letters*, 99(17):177208, 2007.

[165] RS Gilmore. Industrial ultrasonic imaging and microscopy. *Journal of Physics D: Applied Physics*, 29(6):1389, 1996.

[166] RM White and FW Voltmer. Direct piezoelectric coupling to surface elastic waves. *Applied Physics Letters*, 7(12):314–316, 1965.

[167] GR Kline and KM Lakin. 1.0-GHz thin-film bulk acoustic wave resonators on GaAs. *Applied Physics Letters*, 43(8):750–751, 1983.

[168] Yuri V Gulyaev and Fred S Hickernell. Acoustoelectronics: History, present state, and new ideas for a new era. In *Ultrasonics Symposium, 2004 IEEE*, volume 1, pages 182–190. IEEE, 2004.

[169] AR Hutson, JH McFee, and DL White. Ultrasonic amplification in CdS. *Physical Review Letters*, 7(6):237, 1961.

[170] Gabriel Weinreich. Acoustodynamic effects in semiconductors. *Physical Review*, 104(2):321, 1956.

[171] Harold N Spector. Amplification of acoustic waves through interaction with conduction electrons. *Physical Review*, 127(4):1084, 1962.

[172] AB Pippard. Acoustic amplification in semiconductors and metals. *Philosophical Magazine*, 8(85):161–165, 1963.

[173] RF Kazarinov and VG Skobov. On the theory of the amplification of ultrasound by semi-metals in electric and magnetic fields. *Soviet Phys.-JETP*, 16: 1057, 1962.

[174] Brian K Ridley. *Quantum processes in semiconductors*. Oxford University Press, 2013.

[175] TM Fromhold, PN Butcher, G Qin, BG Mulimani, JP Oxley, and BoL Gallagher. Phonon-drag magnetothermopower oscillations in GaAs/As x Ga 1-x As heterojunctions. *Physical Review B*, 48(8):5326, 1993.

[176] JC Jackson. Thermal overstability in fusion plasmas-the saser effect. *Plasma physics and controlled fusion*, 28(4):669, 1986.

[177] EE Mendez, F Agullo-Rueda, and JM Hong. Stark localization in GaAs-GaAlAs superlattices under an electric field. *Physical Review Letters*, 60 (23):2426, 1988.

[178] BA Glavin, VA Kochelap, TL Linnik, KW Kim, and MA Stroscio. Generation of high-frequency coherent acoustic phonons in superlattices under hopping transport. I. linear theory of phonon instability. *Physical Review B*, 65(8): 085303, 2002.

[179] MT Greenaway, AG Balanov, D Fowler, AJ Kent, and T Mark Fromhold. Using sound to generate ultra-high-frequency electron dynamics in superlattices. *Microelectronics Journal*, 40(4):725–727, 2009.

[180] Fabio Bernardini, Vincenzo Fiorentini, and David Vanderbilt. Spontaneous polarization and piezoelectric constants of III-V nitrides. *Physical Review B*, 56(16):R10024, 1997.

[181] Gabriel Bester, Xifan Wu, David Vanderbilt, and Alex Zunger. Importance of second-order piezoelectric effects in zinc-blende semiconductors. *Physical Review Letters*, 96(18):187602, 2006.

[182] Yongke Sun, Scott E Thompson, and Toshikazu Nishida. *Strain effect in semiconductors: theory and device applications*. Springer Science & Business Media, 2009.

[183] Agnes Huynh, Bernard Perrin, and A Lemaître. Semiconductor superlattices: A tool for terahertz acoustics. *Ultrasonics*, 56:66–79, 2015.

[184] AJ Kent, RN Kini, NM Stanton, M Henini, BA Glavin, VA Kochelap, and TL Linnik. Acoustic phonon emission from a weakly coupled superlattice under vertical electron transport: observation of phonon resonance. *Physical Review Letters*, 96(21):215504, 2006.

[185] KJ Ahn, F Milde, and A Knorr. Phonon-wave-induced resonance fluorescence in semiconductor nanostructures: Acoustoluminescence in the terahertz range. *Physical review letters*, 98(2):027401, 2007.

[186] Thomas Czerniuk, Christian Brüggemann, Jan Tepper, Sebastian Brodbeck, Christian Schneider, Martin Kamp, Sven Höfling, Boris A Glavin, Dmitri R Yakovlev, Andrey V Akimov, et al. Lasing from active optomechanical resonators. *Nature communications*, 5, 2014.

[187] Eirini Tzianaki, Makis Bakarezos, George D Tsibidis, Yannis Orphanos, Panagiotis A Loukakos, Constantine Kosmidis, Panos Patsalas, Michael Tatarakis, and Nektarios A Papadogiannis. High acoustic strains in si through ultrafast laser excitation of ti thin-film transducers. *Optics Express*, 23(13):17191–17204, 2015.

[188] Vasily V Temnov, Christoph Klieber, Keith A Nelson, Tim Thomay, Vanessa Knittel, Alfred Leitenstorfer, Denys Makarov, Manfred Albrecht, and Rudolf Bratschitsch. Femtosecond nonlinear ultrasonics in gold probed with ultrashort surface plasmons. *Nature Communications*, 4:1468, 2013.

[189] William H Press. *Numerical recipes 3rd edition: The art of scientific computing*. Cambridge University Press, 2007.

[190] Herbert F. Budd. The generalized path variable method. *Journal of the Physical Society of Japan*, 18(1):142–142, 1963. doi: 10.1143/JPSJ.18.142.

[191] Crawford MacCallum. Kinetic integral solutions of the Boltzmann equation. *Physical Review*, 132(2):930, 1963.

[192] A. A. Ignatov and Yu. A. Romanov. Nonlinear electromagnetic properties of semiconductors with a superlattice. *physica status solidi (b)*, 73(1):327–333, 1976. ISSN 1521-3951. doi: 10.1002/pssb.2220730132.

[193] S Winnerl, E Schomburg, J Grenzer, H-J Regl, AA Ignatov, AD Semenov, KF Renk, DG Pavelev, Yu Koschurinov, B Melzer, et al. Quasistatic and dynamic interaction of high-frequency fields with miniband electrons in semiconductor superlattices. *Physical Review B*, 56(16):10303, 1997.

[194] Timo Hyart, Jussi Mattas, and Kirill N. Alekseev. Model of the influence of an external magnetic field on the gain of terahertz radiation from semiconductor superlattices. *Phys. Rev. Lett.*, 103:117401, Sep 2009. doi: 10.1103/PhysRevLett.103.117401.

[195] AO Selskii, AA Koronovskii, AE Hramov, OI Moskalenko, KN Alekseev, MT Greenaway, F Wang, TM Fromhold, AV Shorokhov, NN Khvastunov, et al. Effect of temperature on resonant electron transport through stochastic conduction channels in superlattices. *Physical Review B*, 84(23):235311, 2011.

[196] M. T. Greenaway, A. G. Balanov, D. Fowler, A. J. Kent, and T. M. Fromhold. Using sound to generate ultra-high-frequency electron dynamics in superlattices. *Microelectronics Journal*, 40:725–727, 2009.

[197] J Wan, C Martijn de Sterke, and MM Dignam. Dynamic localization and quasi-Bloch oscillations in general periodic ac-dc electric fields. *Physical Review B*, 70(12):125311, 2004.

[198] Lev Davidovich Landau and Lifshitz. *Course of theoretical physics, Volume 1*. Elsevier, 2013.

[199] John Michael Tutill Thompson and H Bruce Stewart. *Nonlinear dynamics and chaos*. John Wiley & Sons, 2002.

[200] RF Kazarinov and VG Skobov. On the possibility of amplification of ultrasound in semiconductors in an electric field. *Soviet Phys.-JETP*, 42:910-912, 1962.

[201] Steven H Strogatz. *Nonlinear dynamics and chaos: with applications to physics, biology, chemistry, and engineering*. Westview press, 2014.

[202] Yuri A Kuznetsov. *Elements of applied bifurcation theory*, volume 112. Springer Science & Business Media, 2013.

[203] M Patra, G Schwarz, and E Schöll. Bifurcation analysis of stationary and oscillating domains in semiconductor superlattices with doping fluctuations. *Physical Review B*, 57(3):1824, 1998.

[204] Johanne Hizanidis, Alexander Balanov, Andreas Amann, and E Schöll. Noise-induced front motion: signature of a global bifurcation. *Physical Review Letters*, 96(24):244104, 2006.

[205] Yurii Vasil'evich Gulyaev. Acoustoelectronics (historical review). *Physics-Uspekhi*, 48(8):847–855, 2005.

[206] PJ Morrison. Magnetic field lines, hamiltonian dynamics, and nontwist systems. *Physics of Plasmas*, 7(6):2279–2289, 2000.

[207] Diego del Castillo-Negrete and PJ Morrison. Chaotic transport by Rossby waves in shear flow. *Physics of Fluids A: Fluid Dynamics (1989-1993)*, 5(4): 948–965, 1993.

[208] SM Soskin. Nonlinear resonance for the oscillator with a nonmonotonic dependence of eigenfrequency on energy. *Physical Review E*, 50(1):R44, 1994.

[209] Yu. A. Kuznetsov. *Elements of Applied Bifurcation Theory.* Springer-Verlag New York, 1998.

[210] Mikhail Veniaminovich Nezlin. *Physics of Intense Beams in Plasmas*, volume 2. CRC Press, 1993.

[211] Mikhail V Nezlin. Negative-energy waves and the anomalous doppler effect. *Physics-Uspekhi*, 19(11):946–954, 1976.

[212] IE Tamm. General characteristics of Vavilov-Cherenkov radiation. *Science*, 131, 1960.

[213] MA Gintsburg. On the anomalous doppler effect in a plasma. *Zhur. Eksptl'. i Teoret. Fiz.*, 41, 1961.

[214] Vitalii Lazarevich Ginzburg. Certain theoretical aspects of radiation due to superluminal motion in a medium. *Physics-Uspekhi*, 2(6):874–893, 1960.

[215] LA Ostrovskiĭ, SA Rybak, LS Tsimring. Negative energy waves in hydrodynamics. *Physics-Uspekhi*, 29(11):1040–1052, 1986.

[216] William T Cochran, James W Cooley, David L Favin, Howard D Helms, Reginald A Kaenel, William W Lang, GC Maling, David E Nelson, Charles M Rader, and Peter D Welch. What is the fast Fourier transform? *Proceedings of the IEEE*, 55(10):1664–1674, 1967.

[217] Boris V Chirikov. A universal instability of many-dimensional oscillator systems. *Physics Reports*, 52(5):263–379, 1979.

[218] John R Carson. Notes on the theory of modulation. *Proceedings of the Institute of Radio Engineers*, 10(1):57–64, 1922.

[219] Herbert Kroemer. On the nature of the negative-conductivity resonance in a superlattice Bloch oscillator. *arXiv preprint cond-mat/0007482*, 2000.

[220] Timo Hyart, Kirill N Alekseev, and Erkki V Thuneberg. Bloch gain in dc-ac-driven semiconductor superlattices in the absence of electric domains. *Physical Review B*, 77(16):165330, 2008.

[221] AA Ignatov and Yu A Romanov. Nonlinear electromagnetic properties of semiconductors with a superlattice. *Physica Status Solidi (b)*, 73(1):327–333, 1976.

[222] Anatoly A Ignatov, KF Renk, and EP Dodin. Esaki-Tsu superlattice oscillator: Josephson-like dynamics of carriers. *Physical Review Letters*, 70(13): 1996, 1993.

[223] NV Demarina and Karl Friedrich Renk. Bloch gain for terahertz radiation in semiconductor superlattices of different miniband widths mediated by acoustic and optical phonons. *Physical Review B*, 71(3):035341, 2005.

[224] Harald Willenberg, GH Döhler, and Jerome Faist. Intersubband gain in a Bloch oscillator and quantum cascade laser. *Physical Review B*, 67(8):085315, 2003.

[225] Igor'Vital'evich Altukhov, SE Dizhur, Miron Solomonovich Kagan, SK Paprotskiy, NA Khvalkovskii, AD Buravlev, AP Vasilev, Yu M Zadiranov, Natal'ya Dmitrievna Ilinskaya, Anna Aleksandrovna Usikova, et al. Effect of a terahertz cavity on the conductivity of short-period GaAs/AlAs superlattices. *JETP Letters*, 103(2):122–124, 2016.

[226] Avik W Ghosh and John W Wilkins. Nonlinear THz response of a one-dimensional superlattice. *Physical Review B*, 61(8):5423, 2000.

[227] Rafał Kwiatek and Grzegorz Zwara. The divisibility of integers and integer relatively primes. *Formalized Mathematics*, 1(5):829–832, 1990.

[228] Timo Hyart, Alexey V Shorokhov, and Kirill N Alekseev. Theory of parametric amplification in superlattices. *Physical Review Letters*, 98(22):220404, 2007.

[229] Andreas Wacker. Gain in quantum cascade lasers and superlattices: A quantum transport theory. *Physical Review B*, 66(8):085326, 2002.

[230] Munir H Nayfeh and Morton K Brussel. *Electricity and magnetism.* Courier Dover Publications, 2015.

[231] Alexey V Shorokhov and Kirill N Alekseev. Theoretical backgrounds of nonlinear THz spectroscopy of semiconductor superlattices. *International Journal of Modern Physics B*, 23(20n21):4448–4458, 2009.

[232] AA Ignatov, E Schomburg, J Grenzer, S Winnerl, KF Renk, and EP Dodin. Theory of electron transport in a THz-field irradiated semiconductor superlattice: occurrence of quantized dc voltages and current responsivity. *Superlattices and Microstructures*, 22(1):15–18, 1997.

[233] Andreas Wacker, SJ Allen, JS Scott, MC Wanke, and A-P Jauho. Possible thz gain in superlattices at a stable operation point. *Physica Status Solidi (b)*, 204(1):95–97, 1997.

[234] John R Tucker and Marc J Feldman. Quantum detection at millimeter wavelengths. *Reviews of Modern Physics*, 57(4):1055, 1985.

[235] BK Ridley. Specific negative resistance in solids. *Proceedings of the Physical Society*, 82(6):954, 1963.

[236] Y Shimada, K Hirakawa, Maxim Odnoblioudov, and Koung-An Chao. Terahertz conductivity and possible Bloch gain in semiconductor superlattices. *Physical Review Letters*, 90(4):046806, 2003.

[237] N Sekine and K Hirakawa. Dispersive terahertz gain of a nonclassical oscillator: Bloch oscillation in semiconductor superlattices. *Physical Review Letters*, 94(5):057408, 2005.

[238] A Lisauskas, NV Demarina, E Mohler, and HG Roskos. Comment on" dispersive terahertz gain of a nonclassical oscillator: Bloch oscillation in semiconductor superlattices". *arXiv preprint cond-mat/0605651*, 2006.

[239] A Lisauskas, MM Dignam, NV Demarina, E Mohler, and HG Roskos. Examining the terahertz signal from a photoexcited biased semiconductor superlattice for evidence of gain. *Applied Physics Letters*, 93(2):021122, 2008.

[240] Aizhen Zhang, Dawei Wang, and MM Dignam. Terahertz gain in optically excited biased semiconductor superlattices. *Applied Physics Letters*, 86(17): 1110, 2005.

[241] Dawei Wang, Aizhen Zhang, Lijun Yang, and Marc M Dignam. Tunable terahertz amplification in optically excited biased semiconductor superlattices: Influence of excited excitonic states. *Physical Review B*, 77(11):115307, 2008.

[242] Thomas Feil, RA Deutschmann, Werner Wegscheider, Martin Rother, Dieter Schuh, Max Bichler, Gerhard Abstreiter, Bernhard Rieder, and Joachim Keller. Transport in weakly and strongly modulated two-dimensional electron systems realized by cleaved-edge-overgrowth. *Physica Status Solidi (c)*, 1(8):2111–2130, 2004.

[243] Thomas Feil, Christian Gerl, and Werner Wegscheider. Transport properties of a shunted surface superlattice in an external magnetic field. *Physical Review B*, 73(12):125301, 2006.

[244] Thomas Feil, H-P Tranitz, Christian Gerl, and Werner Wegscheider. Transport in a shunted surface superlattice with a perpendicular magnetic field. *Physica E: Low-dimensional Systems and Nanostructures*, 32(1):301–304, 2006.

[245] David O Winge, Martin Franckié, and Andreas Wacker. Superlattice gain in positive differential conductivity region. *AIP Advances*, 6(4):045025, 2016.

[246] AA Andronov, EP Dodin, DI Zinchenko, and Yu N Nozdrin. Towards Wannier-Stark THz superlattice laser. In *Journal of Physics: Conference Series*, volume 193, page 012079. IOP Publishing, 2009.

[247] AV Shorokhov, MA Pyataev, NN Khvastunov, T Hyart, FV Kusmartsev, and KN Alekseev. Physical principles of the amplification of electromagnetic radiation due to negative electron masses in a semiconductor superlattice. *JETP Letters*, 100(12):766–770, 2015.

[248] Timo Hyart, Natalia V Alexeeva, Jussi Mattas, and Kirill N Alekseev. Possible THz Bloch gain in dc–ac-driven superlattices. *Microelectronics Journal*, 40(4):719–721, 2009.

[249] E Schomburg, F Klappenberger, M Krätschmer, A Vollnhals, R Scheuerer, KF Renk, V Ustinov, A Zhukov, and A Kovsh. InGaAs/InAlAs superlattice detector for THz radiation. *Physica E: Low-dimensional Systems and Nanostructures*, 13(2):912–915, 2002.

[250] Gaetano Scamarcio, Federico Capasso, Carlo Sirtori, Jerome Faist, Albert L Hutchinson, Deborah L Sivco, and Alfred Y Cho. High-power infrared (8-micrometer wavelength) superlattice lasers. *Science*, 276(5313):773–776, 1997.

[251] AV Shorokhov and KN Alekseev. High-frequency absorption and gain in superlattices: Semiquasistatic approach. *Physica E: Low-dimensional Systems and Nanostructures*, 33(1):284–295, 2006.

[252] Kirill N Alekseev, Natalia V Demarina, and Maxim V Gorkunov. Generation of high-frequency radiation in semiconductor superlattices with suppressed space-charge instabilities. *arXiv preprint cond-mat/0503216*, 2005.

[253] AB Hummel, T Bauer, E Mohler, and HG Roskos. The coherent Hall effect of charge carriers in a superlattice: semiclassical description of the wavepacket dynamics. *Journal of Physics: Condensed Matter*, 18(8):2487, 2006.

[254] Timo Hyart, Natalia V Alexeeva, Ahti Leppänen, and Kirill N Alekseev. Terahertz parametric gain in semiconductor superlattices in the absence of electric domains. *Applied Physics Letters*, 89(13):132105, 2006.

[255] GM Zaslavski and BV Chirikov. Stochastic instability of non-linear oscillations. *Physics-Uspekhi*, 14(5):549–568, 1972.

[256] DK Chaĭkovsky and GM Zavlavsky. Channeling and percolation in two-dimensional chaotic dynamics. *Chaos: An Interdisciplinary Journal of Nonlinear Science*, 1(4):463–472, 1991.

[257] G Petschel and T Geisel. Unusual manifold structure and anomalous diffusion in a Hamiltonian model for chaotic guiding-center motion. *Physical Review A*, 44(12):7959, 1991.

[258] Andrey R Kolovsky and Giorgio Mantica. Driven Harper model. *Physical Review B*, 86(5):054306, 2012.

[259] Philip George Harper. Single band motion of conduction electrons in a uniform magnetic field. *Proceedings of the Physical Society. Section A*, 68(10): 874, 1955.

[260] Andrey R Kolovsky. Simulating cyclotron-Bloch dynamics of a charged particle in a 2d lattice by means of cold atoms in driven quasi-1d optical lattices. *Frontiers of Physics*, 7(1):3–7, 2012.

[261] Serge Aubry and Gilles André. Analyticity breaking and anderson localization in incommensurate lattices. *Ann. Israel Phys. Soc*, 3(133):18, 1980.

[262] George M Zaslavsky. Chaos, fractional kinetics, and anomalous transport. *Physics Reports*, 371(6):461–580, 2002.

[263] T Geisel, A Zacherl, and G Radons. Generic 1 f noise in chaotic hamiltonian dynamics. *Physical Review Letters*, 59(22):2503, 1987.

[264] T Geisel, A Zacherl, and G Radons. Chaotic diffusion and 1/f-noise of particles in two-dimensional solids. *Zeitschrift für Physik B Condensed Matter*, 71(1):117–127, 1988.

[265] Karlheinz Ochs. A comprehensive analytical solution of the nonlinear pendulum. *European Journal of Physics*, 32(2):479, 2011.

[266] Allan J Lichtenberg and Blake P Wood. Diffusion through a stochastic web. *Physical Review A*, 39(4):2153, 1989.

[267] Robert W Boyd and Daniel J Gauthier. Controlling the velocity of light pulses. *Science*, 326(5956):1074–1077, 2009.

[268] Lester M Field. Some slow-wave structures for traveling-wave tubes. *Proceedings of the IRE*, 37(1):34–40, 1949.

[269] Eugene I Butikov. Extraordinary oscillations of an ordinary forced pendulum. *European Journal of Physics*, 29(2):215, 2008.

[270] FG Bass, VV Zorchenko, and VI Shashora. Stark-cyclotron resonance in semiconductors with a superlattice. *Soviet Journal of Experimental and Theoretical Physics Letters*, 31:314, 1980.

[271] Yu O Averkov, FG Bass, AP Panchekha, and OM Yevtushenko. Motion of a particle with an arbitrary dispersion relation in a high-frequency oscillating field. *Physical Review B*, 48(24):17995, 1993.

[272] RG Scott, S Bujkiewicz, TM Fromhold, PB Wilkinson, and FW Sheard. Effects of chaotic energy-band transport on the quantized states of ultracold sodium atoms in an optical lattice with a tilted harmonic trap. *Physical Review A*, 66(2):023407, 2002.

[273] MT Greenaway, AG Balanov, and TM Fromhold. Resonant control of cold-atom transport through two optical lattices with a constant relative speed. *Physical Review A*, 87(1):013411, 2013.

[274] BT Seaman, M Krämer, DZ Anderson, and MJ Holland. Atomtronics: Ultracold-atom analogs of electronic devices. *Physical Review A*, 75(2): 023615, 2007.

[275] RA Pepino, J Cooper, DZ Anderson, and MJ Holland. Atomtronic circuits of diodes and transistors. *Physical Review Letters*, 103(14):140405, 2009.

[276] H Ott, E De Mirandes, F Ferlaino, G Roati, G Modugno, and M Inguscio. Collisionally induced transport in periodic potentials. *Physical Review Letters*, 92(16):160601, 2004.

[277] Alexey V Ponomarev, Javier Madronero, Andrey R Kolovsky, and Andreas Buchleitner. Atomic current across an optical lattice. *Physical Review Letters*, 96(5):050404, 2006.

[278] Ulrich Schneider, Lucia Hackermüller, Jens Philipp Ronzheimer, Sebastian Will, Simon Braun, Thorsten Best, Immanuel Bloch, Eugene Demler, Stephan Mandt, David Rasch, et al. Fermionic transport and out-of-equilibrium dynamics in a homogeneous hubbard model with ultracold atoms. *Nature Physics*, 8(3):213–218, 2012.

[279] R Bonifacio, GRM Robb, and BWJ McNeil. Propagation, cavity, and doppler-broadening effects in the collective atomic recoil laser. *Physical Review A*, 56(1):912, 1997.

[280] R Bonifacio and L De Salvo. Collective atomic recoil laser (carl) optical gain without inversion by collective atomic recoil and self-bunching of two-level atoms. *Nuclear Instruments and Methods in Physics Research Section A: Accelerators, Spectrometers, Detectors and Associated Equipment*, 341(1): 360–362, 1994.